

TECH LIBRARY KAFB, NM



0061312



NASA CR-119

0.1

NASA CONTRACTOR REPORT

NASA CR-119-62

**LOAN COPY: RETURN TO
AFWL (DOUL)
KIRTLAND AFB, N. M.**

DYNAMIC ERRORS IN STRAPDOWN INERTIAL NAVIGATION SYSTEMS

Prepared by
THE ANALYTICAL SCIENCES CORPORATION
Reading, Mass. 01867
for





0061312

TECHNICAL REPORT STANDARD TITLE PAGE

1. REPORT NO. NASA CR-1962	2. GOVERNMENT ACCESSION NO.	3. RECIPIENT'S CATALOG NO.	
4. TITLE AND SUBTITLE DYNAMIC ERRORS IN STRAPDOWN INERTIAL NAVIGATION SYSTEMS		5. REPORT DATE December 1971	6. PERFORMING ORGANIZATION CODE M213
		8. PERFORMING ORGANIZATION REPORT # ASC - TR-147-3	
7. AUTHOR (S)		10. WORK UNIT NO.	11. CONTRACT OR GRANT NO. NAS 12-678
9. PERFORMING ORGANIZATION NAME AND ADDRESS The Analytical Sciences Corporation 6 Jacob Way Reading, Mass. 01867		13. TYPE OF REPORT & PERIOD COVERED Low Series Contractor Report	
		14. SPONSORING AGENCY CODE	
12. SPONSORING AGENCY NAME AND ADDRESS National Aeronautics and Space Administration Washington, D. C. 20546		15. SUPPLEMENTARY NOTES This report also summarizes work performed under NASA Contract NAS 12-508.	
16. ABSTRACT Motion-induced errors in strapdown inertial navigation systems are discussed. The errors generated in single-degree-of-freedom gyros and accelerometers are treated in great detail. These sensor errors are related to errors at the system level and common pulse rebalance techniques are compared. Since instrument signal transmission characteristics are found to be important, describing function analysis is applied to nonlinear pulse torqued inertial sensor loops, and the results are compared with simulations. Two means for reducing motion-induced errors are explored -- selection of inertial sensor parameters and active error compensation by measuring the environment, computing the errors generated and correcting for them.			
17. KEY WORDS Strapdown Inertial Navigation Strapdown Sensors Pulse Rebalanced Sensors Strapdown Dynamic Testing		18. DISTRIBUTION STATEMENT	
19. SECURITY CLASSIF. (of this report) U	20. SECURITY CLASSIF. (of this page) U	21. NO. OF PAGES 301	22. PRICE \$6.00

Inertial Navigation

24 Feb 72



FOREWORD

This report summarizes work performed for the NASA Electronics Research Center and the NASA Marshall Space Flight Center under Contracts NAS12-508 and NAS12-678, over a period of about four years. Previously most of this work was documented in four separate reports (Refs. 1, 2, 3 and 14). The present document brings together the major points of the research and attempts to organize them in a logical framework. Of necessity many minor subjects covered in the above-referenced documents have been omitted here. Also, on rare occasions, reference is made to those earlier reports for specific details. However, every reasonable effort has been made to make this document self-contained.

Since the work covered in this report spanned several years, the list of contributors is long and was omitted from the cover page. The research reported here was performed by the following persons at TASC: William S. Beebee, Joe C. Dunn, John H. Fagan, Arthur Gelb, William D. Koenigsberg, Charles F. Price, and Arthur A. Sutherland, Jr., Dr. Herbert Weinstock and Messrs. Lawrence Sher and Edward Koenke of the Electronics Research Center and Messrs. Billy Doran and Samuel O'Hanian at Marshall Space Flight Center provided support and encouragement. This summary volume was edited by A.A. Sutherland, Jr.



TABLE OF CONTENTS

	<u>Page No.</u>
LIST OF FIGURES	ix
LIST OF TABLES	xv
1. INTRODUCTION	
1.1 Background	1-1
1.2 Outline of the Study	1-2
1.3 Organization of the Report	1-4
PART I: ERROR GENERATION	
2. DYNAMIC ERRORS IN STRAPDOWN SENSORS	
2.1 Single-Degree-of-Freedom Gyro	2-1
2.1.1 Angular Motion Error Torques	2-5
2.1.2 Linear Acceleration Error Torques	2-14
2.2 Single-Degree-of-Freedom Pendulous Accelerometer	2-15
2.3 Torquing Errors	2-19
3. RELATIONSHIP BETWEEN STRAPDOWN SYSTEM ERRORS AND INSTRUMENT ERRORS	
3.1 Information Flow	3-1
3.2 Equations for System Errors	3-3
3.3 Typical Errors Generated in System Calculations	3-5
4. POTENTIAL SYSTEM-LEVEL ERRORS	
4.1 Example I: Booster Limit Cycle	4-1
4.2 Example II: Helicopter, Pulse Torqued Gyros	4-5
4.3 Example III: Helicopter, Single-Axis Platform Gyros	4-15

TABLE OF CONTENTS(continued)

Page
No.

PART II: PULSE REBALANCE LOOPS

5.	DESCRIPTION OF PULSE TORQUING SCHEMES	
5.1	Pulse Rebalanced Gyros	5-1
5.2	Gyro Errors Attributable to Pulse Torquing	5-7
5.3	Comparison of Pulse Torquing Techniques	5-12
6.	BINARY PULSE REBALANCE LOOPS	
6.1	Analysis of the Limit Cycling Binary Gyro	6-1
6.1.1	Response to Sinusoidal Inputs	6-2
6.1.2	Limit Cycle Quenching	6-9
6.1.3	Response to Random Inputs	6-12
6.2	Simulation of the Binary Gyro	6-14
6.3	Compensation for the Limit Cycling Binary Gyro	6-21
6.4	Summary	6-27
7.	TERNARY PULSE REBALANCE LOOPS	
7.1	Analysis of the Ternary Gyro	7-1
7.1.1	Response to Sinusoidal Inputs	7-1
7.1.2	Response to Random Inputs	7-13
7.2	Simulation of the Ternary Gyro	7-25
7.3	Summary	7-33
8.	TIME-MODULATED REBALANCE LOOPS	
8.1	Analysis of the Time-Modulated Gyro	8-1
8.1.1	Response to Sinusoidal Inputs	8-1
8.1.2	Response to Random Inputs	8-4
8.2	Simulation of the Time-Modulated Gyro	8-4
8.3	Summary	8-7

PART III: ERROR REDUCTION

9.	SELECTION OF SENSOR PARAMETERS TO REDUCE SYSTEM ERRORS	
9.1	Designable Parameters	9-1

TABLE OF CONTENTS (continued)

	<u>Page No.</u>
9.2 Cost Function and Representation of Random Motion	9-5
9.3 Example I: Binary Gyros	9-11
9.4 Example II: Time-Modulated Gyros	9-19
10. GYRO DYNAMIC ERROR COMPENSATION	
10.1 Introduction	10-1
10.2 Compensating Crosscoupling Errors	10-4
10.2.1 An Approach to Compensation	10-4
10.2.2 Simulation Results	10-8
10.3 Compensating Output Axis Errors	10-9
10.3.1 Open Loop Compensation	10-10
10.3.2 Closed Loop Compensation Using Corrective Torquing	10-15
10.3.3 Closed Loop Compensation in a Computer	10-23
10.4 Compensating Anisoinertia Error	10-27
10.4.1 Closed Loop Compensation	10-30
10.4.2 Open Loop Compensation	10-40
10.5 Summary	10-48
PART IV: SUMMARY	
11. SUMMARY AND CONCLUSIONS	
11.1 Summary	11-1
11.2 Conclusions	11-4
APPENDIX A MOTION INDUCED ERROR TORQUES FOR THE SINGLE-DEGREE-OF-FREEDOM GYRO AND PENDULOUS ACCELEROMETER	A-1
APPENDIX B DETAILED CALCULATIONS OF VIBRATION- INDUCED STRAPDOWN SYSTEM ERRORS	B-1
APPENDIX C MOTION-INDUCED ERRORS IN VIBRATING STRING ACCELEROMETERS	C-1

TABLE OF CONTENTS (concluded)

	<u>Page No.</u>
APPENDIX D ERROR DYNAMICS FOR SINGLE-AXIS-PLATFORM GYROS	D-1
APPENDIX E DESCRIBING FUNCTION CALCULATIONS	E-1
REFERENCES	R-1

LIST OF FIGURES

<u>Figure No.</u>		<u>Page No.</u>
1.2-1	Progression of Motion-Induced Strapdown System Errors	1-3
2.1-1	Single-Degree-of-Freedom Gyro	2-2
2.1-2	Strapdown Gyro Rebalance Loop	2-3
2.1-3	Strapdown Single-Degree-of-Freedom Gyro Error Torques	2-5
2.1-4	Error Model of Rotor Speed Control Loop	2-9
2.1-5	Mass Unbalance Terms for the Float Assembly	2-15
2.2-1	Single-Degree-of-Freedom Pendulous Accelerometer	2-16
2.3-1	Torquer Scale Factor Errors	2-22
3.1-1	Strapdown Inertial Navigator	3-1
4.2-1	Orientation of Data Coordinate Frame in CH 46-C Helicopter	4-6
4.2-2	Sensor Orientation Relative to the Body Coordinate Frame	4-6
4.2-3	Power Spectral Density, z Axis Acceleration	4-7
4.2-4	Power Spectral Density, x Axis Angular Velocity	4-7
4.2-5	Cross Spectral Density (Real Component), y Axis Acceleration, z Axis Angular Velocity	4-7
4.2-6	Linearized Model for Gyros and Accelerometers	4-11
4.2-7	Hamilton Standard 1139 SDF Gyro Gain Diagram	4-11
4.2-8	Kearfott 2401 Pendulous Accelerometer Gain Diagram	4-11
4.2-9	Sample-and-Hold Computer Model Gain Diagram	4-12
4.2-10	Coning Error as a Function of Computer Cycle Time	4-14
4.3-1	Gyro Response to Input Axis Vibrations, Hamilton Standard 1139 SDF Gyro, Operated as a SAP	4-17
5.1-1	Binary Logic	5-3
5.1-2	Representative Torque Output from Delta Modulated Pulse Rebalance Technique	5-3

LIST OF FIGURES (continued)

<u>Figure No.</u>		<u>Page No.</u>
5.1-3	Ternary Logic	5-3
5.1-4	Time-Modulated Torquing	5-4
5.1-5	Torquer Waveform for Time-Modulated Torquing	5-5
5.2-1	Torque Pulse Variation When the Torquer Lag is a Significant Fraction of the Pulse Period	5-9
6.1-1	Binary-Torqued Gyro Loop With Second-Order Gyro Dynamics	6-2
6.1-2	Representation of a Linear Gyro Loop	6-4
6.1-3	Closed Loop Frequency Response as a Function of Float Time Constant	6-7
6.1-4	Closed Loop Frequency Response Showing the Effect of Sampling	6-9
6.1-5	Binary Loop Viewed at the Point Where the Signal Quenches the Limit Cycle	6-11
6.1-6	Limit Cycle Quenching and Its Effect on Frequency Response (Second-Order Gyro Dynamics)	6-13
6.2-1	Simulation Records for Limit-Cycling Binary Gyro	6-15
6.2-2	Binary Gyro Simulation: 20 Hz Input	6-16
6.2-3	Binary Gyro Simulation: 165 Hz Input	6-17
6.2-4	Frequency Response of a Limit Cycling Binary Gyro: Comparison of Analytic and Simulation Results	6-18
6.2-5	Binary Gyro Simulation Record Showing Limit Cycle Quenching	6-19
6.2-6	Frequency Response of a Limit Cycling Binary Gyro: Comparison of Analytic and Simulation Results	6-20
6.2-7	Random Input Response of a Limit Cycling Binary Gyro: Comparison of Analytic and Simulation Results	6-21
6.3-1	Open Loop Gain-Phase Plot for Uncompensated Binary Gyro	6-24

LIST OF FIGURES (continued)

<u>Figure No.</u>		<u>Page No.</u>
6.3-2	Closed Loop Gain for Limit Cycling Binary Gyro: Effect of Loop Compensation	6-26
7.1-1	Ternary-Torqued Gyro Loop	7-1
7.1-2	Linearized Ternary Gyro Loop	7-2
7.1-3	Family of Ellipses from Linear Part of the Ternary Gyro Loop	7-6
7.1-4	Combination of Family of Ellipses and Ternary Sinusoidal Input Describing Function	7-6
7.1-5	Ternary Gyro Closed Loop Gain	7-7
7.1-6	Effect of Input Amplitude on Closed Loop Gain of a Representative Ternary Gyro Loop	7-9
7.1-7	Ternary Gyro Response With Frequency Island	7-11
7.1-8	Ternary Gyro Transfer Characteristics Showing Development of Frequency Islands	7-12
7.1-9	Gain of Ternary Gyro as a Function of Input Amplitude	7-13
7.1-10	Output Gain Characteristic of the Ternary Gyro for a Random Input	7-20
7.1-11	Output Phase Lag of Ternary Gyro for a Random Input	7-20
7.1-12	Power Spectral Density at the Output of the Ternary Gyro: White Noise Input	7-21
7.1-13	Nonlinear Function of the Standard Deviation of the Float Angle	7-22
7.1-14	Time History of Ternary Gyro With a Random Input, Illustrating Multimoding	7-24
7.1-15	Gain Response for Ternary Gyro With Two Modes	7-25
7.2-1	Ternary Gyro Simulation Records: 20 Hz Input	7-27
7.2-2	Ternary Gyro Simulation Records: 150 Hz Input	7-28

LIST OF FIGURES (continued)

<u>Figure No.</u>		<u>Page No.</u>
7.2-3	Gain Response of a Ternary Gyro: Comparison of Analytic and Simulation Results	7-29
7.2-4	Ternary Gyro Simulation Record Illustrating Jump Resonance	7-29
7.2-5	Ternary Gyro Simulation Record Illustrating Origin of Frequency Islands	7-30
7.2-6	Random Input Response of a Ternary Gyro: Comparison of Analytical and Simulation Results	7-32
8.1-1	Gyro Rebalance Loop With Time-Modulated Pulse Torquing	8-1
8.1-2	Linearized Representation of the Time-Modulated Loop	8-3
8.2-1	Sinusoidal Input Response for the Time-Modulated Gyro	8-5
8.2-2	Random Input Response for the Time-Modulated Gyro	8-6
9.1-1	Parameter Grouping in a Ternary Torqued Pulse Rebalanced Gyro	9-4
9.2-1	In-Phase Angular Oscillations	9-6
9.3-1	Orientation of Gyros for Examples I and II	9-13
10.1-1	Open Loop Compensation	10-2
10.1-2	Closed Loop Compensation	10-3
10.2-1	Source of Crosscoupling Error	10-5
10.2-2	Signal Flow Diagram Illustrating Crosscoupling Errors	10-5
10.2-3	Block Diagram of Crosscoupling Error Compensation of One Gyro	10-7
10.3-1	Linear Mathematical Model of Strapdown Gyro	10-11
10.3-2	A Specific Orientation of Three Gyros With Input Axes Orthogonal	10-12
10.3-3	Open Loop Compensation for Three Orthogonal Gyros	10-12

LIST OF FIGURES (continued)

<u>Figure No.</u>		<u>Page No.</u>
10.3-4	Orientation of Three Single-Degree-of-Freedom Strapdown Gyros	10-15
10.3-5	Closed Loop Compensation Involving Corrective Torquing	10-16
10.3-6	Magnitude and Phase of Transfer Function Expressed in Eq. (10.3-6)	10-18
10.3-7	Magnitude and Phase of Transfer Function Expressed in Eq. (10.3-7)	10-18
10.3-8	Magnitude and Phase of Transfer Function Expressed in Eq. (10.3-8)	10-19
10.3-9	Magnitude and Phase of the Transfer Function Expressed in Eq. (10.3-11)	10-21
10.3-10	Magnitude and Phase of the Transfer Function Expressed in Eq. (10.3-10)	10-21
10.3-11	Unstable Closed Loop Compensation in a Computer	10-25
10.3-12	Stable Closed Loop Compensation in a Computer	10-27
10.4-1	Block Diagram Illustrating Effect of Anisoinertia Torque on Gyro Output	10-29
10.4-2	Mechanization of Closed Loop Anisoinertia Error Compensation Technique for a Single Gyro	10-31
10.4-3	Linearized Error Flow Diagram When Anisoinertia-Rotor Speed Errors are Reduced by Closed Loop Compensation	10-33
10.4-4	Simplified Linearized Closed Loop System Associated With Fig. 10.4-3	10-33
10.4-5	Simplified Linearized Closed Loop System Associated With Fig. 10.3-4	10-35
10.4-6	Closed Loop Compensation for the System Represented by Fig. 10.3-4	10-35
10.4-7	Performance of Closed Loop Anisoinertia Error Compensation Technique	10-39

LIST OF FIGURES (continued)

<u>Figure No.</u>		<u>Page No.</u>
10.4-8	Mechanization of Open Loop Anisoinertia Error Compensation Technique for a Single Gyro	10-41
10.4-9	Open Loop Compensation for System Represented by Fig. 10.3-4	10-42
10.4-10	Amplitude-Phase Characteristics for $G(j2\pi f)$ in Eq. (10.4-11)	10-43
10.4-11	Open Loop Compensation for System Represented by Fig. 10.3-4, Including Gyro-Induced Errors	10-45
10.4-12	Evaluation of Open Loop Anisoinertia Compensation by Computer Simulation	10-47
A.1-1	Exploded View of Single-Degree-of-Freedom Gyro Showing Small Misalignment Angles, α and β	A-3
A.2-1	Exploded View of Single-Degree-of-Freedom Pendulous Accelerometer Showing Small Misalignment Angles, α	A-10
B.3-1	Computer Program Flow Diagram	B-13
C-1	Vibrating String Accelerometer (AMBAC Industries D4e Model)	C-2
D-1	Single-Axis-Platform Gyro	D-2
E-1	Nonlinearity Input and Output Waveforms	E-3
E-2	Input and Output Waveforms for Two Nonlinearities With Bias Plus Sinusoid Input	E-4

LIST OF TABLES

<u>Table No.</u>		<u>Page No.</u>
4.1-1	Range of Typical Values of Gyro Parameters	4-2
4.1-2	Maximum Constant Drift Rate	4-4
4.2-1	Computer Program Input Data	4-9
4.2-2	List of Symbols	4-10
4.2-3	Vibration-Induced Errors in a Strapdown Navigator	4-13
4.3-1	SAP Torquer Characteristics	4-16
4.3-2	Vibration-Induced Errors in a SAP Strapdown Navigator	4-18
5.3-1	Comparison of Pulse Torque Techniques	5-14
6.3-1	Loop Compensation Transfer Functions	6-26
9.1-1	Designable Parameters: Single-Degree-of-Freedom Floated Rate Integrating Gyro	9-3
9.4-1	Original and Optimal Set of Designable Parameters: No Practicality Constraints	9-23
9.4-2	Original and Optimal Set of Designable Parameters: Practicality Constraint on I_{00}	9-23
9.4-3	Original and Optimal Set of Designable Parameters: Output Axis Errors Compensated	9-25
B.3-1	Major Sources of Vibration-Induced Error	B-14
B.3-2	Major Gyro Error Expressions	B-16
B.3-3	Major Accelerometer Error Expressions	B-17
B.3-4	List of Symbols (For Tables B.3-2 and B.3-3)	B-18/B-19
B.3-5	Definitions of Fourier Transforms	B-27
B.3-6	Typical System-Level Error Expressions	B-30
B.3-7	Definitions of Standard Integrals	B-31

1.

INTRODUCTION

1.1 BACKGROUND

Strapdown inertial measurement units, in which the sensors are rigidly attached to the vehicle, offer many potential advantages over their gimballed counterparts. These include: lower weight and power consumption, more flexible packaging, easier assembly and maintenance, as well as lower cost and improved reliability. On the other hand, in the strapdown system greater demands are made on the sensors and computer. This report treats a problem of major importance to strapdown systems -- errors which result from interaction between the inertial sensors and their motion environment.

As a result of body mounting, vehicle rotational motions are transmitted directly to the gyros and accelerometers, forcing consideration of many error terms which are of little relative importance when stabilized platforms are used. The sensor torque rebalance loops and the coordinate transformation calculation required in strapdown systems also provide mechanisms for the generation of important system-level errors. All of these factors must be considered in the course of developing high accuracy strapdown inertial reference systems.

One question that arises is "What parameters are at the disposal of the designer, and how should they be chosen to optimize the performance of the strapdown inertial navigation system?" These parameters include: damping coefficient, moments of inertia, gyro rotor speed, maximum rebalance torque, loop sampling frequency, nonlinearity dead-band, etc. They are not necessarily free for independent choice. In addition, the

possibility for active compensation of sensor errors bears heavily on the best choice of design parameters and promises to provide an independent approach to error reduction. This document summarizes studies related to predicting motion-induced strapdown sensor errors and reducing their impact on system performance.

1.2 OUTLINE OF THE STUDY

The goal of the research summarized here was to take a comprehensive look at the effect of motion-induced gyro and accelerometer errors on the accuracy of strapdown inertial navigation systems. Figure 1.2-1 illustrates the progression of errors through a strapdown system, beginning as error torques on the inertial sensors and winding up as system-level drift rates and acceleration errors. The characteristics of the motion-induced error torques in single-degree-of-freedom gyros and accelerometers were explored. Some of these error torques are influenced by sensor (e.g., gyro and rebalance electronics combined) dynamics. It was noted that the dynamic environment can generate constant error torques at the sensor level (rectification at the sensor level), giving constant gyro and accelerometer errors that translate directly into serious drift rates and acceleration errors at the system level. In addition certain oscillatory sensor errors result. The latter do not appear to be serious when viewed at the outputs of the individual sensors but can cause large system-level errors by rectifying in the system calculations.

In order to relate system performance to sensor parameters and the motion environment, it is evident from Fig. 1.2-1 that descriptions of the sensor transmission characteristics are needed. However, strapdown instruments usually contain nonlinear pulse torquing loops and their

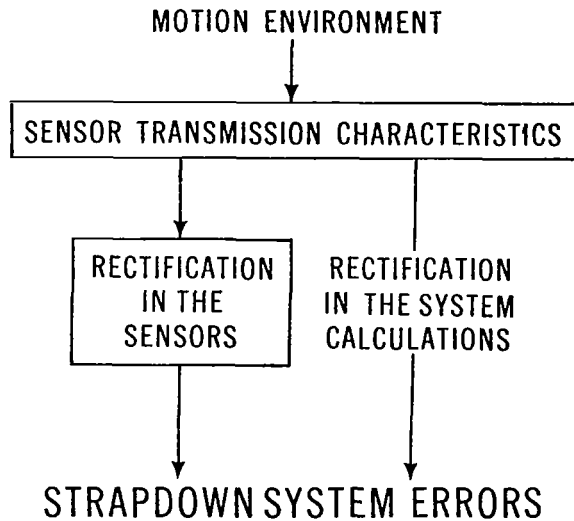


Figure 1.2-1 Progression of Motion-Induced Strapdown System Errors

behavior is difficult to analyze exactly. Describing function theory was successfully applied to this problem; good agreement was noted between analytically predicted sensor loop behavior and that observed during simulation.

Armed with analytic tools which relate system errors to the dynamic environment and the sensor parameters, the question of sensor design to optimize system performance was treated. While it was found that manipulating the designable parameters of the sensors can reduce motion-induced system errors, the required changes in physical parameters are by-and-large impractical. The major contributors to errors in the single-degree-of-freedom gyro, for example, are related to parameters which are vital to the operation of the instrument -- as distinguished from imperfections in the gyro construction. Consequently, physical constraints

often preclude changing these parameters to improve system performance, except within very narrow limits.

Since sensor design, per se, does not appear to be a wholly satisfactory way of reducing strapdown system errors, compensation techniques were investigated. In this case the fact that the error torques result from an interaction between the environment and well-known instrument parameters is advantageous. Given a measurement of the environment and knowledge of the important parameters it is possible to compute the error torques and apply appropriate corrections. This approach to system error reduction was explored at some length.

The research summarized in this document addresses the problem of predicting strapdown system performance in a given environment and explores techniques for reducing motion-induced system errors to an acceptable level.

1.3 ORGANIZATION OF THE REPORT

This report is divided into four main parts. Part I develops error models for the single-degree-of-freedom gyro and the single-degree-of-freedom pendulous accelerometer (Chapter 2), and demonstrates the manner in which sensor errors are translated into strapdown inertial system errors (Chapter 3). At the conclusion of Part I some examples are given in which the system-level motion-induced errors are computed for different motion environments and instrument parameters (Chapter 4).

Part II of the report is devoted to torque rebalance techniques for strapdown gyros and accelerometers. The three most common pulse torquing schemes are described in Chapter 5. In Chapters 6, 7, and 8

describing function analyses are applied to sensor loops which employ these techniques. In each case the predicted loop behavior is compared with the results of a simulation.

Ways to reduce motion-induced errors in strapdown systems are treated in Part III. Chapter 9 explores error reduction by selecting the sensor parameters while Chapter 10 discusses active compensation using the known instrument characteristics and the measured motion environment. Part IV contains a summary of the research effort and states conclusions that can be drawn from it.

PART I: ERROR GENERATION

2. DYNAMIC ERRORS IN STRAPDOWN SENSORS

This chapter discusses those errors in single-degree-of-freedom (SDF) strapdown gyros and SDF pendulous accelerometers which are caused by angular and linear motion and, to some extent, by rebalance mechanisms. The errors treated are expressed in the form of error torques, which constructively act about the output axis of each sensor in a manner similar to the basic quantities that the instrument is intended to measure. The question of whether the error torques always result in errors at the sensor output is treated in Part II of this document.

2.1 SINGLE-DEGREE-OF-FREEDOM GYRO

A single-degree-of-freedom gyro has a spinning rotor mounted in a gimbal that allows only one degree of freedom relative to the case (see Fig. 2.1-1). The equation of motion of an "ideal" linear single-degree-of-freedom gyro can be determined by equating reaction torques about the output axis to the gyroscopic precession torque which results from case motion about the input axis, viz:

$$I_{oo} \ddot{\alpha}_o + C \dot{\alpha}_o + K \alpha_o = H \omega_i \quad (2.1-1)$$

where

α_o = gimbal-to-case angle about the output axis

I_{oo} = rotor plus gimbal moment of inertia

C = viscous damping coefficient

K = spring constant

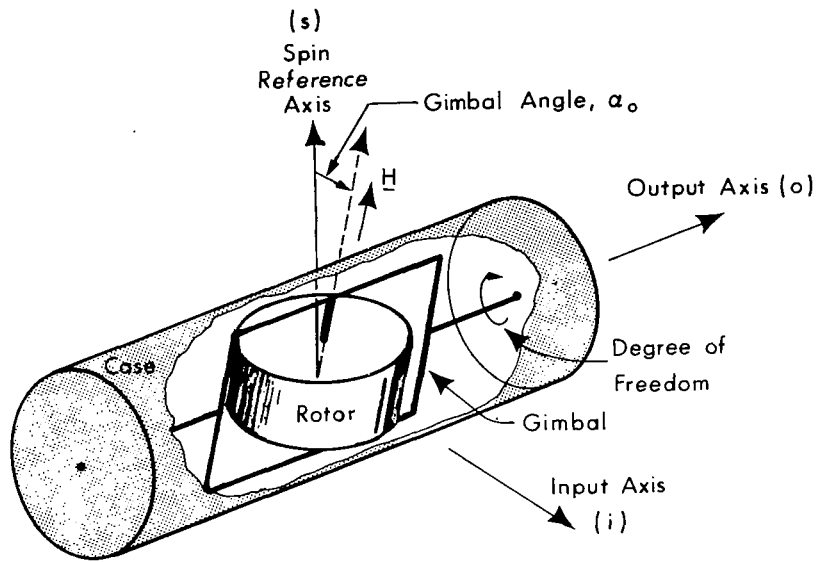


Figure 2.1-1 Single-Degree-of-Freedom Gyro

H = rotor angular momentum

ω_i = angular rate of the case about the input axis

As indicated by Eq. (2.1-1), in the absence of motion about other axes a constant value of ω_i results in the following steady-state value of α_o :

$$\alpha_o = \frac{H}{K} \omega_i$$

Hence, this gyro is referred to as a rate gyro, as the gimbal angle is a direct measure of case rate. In the situation where $K = 0$, we get a steady-state gimbal angle rate,

$$\dot{\alpha}_o = \frac{H}{C} \omega_i$$

Thus, gimbal angle is related directly to the integral of the input rate, and this gyro is therefore called a rate integrating gyro. By mounting the gyro

rotor in an enclosure which serves as the gimbal and floating the whole assembly in a fluid of appropriate density, the gyro output axis bearings are unloaded and thus some uncertainty torques are minimized. This configuration, called the float rate integrating gyro, is extensively used for very high accuracy applications such as inertial navigation.

In gimballed platform applications, the gyro float angle, α_o , is continuously nulled by platform gimbal servo action. In strapdown system applications, the gyro float angle is nulled by the application of a torque generated by passing an electric current through the windings of an output axis torquer. The current, which may be continuous (analog) or a series of pulses (digital), is based on a measurement of the float angle. The closed loop comprised of float dynamics, float angle pick-off, torquing electronics and output axis torquer is called the rebalance loop. The rebalance current is taken as a measure of input rate (for continuous torqued gyros) or incremental input angle (for pulse torqued gyros). Figure 2.1-2 shows a general schematic diagram of a strapdown gyro rebalance loop.

R-3753

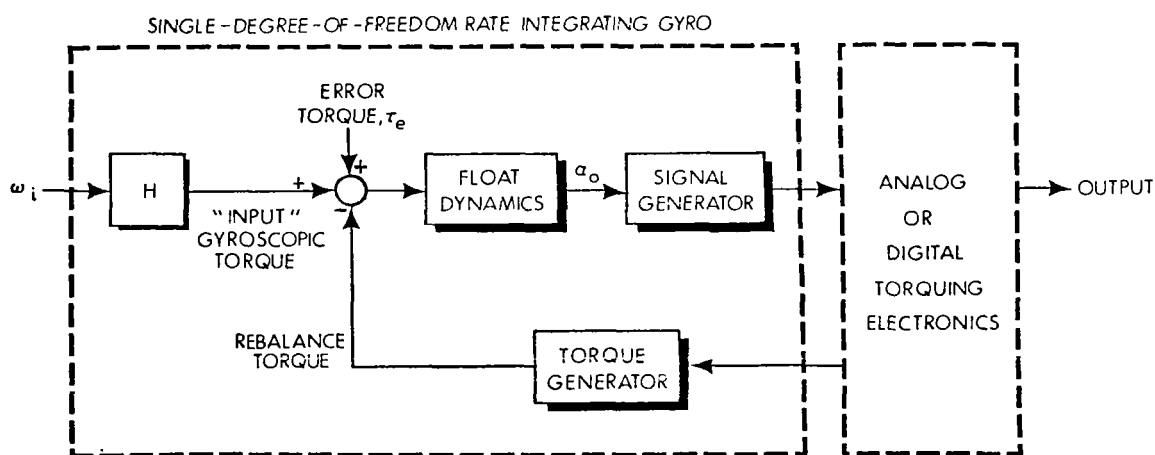


Figure 2.1-2 Strapdown Gyro Rebalance Loop

Gyro drift rate results from unwanted torques on the float. For reference purposes the various types of torques are displayed in Fig. 2.1-3. The nomenclature used in this figure as well as in subsequent sections is presented below. In each case the subscripts o, i, s refer to output, input and spin axes, respectively.

- f_o, f_i, f_s = case specific force -- the difference between inertial acceleration and gravitational acceleration
 $\omega_o, \omega_i, \omega_s$ = case angular rates
 $\dot{\omega}_o, \dot{\omega}_i, \dot{\omega}_s$ = case angular accelerations
 $\alpha_o, \alpha_i, \alpha_s$ = gimbal-to-case angular misalignments
 β_o, β_i = rotor-to-gimbal angular misalignments
 I_{oo}, I_{ii}, I_{ss} = float moments of inertia (including gimbal and rotor components)
 $I_{oo_r}, I_{ii_r}, I_{ss_r}$ = rotor moments of inertia
 $I_{os_g}, I_{oi_g}, I_{si_g}$ = gimbal products of inertia
 Ω_s = rotor spin rate relative to the gimbal
 $\delta_o, \delta_i, \delta_s$ = float center of mass displacements
 K_{ii}, K_{ss} = direct compliances
 $K_{is}, K_{si}, K_{so}, K_{io}$ = cross compliances
 K_{sg} = signal generator gain
 K_{tg} = torque generator gain
 $H = I_{ss_r} \Omega_s$
 m = float mass

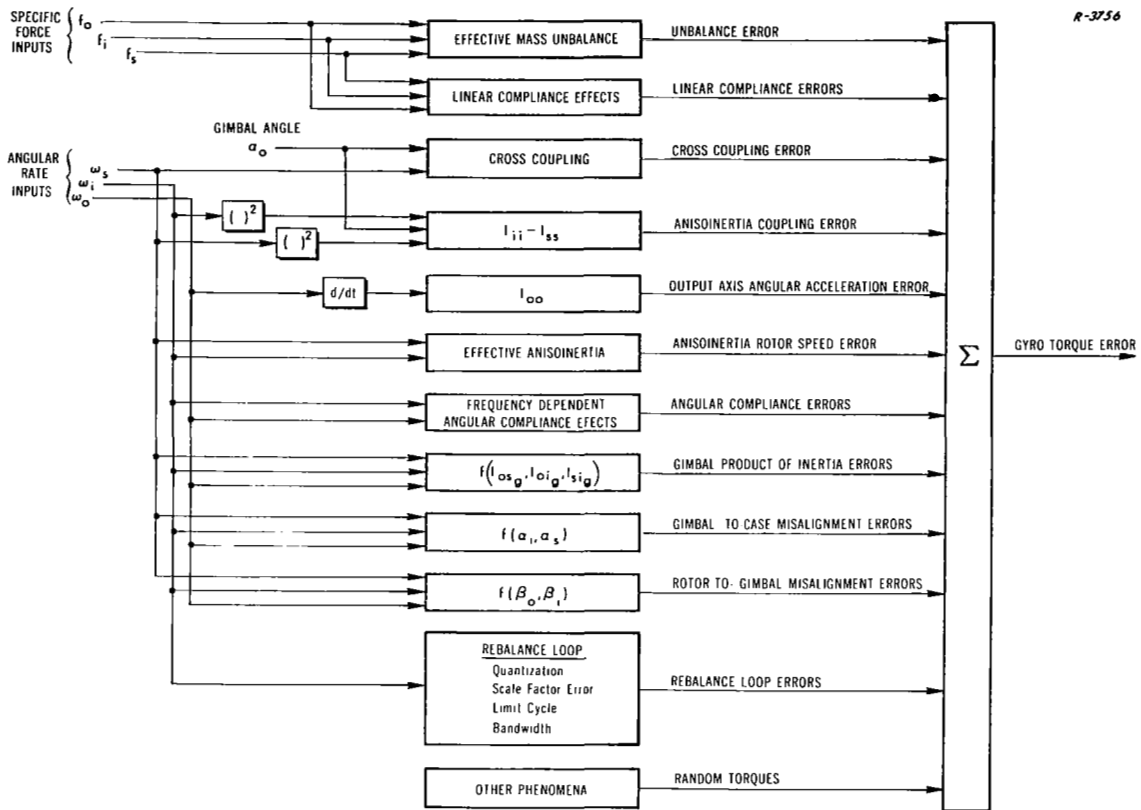


Figure 2.1-3 Strapdown Single-Degree-of-Freedom Gyro Error Torques

2.1.1 Angular Motion Error Torques

The error torques (τ_e) due to rotational motion are derived in Appendix A, and are presented below. It is assumed that the only angular motion between the gyro parts shown in Fig. 2.1-1 occurs along the gimbal output axis.

$$\begin{aligned}
\tau_e = & -I_{oo}(\ddot{\alpha}_o + \dot{\omega}_o) + (I_{ss} - I_{ii}) \omega_s \omega_i + I_{os_g} (\omega_o \omega_i - \dot{\omega}_s) \\
& -I_{oi_g} (\dot{\omega}_i + \omega_o \omega_s) + I_{si_g} (\omega_i^2 - \omega_s^2) + \alpha_o \left[(I_{ii} - I_{ss})(\omega_s^2 - \omega_i^2) - H\omega_s \right] \\
& + \alpha_s \left[(I_{ss} - I_{ii}) \omega_o \omega_s + H\omega_o + I_{oo} \dot{\omega}_i \right] + \alpha_i \left[(I_{ii} - I_{ss}) \omega_o \omega_i - I_{oo} \dot{\omega}_s \right] \\
& + \beta_o \left[(I_{ii_r} - I_{ss_r})(\omega_s^2 - \omega_i^2) - H\omega_s \right] + \beta_i \left[(I_{ss_r} - I_{oo_r})(\dot{\omega}_s - \omega_o \omega_i) + I_{ss_r} \dot{\omega}_s \right]
\end{aligned}
\tag{2.1-2}$$

The first term in Eq. (2.1-2), $-I_{oo} \ddot{\alpha}_o$, is the inertia reaction corresponding to gimbal-to-case angular acceleration. In combination with float viscous damping torque, $-C\dot{\alpha}_o$ it is responsible for the basic gyro time constant, and appears in the "ideal" gyro model of Eq. (2.1-1).

Output Axis Angular Acceleration — This error results from case motion about the output axis. It is given by

$$\begin{aligned}
\text{output axis angular} \\
\text{acceleration torque} = & -I_{oo} \dot{\omega}_o
\end{aligned}
\tag{2.1-3}$$

and is one of the larger error contributors in strapdown system mechanizations (see Chapter 4). Several schemes for compensation of this error are discussed in Chapter 10.

Cross-Coupling — Cross-coupling error torques are caused by failure to null the float angle, α_o . The cross-coupling terms in Eq. (2.1-2) are:

$$\begin{aligned}
\text{cross-coupling} \\
\text{torques} = & \alpha_o \left[(I_{ii} - I_{ss})(\omega_s^2 - \omega_i^2) - H\omega_s \right]
\end{aligned}
\tag{2.1-4}$$

The first term is commonly called anisoinertia coupling. The second term is often referred to as cross-coupling, and results from a portion of the case rate about the spin reference axis being applied along the actual gimbal input axis.

It is easily demonstrated that the cross-coupling term can result in a rectified gyro float torque. Consider the following case input rates:

$$\begin{aligned}\omega_i &= W_i \sin \nu t \\ \omega_o &= W_o \sin (\nu t + \gamma_o) \\ \omega_s &= W_s \sin (\nu t + \gamma_s)\end{aligned}\quad (2.1-5)$$

Presuming that the dominant torques acting on the float are given by

$$\text{dominant float torques} \cong H\omega_i - I_{oo}\dot{\omega}_o$$

it can be seen that for a linear, continuous rebalance loop the steady-state float angle response can (approximately) be expressed as a combination of sinusoids, each at frequency ν . Thus, writing the float angle as the linear rebalance loop response to the dominant float torques yields

$$\alpha_o(t) \cong W_i L_1(\nu) \sin (\nu t + \lambda_1(\nu)) + \nu W_o L_2(\nu) \sin (\nu t + \gamma_o + \lambda_2(\nu))\quad (2.1-6)$$

where

$$\begin{aligned}L_1(\nu) &= \frac{H}{\sqrt{(K_{sg} K_{tg} K_1 - I_{oo} \nu^2)^2 + (C\nu)^2}}, & L_2(\nu) &= \frac{I_{oo}}{H} L_1(\nu) \\ \lambda_1(\nu) &= -\tan^{-1} \frac{C\nu}{K_{sg} K_{tg} K_1 - I_{oo} \nu^2}, & \lambda_2(\nu) &= \lambda_1(\nu) - \frac{\pi}{2}\end{aligned}$$

and K_1 represents the gain of linear torquing electronics in Fig. 2.1-2. The second term in Eq. (2.1-6), proportional to ν , is the float response to output axis angular acceleration. From Eqs. (2.1-6) and (2.1-4) it can be seen that the cross-coupling term results in a non-zero average value (i.e., rectified) torque. It is given by

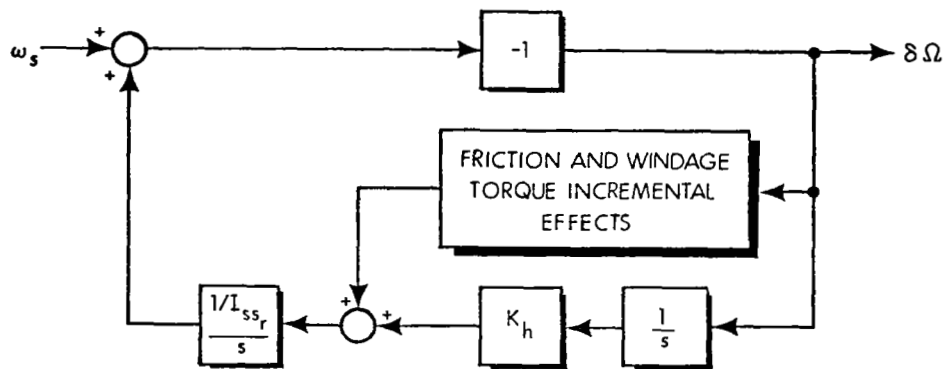
$$\begin{aligned} \text{average cross-coupling torque} = & -\frac{HW_s}{2} \left[W_i L_1(\nu) \cos(\lambda_1(\nu) - \gamma_s) \right. \\ & \left. + \nu W_o L_2(\nu) \cos(\gamma_o + \lambda_2(\nu) - \gamma_s) \right] \end{aligned} \quad (2.1-7)$$

The first term in this equation is called spin-input rectification, and the second is called spin-output rectification.

Anisoinertia-Rotor Speed Error — Conventionally, the anisoinertia torque has been taken as the term $(I_{ss} - I_{ii}) \omega_s \omega_i$ appearing in Eq. (2.1-2). But proper consideration of anisoinertia errors requires simultaneous treatment of rotor speed errors. This is shown in the following.

The rotor is driven by a hysteresis synchronous motor. When rotating in synchronism, the torque applied to the rotor is proportional to the phase difference between the rotor and the rotating field. This leads to the simplified rotor speed error model illustrated in Fig. 2.1-4, where ω_s is the input and $\delta\Omega$ is the output. In Laplace transform notation, we get (friction and windage torques, which are relatively small, are neglected):

$$\delta\Omega(s) = -\frac{s^2}{s^2 + K_h/I_{ssr}} \omega_s(s) \quad (2.1-8)$$



$\delta\Omega$ = CHANGE IN ROTOR SPEED RELATIVE TO THE GIMBAL
 K_h = TORQUE CONSTANT (HYSTERESIS SYNCHRONOUS MOTOR)

Figure 2.1-4 Error Model of Rotor Speed Control Loop

Considering the "ideal" gyroscopic torque to be $H\omega_i$, or, equivalently, $I_{ssr}\Omega_s\omega_i$, it can be seen that a rotor speed error leads to the following error torque:

$$\text{rotor speed error torque} = I_{ssr} \delta\Omega \omega_i$$

Thus, the effective anisoinertia error torque can be written as

$$\text{effective anisoinertia error torque} = (I_{ss} - I_{ii}) \omega_s \omega_i + I_{ssr} \delta\Omega \omega_i \quad (2.1-9)$$

The importance of the additional term can be seen by considering two limiting cases. First, assume ω_s to be slowly varying so that $\delta\Omega \cong 0$ at all times. From Eq. (2.1-9) we get

$$\text{anisoinertia error torque} = (I_{ss} - I_{ii}) \omega_s \omega_i \quad (2.1-10)$$

Eliminating this term thus becomes a matter of setting I_{ii} and I_{ss} equal. Since

$$I_{ii} = I_{ii_g} + I_{ii_r} \quad I_{ss} = I_{ss_g} + I_{ss_r} \quad (2.1-11)$$

an inertially asymmetric rotor leads to the requirement for an inertially asymmetric gimbal.

Next, consider the situation where ω_s is varying so rapidly that the speed control loop can not follow it at all. That is, $\delta\Omega \cong -\omega_s$. From Eq. (2.1-9) we now get

$$\begin{aligned} \text{anisoinertia error torque} &= (I_{ss} - I_{ii}) \omega_s \omega_i - I_{ss_r} \omega_s \omega_i \\ &= (I_{ss_g} - I_{ii}) \omega_s \omega_i \end{aligned} \quad (2.1-12)$$

Eliminating this error torque places different requirements on gimbal and rotor inertias. This effect can be argued physically by observing that the gyro rotor is essentially uncoupled (about the spin axis) from the rest of the instrument when the case experiences a high frequency angular oscillation about the spin axis. As a result of this uncoupling, the inertia of the rotor about the spin axis does not contribute to float error torques.

Of course, the changing effective anisoinertia term is a problem when attempts are made to reduce gyro error torques. For the input rates described in Eq. (2.1-5), it is readily shown that Eqs. (2.1-8) and (2.1-9) yield a rectified torque term given by:

$$\text{average effective anisoinertia torque} = \left[I_{ss_g} - I_{ii} + I_{ss_r} \left(\frac{K_h / I_{ss_r}}{K_h / I_{ss_r} - \nu^2} \right) \right] \frac{W_s W_i}{2} \cos \gamma_s \quad (2.1-13)$$

The frequency sensitive nature of this term is apparent.

Gimbal Products of Inertia — While they are usually small relative to other torques on an instantaneous basis, gimbal product of inertia terms can nevertheless be responsible for rectified float torques as well. The product of inertia terms are, from Eq. (2.1-2),

$$\begin{aligned} \text{gimbal product of} \\ \text{inertia torques} &= I_{os_g} \left[\omega_o \omega_i - \dot{\omega}_s \right] + I_{si_g} \left[\omega_i^2 - \omega_s^2 \right] \\ &\quad - I_{oi_g} \left[\dot{\omega}_i + \omega_o \omega_s \right] \end{aligned} \quad (2.1-14)$$

When subjected to the case angular rates described by Eq. (2.1-5), the non-zero average value of the gimbal product of inertia torques is

$$\begin{aligned} \text{average gimbal} \\ \text{product of} \\ \text{inertia torque} &= \frac{1}{2} \left[I_{os_g} W_o W_i \cos \gamma_o \right. \\ &\quad \left. + I_{si_g} (W_i^2 - W_s^2) - I_{oi_g} W_o W_s \cos(\gamma_o - \gamma_s) \right] \end{aligned} \quad (2.1-15)$$

Gimbal and Rotor Misalignment — We have already discussed the error torques due to gimbal-to-case misalignment about the output axis, α_o . There are also important torques caused by gimbal-to-case misalignments about the spin and input axes, as well as rotor-to-gimbal misalignments about the input and output axes. Rotor-to-gimbal misalignment about the spin axis is of no significance. The pertinent error torques are, from Eq. (2.1-2),

$$\begin{aligned}
\text{gimbal-to-case} \\
\text{misalignment} \\
\text{torques} &= \alpha_s \left[\left(I_{ss} - I_{ii} \right) \omega_o \omega_s + H \omega_o + I_{oo} \dot{\omega}_i \right] \\
&+ \alpha_i \left[\left(I_{ii} - I_{ss} \right) \omega_o \omega_i - I_{oo} \dot{\omega}_s \right] \quad (2.1-16)
\end{aligned}$$

and

$$\begin{aligned}
\text{rotor-to-gimbal} \\
\text{misalignment} \\
\text{torques} &= \beta_o \left[\left(I_{ii_r} - I_{ss_r} \right) \left(\omega_s^2 - \omega_i^2 \right) - H \omega_s \right] \\
&+ \beta_i \left[\left(I_{ss_r} - I_{oo_r} \right) \left(\dot{\omega}_s - \omega_o \omega_i \right) + I_{ss_r} \dot{\omega}_s \right] \quad (2.1-17)
\end{aligned}$$

where the misalignment angles are all treated as small and constant. The terms in these equations are similar in origin to others already discussed. There are anisoinertia terms, cross-coupling terms, anisoinertia coupling terms, case angular-acceleration terms due to cross-coupling, and rotor speed error terms. In the presence of constant angular rates or accelerations for long durations, these terms may be significant.

When subjected to the case angular rates described by Eq.(2.1-5), the non-zero average value of the misalignment terms is as follows:

$$\begin{aligned}
\text{average value of} \\
\text{misalignment} \\
\text{torques} &= \frac{\alpha_s}{2} \left(I_{ss} - I_{ii} \right) W_o W_s \cos(\gamma_o - \gamma_s) + \frac{\alpha_i}{2} \left(I_{ii} - I_{ss} \right) W_o W_i \cos \gamma_o \\
&+ \frac{\beta_o}{2} \left(I_{ii_r} - I_{ss_r} \right) \left(W_s^2 - W_i^2 \right) - \frac{\beta_i}{2} \left(I_{ss_r} - I_{oo_r} \right) W_o W_i \cos \gamma_o \quad (2.1-18)
\end{aligned}$$

The gimbal and rotor misalignment errors have, in addition to a constant portion resulting from imperfect gyro construction, time-varying characteristics which result from radial and axial suspension system compliance. These additional contributions are generated by gyroscopic torques due to output axis angular rates and inertia torques caused by angular accelerations. They can provide motion-induced error torques over and above those shown in Eq. (2.1-18) for constant misalignment. When designing suspension systems for the rotor and gimbals these errors must be computed and sufficient stiffness provided to keep them within acceptable limits.

Rotational Compliance — The gyro model employed thus far permits only one rotational degree of freedom about the spin axis, assuming that the rotor is otherwise rigidly connected to the float structure. Similarly, one rotational degree of freedom -- about the output axis -- is permitted and the float is otherwise rigidly connected to the case. In a real gyroscope, however, angular compliance is present between the rotor and the float and between the float and the case about all axes. The additional degrees of freedom are responsible for high frequency resonant phenomena in the gyroscope. A discussion of suitable spring-mass models for the compliance effects can be found in Ref. 4. For our present purposes it is sufficient to recognize the existence of these terms, and to note that the resonant frequencies involved bracket the structural natural frequency given by $\sqrt{K/I_{ijr}}$, where K is the spring constant between the rotor and gimbal about the input (output) axis, in dyne-cm/rad. This frequency is typically on the order of 400 or more Hz.

Rotor Dynamic Unbalance — A disturbance torque about the gyro output axis can result if the rotor does not have perfect dynamic balance. This introduces an oscillatory error at the rotor spin frequency and is

independent of the environment. It has some bearing on compensation schemes within the gyro loop; since the torque enters the loop as a disturbance at rotor spin frequency care must be taken not to provide a high gain at that frequency when placing compensation in the rebalance loop. Rotor dynamic imbalance in two gyros is a potential source of system coning error (see Chapter 3).

2.1.2 Linear Acceleration Error Torques

The gyro error torques produced by linear case accelerations -- or more correctly, specific force -- are derived in Appendix A. For convenience they are summarized below:

$$\tau_e = m\delta_{iS}f_s - m\delta_{Si}f_i + m\delta_{Oo}f_o + m^2 \left[K_{io}f_o f_s + K_{is}f_s^2 + (K_{ii} - K_{ss})f_i f_s - K_{so}f_o f_i - K_{si}f_i^2 \right] \quad (2.1-19)$$

Mass Unbalance — The first two terms in Eq. (2.1-19) which are proportional to the first power of the float mass are called mass unbalance terms because they are related to effective offsets of the float center of gravity from the gimbal axis (see Fig. 2.1-5). The third term, $m\delta_{Oo}f_o$, represents an experimentally observed effect which is thought to result from thermal convection currents in the flotation fluid.

Linear Compliance — The remaining terms in Eq. (2.1-19) are proportional to the square of the float mass and result from linear compliance. The quantity $(K_{ii} - K_{ss})f_i f_s$, similar in form to the anisoinertia terms of Section 2.1-1 is called the anisoelastic torque. Observe that each

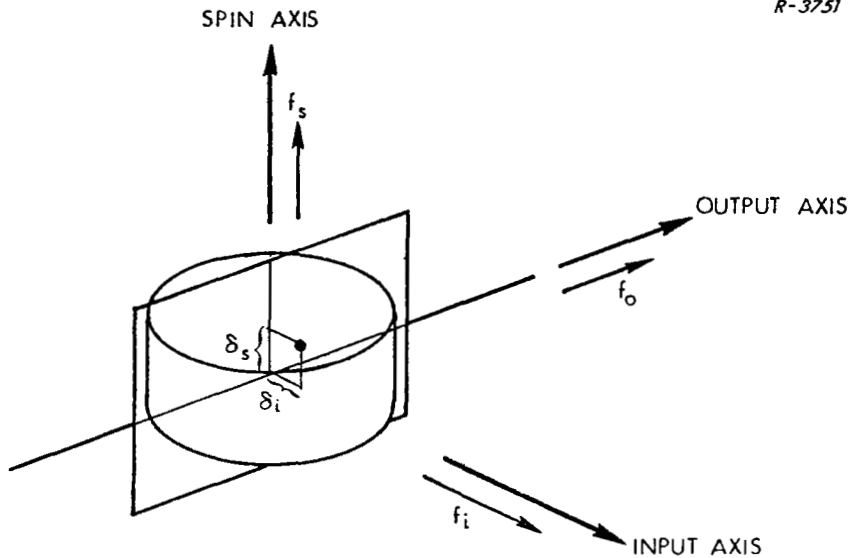


Figure 2.1-5 Mass Unbalance Terms for the Float Assembly

term in the brackets can produce a non-zero average torque when the specific force components f_i , f_s , and f_o are properly correlated.

2.2 SINGLE-DEGREE-OF-FREEDOM PENDULOUS ACCELEROMETER

Errors introduced in the single-degree-of-freedom pendulous accelerometer are discussed below. Whenever possible the error torque mechanisms are related to those given for the SDF gyroscope in Section 2.1. Free use is made of both the derivations and discussions presented there and in Appendix A.

The SDF pendulous accelerometer is illustrated in Fig. 2.2-1. Two major differences between this instrument and the SDF gyro are obvious. The direction perpendicular to the output and input axes is

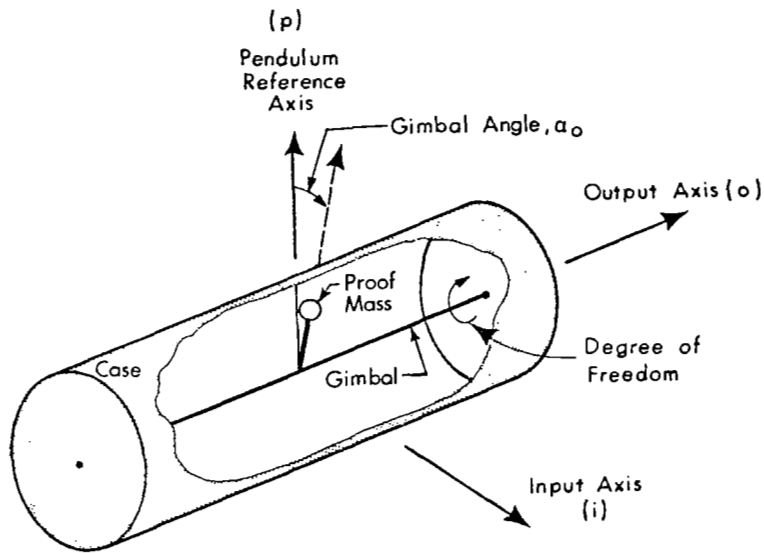


Figure 2.2-1 Single-Degree-of-Freedom Pendulous Accelerometer

called the pendulum (p) axis rather than the spin (s) axis. Also, the instrument is assumed to consist of only two basic parts: a case and a combination gimbal and pendulum. The error torques induced in the SDF pendulous accelerometer by angular motion can be expressed by appropriately modifying the equations for the gyro. The resulting expression for output axis torques produced by angular motion is developed in Appendix A. It is repeated here:

$$\begin{aligned}
 \tau_e = & -I_{oo}(\ddot{\alpha}_o + \dot{\omega}_o) + (I_{pp} - I_{ii})\omega_p \omega_i + I_{op}(\omega_o \omega_i - \dot{\omega}_p) \\
 & -I_{oi}(\dot{\omega}_i + \omega_o \omega_p) + I_{pi}(\omega_i^2 - \omega_p^2) + \alpha_o(I_{ii} - I_{pp})(\omega_p^2 - \omega_i^2) \\
 & + \alpha_p \left[(I_{pp} - I_{ii})\omega_o \omega_p + I_{oo}\dot{\omega}_i \right] + \alpha_i \left[(I_{ii} - I_{pp})\omega_o \omega_i - I_{oo}\dot{\omega}_p \right] \quad (2.2-1)
 \end{aligned}$$

Since the ideal accelerometer is insensitive to angular motion, all of the terms in Eq. (2.2-1) must be considered as error torques. However, as in the case of the SDF gyro, the first term, $-I_{OO} \ddot{\alpha}_O$, together with any damping torque about the instrument output axis, is usually considered as part of the unavoidable sensor dynamics and included in any "ideal" SDF pendulous accelerometer model. The remaining error terms can be divided into several broad categories similar to many exhibited by the gyro.

Output Axis Angular Acceleration — Sensitivity to angular accelerations is present. The principal contribution, that caused by angular acceleration about the sensor output axis ($-I_{OO} \dot{\omega}_O$), is unavoidable because of the nature of the pendulous acceleration sensing instrument.

Anisoinertia — Several anisoinertia terms appear. Because the gimbal and pendulum of the accelerometer can be viewed as a rigid body, the opportunity exists here to design an instrument which experiences no error torques from this cause.

Products of Inertia — Product of inertia terms appear in Eq. (2.2-1). The first of these terms can be larger than that experienced by a SDF gyro if the pendulum shown in Fig. 2.2-1 deviates from the p' direction in the $o'-p'$ plane. (See Appendix A for definition of primed axis directions.)

Misalignment — Misalignments contribute to errors in the SDF pendulous accelerometer. Many of the misalignment terms in Eq. (2.2-1) are similar to those in the corresponding expression for gyro error torquer. However, the instrument is less sensitive to those effects involving misalignment and angular motions, since no large angular momentum is present in the accelerometer.

Linear Motion — An equation for the error torques generated by linear motion (acceleration) of the SDF pendulous accelerometer is established in Appendix A;

$$\text{output axis torque} = -m\delta_p (f_i + \alpha_o f_p - \alpha_p f_o) + m\delta_i (f_p + \alpha_i f_o - \alpha_o f_i) \quad (2.2-2)$$

In Eq. (2.2-2) $f_i, f_o,$ and f_p are specific force components resolved into accelerometer case input, output, and pendulum axes, m is the mass of the gimbal and pendulum combination, δ_p and δ_i are components of the displacement between the pendulum center of mass and the gimbal output axis, resolved in gimbal coordinates, and $\alpha_o, \alpha_i,$ and α_p correspond to $\alpha_o, \alpha_i,$ and α_s for the gyro.

The effect of linear compliance on accelerometer errors can be illustrated by describing the center of mass displacement as a function of linear acceleration:

$$\begin{aligned} \delta_p &= m(K_{pi}f_i + K_{po}f_o + K_{pp}f_p) + \delta'_p \\ \delta_i &= m(K_{ii}f_i + K_{io}f_o + K_{ip}f_p) + \delta'_i \end{aligned} \quad (2.2-3)$$

where δ'_p and δ'_i are the mass displacements in the absence of specific force. Substituting Eq. (2.2-3) into Eq. (2.2-2), a more detailed torque equation results:

$$\begin{aligned} \text{output axis torque} &\cong -m\delta'_p (f_i + \alpha_o f_p - \alpha_p f_o) \\ &+ m\delta'_i (f_p + \alpha_i f_o - \alpha_o f_i) \\ &+ m^2 \left[K_{ip} f_p^2 + K_{io} f_o f_p + (K_{ii} - K_{pp}) f_i f_p - K_{po} f_i f_o - K_{pi} f_i^2 \right] \end{aligned} \quad (2.2-4)$$

The first term of Eq. (2.2-4), $-m\delta'_p f_i$, measures linear acceleration along the input axis. Only this term contributes to output axis torque in the ideal pendulous accelerometer. The pendulosity $m\delta'_p$ is designed into the instrument with care. All the remaining terms in this equation contribute errors to the accelerometer.

The term $m\delta'_p \alpha_o f_p$ is basically a cross-coupling error arising from rotation about the single axis of freedom and $m\delta'_p \alpha_p f_o$ results from gimbal-to-case misalignment. Since accelerations along the input axis may cause considerable excursions of the gimbal angle, α_o , from null, sizeable rectification (vibro-pendulous) errors can be produced in this instrument by properly phased linear vibrations with components along the input and pendulum axes.

The second line of Eq. (2.2-4) illustrates error torque contributions from unwanted mass unbalance and the last line expresses compliance error terms. It can be seen that linear compliance effects can produce constant error torques. The accelerometer is also subject to random error torques similar to those in an SDF gyro. The error in indicating linear accelerations along the case fixed input axis of an SDF pendulous accelerometer is simply the sum of all error torques (all terms in Eq. (2.2-4) other than $-m\delta'_p f_i$), divided by the pendulosity, $m\delta'_p$.

2.3 TORQUING ERRORS

In strapdown systems employing sensors of the type treated here, both gyros and accelerometers are torqued. Part II of this document describes the three most common pulse torquing techniques in some detail and shows how to analyze the closed loop response of instruments using these

rebalance schemes. In this section sensor-level errors introduced by unequal positive and negative torque-pulse weights are treated.

In Part II three pulse rebalance schemes are analyzed -- binary, ternary and time-modulation. For the purpose of the discussion that follows here the latter technique will be lumped with the first and described as "binary torquing". The two share a common feature -- they are always producing a torque on the float regardless of the input -- which makes them produce identical errors of the type discussed here.

Binary Torquing -- In the case of binary torquing we can model the torquing error in terms of a general plus-pulse weight and a general minus-pulse weight -- each of which differs a bit from standard. Taking the standard pulse weight as the incremental angle $\Delta\theta$ and general plus- and minus-pulse weights as $\Delta\theta(1 + \eta^+)$ and $-\Delta\theta(1 + \eta^-)$, respectively, for a pulse duration of T sec the drift rate becomes

$$\begin{array}{l} \text{binary limit cycle error} \\ \text{(small input case)} \end{array} \cong \frac{\Delta\theta}{2T} (\eta^+ - \eta^-) \quad (2.3-1)$$

This expression is valid for small inputs, which do not materially affect the limit cycle waveform. For large, monotonic inputs, the binary rebalance loop pulse train must assume a non-zero average value corresponding to the input rate. The resulting moding pattern will be periodic, with n^+ positive pulses and n^- negative pulses during a time interval $(n^+ + n^-)T$ such that

$$\left(\frac{n^+ - n^-}{n^+ + n^-} \right) \frac{\Delta\theta}{T} = \omega_i$$

for rational values of $\omega_i / (\Delta\theta/T)$. The corresponding error in indicated input angular rate is

$$\left(\frac{n^+ \eta^+ - n^- \eta^-}{n^+ + n^-} \right) \frac{\Delta\theta}{T}$$

which can be rewritten as

$$\text{binary moding pattern error (large input case)} = \frac{\Delta\theta}{2T} (\eta^+ - \eta^-) + \left(\frac{\eta^+ + \eta^-}{2} \right) \omega_i \quad (2.3-2)$$

In the case where $\eta^+ = \eta^- = \eta$, this reduces to $\eta \omega_i$.

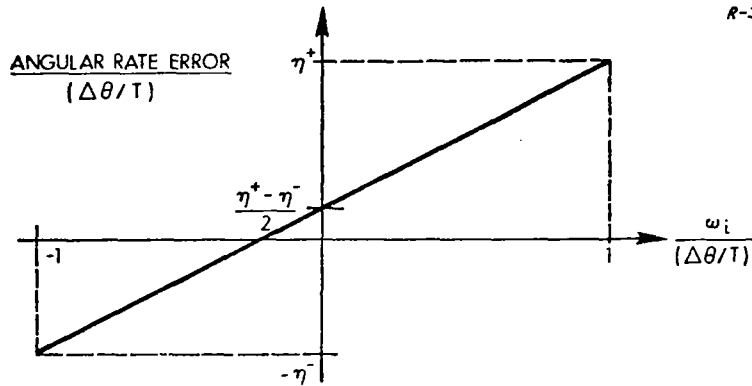
Ternary Torquing — For ternary torquing we can distinguish errors in plus-pulse weight, in minus-pulse weight, and in the zero torque level. Drift in the absence of an input is due to errors in the zero torque level:

$$\text{ternary calibration error (no inputs)} = \eta^0 \left(\frac{\Delta\theta}{T} \right) \quad (2.3-3)$$

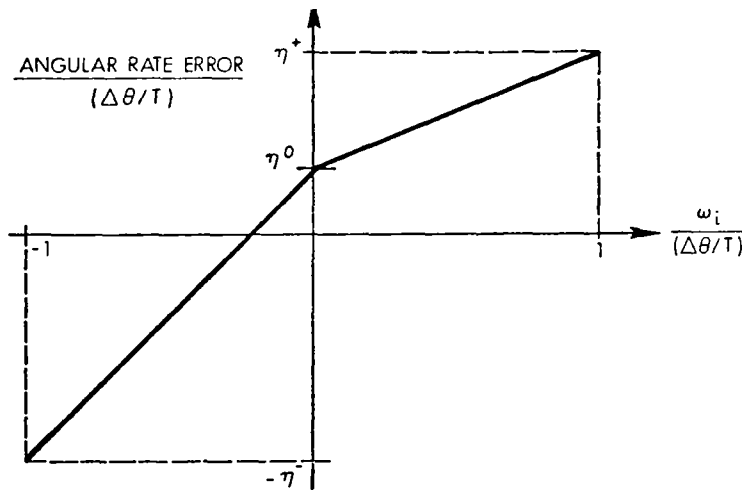
Again, the expression is approximately valid for small inputs. If we consider ratios of $\omega_i / (\Delta\theta/T)$ of the nature $1/q$ where q is an integer (other rational ratios do not provide unique moding without specification of gyro dynamics) the error rate with ternary torquing is:

$$\text{ternary moding error (large inputs with rational } \omega_i / (\Delta\theta/T)) = \eta^0 \left(\frac{\Delta\theta}{T} \right) + (\eta^* - \eta^0) \omega_i \quad (2.3-4)$$

The quantity η^* represents η^+ or η^- depending on whether ω_i is positive or negative. Figure 2.3-1 is a plot of the errors described by Eqs. (2.3-2), (2.3-3) and (2.3-4). Of course the errors indicated are only correct for rational values of $\omega_i / (\Delta\theta/T)$ with binary switching and ratios with characteristic $1/q$ for ternary switching.



(a) Binary Torquing



(b) Ternary Torquing

Figure 2.3-1 Torquer Scale Factor Errors

It is also to be noted that following calibration the stability of the pulse weights is of major importance. The effects of changes in torquer scale factor can differ, depending on the scheme used. For example, if η_0 is much more stable than η^+ and η^- a ternary torquer will give smaller bias errors in a benign environment.

It can be seen that the binary gyro torquer can be calibrated using two precise input angular rates (to define the straight line) while three accurate inputs are needed for the ternary torqued instrument.

3. RELATIONSHIP BETWEEN STRAPDOWN SYSTEM
ERRORS AND INSTRUMENT ERRORS

A measure of the quality of any inertial system, gimballed or strapdown, is some weighted combination of its attitude, position and velocity indication capabilities, depending on the mission involved. This chapter deals with the relationship between the individual gyro and accelerometer errors and the accuracy of a strapdown inertial reference system, placing particular emphasis on those errors generated in the system calculations.

3.1 INFORMATION FLOW

Figure 3.1-1 is a schematic representation of a strapdown inertial navigation system. The navigation computations are the same as for gimballed inertial systems.* The unique feature of strapdown systems is the

R-3076

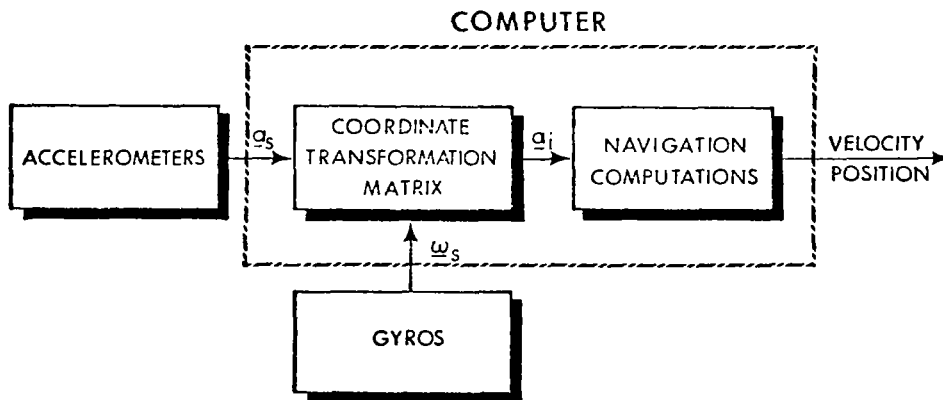


Figure 3.1-1 Strapdown Inertial Navigator

* For ease of presentation it is assumed here that navigation takes place in a set of inertially-fixed coordinates, represented by the subscript i.

coordinate transformation which resolves the acceleration (specific force) vector, \underline{a}_s , from system (body) axes to navigation axes, using the direction cosine matrix C_i^s :

$$\underline{a}_i = C_i^s \underline{a}_s \quad (3.1-1)$$

The gyros measure inertial angular rate in body axes, $\underline{\omega}_s$. This measurement can be used to update the attitude matrix, using the relation

$$\dot{C}_i^s = C_i^s \Omega_s \quad (3.1-2)$$

where the skew-symmetric matrix Ω is composed of the elements of $\underline{\omega}_s$, viz:

$$\Omega_s = \begin{bmatrix} 0 & -\omega_{z_s} & \omega_{y_s} \\ \omega_{z_s} & 0 & -\omega_{x_s} \\ -\omega_{y_s} & \omega_{x_s} & 0 \end{bmatrix}; \quad \underline{\omega}_s \triangleq \begin{bmatrix} \omega_{x_s} \\ \omega_{y_s} \\ \omega_{z_s} \end{bmatrix} \quad (3.1-3)$$

As demonstrated in Chapter 2 a variety of potential errors are introduced in the gyro and accelerometer measurements of \underline{a}_s and $\underline{\omega}_s$. It is easy to see that some of them, notably those which appear as constant errors at the outputs of the sensors themselves, can seriously impair the accuracy of a strapdown navigator. Still others, which do not appear to be serious when viewed at the level of the individual sensors, can combine in the calculations represented by Eqs. (3.1-1) through (3.1-3) to produce large errors at the system level. The mechanism for producing such errors

can be viewed as a rectification of oscillatory errors* from different sensors as the information is processed. Gyro errors affect the attitude matrix through Eq. (3.1-2). Errors in C_i^S then influence the calculation of \underline{a}_i through Eq. (3.1-1) and the update of the coordinate transformation, again through Eq. (3.1-2). The latter mechanism is responsible for the fact that serious rectification errors result not only from properly-phased outputs from gyros and accelerometers but from pairs of gyros as well. Finally, it will be shown that gyro and accelerometer errors need not take the substantive form suggested by the error torque equations of Chapter 2 in order to be dangerous; serious rectified system errors can result from failure of the inertial sensors to indicate true motion, as a consequence of bandwidth limitations. For this reason the loop response characteristics treated in Part II are as pertinent to the generation of system-level errors as the motion-induced error torques already described.

3.2 EQUATIONS FOR SYSTEM ERRORS

General equations for the propagation of errors in a strapdown navigation system are as follows:

$$\delta \ddot{\underline{r}}_i = \delta \left[C_i^S \underline{a}_s \right] - \delta \underline{G} \quad (3.2-1)$$

$$\delta \dot{C}_i^S = \delta \left[C_i^S \Omega_s \right] \quad (3.2-2)$$

* In actuality, the largest errors generated in the system calculations result from rectifying errors from one sensor with correct measurements from another, rather than errors from pairs of instruments.

where

\underline{r}_i = inertial position of the navigator

δ = error quantity

The sensor errors that rectify in the system calculation are oscillatory in nature, usually caused by vibratory motion. In order to treat the vibrational and nominal motions of the navigator separately, we will isolate the vibration-induced error contributions in Eqs. (3.2-1) and (3.2-2):

$$\underline{a}_s = \underline{a}_{\text{nominal}} + C_s^b \underline{a}_b$$

$$\underline{\Omega}_s \cong \underline{\Omega}_{\text{nominal}} + C_s^b \underline{\Omega}_b C_b^s$$

where

b = body coordinate frame, defining actual orientation of the navigator

s = system coordinate frame, defining nominal orientation of the navigator

\underline{a}_b = linear vibration vector, resolved in body coordinates

$\underline{\omega}_b$ = angular rate vibration vector resolved in body coordinates

$\underline{\Omega}_b$ = skew-symmetric matrix composed from navigator angular rate vibration components about body axes

C_s^b = transformation matrix from actual body frame to nominal body frame -- a function of the rotational vibrations

Substituting these definitions into Eqs. (3.2-1) and (3.2-2) yields

$$\delta \ddot{\mathbf{r}}_{-i} = \delta C_i^S \mathbf{a}_{-s} + C_i^S \delta(\mathbf{a}_{\text{nominal}}) - \delta \mathbf{G} + C_i^S \left[\delta \left(C_s^b \mathbf{a}_{-b} \right) \right] \quad (3.2-3)$$

$$\delta \dot{C}_i^S = \delta C_i^S \Omega_s + C_i^S \delta(\Omega_{\text{nominal}}) + C_i^S \left[\delta \left(C_s^b \Omega_b C_b^S \right) \right] \quad (3.2-4)$$

The first two terms on the right sides of Eqs. (3.2-3) and (3.2-4) illustrate the effects of misresolving nominal motion because of attitude errors (δC_i^S), and of the substantive errors in the outputs of the inertial sensors -- $\delta(\mathbf{a}_{\text{nominal}})$ and $\delta(\Omega_{\text{nominal}})$. The latter are simply resolved into errors in the inertial frame through the correct attitude matrix, C_i^S . The third entry on the right side of Eq. (3.2-3) accounts for errors in computing the gravitational specific force. The remainder of the terms in these two equations will be used in the next section to demonstrate how oscillatory errors are rectified in the system computer. It should be noted that any contributions which result from the bracketed terms can be viewed as additional errors emerging from strapdown gyros and accelerometers whose input axes are coincident with the nominal, or system coordinate frame, since the brackets are preceded by the transformation C_i^S . This is a useful way to represent system-level errors which are generated in the computer.

3.3 TYPICAL ERRORS GENERATED IN SYSTEM CALCULATIONS

Four classes of system-level errors generated in the computer are described here -- pseudo-coning, undetected coning, pseudo-sculling and undetected sculling. Together they represent all serious errors of this type that result from anomalous sensor behavior.

Pseudo-Coning Errors — Oscillatory errors at the gyro outputs can result in system-level errors that have the same effect as constant gyro drift rates. These pseudo-coning errors can result from properly phased pairs of gyro errors or from a similarly-related combination of errors from one gyro and actual motion indicated by another gyro. They derive their name from the fact that true coning -- an angular motion that returns the body to its original orientation periodically -- produces oscillatory angular rates about two orthogonal body axes, which are not in phase, and an average angular rate about the third orthogonal axis.* The magnitude of the latter depends on the relative phase and the amplitudes of the oscillations. If all the body angular rates are properly measured they will, to within the limits of the attitude matrix update algorithm used, be properly combined in the computer and no system error will result. If, on the other hand, oscillatory angular motion is incorrectly indicated by a gyro or gyros it can be interpreted as coning motion by the computer -- hence the term pseudo-coning. When errors of this type arise, the necessary average rate about a third axis is presumed to be cancelled by an opposing inertial angular rate of the system. A drift rate error about the third axis occurs.

One of the principal causes of pseudo-coning errors in strapdown systems is the error generated in single-degree-of-freedom gyros by output axis angular acceleration (see Section 2.1-1). The effect can be demonstrated by considering a pair of strapdown gyros. (There are three such pairs in a triad.) If an oscillatory angular motion ω_x occurs about the input axis of one gyro and about the output axis of the other, an error proportional to $\dot{\omega}_x$ is generated in the latter. The computer receives indications of ω_x from the first instrument and a false measurement $\delta\omega_y$ from the other. Expanding the third term in Eq. (3.2-4) will show how they combine to give an average system drift rate:

* See the succeeding discussion of undetected coning errors for a more precise description of coning motion.

$$\begin{aligned} \delta(C_s^b \Omega_b C_b^s) &= C_s^b \Omega_b \delta C_b^s + C_s^b \delta \Omega_b C_b^s + \delta C_s^b \Omega_b C_b^s + C_s^b \delta \Omega_b \delta C_b^s \\ &\quad + \delta C_s^b \Omega_b \delta C_b^s + \delta C_s^b \delta \Omega_b C_b^s + \delta C_s^b \delta \Omega_b \delta C_b^s \end{aligned} \quad (3.3-1)$$

For small oscillations the error $\delta\omega_y$ will cause errors in the attitude matrices as follows:

$$\delta C_s^b \cong \begin{bmatrix} 0 & 0 & \delta\varphi_y \\ 0 & 0 & 0 \\ -\delta\varphi_y & 0 & 0 \end{bmatrix} \quad \delta C_b^s \cong \begin{bmatrix} 0 & 0 & -\delta\varphi_y \\ 0 & 0 & 0 \\ \delta\varphi_y & 0 & 0 \end{bmatrix}$$

The error in the angular rate matrix is

$$\delta \Omega_b \cong \begin{bmatrix} 0 & 0 & \delta\omega_y \\ 0 & 0 & 0 \\ -\delta\omega_y & 0 & 0 \end{bmatrix}$$

where $\delta\varphi_y = \int \delta\omega_y dt$. The true attitude matrices are given by

$$C_s^b \cong \begin{bmatrix} 1 & 0 & 0 \\ 0 & 1 & -\varphi_x \\ 0 & \varphi_x & 1 \end{bmatrix}$$

$$C_b^s \cong \begin{bmatrix} 1 & 0 & 0 \\ 0 & 1 & \varphi_x \\ 0 & -\varphi_x & 1 \end{bmatrix}$$

where $\varphi_x = \int \omega_x dt$, and

$$\Omega_b = \begin{bmatrix} 0 & 0 & 0 \\ 0 & 0 & -\omega_x \\ 0 & \omega_x & 0 \end{bmatrix}$$

Multiplying out the first three terms in Eq. (3.3-1) (the remainder of Eq. (3.3-1) consists of higher order terms):

$$\delta(C_s^b \Omega_b C_b^s) \cong \begin{bmatrix} 0 & \delta\varphi_y \omega_x - \varphi_x \delta\omega_y & \varphi_x \delta\varphi_y \omega_x + \delta\omega_y \\ \varphi_x \delta\omega_y - \delta\varphi_y \omega_x & 0 & 0 \\ -\varphi_x \delta\varphi_y \omega_x - \delta\omega_y & 0 & 0 \end{bmatrix}$$

Since ω_x is assumed oscillatory $\delta\omega_y$ will not have any average value. However, $\delta\omega_y$ is proportional to the derivative of the true angular rate and therefore π radians out of phase with φ_x . The terms $\varphi_x \delta\omega_y$ and $\delta\varphi_y \omega_x$ will have definite non-zero average values, of equal magnitude and opposite signs, while the terms $\delta\omega_y$ and $\varphi_x \delta\varphi_y \omega_x$ will average to zero. The result is a constant contribution to the derivative of the error in the attitude matrix C_i^s . By comparing Eq. (3.2-4) with Eqs. (3.1-2) and (3.1-3) it can be seen that the average error generated can be interpreted as a constant drift rate, $\delta\omega_z$, in the third gyro of a triad.

Pseudo-coning errors can also be generated by properly phased errors in both gyros of a pair, represented by certain of the higher ordered terms in Eq. (3.3-1). However, these tend to be small in comparison with those provided by the combination of errors and true motion described above.

Undetected Coning Errors — Since coning motion can be experienced by vehicles containing strapdown inertial systems it is important that its presence be detected. If the oscillatory angular motion that is often a part of coning is of a frequency beyond the effective bandwidth of the strapdown gyros only the average body angular rate will be reported to the system computer; while the vehicle periodically returns to the same orientation, the attitude matrix will indicate a slow turning about one body axis.

Coning motion is characterized by out-of-phase vibrations about one body-fixed axis and one space-fixed axis. If $q = Q \sin \nu t$ represents the body-fixed angular rate oscillation about the x body axis and $r = R \cos \nu t$ represents the space-fixed angular oscillation about an axis nearly coincident with y body axis

$$C_s^b = (C_b^s)^T \cong \begin{bmatrix} 1 & 0 & \varphi \\ 0 & 1 & -\rho \\ -\varphi & \rho & 1 \end{bmatrix}$$

$$\Omega_b \cong \begin{bmatrix} 0 & -r\rho & r \\ r\rho & 0 & -q \\ -r & q & 0 \end{bmatrix}$$

where $q = \dot{\rho}$ and $r = \dot{\varphi}$. If the gyros measuring q , r , and $r\rho$ do not pass signals at frequencies of ν and higher

$$\delta\Omega_b = \begin{bmatrix} 0 & -(RQ/2\nu)\cos 2\nu t & -r \\ (RQ/2\nu)\cos 2\nu t & 0 & q \\ r & -q & 0 \end{bmatrix}$$

and

$$\delta C_s^b = (\delta C_b^s)^T \cong \begin{bmatrix} 0 & 0 & -\varphi \\ 0 & 0 & \rho \\ \varphi & -\rho & 0 \end{bmatrix}$$

Substituting the above expressions for $\delta\Omega_b$, δC_s^b and δC_b^s into Eq. (3.3-1) and eliminating higher order terms and terms which have no average value over one period $T = 2\pi/\nu$ yields:

$$\delta(C_s^b \Omega_b C_b^s) = \begin{bmatrix} 0 & -q\varphi & 0 \\ -r\rho & 0 & 0 \\ 0 & 0 & 0 \end{bmatrix} \quad (3.3-3)$$

The two non-zero entries in Eq. (3.3-3) are of equal magnitude and have opposite signs. In fact, Ref. 6 shows* that the average angular rate sensed by the third (z) gyro in the triad undergoing coning motion is given by

$$\begin{aligned} \omega_z &= -r\rho \\ &= q\varphi \end{aligned}$$

Equation (3.3-3) can be written as

$$\delta(\dot{C}_s^b) \cong \begin{bmatrix} 0 & -\omega_z & 0 \\ \omega_z & 0 & 0 \\ 0 & 0 & 0 \end{bmatrix} \quad (3.3-4)$$

* Equation [9], with some manipulation.

Equation (3.3-4) bears out the intrinsic feeling that since the only motion reported to the attitude update computer is the average angular rate about one body axis, ω_z , the attitude error will behave as though the z gyro exhibits a bias error of the same magnitude.

Pseudo-Sculling — Rectification of oscillatory errors from a gyro and an accelerometer with input axes not coincident, or of true motion and gyro or accelerometer errors properly phased, can cause apparent accelerometer bias errors at the system level. The point is illustrated by considering output axis angular acceleration errors in a pendulous accelerometer (see Section 2.2.2). The part of the last term of Eq. (3.2-3) that lies within the square brackets can be expanded to give

$$\delta \left(C_{s \underline{a}}^b \right) = C_{s \underline{a}}^b \delta \underline{a}_b + \delta C_{s \underline{a}}^b + \delta C_{s \underline{a}}^b \delta \underline{a}_b \quad (3.3-5)$$

If this expression has an average value it can be interpreted in terms of constant errors in the accelerometers.

If it is assumed that an angular oscillation takes place about one axis (x) and that the pendulous accelerometer whose purpose is to measure specific force along an orthogonal axis (y) has its output axis parallel to the direction of rotation, the following expressions apply for terms in Eq. (3.3-5).

$$C_{s \underline{a}}^b \cong \begin{bmatrix} 1 & 0 & 0 \\ 0 & 1 & -\varphi_x \\ 0 & \varphi_x & 1 \end{bmatrix} ; \quad \delta C_{s \underline{a}}^b = 0$$

$$\underline{a}_b = 0 ; \quad \delta \underline{a}_b = \begin{bmatrix} 0 \\ \delta a_y \\ 0 \end{bmatrix}$$

Substituting into Eqs. (3.3-5) and (3.2-3) gives

$$\underline{\delta \ddot{r}}_i = C_i^s \delta(C_s^b \underline{a}_b) = C_i^s \begin{bmatrix} 0 \\ \delta a_y \\ \varphi_x \delta a_y \end{bmatrix} \quad (3.3-6)$$

The average value of δa_y is zero but since

$$\varphi_x = \int \omega_y dt$$

and δa_y is proportional to $\dot{\omega}_y$ the product $\varphi_x \delta a_y$ has an average value; an apparent constant acceleration along the third orthogonal axis is generated in the system computations.

Undetected-sculling -- Since true sculling motion -- characterized by oscillatory linear and angular motion on body axes which results in an average acceleration in the system coordinate frame -- can occur, any failure to transmit information about the vibration can result in the system failing to properly detect the presence of sculling. For example, if a linear vibration along the y axis is accompanied by an angular vibration about the x axis and the accelerometers fail to pass the high frequency information

$$C_s^b = \begin{bmatrix} 1 & 0 & 0 \\ 0 & 1 & -\varphi_x \\ 0 & \varphi_x & 1 \end{bmatrix}; \quad \delta C_s^b = 0$$

$$\underline{a}_b = \begin{bmatrix} 0 \\ a_y \\ 0 \end{bmatrix}; \quad \underline{\delta a}_b = \begin{bmatrix} 0 \\ -a_y \\ 0 \end{bmatrix}$$

Equation (3.3-5) gives

$$\underline{\delta \ddot{r}}_i = C_i^S \begin{bmatrix} 0 \\ -a_y \\ -\phi_x a_y \end{bmatrix} \quad (3.3-7)$$

while the true acceleration \ddot{r}_i is given by

$$\begin{aligned} \ddot{r}_i &= C_i^S C_s^b a_b \\ &= C_i^S \begin{bmatrix} 0 \\ a_y \\ \phi_x a_y \end{bmatrix} \end{aligned} \quad (3.3-8)$$

As expected, the comparison of Eqs. (3.3-7) and (3.3-8) reveals that the error caused by failing to provide all of the motion information to the system computer is of equal magnitude and of opposite sign from the motion taking place -- the sculling motion is not detected. Of course the same error can be caused by inability to measure the angular vibration or by detecting neither linear nor angular oscillations. Obviously, the point is that if average linear (sculling) or angular (coning) motion is generated by unmeasured vibrations it will be misinterpreted by the system. An evident tradeoff exists regarding the bandwidth of the inertial sensors and the frequency of the attitude matrix calculations. (The latter are generally discrete in nature and also serve to reject high frequency instrument outputs). While a high overall bandwidth is needed to prevent errors due to undetected motion it also permits the transmission of high frequency sensor errors, which generate pseudo-coning and pseudo-sculling errors. The best band-

bandwidth for the sensor-computer combination depends on the sensors employed and the vibration environment.

It will be demonstrated in the succeeding chapter that errors generated in the manner described in this chapter can assume magnitudes larger than drift rates and accelerometer errors associated with good contemporary inertial sensors.

In this chapter the magnitude of motion-induced errors at the system level is illustrated. The purpose of these calculations is to demonstrate that dynamic errors in strapdown instruments of the type treated here can produce serious errors. Sections 4.2 and 4.3 also serve to introduce the reader to a complex computer program that is available for relating the dynamic environment to strapdown system errors.

4.1 EXAMPLE I: BOOSTER LIMIT CYCLE

Simple calculations of motion-induced errors are used here to illustrate the potential seriousness of the system level errors that can occur in a strapdown navigator. For simplicity only the effects of strapdown gyro errors are displayed.

Environmental disturbances acting on a single-degree-of-freedom gyro are capable of generating constant torques, as shown in Chapter 2. The maximum amplitude of the resultant constant drift rate is calculated in this section for several of these effects. Angular-motion-induced drift rates are emphasized because these are unique to the strapdown case. Table 4.1-1 displays the range of values assumed by important coefficients in a group of nine typical single-degree-of-freedom floated gyros intended for strapdown system usage. For purposes of this illustration, the following representative group of parameters is chosen:*

* Note that these parameters are not necessarily identical with those given in preceding or subsequent examples.

TABLE 4.1-1

RANGE OF TYPICAL VALUES OF GYRO PARAMETERS

Parameter	Symbol	Units	Typical Range	
			Minimum	Maximum
Rotor Angular Momentum	H	$\frac{\text{gm-cm}^2}{\text{sec}}$	5×10^4	3×10^6
Float Output Axis Moment	I_{oo}	gm-cm ²	100	250
Linear Damping Coefficient	C	dyne-cm-sec	6×10^4	8×10^5
Float Time Constant	τ_f	msec	0.25	6.0
Rotor Spin Axis Moment of Inertia	I_{ssr}	gm-cm ²	40	140
Anisoinertia Error Coefficient	$\frac{I_{ss} - I_{ii}}{H}$	$\frac{\text{deg/hr}}{(\text{rad/sec})^2}$	4	30
Uncertainty in Float Mass Unbalance	$\frac{m\delta_i}{H}, \frac{m\delta_s}{H}$	$\frac{\text{deg/hr}}{g}$	5×10^{-3}	3.3×10^{-1}
Anisoelastic Error Coefficient	$\frac{m^2}{H} (K_{ss} - K_{ii})$	$\frac{\text{deg/hr}}{g^2}$	4×10^{-3}	1×10^{-1}
Torquer Scale Factor Error	η	%	1×10^{-2}	5×10^{-2}
Torquer Time Constant	τ_{tg}	μsec	25	100
Misalignment Angles	$\alpha_i, \alpha_s, \beta_o, \beta_i$	sec	1	15
Torquer Sensitivity	K_{tg}	$\frac{\text{deg/hr}}{\text{ma}}$	75	1200
Signal Generator Sensitivity	K_{sg}	volt/rad	5	40

$$\begin{aligned}
H &= 2 \times 10^5 \text{ gm-cm}^2/\text{sec}, & I_{oi_g} &= I_{os_g} = 1.50 \text{ gm-cm}^2 \\
I_{oo} &= 250 \text{ gm-cm}^2, & I_{si_g} &= 0.30 \text{ gm-cm}^2 \\
I_{ss_r} &= 80 \text{ gm-cm}^2, & \frac{I_{ss} - I_{ii}}{H} &= 4(\text{deg/hr})/(\text{rad/sec})^2 \\
I_{ii_r} &= I_{oo_r} = 50 \text{ gm-cm}^2 \\
L_1(0) &= 2.0 \times 10^{-3} \frac{\text{rad}}{\text{rad/sec}}, & & \text{a measure of rebalance loop} \\
& & & \text{stiffness at low frequencies} \\
\frac{m\delta_i}{H} \text{ or } \frac{m\delta_s}{H} &= 5 \times 10^{-2} \frac{\text{deg/hr}}{g}, & \text{Torquer nonlinearity} &= \epsilon_{tg} = 0.01\% \\
\frac{m^2}{H} (K_{ss} - K_{ii}) &= 10^{-2} \frac{\text{deg/hr}}{g^2}, & \text{Misalignment angles} &= \pm 5 \widehat{\text{sec}}
\end{aligned}$$

The strapdown system is assumed to experience a six-g specific force and angular rate oscillations which, in the terminology of Sec. 2.1.1, give

$$W_i = W_o = W_s = 0.2 \text{ rad/sec}$$

$$\nu = 10 \text{ rad/sec}$$

for each gyro. The vibrations are representative of those anticipated in a typical boost vehicle as a consequence of limit cycling in the attitude autopilot. The peak constant gyro drift rates (assuming the worst combinations of misalignment, λ_1 , λ_2 , γ_o and γ_s and specific force orientation) in a single gyro were computed, using the relations presented in Chapter 2. They are presented in Table 4.1-2.

TABLE 4.1-2

MAXIMUM CONSTANT DRIFT RATE

Error Terms	Constant Drift Rate (deg/hr)
Spin-Input Cross Coupling	8.00
Spin-Output Cross-Coupling	0.10
Anisoinertia (Rotor Coupled)	0.08
Anisoinertia (Rotor Uncoupled)	1.52
Float Mass Unbalance	0.30
Anisoelasticity	0.06
Torquer Nonlinearity	2.60
Gimbal Products of Inertia	0.08
Misalignment*	0.50
Pseudo-Coning due to Output Axis Effect**	5.00

It should be noted that the anisoinertia error coefficient chosen in this example was at the low end of the range presented. This was done to illustrate the fact that choosing rotor and gimbal inertias to minimize drift rate when the rotor is coupled to the gimbal by the rotor speed regulation loop causes excessive drift rates when the rotor is uncoupled.

It can be seen from the simple calculations performed here that the strapdown rotational environment produces gyro drift rates which are large compared to the drift rates that are characteristic of gimballed platform systems. This observation prompted the development of a

* Computed on the basis of 0.05 rad/sec constant angular rates.

** A system-level error. See Chapter 3.

computer program for performing a more precise determination of motion-induced errors in strapdown systems (see Appendix B). The application of that software tool to a particular problem is described in the following sections.

4.2 EXAMPLE II: HELICOPTER, PULSE TORQUED GYROS

A digital computer program has been written for the purpose of calculating, source by source, system level errors generated by strapdown inertial sensors (see Appendix B). The program presently is capable of computing such errors for strapdown systems employing one particular (single-degree-of-freedom) gyro, in the pulse-torqued or single-axis-platform modes, and one of two accelerometers (single-degree-of-freedom pendulous and vibrating string), though it is by no means restricted to these. The set of equations coded take as their inputs instrument dynamic error coefficients and transfer characteristics, and up to 36 detailed spectral density functions describing the measured or postulated vibration environment. Devices to perform precise measurements of environment are becoming available (Ref. 7) and the value of the details incorporated in the program will increase as accurate vibration data are gathered for a variety of vehicles.

Vibration spectral data for the cruise and hover phases of a CH-46C helicopter flight were generated (Ref. 8) for use in the analysis of vibration-induced strapdown system errors. The orientation of the data coordinate frame is shown in Fig. 4.2-1. It was assumed in the analysis that the strapdown navigator frame, or body frame, was coincident with this set of axes. The orientation of the inertial instruments relative to the body frame is shown in Fig. 4.2-2. The vibration spectra, typical samples of which are shown in Figs. 4.2-3, 4.2-4, and 4.2-5, reflect the harmonics of the fundamental rotor frequency, 4Hz, and also

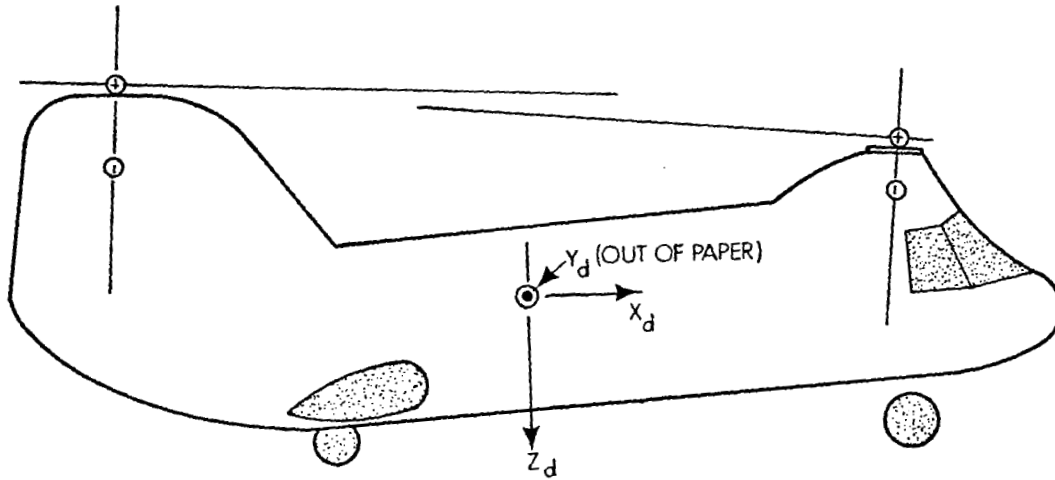


Figure 4.2-1 Orientation of Data Coordinate Frame in CH 46-C Helicopter

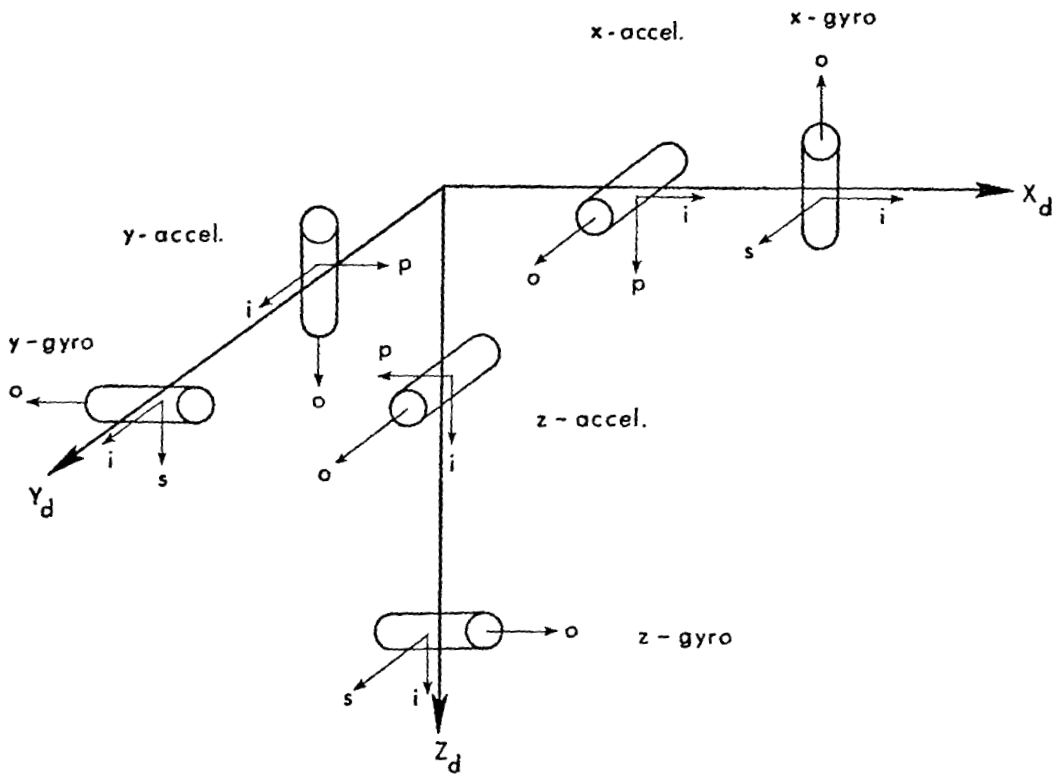


Figure 4.2-2 Sensor Orientation Relative to the Body Coordinate Frame

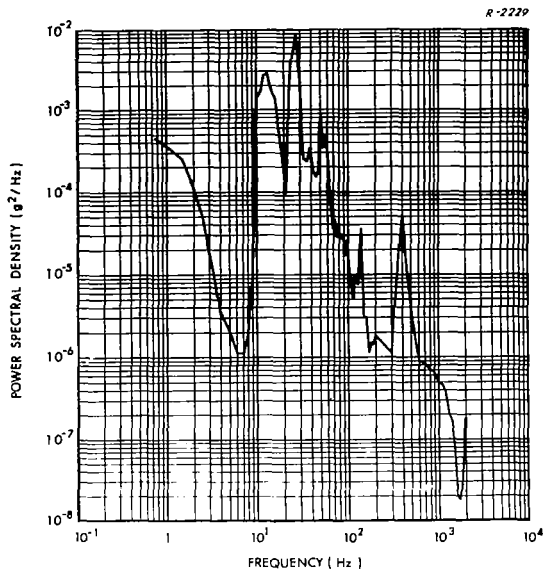


Figure 4.2-3 Power Spectral Density, z Axis Acceleration

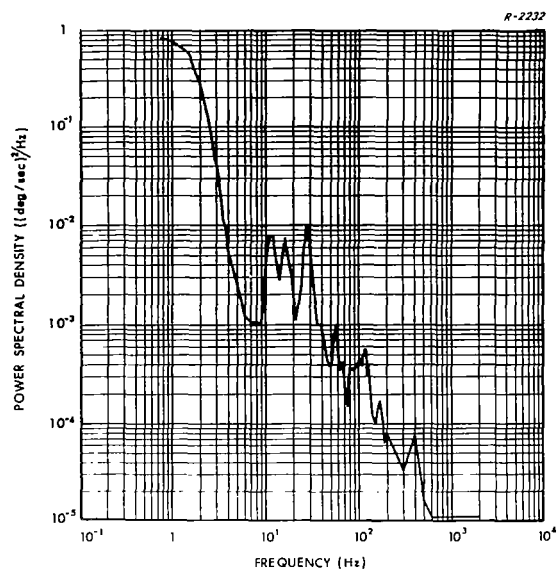


Figure 4.2-4 Power Spectral Density, x Axis Angular Velocity

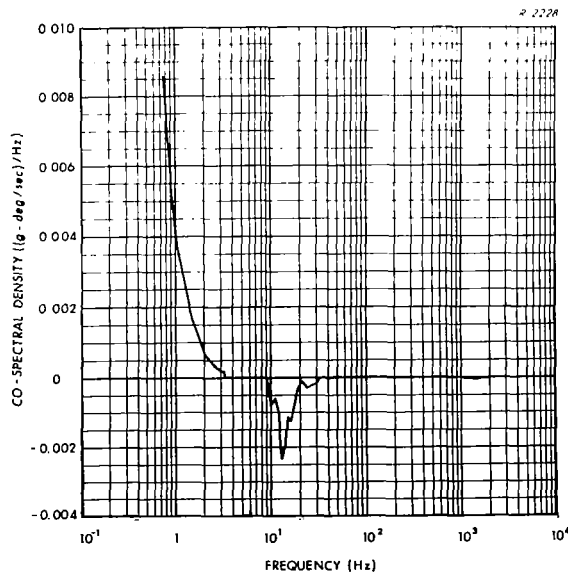


Figure 4.2-5 Cross Spectral Density (Real Component), y Axis Acceleration, z Axis Angular Velocity

contain power at higher frequencies due to the turbine engines. In this helicopter, the most significant angular vibrations occur about the longitudinal axis and vertical linear vibration is dominant.

Tables 4.2-1 and 4.2-2 and Fig. 4.2-6 contain the input data describing the physical parameters of the instruments (Norden 1139 gyro and Kearfott 2401 accelerometer), from which the error coefficients are defined. The remaining data in the tables establish the transfer characteristics of the gyro, accelerometer and computer, for which gain diagrams are shown in Figs. 4.2-7, 4.2-8, 4.2-9. If bandwidth is taken as the frequency at which the closed loop gain falls to $1/\sqrt{2}$ of its low frequency value, the gyro, accelerometer and computer bandwidths are approximately 70 Hz, 85 Hz and 25 Hz respectively. Indications of motion at frequencies higher than 25 Hz will not enter the system calculations since, for the computer algorithm cycle time selected, the computer effectively reduces the instrument bandwidths. From an examination of Figs. 4.2-3 and 4.2-4, it is evident that the dominant rotational vibrations, which occur at lower frequencies, will enter the system calculations, but that significant high-frequency linear vibrations will not be detected. The error analysis performed with the computer program substantiates these observations.

It is difficult to determine, from the vibration spectral data employed in this study, whether or not the strapdown navigator experiences true coning and true sculling motion, characterized by no net rotation or translation of the navigator coordinate axes. In order to verify that such motions do occur, it would be necessary to define the vibration environment in both the body coordinate frame and the system coordinate frame. In the error analysis described here it was assumed, without verification, that the strapdown system under consideration is undergoing true coning and true sculling motion and the system-level

TABLE 4.2-1

COMPUTER PROGRAM INPUT DATA

Norden 1139 Single-Degree-of-Freedom Gyro	Kearfott 2401 Pendulous Accelerometer
$I_{oo} = 354.0 \text{ gm-cm}^2$	$I_{oo} = 0.16 \text{ gm-cm}^2$
$C = 1.38 \times 10^6 \text{ dyne-cm-sec}$	$C = 400.0 \text{ dyne-cm-sec}$
$T_1 = 0.0143 \text{ sec}$	$M = 735.0 \text{ dyne-cm/rad}$
$T_2 = 1.0 \text{ sec}$	$T_4 = 0.00196 \text{ sec}$
$T_4 = 0.00143 \text{ sec}$	$T_a = 0.634 \times 10^{-8} \text{ sec}^2$
$T_a = 0.634 \times 10^{-8} \text{ sec}^2$	$T_b = 0.1125 \times 10^{-3} \text{ sec}$
$T_b = 0.1125 \times 10^{-3} \text{ sec}$	$T_c = 1.0$
$T_c = 1.0$	$K_{po} = 40.0 \text{ mv (rms)/mrad}$
$K_{po} = 70.0 \text{ mv (rms)/mrad}$	$K_{ac} = 153.0 \text{ volts (dc)/volt (rms)}$
$K_{ac} = 442.0 \text{ volts (dc)/volt (rms)}$	$K_{dc} = 33.0$
$K_{dc} = 33.0$	$K_{sg} = 0.62 \text{ ma/volt (dc)}$
$K_{sg} = 22.0 \text{ ma/volt (dc)}$	$K_{tg} = 163.0 \text{ dyne-cm/ma}$
$K_{tg} = 1110.0 \text{ dyne-cm/ma}$	$K_{sf} = 0.62 \text{ g/volt (dc)}$
$K_{sf} = 0.0978 \text{ rad/sec/volt (dc)}$	$P = 1100 \text{ gm-cm}$
$H = 2.5 \times 10^5 \text{ gm-cm}^2/\text{sec}$	$I_{oo} = 14 \text{ gm-cm}^2$
$I_{ii} = 592 \text{ gm-cm}^2$	$(I_{ii} - I_{pp})/P = 1.5 \text{ } \mu\text{g}/(\text{deg}/\text{sec})^2$
$I_{oo} = 400 \text{ gm-cm}^2$	$SF_a = 100 \text{ ppm}$
$I_{ssg} = 388 \text{ gm-cm}^2$	$K_2 = 10 \text{ } \mu\text{g}/\text{g}^2$
$I_{ssr} = 210 \text{ gm-cm}^2$	$D_{ap} = 0.5 \text{ } \widehat{\text{min}}$
$(K'_{ss} - K'_{ii}) = 0.06 \text{ deg/hr/g}^2$	$\epsilon = 10 \text{ ppm}$
$\delta'_i = \delta'_o = \delta'_s = 1.5 \text{ deg/hr/g}$	$p_{x1} = 15.9 \text{ cm}$
$SF_g = 100 \text{ ppm}$	$p_{x2} = 2.3 \text{ cm}$
$D_{go} = D_{gs} = 0.5 \text{ } \widehat{\text{min}}$	$p_{x3} = 6.6 \text{ cm}$
$\epsilon = 100 \text{ ppm}$	$p_{y1} = 2.3 \text{ cm}$
	$p_{y2} = 6.6 \text{ cm}$
	$p_{y3} = 2.3 \text{ cm}$
	$p_{z1} = 9.4 \text{ cm}$
	$p_{z2} = 26.8 \text{ cm}$
	$p_{z3} = 5.0 \text{ cm}$

TABLE 4.2-2

LIST OF SYMBOLS

<u>Transfer Function Parameters</u> <u>Applicable to Both Instruments</u>	
I_{oo}, C, M	sensor transfer function parameters
T_1, T_2, T_4	compensation network parameters
T_a, T_b, T_c	bandpass filter parameters
K_{po}	sensor pickoff gain
K_{ac}	demodulator ac gain
K_{dc}	compensation network dc gain
K_{sg}	signal generator gain
K_{tg}	torque generator gain
K_{sf}	instrument scale factor
<u>Gyro Parameters</u>	
H	gyro angular momentum
I_{ii}	moment of inertia of the gimbal-rotor combination about the gyro input axis
I_{oo}	moment of inertia of the gimbal-rotor combination about the gyro output axis
I_{ssg}	moment of inertia of the gimbal about the gyro spin axis
I_{ssr}	moment of inertia of the rotor about the gyro spin axis
$K'_{is} = \frac{m^2}{H} K_{is}$	where m is the rotor mass and K_{is} is the structural compliance coefficient relating rotor center of mass displacement along the gyro input axis to acceleration along the gyro spin axis; similar expressions apply for the other coefficients
$\delta'_i = \frac{m}{H} \delta_i$	where m is the rotor mass and δ_i is the displacement of the float center of mass along the input axis; similar expressions apply for the other coefficients
SF_g	gyro output scale factor error
D_{g_o}, D_{g_s}	misalignment of the gyro coordinate frame about the output and spin axes respectively.
ϵ	torque generator scale factor asymmetry
<u>Accelerometer Parameters</u>	
P	pendulosity of pendulum-gimbal combination
I_{ii}	moment of inertia of the pendulum-gimbal combination about the accelerometer input axis
I_{oo}	moment of inertia of the pendulum-gimbal combination about the accelerometer output axis
I_{pp}	moment of inertia of the pendulum-gimbal combination about the accelerometer pendulous axis
I_{op}	product of inertia of the pendulum-gimbal combination about the accelerometer output and pendulous axes
$K'_{ip} = \frac{m^2}{P} K_{ip}$	where m is the mass gimbal-pendulum structure and K_{ip} is the structural compliance coefficient relating the gimbal-pendulum center of mass displacement along the accelerometer input axis to acceleration along the accelerometer pendulous axis; similar expressions apply for the other coefficients.
SF_a	accelerometer output scale factor error
K_2	accelerometer output scale factor non-linearity
D_{ap}	misalignment of the accelerometer coordinate frame about the pendulous axis
ϵ	torque generator scale factor asymmetry
P	vector of displacement components of accelerometer axis system from the body coordinate frame

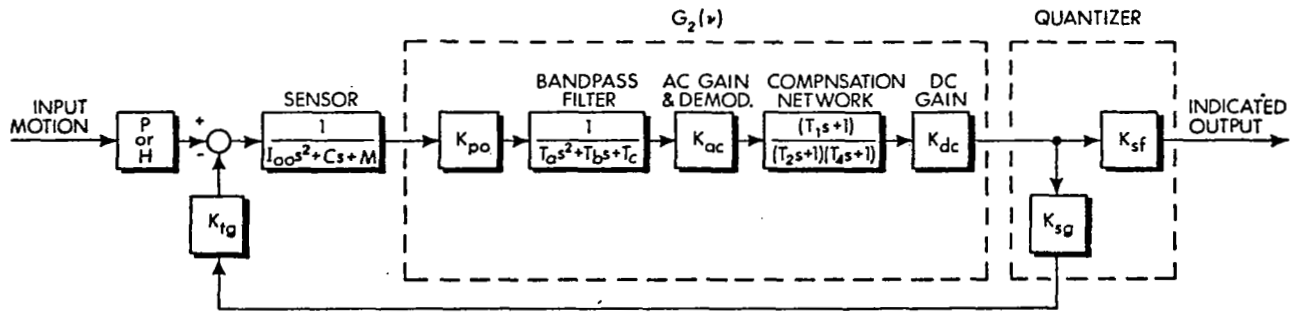


Figure 4.2-6 Linearized Model for Gyros and Accelerometers

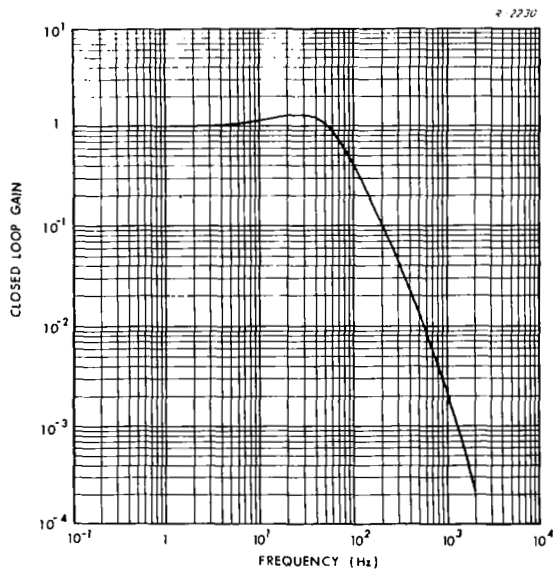


Figure 4.2-7 Hamilton Standard 1139 SDF Gyro Gain Diagram

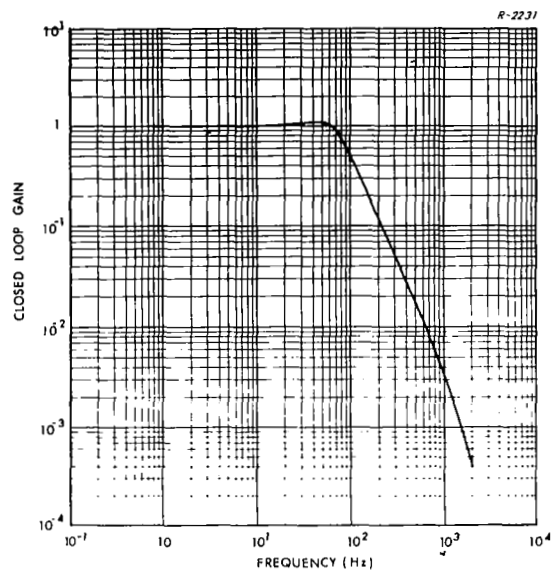


Figure 4.2-8 Kearfott 2401 Pendulous Accelerometer Gain Diagram

errors were defined accordingly. If, on the other hand, the navigator actually experiences a net angular or linear translation in this particular vibration environment, the error introduced is the negative of that computed here.

The dominant sources of vibration-induced error computed for the helicopter when the gyros are pulse-rebalanced are summarized in

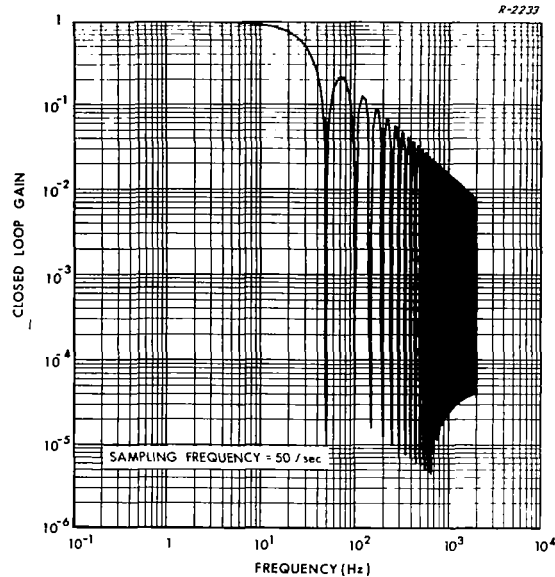


Figure 4.2-9 Sample-and-Hold Computer Model Gain Diagram

Table 4.2-3. For this mission, rebalance loop asymmetry in the gyros is a major source of vibration-induced error. Gyro output axis sensitivity, an error arising from the instrument's sensitivity to angular acceleration about its output axis, also contributes significantly to constant angular velocity error. As can be predicted from the examination of the effective sensor bandwidths, undetected coning is a relatively insignificant source of system error but undetected sculling is the largest effective accelerometer error. Accelerometer size effect, due to the physical separation of the accelerometers from the center of the strapdown package, is also a major source of vibration-induced error in the system.

It is useful to compare these error values with representative gyro and accelerometer bias errors in order to measure their relative significance. A $100 \mu\text{g}$ bias is a representative figure for pendulous accelerometers so that vibration-induced accelerometer errors are unimportant for this mission. However, gyro bias errors of 0.01 deg/hr

TABLE 4.2-3

VIBRATION-INDUCED ERRORS IN A STRAPDOWN NAVIGATOR

Vehicle:	CH-46C Twin Rotor Helicopter		
Inertial Instruments:	Norden 1139 SDF Gyro Kearfott 2401 Pendulous Accelerometer		
Principal Sources of Vibration-Induced Error			
<u>System Drift Rates (deg/hr)</u>	<u>x</u>	<u>Axes y</u>	<u>z</u>
• Gyro Output Axis Sensitivity	.004	.252	.208
• Rebalance Loop Asymmetry (rms error)	.123	.121	.059
• Anisoinertia	.025	.012	.010
• Undetected Coning Motion	.005	-.005	-.038
<u>System Acceleration Errors (μg)</u>			
• Undetected Sculling Motion	-4.47	-1.92	3.20
• Size Effect	-3.95	-1.95	-0.43
• Rebalance Loop Asymmetry (rms error)	0.26	0.32	0.89
• Anisoinertia	-0.47	-0.49	0.47
• 2nd Order Nonlinearity (rms error)	0.20	0.20	0.77
• Gyro Output Axis Sensitivity (contributing to pseudo-sculling error)	0.55	0.13	-0.46
• Input-Pendulous Crosscoupling	-0.50	0.05	0.50

are regarded as typical and rebalance loop asymmetry and output axis sensitivity result in vibration-induced errors that are an order of magnitude larger. It can be concluded that, for the inertial sensors considered and in the helicopter vibration environment, a serious system attitude drift rate will be caused by motion-induced errors unless steps are taken to compensate certain error torques arising in the gyros.

Additional results obtained with the program illustrate its further usefulness as a design tool. As mentioned in Chapter 3, a decrease

in the cycle frequency of the navigation system computer can effectively reduce the bandwidth of the inertial sensors, preventing higher frequency vibrations from entering the system calculations. The effect of pseudo-coning and pseudo-sculling errors can be reduced in this manner but the errors due to undetected motion are consequently increased. Figure 4.2-10 illustrates the tradeoff for pseudo-coning about the y body axis caused by gyro sensitivity to output axis angular acceleration and undetected coning about the y body axis. A computer sampling period of 0.18 seconds balances the effect of these error sources.

R-2234

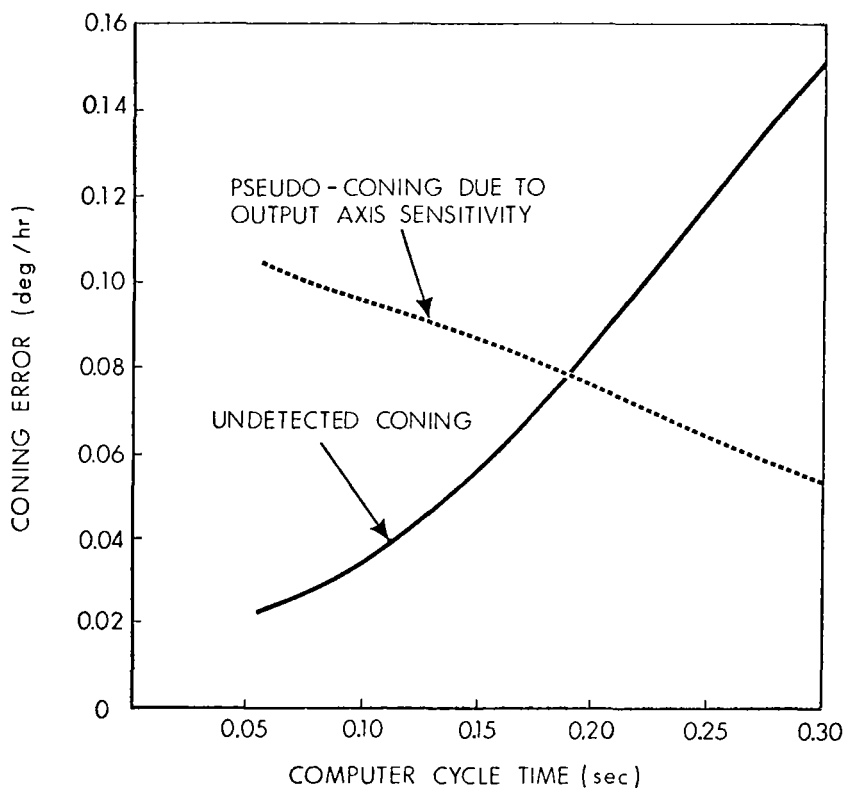


Figure 4.2-10 Coning Error as a Function of Computer Cycle Time

4.3 EXAMPLE III: HELICOPTER, SINGLE-AXIS-PLATFORM GYROS

Table 4.2-3 shows that, for a typical helicopter vibration environment, the SDF gyro torque rebalance loop is a significant source of strapdown system error. Also, one error caused in part by angular motion about the gyro input axis (anisoinertia error) is significant. These kinds of errors can be largely eliminated by utilizing single-axis platforms (SAP's) to isolate each gyro from angular vibrations about its input axis and to convert it into a null-seeking instrument. The effects of other sources of rectified error which involve input-axis angular vibrations, such as spin-input crosscoupling, can also be considerably reduced by employing the SAP configuration.

The TASC computer program described in Ref. 3 was modified to analyze vibration-induced errors in strapdown systems which use gyros in the SAP mode. To compare vibration-induced system errors for the two modes of gyro operation, program input data employed in the previous example was used to generate error values for the SAP strapdown system. The nominal orientation of the gyro axes, in the absence of angular motion of the body, was assumed to be the same as shown in Fig. 4.2-2. In the SAP system, each gyro is isolated from angular motion about the input axis by the gimbal system. Changes in SAP orientation with respect to the body axes result only from imperfect isolation. This relative motion is accounted for in the program by appropriate transformations of the vibration spectral data. All of the Norden 1139 SDF gyro characteristics identified in Table 4.2-1 are used in the SAP analysis, except those associated with the torque rebalance loop. Additional parameters needed to describe the dynamics of the SAP gimbal model used in this analysis are summarized in Table 4.3-1.

TABLE 4.3-1

SAP TORQUER CHARACTERISTICS

Parameter	Symbol	Units	Typical Value
Coefficient of viscous damping between the shaft and the vehicle	B	dyne-cm-sec	0
Moment of inertia of the gyro and SAP gimbal shaft about the gyro input axis	I_{iiG}	gm-cm ²	5600
Constant flux motor coefficient	K	dyne-cm/amp	2.46×10^6
Armature reactance	R	ohms	8.55
Torque motor time constant	τ_m	sec	2.59×10^{-4}
Constant gain, float angle to armature voltage transfer function	K_T	volts/rad	1.0×10^5
Transfer function parameters, float angle to armature voltage transfer function	ω_1	rad/sec	1.0×10^3
	ζ_1	—	0.5
	ω_2	rad/sec	1.0×10^4
	ζ_2	—	0.95

The closed-loop transfer characteristics for the Norden 1139 gyro in a SAP configuration, involving both the sensor and gimbal torquer dynamics, are derived in Appendix D. The SAP electronics transfer function $L(s)$ (see Appendix D) is represented by

$$L(s) = \frac{K_T \left(s^2/\omega_1^2 + 2\zeta_1 s/\omega_1 + 1 \right)}{\left(s^2/\omega_2^2 + 2\zeta_2 s/\omega_2 + 1 \right)}$$

The gyro error response to vibrations about its input axis is shown in Fig. 4.3-1. As shown, the gyro error becomes more sensitive to input-axis vibrations as the vibration frequency increases but remains relatively small over the entire 2000 Hz vibration bandwidth. This transfer characteristic provides effective vibration isolation since the dominant angular

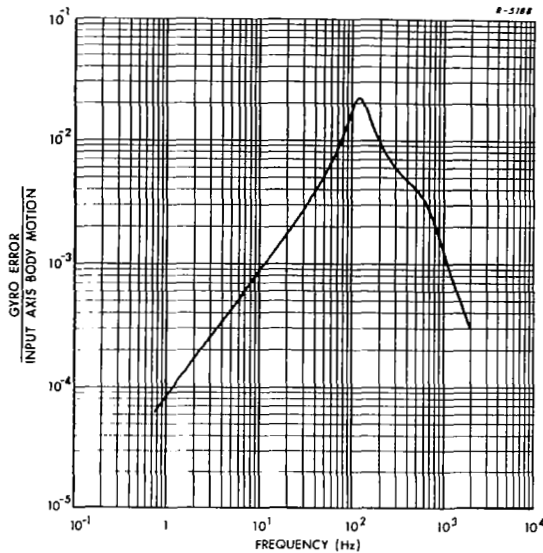


Figure 4.3-1 Gyro Response to Input Axis Vibrations, Hamilton Standard 1139 SDF Gyro, Operated as a SAP

vibrations typical of a helicopter environment occur at lower frequencies, as shown in Fig. 4.2-4. Errors still result from angular vibrations about the output and spin axes of the gyro, since no motion-isolation is provided about these axes, and from linear vibrations, as in a conventional strap-down configuration. The transfer characteristics which describe the response of the gyro to these disturbances are also derived in Appendix D.

The Kearfott 2401 pendulous accelerometers remain in a body-fixed orientation in the SAP system and the accelerometer data contained in Table 4.2-1 are directly applicable to this analysis. The sample-and-hold computer model described in Section 4.2, having a sample rate of 50 Hz, is also used in generating the SAP vibration-induced errors. The results of this analysis are summarized in Table 4.3-2.

The largest vibration-induced drift rates in the SAP strapdown system are caused by disturbance torques due to angular accelerations

TABLE 4.3-2

VIBRATION-INDUCED ERRORS IN A
SAP STRAPDOWN NAVIGATOR

Vehicle:	CH-46C Twin Rotor Helicopter		
Inertial Instruments:	Norden 1139 SDF Gyro With SAP Kearfott 2401 Pendulous Accelerometer		
Principal Sources of Vibration-Induced Error			
<u>System Drift Rates (deg/hr)</u>	<u>x</u>	<u>Axes y</u>	<u>z</u>
• Gyro Output Axis Sensitivity	- .001	.234	.197
• Undetected Coning Motion	- .040	.022	- .022
<u>System Acceleration Errors (μg)</u>			
• Undetected Sculling Motion	-3.14	-3.81	2.73
• Size Effect	-1.71	-1.12	2.94
• Rebalance Loop Asymmetry (rms error)	0.26	0.32	0.89
• Anisoinertia	-0.47	-0.49	0.47
• 2nd Order Nonlinearity (rms error)	0.20	0.20	0.77
• Input-Pendulous Crosscoupling	-0.50	0.05	0.50
• Gyro Output Axis Sensitivity (contributing to pseudo-sculling error)	0.71	0.11	-0.37

about each gyro output axis. The SAP configuration does not isolate the gyro from output axis motion and the resulting error magnitudes are about the same as for a torque rebalanced gyro. The minor difference in drift rates results from slightly different gyro response characteristics in the two modes. A comparison of Tables 4.2-3 and 4.3-2 also shows that, for the design parameters chosen in this analysis, undetected coning is a slightly more serious problem for the SAP strapdown system. But for both configurations the undetected coning error is about an order of magnitude smaller than the largest vibration-induced errors in the

system. System drift rates due to the remaining sources of vibration-induced error are all below a level of 0.01 deg/hr. As noted earlier, rebalance loop asymmetry, a prominent source of error in Table 4.2-3, does not exist in the SAP strapdown system. The vibration isolation provided by the SAP also greatly reduces the significance of anisoinertia effects and spin-input crosscoupling. In spite of these improvements, the remaining vibration-induced errors in the system are still much larger than typical platform gyro bias errors of 0.01 deg/hr.

Accelerometer error sources which result in a rectification of vibrations in the instrument are of course unaffected by the change in gyro configuration. These error sources are identified as those which have exactly equivalent values in Tables 4.2-3 and 4.3-2. The remaining acceleration errors rectify at the system level and hence involve indicated system attitude, obtained from gimbal angle readouts in the SAP configuration. Differences in the gyro transfer characteristics in the different modes of operation are reflected in the slightly different error values in the two tables.

The order of significance of the acceleration errors is the same in both the strapdown and SAP configurations, with undetected sculling motion and size effect as the major contributors. As noted in Section 4.2, this level of vibration-induced error is well below the typical pendulous accelerometer bias error of 100 μ g.

From the calculations performed in this chapter it is evident that strapdown inertial systems with motion-induced errors may be unsatisfactory unless the sensor parameters are carefully chosen or some form of compensation is provided. While the SAP gyro configuration offers some relief by isolating each gyro from input axis vibrations it does not appear to reduce the overall level of system drift rate to any great degree.

PART II: PULSE REBALANCE LOOPS

5. DESCRIPTION OF PULSE TORQUING SCHEMES

5.1 PULSE REBALANCED GYROS

Gyros used in strapdown navigators are likely to experience large angular motions about the case input* axis. In order to avoid the complications connected with a large output angle, α_0 , a powerful torque generator is included in the instrument and the rotor spin axis is kept in close coincidence with the spin reference axis. By keeping the output angle small, variations in α_0 can be attributed to angular motion about the case-fixed input axis. Information concerning angular motion about the input axis is largely contained in the history of torque required to cage, or restrain, the gyro about its output axis.

Direct determination of the torque applied is difficult and most designers rely on measurements of current flow in the torquer windings to indicate the moment produced. Unfortunately, the torque generator does not exhibit a gain characteristic which is sufficiently linear, and, if a wide range of torquer currents is employed, extensive calibration is required. A common way to avoid problems with torquer nonlinearity is to permit application of only two torque levels, equal in magnitude and opposite in sign. (A third, or zero level may also be considered.) In this case, the torque generator need only be calibrated and adjusted at two (or at most three) distinct points on its gain curve, permitting very accurate control of the moments applied to the gyro output axis. A further refinement to the gyro rebalance mechanism is provided by carefully dividing the torquer current into pulses of known duration. Each pulse then represents a fixed

* Figure 2.1-1 illustrates the axes discussed here.

incremental rotation of the gyro about its input axis and the gyro rebalance loop output is well suited for calculating system attitude changes using a digital computer. Ideally, the rebalance torque occurs as a sequence of pulses of positive and negative torque, each pulse having the same weight, and the strapdown gyro output consists of a train of positive and negative electronic impulses accurately representing incremental rotations about the sensor input axis. The gyro is thus said to be "pulse rebalanced."

Binary Delta Modulation — The binary delta modulation pulse rebalance scheme always provides a rebalance torque; the possibility of omitting a torque pulse is purposely excluded. This mechanization can be represented by a binary logic element inserted between the torquer and a signal representing the gyro output angle (see Fig. 5.1-1). The torquer current, of magnitude D , is supplied with a direction (sign) depending on the sign of the output angle. Pulses of torque are created by only allowing the logic output to change at fixed intervals, T . A further refinement may be employed, permitting torque to be applied only over a known fraction of each interval, but this has little bearing on the aspects of pulse rebalance techniques under consideration here. Figure 5.1-2 shows a representative train of torque pulses applied to a gyro gimbal when binary pulse torquing is employed. The shape of the pulses generated differs from a rectangle because of lags in both the torquer and the current source driving it.

Ternary Delta Modulation — The ternary delta modulation technique differs from the scheme described above because it permits the absence of a torque pulse when the output angle magnitude is small. The mechanization can be represented by a relay with an input deadzone inserted between the output angle signal and the torquer. Figure 5.1-3 illustrates the ternary detection logic. The deadzone width, 2δ , is symmetric about zero and defines a range of output angles for which no rebalance torque is applied.

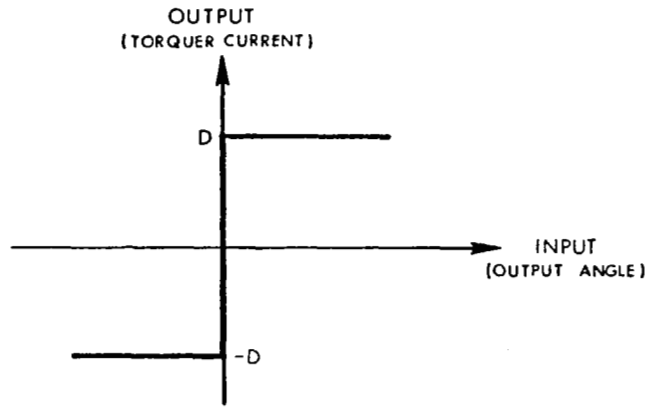


Figure 5.1-1 Binary Logic

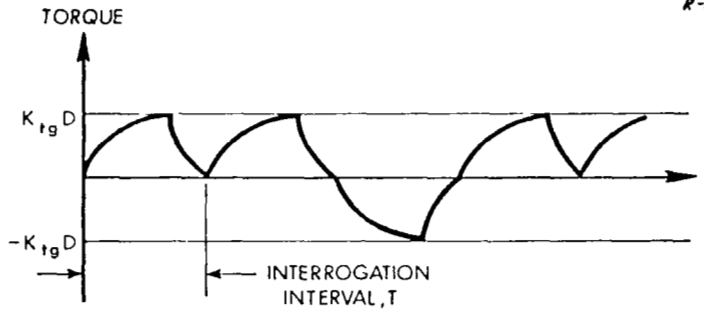


Figure 5.1-2 Representative Torque Output from Binary Delta Modulated Pulse Rebalance Technique

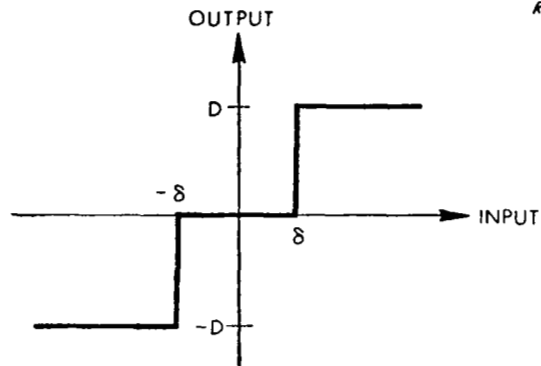


Figure 5.1-3 Ternary Logic

For low-frequency inputs δ can be related through the gyro gain H/C to an angular rotation about the input axis which will not be detected by a gyro using this rebalance technique. However, for input frequencies above the float bandwidth, the relation is more complex. All other aspects of the ternary delta modulation technique are identical to those of the binary approach just discussed.

Time Modulation — A third pulse torquing technique, time-modulated torquing, adds the gyro output angle to a periodic waveform and employs binary logic on the sum. Figure 5.1-4 illustrates this approach. The binary logic is interrogated at a frequency which is a multiple of the sawtooth frequency. In this manner, each period of the added waveform is divided into an even integral number of parts. Current driving the torque generator can only be switched at the moment the binary logic is interrogated.

If the output angle is zero, the torquer provides a pair of pulses, one positive and one negative. The torque pulses are of equal duration and occur at the frequency of the sawtooth wave. The net effect of each pulse

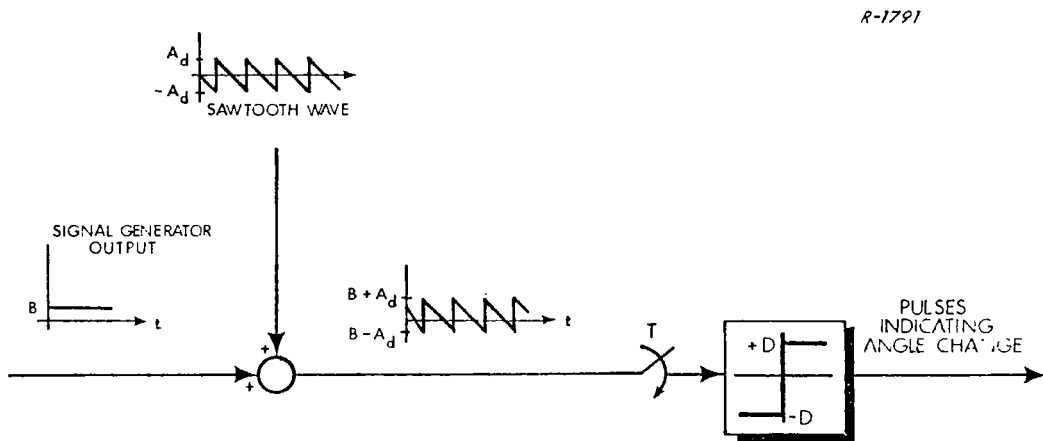


Figure 5.1-4 Time-Modulated Torquing

pair on the output angle is zero, but the float will oscillate at the sawtooth frequency. To avoid detecting this float oscillation the signal representing output angle is usually passed through an appropriate filter. If the filtered indication of output angle differs from null, the pulse pairs appear at the same frequency but the pulses in each pair are of different duration, as illustrated in Fig. 5.1-5. The difference between the length of two adjacent pulses is such that the net effect is to drive the output angle toward null. The sawtooth amplitude is chosen to ensure that the torquer always provides a moment in the same direction at the start of each sawtooth period; the amplitude of the added waveform is larger than any anticipated signal representation of α_0 . For this reason, the torquer current always changes sign at the start of a new sawtooth. Also, the current is only allowed to reverse once during each period of the added waveform. These restrictions ensure the appearance of one positive and one negative pulse, in the same order, each sawtooth period.

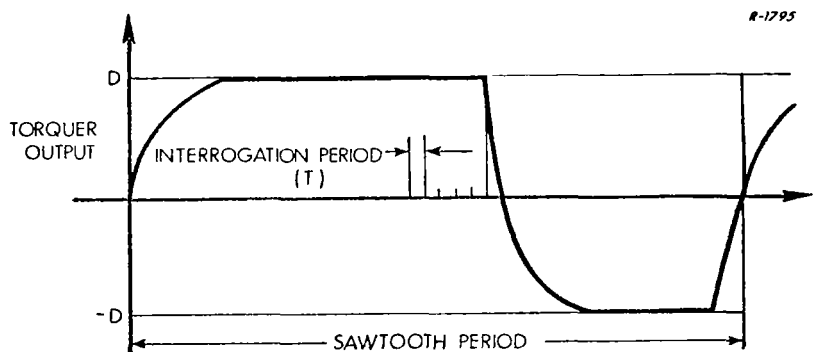


Figure 5.1-5 Torquer Waveform for Time-Modulated Torquing

When time-modulated torquing is employed, the gyro output can take two forms. In one case a pulse sequence is provided at an even multiple of the sawtooth frequency, corresponding to the rate at which the binary logic is interrogated. The output appears as a long series of pulses of one

sign followed by a long series of pulses with the opposite value. Each pulse represents an incremental rotation about the input axis, of a magnitude determined by the torquer capability and the interrogation frequency. Most of the information contained in this form of output represents the added waveform. Only the difference between the number of pulses in two successive series can be construed to represent α_0 and consequently motion about the gyro input axis. More commonly, this difference is determined by summing pulses over each period of the sawtooth. The net difference, available at the frequency of the sawtooth wave, represents the information content of the gyro output. Since the sawtooth period is typically on the order of one millisecond the latter form of the gyro output has a bandwidth compatible with many of the computers used to process angular motion information.

If a fixed increment Digital Differential Analyzer (DDA) is used to process gyro outputs, the high frequency pulse train can be employed. However, as stated earlier most of the information contained is related to the oscillatory signal that was added to α_0 and the attitude calculations will exhibit this oscillation; if all gyros are not using the same sawtooth wave, serious pseudo-coning system drift rates can be caused.

Summary — All three pulse-torquing techniques provide digital outputs which represent increments of angular rotation about the sensor input axis. Angular motion is implied from carefully calibrated torque pulses applied to the gyro gimbals, corresponding to each output pulse. Any deviation of the actual time integral of torque from that represented by each output pulse will cause an error which is not recoverable, i.e., differs in nature from gyro output errors caused by storage of information by the float. Constant deviation of the torque pulse weight can cause constant gyro drift rates while random variations provide random output errors. Any difference between the net torque pulse generated and that

implied by each output quantum is a significant potential source of errors in strapdown sensors.

When system accuracy is considered, factors such as quantization and the information rate of pulse rebalanced gyros are important. The presence of unforced oscillations in the gyro output is also considered when comparing strapdown gyro torquing schemes. In addition, frequency response characteristics and energy dissipation in the gyro loops are significant. The major causes of pulse rebalancing errors are described below, followed by a discussion of the relative advantages of each torquing scheme.

5.2 GYRO ERRORS ATTRIBUTABLE TO PULSE TORQUING

Torque Pulse Variations — Frequently the magnitudes of torque pulses applied to the float differ from those inferred by the corresponding electrical impulses at the gyro output. If the deviations are constant, calibration of the strapdown gyro loop will eliminate some of the errors generated. Recalling the discussion in Section 2.3, bias and scale factor errors are present in both the binary and ternary pulse rebalanced sensors. However, removing errors of this kind from the ternary gyro generally requires two scale factor corrections; the correction used at a particular time depends on the sign of the input angular rate. This represents an unwanted complication in processing the gyro output. When the rebalance electronics drift, causing uncompensated variations in torque pulse weights, new values of bias and scale factor errors result in the binary gyro. The bias error is caused by the fact that torque pulses are always being generated in the binary rebalance loop; it is independent of the angular motion environment. Only scale factor errors are generated in the ternary loop when the rebalance electronics drift. Consequently, if the input angular

rates are small the ternary gyro will be less sensitive to unknown variations in torque pulse weights.

Quantization — The output of each pulse rebalanced strapdown gyro is a series of digital pulses representing incremental rotations about the input axis. This form is not well suited for drift-free calculation of the direction cosine matrix because information is lost regarding the order in which rotations take place about the system axes. The commutativity errors which can result are largely related to the gyro output quantization level and the manner and speed with which the outputs are processed. (Reference 9 provides an approximate expression for commutation errors generated by gyro output quantization.) As a general rule, fine quantization is to be preferred.

Delta modulation pulse torquing schemes achieve fine quantization by interrogating the nonlinear logic element at a high frequency, permitting the torque level to change sign rapidly. While the size of the output quantum in the time-modulation technique is also determined by the interrogation frequency, the rate at which torquer current changes sign is determined by the frequency of the sawtooth wave. In gyros employing delta modulation rebalance schemes, quantization is limited by time constants in the torque generation mechanisms. If the pulses are of too short a duration, the torquer current will not reach its design level before the next potential switching time occurs. Because of eddy current effects, when the torquer lag is on the order of the pulse period, two consecutive torque pulses in the same direction will not have the same time integral (effect on α_0) as the sum of two separate pulses (see Fig. 5.2-1). Consequently, all current pulses will not have equal weight and an accurate measure of angular motion about the gyro input axis cannot be found by counting output pulses.

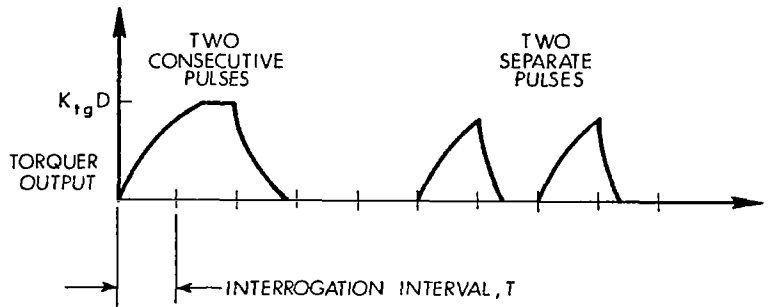


Figure 5.2-1 Torque Pulse Variation when the Torquer Lag is a Significant Fraction of the Pulse Period

In the time-modulation torquing scheme, quantization is not tied directly to torque pulse width. The current switching frequency is strictly limited and quantization is determined by the number of points in each cycle of the sawtooth at which the torque can change sign. In the absence of switching delays, infinitesimal quantization is possible. The practical limit is imposed by the ability to switch the torque levels accurately in time. Using this approach, torquer time constant problems are eliminated by choosing the amplitude of the added waveform so that torquer current always reaches the desired level before the next change occurs.

Information Rate — The information rate, defined here as the frequency with which new indications of system angular motion will be available to the attitude transformation computer, can depend on the pulse torquing technique chosen. Typically, a gyro with time-modulation rebalance torquing can provide output impulses faster than one using either of the delta modulation approaches. Each impulse is interpreted as an increment of angular rotation about the instrument's input axis. However, as

discussed earlier, most of the information actually present in the raw output of this rebalance technique relates to the oscillatory signal added to α_0 and not to angular motion experienced by the gyro. The information rate of a gyro employing time-modulated torquing is essentially limited by the frequency of the additive oscillatory signal used in mechanizing this approach. It would then appear that the information rate of gyros using the delta modulation approach to rebalance torquing is higher than those employing the time-modulation technique, when present interrogation frequencies are considered. However, the practical rate at which angular motion can be sensed by this kind of strapdown gyro is usually limited by lags in the float dynamics, not the sampling frequency; output pulses which change sign at a rate near that of the interrogation clock are more likely to be caused by electrical noise than high frequency motion inputs. In summary, the useful information rate of a contemporary floated single-degree-of-freedom strapdown gyro generally is limited not by the pulse rebalance technique employed but by float dynamics.

Unforced Oscillations — All three pulse torquing schemes produce unforced oscillations in the gyro loop at one time or another. The limit cycle behavior of a control loop containing a binary nonlinearity is well known (Ref. 10). In the presence of certain inputs, the three level pulse torqued gyro and the time modulation scheme will also exhibit cyclic errors. The unwanted oscillations all result from the use of torque pulses to rebalance the gyro. Limit cycles in pulse rebalanced gyros can be mistaken for coning motion if they occur with proper phase and at the same frequency. (System attitude drift rates are generated in this manner.) The binary delta modulation scheme is usually thought to be the least satisfactory from this point of view. However, it can be shown that slight differences between limit cycle periods of the different gyros in a strapdown

triad will prevent large system coning errors (see Ref. 1). Thus, gyros with slightly different characteristics may be desired if this form of torquing is used.

Gyro Frequency Response Characteristics -- Closed loop response to sinusoidal inputs is a useful description of behavior. Closed loop gain and phase shift characteristics are useful in determining strap-down system errors when the gyro loop is assumed to be linear (see Chapter 4). Approximate determination of these characteristics is discussed in the three succeeding chapters. Torque loops employing binary logic appear to be more readily described in terms of linear behavior than those using ternary logic, offering an advantage when analyzing and compensating dynamic system errors.

Energy Dissipation — Temperature gradients within the gyro structure are a major cause of single-degree-of-freedom gyro drift. If the gradients can be held constant, proper testing will enable accurate compensation of these effects. While it consumes less power in most motion environments, the ternary delta modulation torquing scheme does not usually provide a uniform energy flow into the torquer. To avoid this obvious cause of varying temperature gradients, the current source can be switched into a dummy load when no torque is called for. However, if the same heat pattern is to be produced, this requires a dummy winding the same size as the torquer. Situations do exist where the ternary technique will provide essentially constant energy flow without the extra winding; for example, while operating in the angular rate environment generated by a limit cycling spacecraft attitude control system.

5.3 COMPARISON OF PULSE TORQUING TECHNIQUES

Binary Delta Modulated Torquing — The binary delta modulation rebalance technique provides a gyro loop response which is linear because of the limit cycle always present in this kind of system (see Chapter 6). However, some compensation within the gyro loop may be desired to improve its behavior. Because torque is always being generated, energy is dissipated within this kind of an instrument at a constant rate and no significant errors are caused by variations in temperature gradients. A high rate of power consumption results, even in the most benign motion environment. A limit cycle, from which strapdown system attitude drift rates can result, is always present in this instrument. The output quantization level of a gyro using this rebalance technique is limited by torquer dynamics and the output resolution is generally poorer than can be obtained from sensors using time-modulation torquing. Also, the instrument is relatively sensitive to uncompensated deviations in the size of rebalance torque pulses. Binary delta modulation requires a minimum of electronic components, suggesting better reliability.

Ternary Delta Modulated Torquing — Gyros employing ternary delta modulated torquing can conserve electrical energy in a benign environment such as that encountered during long space missions. In addition, there is less tendency to exhibit cyclic output errors. Because a null torquer current can be achieved with high accuracy, they usually have a lower drift rate in the absence of an input and are less sensitive to deviations in torque pulse size. However, in a variable environment unstationary temperature gradients can be generated inside the instrument unless a dummy electrical load is used to dissipate energy when no torque pulse is called for. If this additional device is added to the gyro, the lower power consumption feature is sacrificed and the weight and size of the instrument are

increased. As with the gyro using binary delta modulated torquing, the ternary rebalanced sensor suffers from an output resolution that is limited by torquer dynamics. A gyro loop using this torquing scheme exhibits a nonlinear response to high frequency inputs (see Chapter 7), casting doubt on its value as a strapdown sensor in vigorous angular vibration environments. The ternary gyro also displays ambiguous response characteristics in the high frequency range.

Time-Modulated Torquing — The output resolution of a gyro employing time-modulated torquing is essentially independent of torquer dynamics. Consequently, this type of instrument provides finer quantization than is commonly found in other pulse rebalanced gyros. An oscillatory error can appear in the gyro output but this is much smaller than those occurring with binary delta modulation techniques. High power consumption is characteristic of this rebalance scheme but temperature gradients within the device are held constant. This type of instrument exhibits a relatively large sensitivity to variations in torque pulse weight. Analysis indicates that a more satisfactory linear response can be obtained from this type of gyro than is possible using simple binary torquing in an uncompensated loop. Of the three techniques discussed, time-modulated torquing requires the largest number of electronic components.

Summary — The three pulse torquing techniques discussed are compared in Table 5.3-1. Some representative values of important parameters are listed to aid in the comparison. None of the approaches discussed offers a clear advantage in all situations. If constant energy dissipation over a wide range of inputs and linear response are required at the outset, the ternary approach can probably be ruled out. However, when the angular motion environment is quiet and reasonably constant the ternary gyro has the advantage of low power consumption and is less affected by torque

pulse deviations. All three techniques appear capable of providing the same information rate, but the time-modulation approach can give better output resolution because it permits output quantization to be specified independent of the torquer design.

TABLE 5.3-1

COMPARISON OF PULSE TORQUE TECHNIQUES

UNDESIRABLE FEATURES	REBALANCE TECHNIQUES			COMMENTS
	BINARY DELTA MODULATION	TERNARY DELTA MODULATION	TIME MODULATION	
Output Quantum Level Limited by Torquer Dynamics.	X	X		Gyro output quantum, $\Delta\theta$, is independent of torque lags when the time modulation technique is employed.
	$\Delta\theta_{\min} > 3\omega_{i\max} \tau_{tg}$, about 20 $\widehat{\text{sec}}$ or more when $\omega_{i\max} = 1 \text{ rad/sec}$		$\Delta\theta < 1 \widehat{\text{sec}}$ for the Hamilton Standard RI-1170 under similar circumstances.	
Unforced Oscillations in the Sensor Output.	X		X	Ternary gyro can also exhibit output oscillations. The finer quantization available with the time modulation schemes reduces the amplitude of these errors.
Amplitude Dependent Response Characteristics.		X		See Fig. 7.1-6 for an illustration of the amplitude dependent response characteristics of the ternary gyro.
Nonstationary Temperature Gradients in the Gyro.		X		This can be avoided in the ternary gyro also but at the expense of significant increases in torquer size and weight.
High Power Consumption in a Benign Environment.	X		X	The ternary gyro also suffers this problem if a dummy electrical load is added to give stationary temperature gradients.

Certain system-level errors in strapdown inertial navigators depend on the transmission characteristics of the instruments used to measure angular and linear motion. Unfortunately when pulse rebalanced sensors are employed, simple exact mathematical expressions for the gain and phase lag introduced by the gyro and accelerometer loops do not exist; the instruments are highly nonlinear in nature. It is the purpose of this chapter and the two which follow to present approximate techniques for predicting the transmission characteristics of pulse rebalanced strapdown sensors. A separate aspect of pulse torqued gyros and accelerometers -- their tendency to exhibit self-excited oscillations -- is closely related to analysis of their response to inputs, and the two subjects are treated simultaneously.

This chapter demonstrates techniques for analyzing inertial instruments which are torqued using the binary delta modulation technique presented in Chapter 5. The discussion centers on gyroscopes but the techniques developed are applicable to a very broad range of instruments, including accelerometers.

6.1 ANALYSIS OF THE LIMIT CYCLING BINARY GYRO

This section discusses analytic techniques for deriving the closed loop transfer characteristics of the binary pulse torqued loop. Closed loop gain characteristics predicted analytically are displayed to illustrate the effects of different instrument parameters.

6.1.1 Response to Sinusoidal Inputs

Figure 6.1-1 is a simple representation of a binary pulse re-balanced gyro loop. The rotor and gimbal are assumed to behave as a single rigid body for angular motion about the gyro output axis and act as a summing point for torques about the output axis. More complex representations of gyro dynamics have also been treated (see Ref. 2).

R-3754

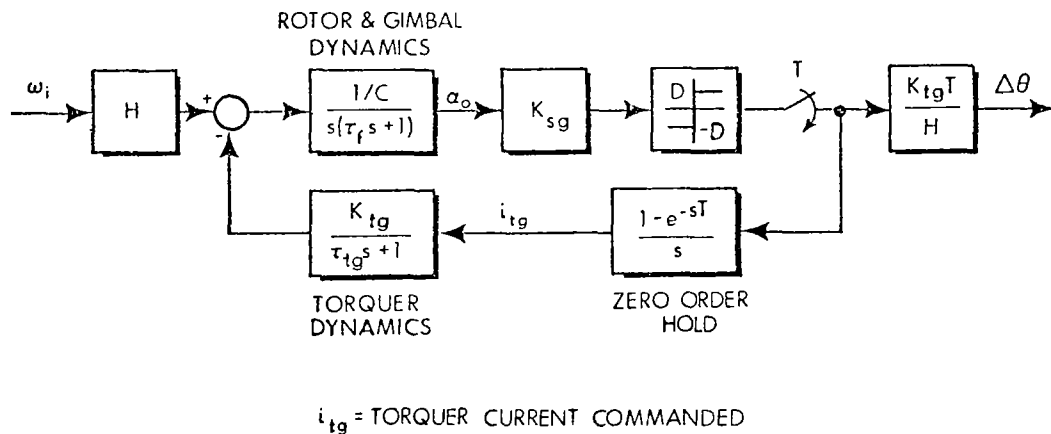


Figure 6.1-1 Binary-Torqued Gyro Loop With Second Order Gyro Dynamics

Limit Cycle — In the absence of angular rate inputs the gyro loop will experience a self-excited oscillation or limit cycle. This is a consequence of the binary nonlinearity and the fact that the linear elements are capable of providing 180 deg. of phase lag (see Ref. 10). If the sampling process shown in Fig. 6.1-1 is ignored, the describing function condition for a loop limit cycle is

$$N_A(A) G(j\omega_\ell) = -1 \quad (6.1-1)$$

where $N_A(A)$ is the Sinusoidal Input Describing Function (gain) representation of the non-linearity response to a sinusoidal input of amplitude A , $G(j\omega_\ell)$ is the transfer function of the open-loop linear elements, evaluated at the limit cycle frequency, ω_ℓ rad/sec, viz:

$$G(j\omega_\ell) = \frac{K_{sg} K_{tg}/C}{j\omega_\ell (\tau_f j\omega_\ell + 1) (\tau_{tg} j\omega_\ell + 1)} \quad (6.1-2)$$

where $\tau_f = I_{OO}/C$ is the float time constant. Appendix E shows that the describing function for the binary element in Fig. 6.1-1 is given by

$$N_A(A) = \frac{4D}{\pi A} \quad (6.1-3)$$

Inserting Eqs. (6.1-2) and (6.1-3) in Eq. (6.1-1) yields the following magnitude and angle conditions required for a solution:

magnitude condition:

$$\left(|N_A| |G(j\omega_\ell)| = 1 \right)$$

$$\frac{4D}{\pi A} \frac{K_{sg} K_{tg}}{C} \frac{1}{\omega_\ell \sqrt{\tau_f^2 \omega_\ell^2 + 1} \sqrt{\tau_{tg}^2 \omega_\ell^2 + 1}} = 1 \quad (6.1-4)$$

angle condition:

$$\left(\angle N_A + \angle G(j\omega_\ell) = -\pi \right)$$

$$-\frac{\pi}{2} - \tan^{-1} \tau_f \omega_\ell - \tan^{-1} \tau_{tg} \omega_\ell = -\pi \quad (6.1-5)$$

Equation (6.1-5) can be solved for ω_l , giving

$$\omega_l = \sqrt{\frac{1}{\tau_f \tau_{tg}}} \text{ rad/sec} \quad (6.1-6)$$

Inserting this result into Eq. (6.1-4) yields

$$A = \frac{4D}{\pi} \frac{K_{sg} K_{tg}}{C} \frac{\tau_f \tau_{tg}}{\tau_f + \tau_{tg}} \quad (6.1-7)$$

Note that the limit cycle frequency depends only on the time constants of the linear loop components.

Linearized Gyro Loop — Consider the linear continuous-torqued rebalance loop shown in Fig. 6.1-2. The gain K_1 has units of milliamp/millivolt and represents the operation of linear conversion of signal generator voltage output to torque generator current input. As a good approximation in this linear system, torquer dynamics have been omitted. $\hat{\omega}_i$ denotes the continuous output, which is an estimate of the input rate ω_i . The second-order transfer function from ω_i to $\hat{\omega}_i$ can be written as follows:

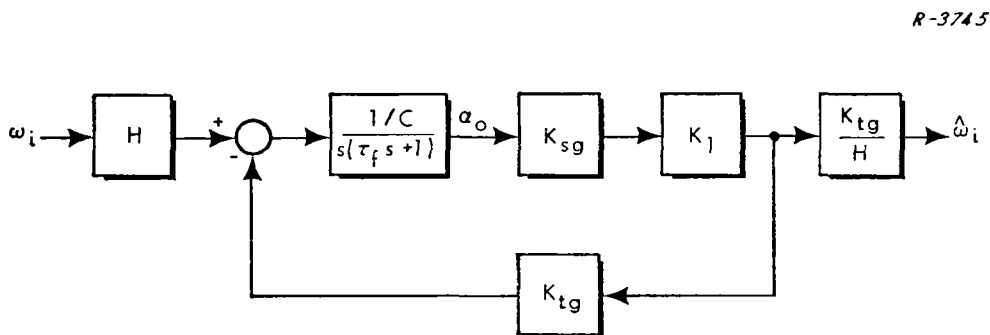


Figure 6.1-2 Representation of a Linear Gyro Loop

$$\begin{aligned} \frac{\hat{\omega}_i}{\omega_i}(s) &= \frac{K_{sg} K_{tg} K_1 / I_{oo}}{s^2 + (C/I_{oo}) s + (K_{sg} K_{tg} K_1 / I_{oo})} \\ &= \frac{\omega_n^2}{s^2 + 2\zeta \omega_n s + \omega_n^2} \end{aligned} \quad (6.1-8)$$

where the natural frequency and damping ratio are given as

$$\omega_n = \sqrt{K_{sg} K_{tg} K_1 / I_{oo}} \quad \text{rad/sec} \quad (6.1-9)$$

$$\zeta = \frac{C}{2\sqrt{I_{oo} K_{sg} K_{tg} K_1}} \quad (6.1-10)$$

The limit cycling, binary torqued loop can be approximated by the linear loop in Fig. 6.1-2 if the equivalent nonlinearity gain to signals of interest can be specified, assuming once again that dynamics of the sample and hold operations can be ignored. In the case of slowly varying input signals (relative to the limit cycle period), the signal appearing at the input to the nonlinearity can be modeled as a sinusoid (the limit cycle) plus a bias (response to the input signal). The gain to the bias, defined as the ratio of nonlinearity output dc amplitude to nonlinearity input dc amplitude (the bias, B), has been called the Dual Input Describing Function, $N_B(A, B)$.

The calculation of the Dual Input Describing Function for a binary nonlinearity (Appendix E) reveals that

$$N_B(A, B) = \frac{2D}{\pi B} \sin^{-1} \left(\frac{B}{A} \right) \quad (6.1-11)$$

In the limit of small B/A this becomes

$$N_B(A, 0) = \frac{2D}{\pi A} \quad (6.1-12)$$

A very important result of recent research in describing function theory suggests that "the gain of the nonlinearity to a small signal in the presence of other signals is the same regardless of the shape of the small signal," (Ref. 10). This means that the use of $N_B(A, 0)$ to represent the nonlinearity gain to information passing through the rebalance loop can be justified on the basis of "smallness" as well as "slowness."

To compute the parameters of the linearized binary loop we can use Eqs. (6.1-9) and (6.1-10), with K_1 replaced by $N_B(A, 0)$:

$$\zeta = \sqrt{\frac{1}{2\tau_f} \left(\frac{\tau_f \tau_{tg}}{\tau_f + \tau_{tg}} \right)} \quad (6.1-13)$$

$$\omega_n = \sqrt{\frac{1}{2\tau_f} \left(\frac{\tau_f + \tau_{tg}}{\tau_f \tau_{tg}} \right)} \quad (6.1-14)$$

Neglecting the torquer lag in the feedback path causes no important error in these calculations. Note that a very interesting phenomenon has occurred. Both ω_n and ζ are independent of all of the loop gains (K_{sg} , K_{tg} , D)! It is this very behavior which is capitalized upon in the design of certain adaptive control systems.

The linearization of the binary gyro loop is a consequence of the limit cycle usually found in a system of this type. Under certain circumstances (to be discussed subsequently) an oscillatory input to the gyro loop can cause the limit cycle to vanish. In that case, the closed loop characteristics of the binary torqued instrument differ significantly from those

presented above. When the limit cycle is not "quenched," Eqs. (6.1-13) and (6.1-14) can be used to study the effect of varying gyro parameters. Figure 6.1-3 illustrates the behavior of the closed loop gain as the float time constant is varied. A similar comparison could be made of phase shift. It will be shown later that compensation can be employed in the gyro loop to reduce peaking in the gain response.

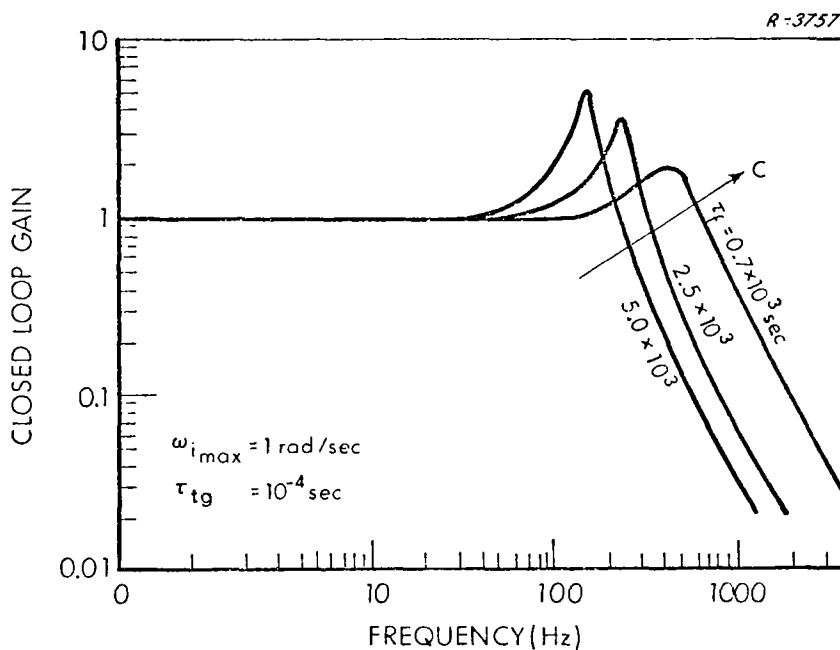


Figure 6.1-3 Closed Loop Frequency Response as a Function of Float Time Constant

Effects of Sampling in the Gyro Loop — In the above discussion the effect of sampling in the loop has been ignored for the sake of simplicity. The sample and hold operation contributes an additional frequency-sensitive phase lag to the open loop dynamics. This can cause the limit cycle frequency and amplitude to be different from those experienced in a continuous binary gyro loop. Consequently, there may be different value for the

nonlinearity gain to the signal and the closed loop frequency response is not the same. While an exact analysis of the effects of sampling is possible, the one discussed here will be approximate, in the interest of simplicity.

The sample and hold transfer function is

$$S(j\nu) = e^{-j\nu T/2} \frac{\sin \frac{\nu T}{2}}{\frac{\nu T}{2}} \quad (6.1-15)$$

where T is the sampler period in seconds. If $\nu T/2 \ll 1$ because the sampler frequency is much higher than other frequencies encountered in the loop, the transfer function is approximately

$$S(j\nu) \cong \frac{1}{1 + j \frac{\nu T}{2}} \quad (6.1-16)$$

The equivalent closed loop natural frequency and damping ratio given in Eqs. (6.1-14) and (6.1-13) can be derived including the effect of the sampler lag expressed by Eq. (6.1-16). The resulting relations are given below.

$$\omega_n = \sqrt{\left(\frac{\tau_f + \tau_{tg}}{2\tau_f}\right) \left(\frac{\tau_f \tau_{tg} + \frac{T}{2}(\tau_f + \tau_{tg}) + \left(\frac{T}{2}\right)^2}{\left(\tau_f \tau_{tg} + \frac{T}{2}(\tau_f + \tau_{tg})\right)^2}\right)} \quad (6.1-17)$$

$$\zeta = \sqrt{\left(\frac{1}{2\tau_f(\tau_f + \tau_{tg})}\right) \left(\frac{\left(\tau_f \tau_{tg} + \frac{T}{2}(\tau_f + \tau_{tg})\right)^2}{\tau_f \tau_{tg} + \frac{T}{2}(\tau_f + \tau_{tg}) + \left(\frac{T}{2}\right)^2}\right)} \quad (6.1-18)$$

The effect of a finite sampling rate on the closed loop gain is illustrated in Fig. 6.1-4 where response curves are shown for a very high sampling frequency and a 10 kHz rate. It can be seen that sampling in the gyro loop tends to reduce the useful bandwidth of the instrument.

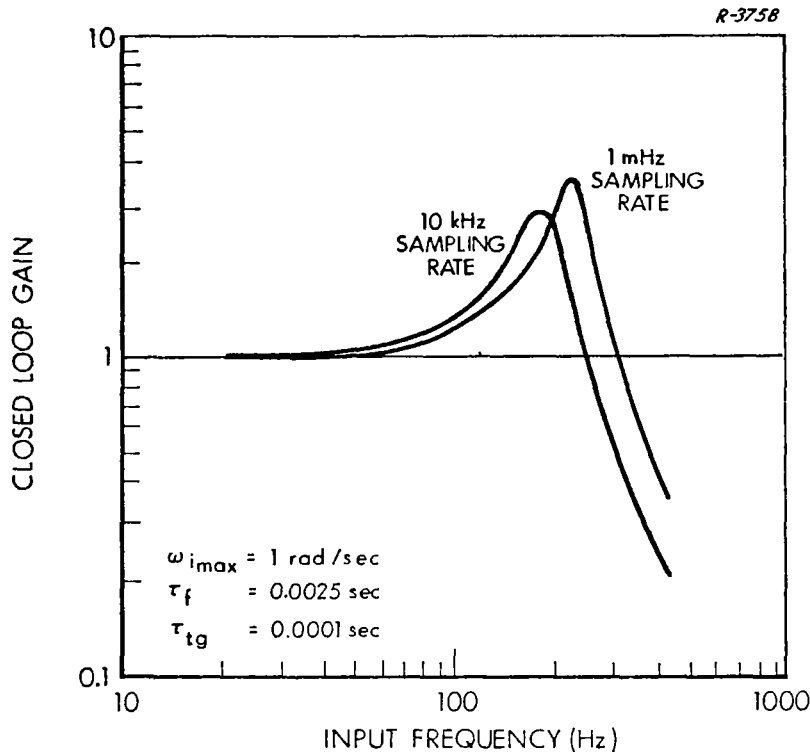


Figure 6.1-4 Closed Loop Frequency Response Showing the Effect of Sampling

6.1.2 Limit Cycle Quenching

It can be seen from the magnitude condition for the existence of a limit cycle, Eq. (6.1-4), that an unforced oscillation cannot exist in the binary loop if

$$N_A \leq \frac{1}{|G(j\omega_\ell)|} \quad (6.1-19)$$

The describing function gain, N_A , of the binary nonlinearity is in general dependent on the limit cycle and input amplitudes A and B. From the theory of Two-Sinusoid-Input Describing Functions (TSIDF's) (see Ref. 10),

$$N_A(A, B) = \frac{8D}{\pi^2 A} E\left(\frac{B}{A}\right) \quad (6.1-20)$$

where $E(B/A)$ is the complete elliptic integral of the first kind and it is assumed that $A/B > 1$. Maximizing N_A over all values of A yields $N_{A_{\max}}$ as a function of B:

$$N_{A_{\max}} = \frac{0.855D}{B}; \quad \frac{B}{A} = 0.909 \quad (6.1-21)$$

Note that the peak gain to the limit cycle decreases as the input amplitude, B, is made larger. Using Eqs. (6.1-21), the amplitude, B_q , of the input sinusoid above which the inequality in Eq. (6.1-19) always holds (the limit cycle is "quenched") is found:

$$B_q = 0.855D |G(j\omega_\ell)| \quad (6.1-22)$$

The nonlinearity describing function gain to the signal when the limit cycle is just quenched is found by substituting $B/A = 0.909$ into the relation for $N_B(A, B)$ given in Ref. 10 and employing Eq. (6.1-22):

$$\begin{aligned}
 N_B(A, B) \Big|_{B=B_q} &= \frac{2.089D}{\pi B_q} \\
 &= \frac{0.778}{|G(j\omega_\ell)|}
 \end{aligned}
 \tag{6.1-23}$$

The binary torqued gyro loop can be viewed as the system shown in Fig. 6.1-5 when the limit cycle is at the point of being quenched.

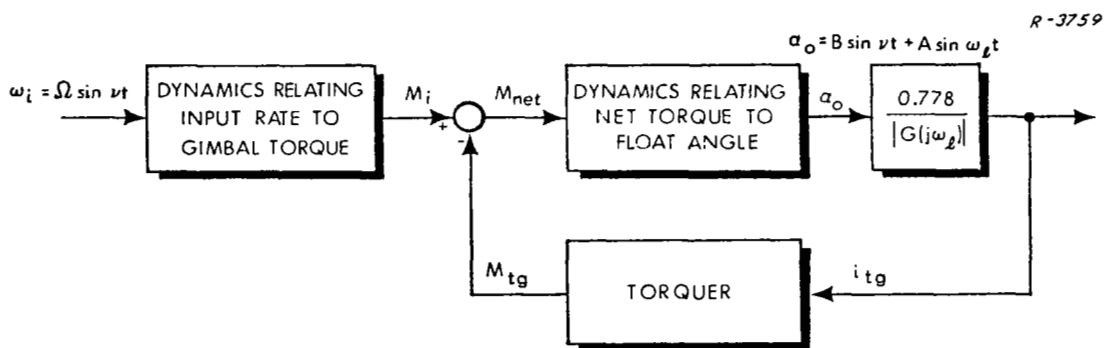


Figure 6.1-5 Binary Loop Viewed at the Point where the Signal Quenches the Limit Cycle

In order to determine the values of input frequency and amplitude which cause the limit cycle to be quenched, the transfer function between input angular rate ω_i and float angle α_o is written in terms of the transfer function for the various blocks in Fig. 6.1-5.

$$\frac{\alpha_o}{\omega_i}(s) = \frac{\frac{M_i}{\omega_i}(s) \frac{\alpha_o}{M_{net}}(s)}{1 + \frac{\alpha_o}{M_{net}}(s) \frac{M_{tg}}{i_{tg}}(s) N_B}
 \tag{6.1-24}$$

From Eqs. (6.1-22), (6.1-23) and (6.1-24), the solution for the input amplitude required to quench the limit cycle can be written:

$$\Omega_{\text{quench}} = \left| \frac{\omega_i(s)}{\alpha_o} \right|_{s=j\nu} B_q$$

$$= \left| \frac{1 + \frac{\alpha_o}{M_{\text{net}}}(s) \frac{M_{\text{tg}}}{i_{\text{tg}}}(s) \frac{0.778}{|G(j\omega_\ell)|}}{\frac{M_i}{\omega_i}(s) \frac{\alpha_o}{M_{\text{net}}}(s)}} \right|_{s=j\nu} 0.855D |G(j\omega_\ell)| \quad (6.1-25)$$

The most convenient way to display Eq. (6.1-25) is a plot of Ω_{quench} as a function of ν . For a particular set of gyro parameters, a single-valued curve results, delineating the boundary between the regions where quenching does and does not occur. Figure 6.1-6 is such a curve, for the same set of parameters used for the calculations in Section 6.2. When the limit cycle is quenched, the loop output is a square wave at the input signal frequency with an amplitude equal to the nonlinearity drive level. If, for example, torquer current is equivalent to 1 rad/sec, the fundamental component of the output has an amplitude of $4/\pi = 1.276$ rad/sec and the gain of the loop is $1.276/\Omega$. These relations are illustrated in the theoretical response curve in Fig. 6.2-4, where $\Omega = 0.1$; the range of frequencies for which the limit cycle is quenched agrees with Fig. 6.1-6 and the loop gain in that range is $1.276/0.1 = 12.76$.

6.1.3 Response to Random Inputs

While the response of binary torqued sensors to sinusoidal inputs is of interest, the motion experienced by strapdown inertial systems is

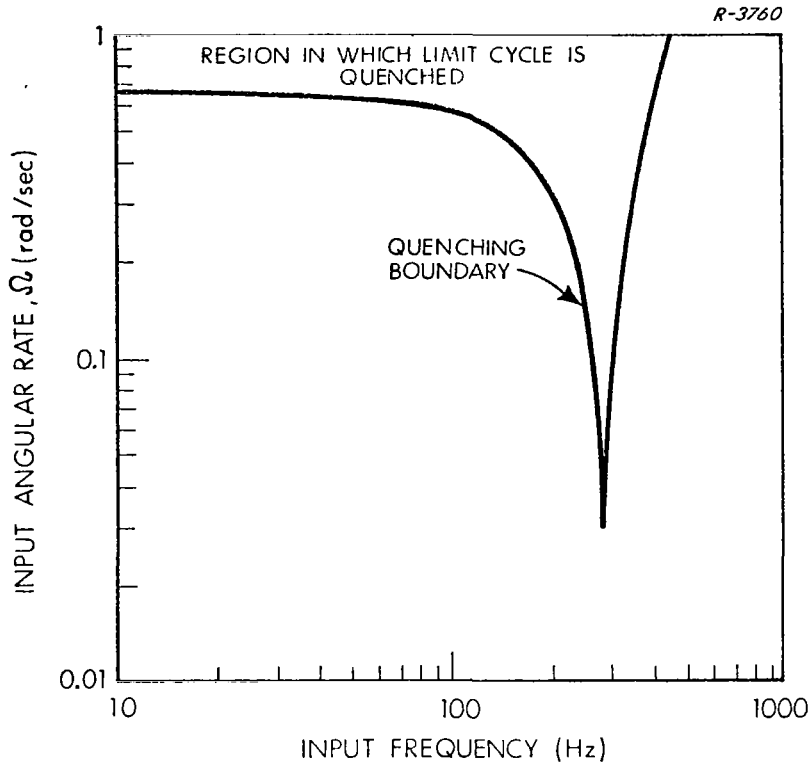


Figure 6.1-6 Limit Cycle Quenching and Its Effect on Frequency Response (Second Order Gyro Dynamics)

more likely to be random and broad bandwidth in nature. Since the limit cycle usually present in the instrument under consideration tends to linearize its response to inputs, it is reasonable to anticipate that an approximate description of the relations between the input spectral density, output spectral density, and co-spectral density between input and output can be obtained from the linearized description just developed for the gyro loop. That is, a second-order linear system whose parameters are given by Eq. (6.1-13) and (6.1-14) (or Eqs. (6.1-17) and (6.1-18)) can be assumed and the usual techniques of linear analysis for random signals can be used. The simulation results displayed in Section 6.2 tend to verify this rather intuitive approach.

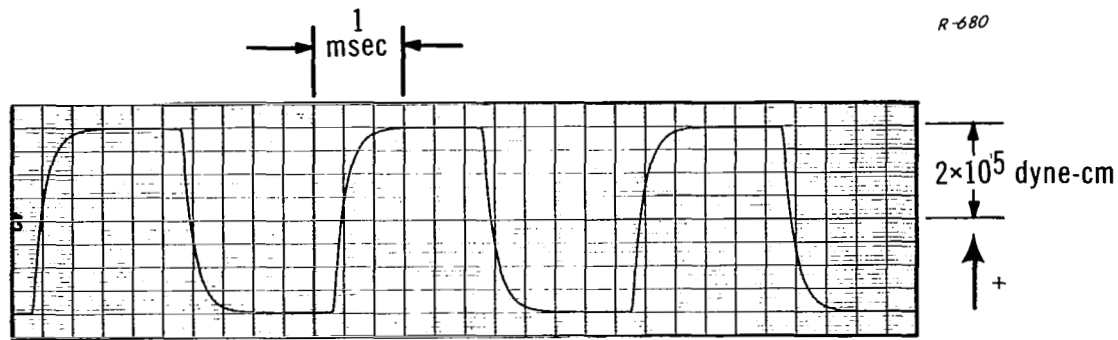
6.2 SIMULATION OF THE BINARY GYRO

The analyses of Section 6.1 provide interesting insights into the closed loop behavior of the binary torqued gyro. The accuracy of these predictions depends on how well the describing function linearization characterizes the true nonlinearity response to a signal in the presence of a limit cycle. As a check on this approach, typical gyro loops were analyzed by the methods discussed in Section 6.1 and then simulated on a hybrid computer to verify the gyro transfer characteristics predicted analytically. The important gyro parameters for this comparison are:

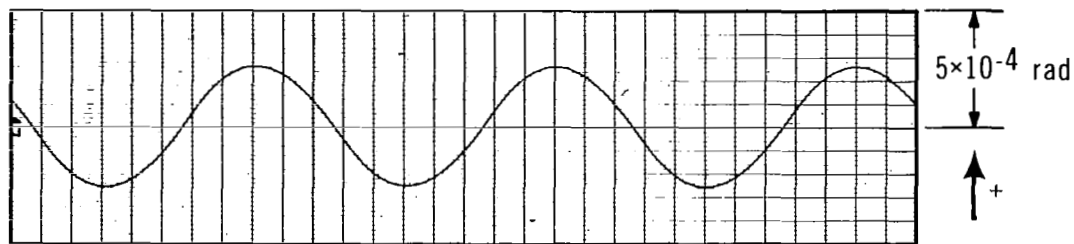
$$\begin{aligned} H &= 2 \times 10^5 \text{ gm-cm}^2/\text{sec} & \tau_f &= 0.0025 \text{ sec} \\ \omega_{i_{\max}} &= 1 \text{ rad/sec} & \tau_{tg} &= 0.0001 \text{ sec} \end{aligned}$$

Figure 6.2-1 displays simulation records of the binary gyro float angle and torquer output in the absence of an input angular rate. A very high sampling rate (1 MHz) was used. The limit cycle observed ($\omega_l \cong 320 \text{ Hz}$) was in close agreement with that predicted for a continuous loop.

An oscillatory angular rate with a peak amplitude of 0.1 rad/sec was applied to the gyro loop. Figures 6.2-2 and 6.2-3 display simulation records of gyro input, float angle and torquer output for two values of input frequency. It can be seen that for a low frequency input the gyro float angle follows the input very closely; despite the simultaneous presence of a limit cycle oscillation. At a higher input frequency, however, it is more difficult to identify signal and limit cycle effects separately. The closed loop frequency response predicted analytically for this system is seen in



(a) Torquer Output, M_{tg}



(b) Float Angle, α_0

Figure 6.2-1 Simulation Records for Limit-Cycling Binary Gyro

Figure 6.2-4, together with points obtained by simulation. There is a good agreement between the two techniques.

Figure 6.1-6 indicates that, for an input amplitude of 0.1 rad/sec, the limit cycle seen in this system is quenched over a range of frequencies above 200 Hz. In accordance with the discussion in Section 6.1, the predicted gain of the closed loop is a constant value of 12.73. Moreover, all information about the input signal amplitude (except that it is large enough to extinguish the limit cycle) is lost, and the gyro loop ceases to function as a linear system. Limit cycle quenching can represent a definite restriction on the range of the amplitudes and frequencies that can be

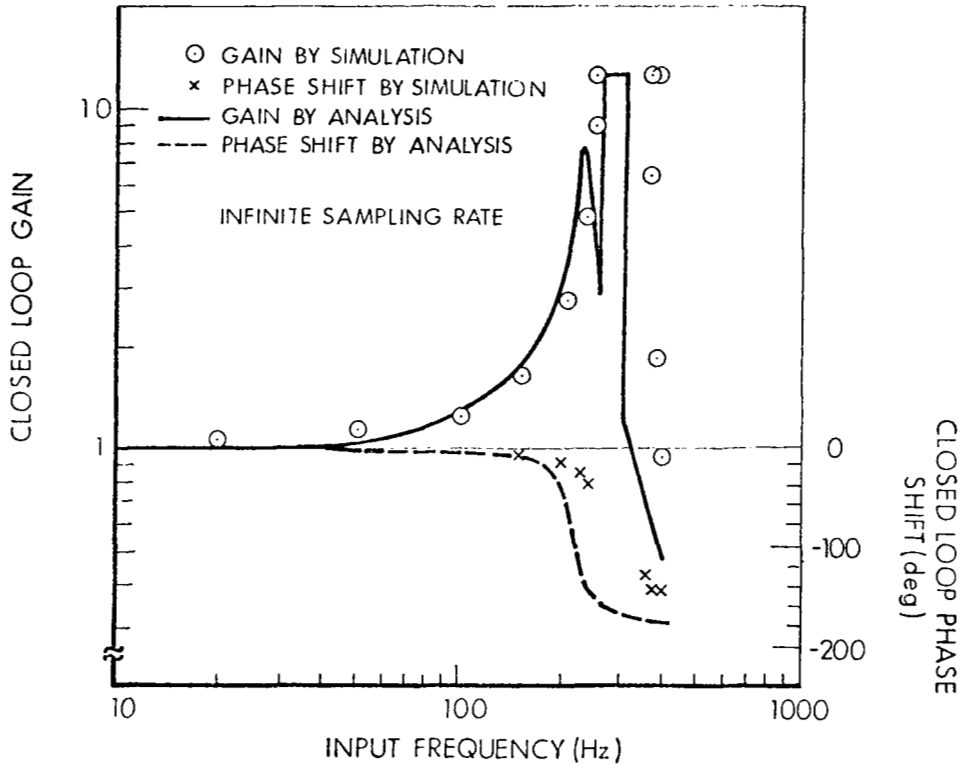


Figure 6.2-4 Frequency Response of a Limit Cycling Binary Gyro: Comparison of Analytic and Simulation Results

accurately detected by a binary gyro. However, quenching is not common at frequencies well below that of the limit cycle.

Figure 6.2-5 presents simulation records illustrating limit cycle quenching. The frequency of the sinusoidal input was increased slowly but the change is not perceptible in the figure. Limit cycle quenching is seen as an abrupt change in loop behavior as reflected in the float angle.

Sampling — Simulations were also conducted for the binary limit cycling gyro with significant sampling lags. Figure 6.2-6 shows the frequency response for a loop with 10^4 samples per second. It differs

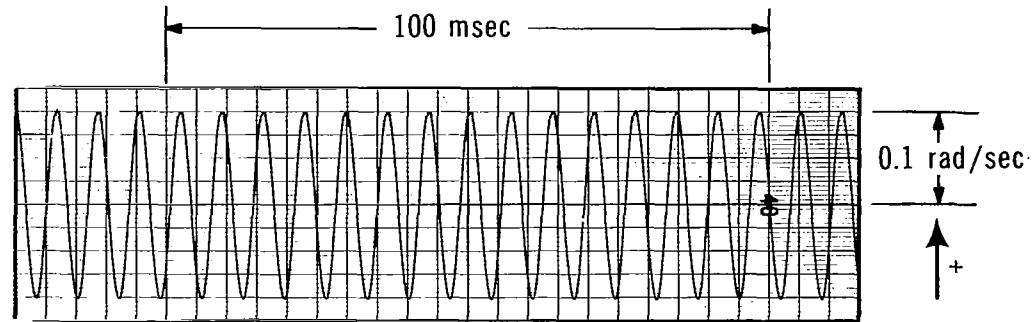
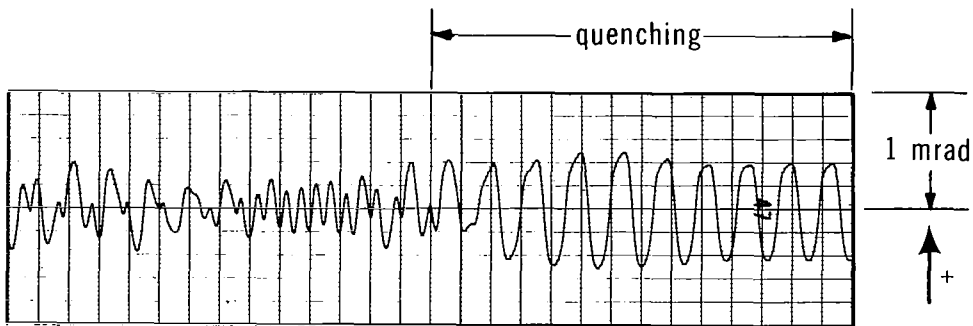
(a) Input Angular Rate, ω_1 (b) Float Angle, α_0

Figure 6.2-5 Binary Gyro Simulation Record
Showing Limit Cycle Quenching

noticeably from that shown in Fig. 6.2-4. The solid line indicates the response computed using describing function theory; points obtained by simulation are also shown. Good agreement between analysis and simulation is indicated.

Random Input Response — A random (broad bandwidth) signal was used to excite the simulated binary rebalanced gyro and the spectral density of the output was measured at various frequencies. The gain to sinusoidal inputs that is predicted from the linearized gyro loop model

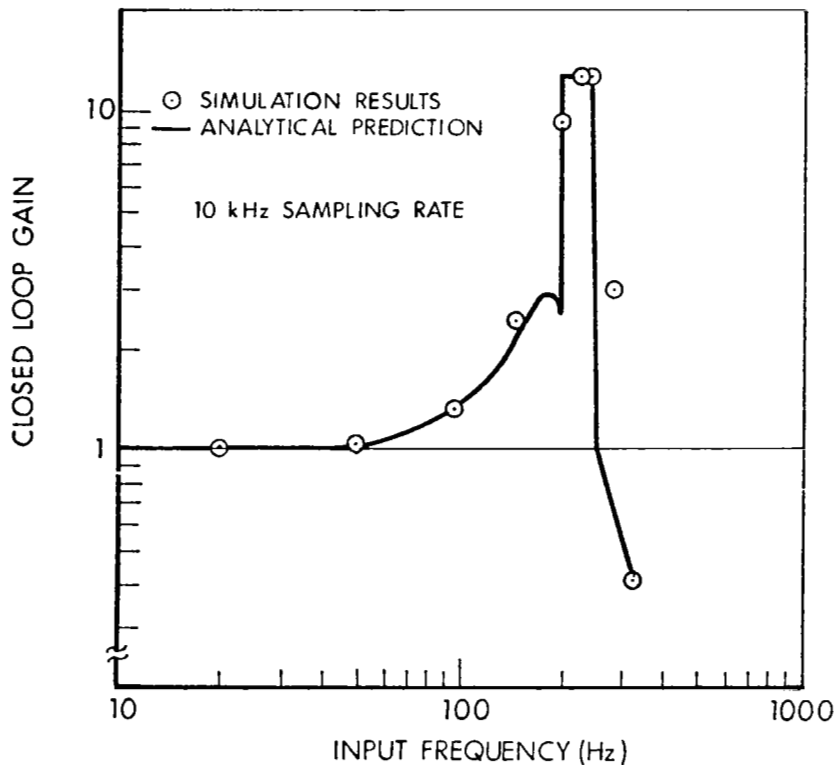


Figure 6.2-6 Frequency Response of a Limit Cycling Binary Gyro: Comparison of Analytic and Simulation Results

developed in Section 6.1.1 was used to anticipate the gain of the sensor to random inputs -- expressed as the square root of the ratio of power spectral densities. Figure 6.2-7 illustrates the root-spectral-density ratios predicted and those measured, for very high sampling rates. Good agreement was obtained for frequencies up to that at which the response peaks (the linearized loop natural frequency). The higher-than-expected output densities at high frequencies are probably due in part to the presence of harmonics of the lower frequency outputs.

No simulation results are available regarding the cross spectral densities between sensor input and output because appropriate signal analysis equipment was not available.

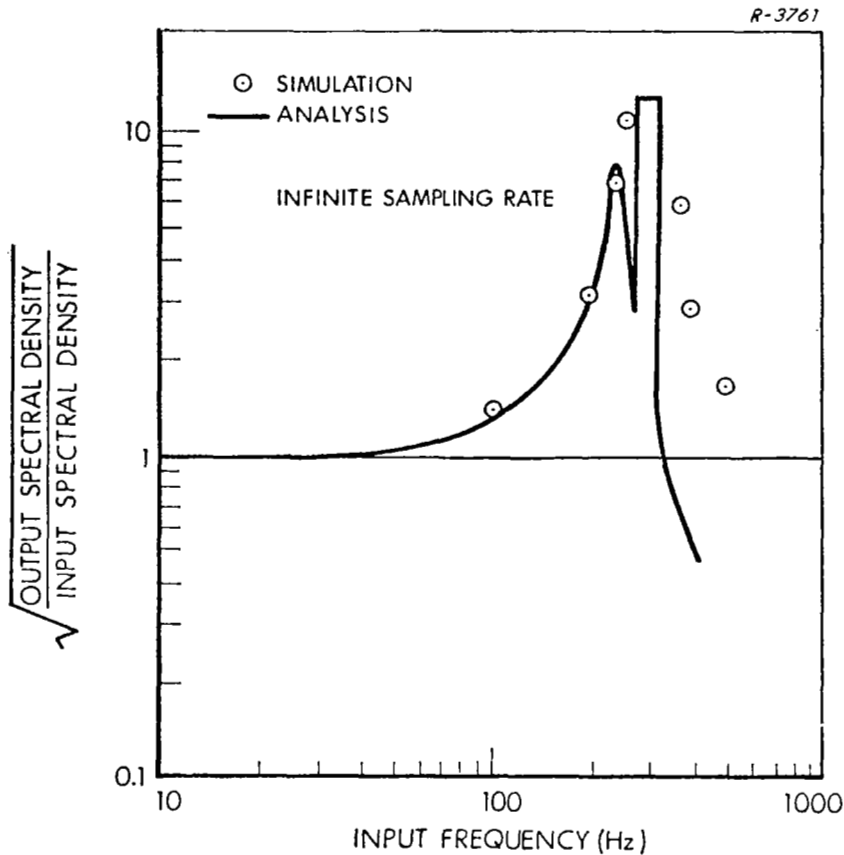


Figure 6.2-7 Random Input Response of a Limit Cycling Binary Gyro: Comparison of Analytic and Simulation Results

6.3 COMPENSATION FOR THE LIMIT CYCLING BINARY GYRO

Introduction — The binary gyro loop limit cycles whether or not a rate signal is present at the input (unless the signal is of high enough amplitude or suitably shaped to quench the limit cycle). As a consequence of the limit cycling property, the closed loop frequency response to an input signal is largely determined by float and torquer time constants and not by easily manipulated electrical gains (see Section 6.1.1). Specifically, if the loop is linearized using describing function techniques, a response

characteristic approximately that of a second order system can result with natural frequency and damping ratio given by Eqs. (6.1-13) and (6.1-14). These frequency response characteristics cannot be changed without making hardware modifications to change τ_f and τ_{tg} . In general, τ_{tg} is made as small as possible in order to permit high sampling rates. Also the float time constant is related to gyro noise effects through the damping coefficient, C. Raising the damping reduces gyro resolution and increases the effect of electrical noise in the pickoff. In addition, no reasonable choice of the time constants can make the damping ratio greater than 1/2. Thus, the frequency response is forced to have a peak near the natural frequency. Clearly, some frequency-sensitive compensation may be desired to remove this peak and, more generally, to permit control of the frequency response characteristics without changing τ_f and τ_{tg} .

Analysis — It is useful to return momentarily to the Two Sinusoid Input Describing Function (TSIDF) used in Section 6.1.2. This representation of the nonlinearity is derived for the case where two sinusoids, at frequencies which are not harmonically related, appear at the input to the nonlinearity. The gains to each sinusoid are computed separately. When the amplitude of the input sinusoid (here B, representing the gyro input) is much smaller than that of the limit cycle (A), the same describing function gains developed in Section 6.1 and Appendix E using Dual Input Describing Function theory result, namely:

$$\left. \begin{aligned} N_B &\cong \frac{2D}{\pi A} \\ N_A &\cong \frac{4D}{\pi A} \end{aligned} \right\} B \ll A \quad (6.3-1)$$

Errors in approximations are less than 10% for $B/A < 0.6$ (Ref. 2). This form of the describing function is useful in the subsequent analysis since

it does not depend on the existence of a large difference in input frequencies, as the Dual Input Describing Function does. The definition of the limit cycle requires that, at the limit cycle frequency, ω_ℓ ,

$$G(j\omega_\ell)N_A = 1 \angle -180^\circ \quad (6.3-2)$$

The limit cycle amplitude A and frequency ω_ℓ adapt to maintain this equality regardless of the compensation introduced. From Eqs. (6.3-1), it can be seen that

$$N_A \cong 2N_B \quad B \ll A \quad (6.3-3)$$

Substituting for N_A in Eq. (6.3-2) yields

$$G(j\omega_\ell)N_B = \frac{1}{2} \angle -180^\circ \quad (6.3-4)$$

Here, $G(j\omega_\ell)N_B$ is the expression for the complex open loop gain as seen by the signal sinusoid. We conclude that, due to the adaptive properties of the limit cycle amplitude and frequency, the open loop gain and phase shift as seen by the signal sinusoid will always be $1/2 \angle -180^\circ$ at ω_ℓ .

The linear analysis technique used to investigate in-loop compensation of binary pulse torqued gyros makes use of the rectangular gain-phase plot (Nichols chart). The open loop gain and phase characteristics are plotted as a function of frequency. On the same plot, lines of constant M (closed loop amplitude ratio) are constructed. The closed loop amplitude ratio for any sinusoidal input is the value of M intersected by the open loop gain-phase curve at the same frequency. The $M = 1$ line represents the desired unity closed loop gain. Figure 6.3-1 shows the $M = 1$ line and the open loop gain-phase curve of the uncompensated gyro loop with the following parameters:

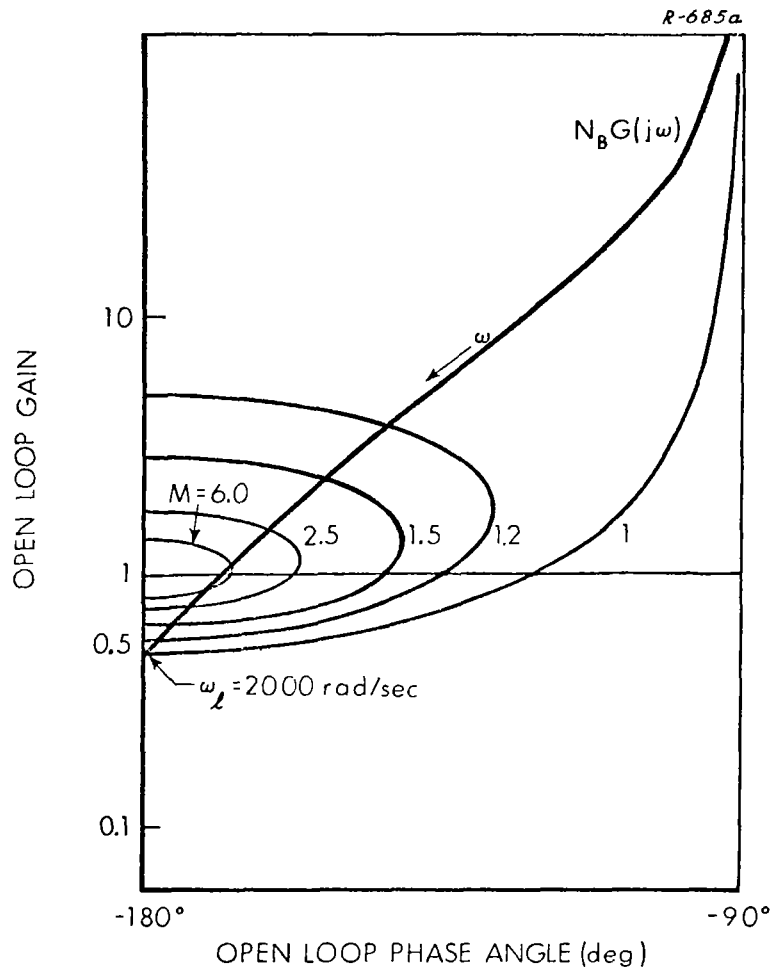


Figure 6.3-1 Open Loop Gain-Phase Plot for Uncompensated Binary Gyro

$$\tau_{tg} = 10^{-4} \text{ sec} \quad \tau_f = 2.5 \times 10^{-3} \text{ sec}$$

Note that the gain-phase curve cuts through high closed loop gain lines at frequencies lower than ω_ℓ , producing a peaked frequency response.

In order to obtain unity closed loop gain at all frequencies below the limit cycle, we must make gain and phase changes to the open loop which cause the compensated gain-phase curve to coincide with the $M = 1$

line. As discussed earlier, the complex open loop gain must always be $1/2 \angle -180^\circ$ at the limit cycle frequency, ω_ℓ ; that is, the gain-phase curve always crosses the -180° phase shift line with a gain of $1/2$ at ω_ℓ whether or not compensation is used. It can be seen from Fig. 6.3-1 that the $M = 1$ line also intersects the -180° line at $1/2$. Three sets of linear dynamic compensation schemes which were tried are listed in Table 6.3-1. In each case the compensation is assumed to be placed in the forward signal path between the signal generator and the nonlinearity. The closed loop gains for gyros employing the three compensation schemes are shown in Fig. 6.3-2, with parameters chosen to give the best loop behavior in terms of a flat response in the low frequency range. The damped second-order plus lag compensation reduces the response peak somewhat, but at the expense of good low frequency behavior. It also lowered the limit cycle frequency in the case studied from 318 Hz to 216 Hz; this has the effect of increasing the limit cycle amplitude. The lead-lag-lag-lead compensation also altered low frequency behavior, but by properly selecting τ_c the limit cycle behavior of the uncompensated loop was maintained. In terms of increasing the region of good (near unity) response the lead-lag compensation appears superior, even though the response peak is not reduced much.

Integral-bypass compensation was also investigated. The motivation for using this form of compensation is to reduce the average low-frequency float angle (taken over one or more limit cycle periods). Specifically, it is desired to use compensation which approximates a pure integrator at low frequencies, thus giving the open loop a double integration characteristic for constant inputs. When the additional integration is inserted in the loop, the average float angle is zero for a constant input. This compensation also reduces the float angles caused by low frequency inputs.

TABLE 6.3-1

LOOP COMPENSATION TRANSFER FUNCTIONS

Damped Second-Order Plus Lag	$\frac{\omega_n^2}{(s^2 + 2\zeta\omega_n s + \omega_n^2)(\tau_c s + 1)}$
Lead-Lag	$\frac{(s\alpha\tau_c + 1)}{(s\tau_c + 1)}$
Lead-Lag, Lag-Lead	$\frac{(s\alpha\tau_c + 1)\left(s\frac{\tau_c}{\alpha} + 1\right)}{(s\tau_c + 1)^2}; \alpha > 1$

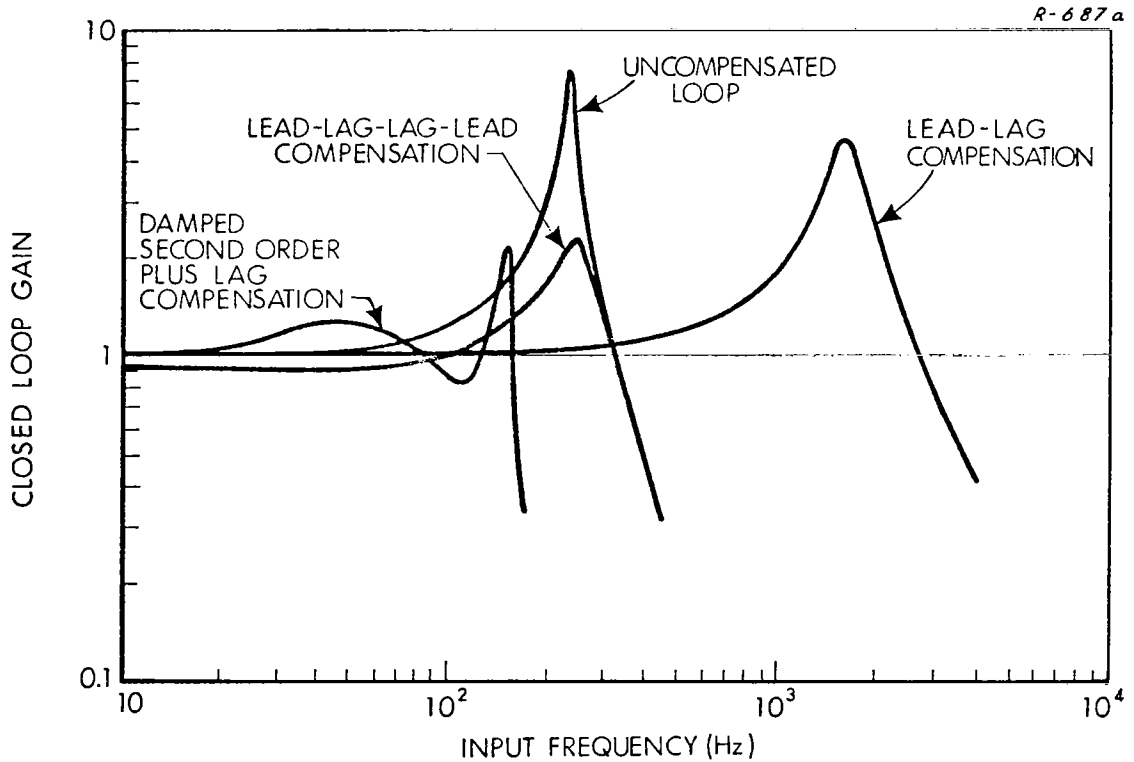


Figure 6.3-2 Closed Loop Gain for Limit Cycling Binary Gyro: Effect of Loop Compensation

Integral-bypass compensation has the transfer function

$$\frac{s + K}{s}$$

At low frequencies the transfer function is approximately K/s , while at high frequencies the compensation has unity gain, no phase shift and does not influence the loop response. It was found that values of K as high as 10 have little effect on the limit cycle frequency or the closed loop response near ω_{ℓ} . For values of $K \leq 10$, integral bypass compensation reduces the average float hangoff from low frequency inputs and leaves the closed loop response essentially unchanged.

Conclusions — The value of compensation in the limit cycling binary gyro loop has been studied analytically. Two forms of compensation which reduced the peak closed loop gain gave poor behavior at low frequencies. A third form of compensation, introducing lead into the gyro loop, increased the bandwidth of the gyro loop. Integral compensation was investigated as a means for stiffening the response of the gyro float to low frequency inputs.

6.4 SUMMARY

An approximate analytic technique, based on describing function theory, was developed for establishing the closed-loop transfer characteristics of binary torqued inertial sensors. The loop behavior predicted by analysis was compared with that found by simulation. The two were seen to be in close agreement. The approximate linear behavior of binary torqued instruments is seen to be a consequence of the limit cycle usually present in these devices. It was also demonstrated that the conditions

under which a limit cycle will not be present can be predicted by analysis. The gain of the uncompensated binary loop to sinusoidal inputs was found to peak below the limit cycle frequency. Several in-loop compensation techniques were briefly explored, in an attempt to improve the gain response.

In Chapter 6 describing function analysis was shown to be of considerable value for treating sensors using binary delta modulation torquing. Similar techniques are applied below to the ternary-torqued gyro of Fig. 7.1-1. Though the approach is basically the same, the effort involved is greater. Again, in order to simplify the problem the sampling nature of the pulsed gyro loop is sometimes ignored.

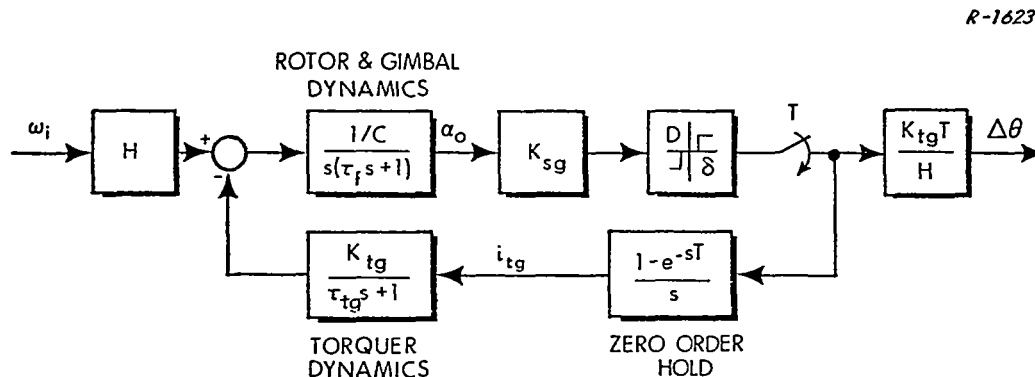


Figure 7.1-1 Ternary-Torqued Gyro Loop

7.1 ANALYSIS OF THE TERNARY GYRO

7.1.1 Response to Sinusoidal Inputs

As in Chapter 6, we desire to make approximations which will permit application of linear analysis techniques for determining the closed loop response to sinusoidal inputs, modeling the loop as shown in Fig. 7.1-2. With the binary gyro, the presence of a limit cycle allows us to approximate the describing function gain by a quantity which depends only on the

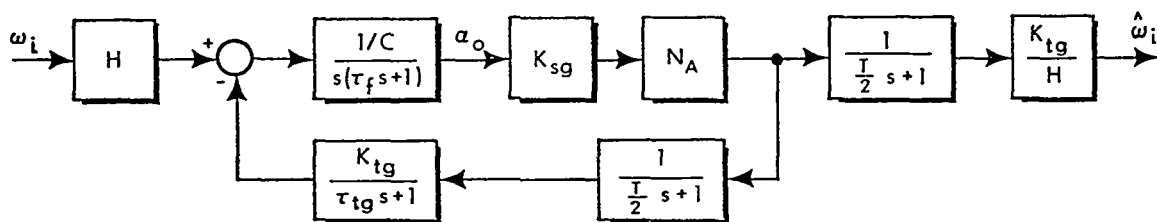


Figure 7.1-2 Linearized Ternary Gyro Loop

limit cycle amplitude. Unfortunately, the ternary gyro does not exhibit a clearly defined limit cycle and the describing function gain of the three-level nonlinearity must be treated as a function of the amplitude of the signal entering it. Also, because the float provides frequency-dependent attenuation, the amplitude of a sinusoid entering the nonlinearity is a function of both the magnitude and frequency of the gyro loop input. Consequently, a different size sinusoid appears at the input of the nonlinearity for each frequency and amplitude combination applied at the loop input. For each input combination explored in the course of a frequency response analysis, a different nonlinearity equivalent gain must be calculated and a separate determination of system output amplitude made -- to obtain one point on the closed loop gain curve.

Describing Function Analysis -- If a sinusoidal input angular rate, $\omega_i = W \sin \nu t$, is applied to the loop shown in Fig. 7.1-2 and the resulting float angle, α_o , is a sinusoid of the form

$$\alpha_o = A \sin (\nu t + \varphi)$$

then the effect of the nonlinearity on the gyro response can be approximated by a simple linear gain which causes no phase shift. The assumption concerning the float angle is valid if there is sufficient low pass filtering in

the system such that the signal at the input to the nonlinearity is basically sinusoidal. The describing function is derived by calculating the Fourier series of the output waveform when the input (float angle) takes the form prescribed above; the magnitude of the first harmonic term of the output divided by the magnitude of the input sinusoid is the desired describing function.

From Fig. 7.1-2 the magnitude of the transfer characteristic from the input ω_i to the float angle α_o , at a particular frequency ν , is given by

$$\left| \frac{\alpha_o(j\nu)}{\omega_i(j\nu)} \right| = \frac{L_1}{\sqrt{1 + 2L_1L_2N_A \cos \phi + (L_1L_2N_A)^2}} \quad (7.1-1)$$

where

$$L_1 = \frac{H/C}{\nu \sqrt{1 + \tau_f^2 \nu^2}} \quad L_2 = \frac{K_{sg} K_{tg}/H}{\sqrt{(\tau_{tg}^2 \nu^2 + 1) \left(\frac{T^2}{4} \nu^2 + 1 \right)}}$$

$$\phi = -\frac{\pi}{2} - \tan^{-1}(\tau_f \nu) - \tan^{-1}(\tau_{tg} \nu) - \tan^{-1}\left(\frac{T}{2} \nu\right)$$

and N_A is the Sinusoidal Input Describing Function of the ternary nonlinearity. It is assumed in Fig. 7.1-2 that the sampling frequency is high compared to all frequencies of interest. Thus the sampler and zero order hold are approximated by the transfer function $1/(Ts/2 + 1)$. Equation (7.1-1) can be rewritten as

$$A \sqrt{1 + 2L_1L_2N_A \cos \phi + (L_1L_2N_A)^2} = W L_1 \quad (7.1-2)$$

where W and A are the peak values of ω_i and α_o , respectively. Squaring both sides of this equation and solving for AN_A gives

$$AN_A = -\frac{A \cos \phi}{L_1 L_2} \pm \frac{1}{L_1 L_2} \sqrt{L_1^2 W^2 - A^2 \sin^2 \phi} \quad (7.1-3)$$

The nonlinearity gain as given by the sinusoidal input describing function is (Ref. 10)

$$N_A = \frac{4D}{\pi A} \sqrt{1 - \left(\frac{\delta}{A}\right)^2} ; \quad A \geq \delta$$

$$N_A = 0 ; \quad A < \delta \quad (7.1-4)$$

This can be written in an alternate form as

$$AN_A = \frac{4D}{\pi} \sqrt{1 - \left(\frac{\delta}{A}\right)^2} ; \quad A \geq \delta$$

$$AN_A = 0 ; \quad A < \delta \quad (7.1-5)$$

Thus we have two relations for the quantity AN_A (Eqs. (7.1-3) and (7.1-5))--one embodying the input magnitude W and linear characteristics in the gyro loop, the other representing the nonlinearity in the system.

Graphical Technique -- The graphical technique for obtaining the frequency response of the ternary gyro can be summarized as follows. An appropriate input amplitude is chosen and held constant during the calculations. An initial input frequency, ν , is selected and the right side of

Eq. (7.1-3) is plotted. An elliptical figure results from this operation. Another value for ν is selected and another ellipse is plotted. This process is continued until a family of ellipses is generated as shown in Fig. 7.1-3. If Eq. (7.1-5) is plotted on the same coordinates, Fig. 7.1-4 results. Intersections between the sinusoidal input describing function gain curve and individual ellipses determine the magnitude of the float angle and the value of the sinusoidal input describing function gain at the frequency at which the ellipse was generated.

From Fig. 7.1-2 the gyro transfer characteristics from input to output are

$$\frac{\hat{\omega}_i(j\nu)}{\omega_i(j\nu)} = \frac{L_1(j\nu) N_A K_{tg}/H}{1 + N_A L_1(j\nu) L_2(j\nu)} \quad (7.1-6)$$

where all frequencies other than that of the input have been neglected. The nonlinearity gain N_A has been determined for various values of frequency, ν , from the graphical intersections. Combining this data with Eq. (7.1-6) gives the transfer characteristics (both magnitude and phase) of the ternary gyro. The float angle response can be obtained in a similar manner, to aid in computing cross-coupling errors.

Figure 7.1-5 illustrates a loop gain curve drawn from the intersection points determined in Fig. 7.1-4. The peaked portion of the closed loop response curve exhibits a "jump resonance" characteristic similar to that given by a softening spring. The effect of deadzone on the closed loop gain is seen as an abrupt drop to zero at the frequency ν_c . If there was no deadzone, the response gain would fall off gradually with increasing

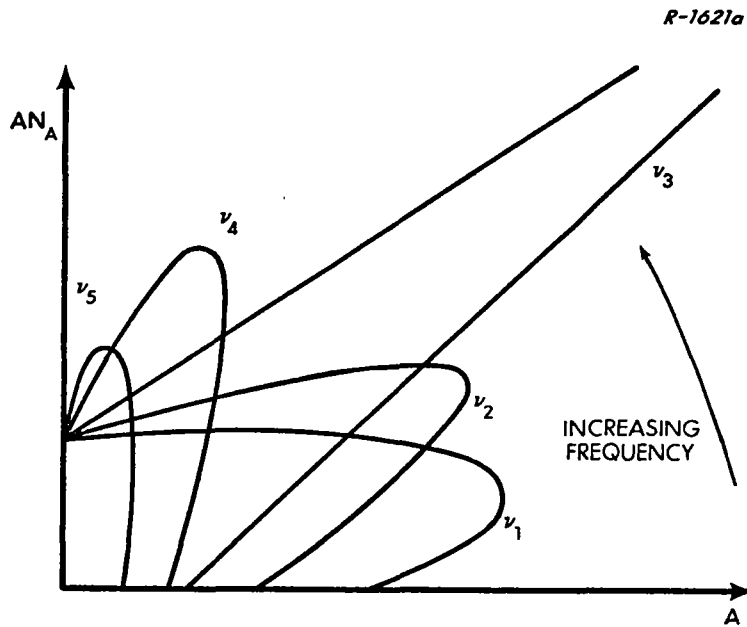


Figure 7.1-3 Family of Ellipses from Linear Part of the Ternary Gyro Loop

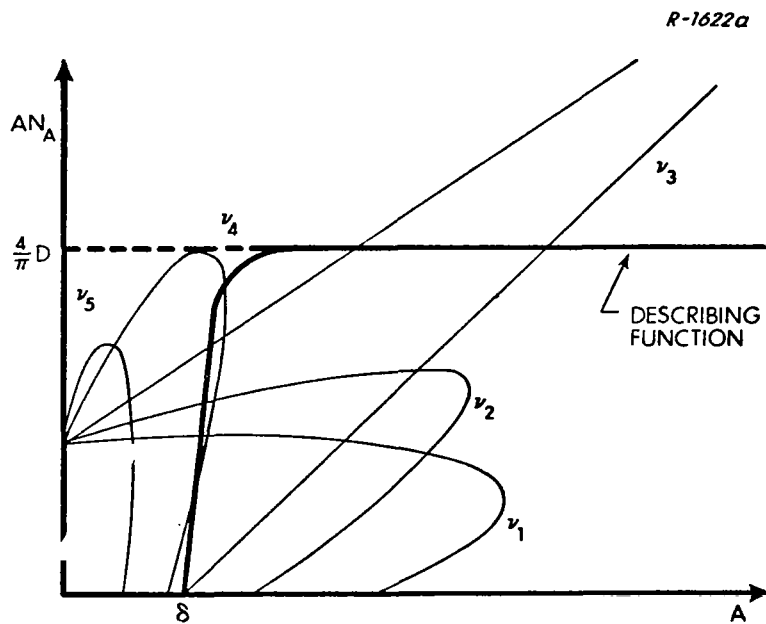


Figure 7.1-4 Combination of Family of Ellipses and Ternary Sinusoidal Input Describing Function

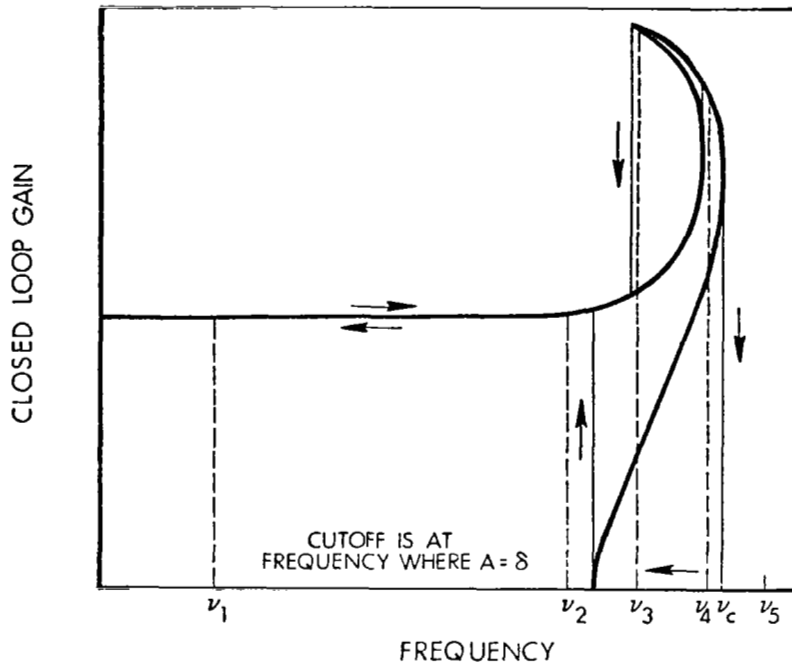


Figure 7.1-5 Ternary Gyro Closed Loop Gain

frequency. However, the deadzone causes the relay to block all signals whose amplitude at the nonlinearity input is less than δ . As frequency increases, the float gain decreases until, at frequency ν_c , the signal at the nonlinearity input is less than δ . Then the output, and consequently the loop gain, drops abruptly to zero. Deadzone also causes the overhanging nature of the response curve. At high input frequencies, attenuation by float dynamics prevents the input to the nonlinearity from exceeding δ . As frequency is decreased the float angle eventually becomes larger than the deadzone, providing a loop output and generating signals at all points in the loop. This occurs at a frequency different from ν_c because the gyro is essentially an open loop system until an output appears at the nonlinearity.

Effect of Input Amplitude — Because the gain of the ternary nonlinearity depends on the amplitude of its input, the ternary gyro loop exhibits

nonlinear gain characteristics. When plotted for different magnitudes of the input sinusoid, the frequency response curves have various shapes (see Fig. 7.1-6). If the input amplitude is small enough (0.01 rad/sec in the figure) the closed loop response for the gyro has no peak. As the size of the input increases, the jump resonance characteristics and dual gain cutoffs discussed above become more pronounced. A look at Fig. 7.1-4 provides an explanation. The ellipsoidal curves obtained from linear analysis are changing size and rotating. As frequency increases, the length of the major axis first increases, then declines. However, rotation of the major axis is monotonic. For the smallest input amplitude plotted in Fig. 7.1-6 no appreciable rotation of the ellipses takes place before the loop output drops to zero. When the gyro input amplitude is raised to 0.03 rad/sec the ellipses rotate and the intersection points occur at higher values of AN_A , giving a peaked loop response. When the largest input is analyzed, the ellipses not only rotate but also become long enough to provide several intersection points at some frequencies; a jump resonance characteristic results. The fact that ternary gyros have a gain which depends on the input amplitude is a serious disadvantage for this type of instrument. If it is necessary to accurately measure high frequency angular vibrations, the ternary pulse rebalanced gyro does not appear satisfactory.

Computer Technique — The above graphical procedure for generating the frequency response curve is tedious and time-consuming because it requires carefully plotting a very large family of ellipses to ensure accurate results. A technique which involves solution of the same set of simultaneous equations by a digital computer can be devised. Examining Eqs. (7.1-3) and (7.1-5) we see that they are two different expressions for the same quantity. For a given frequency of the input we can equate the right side of both equations, thus eliminating the describing function gain, N_A .

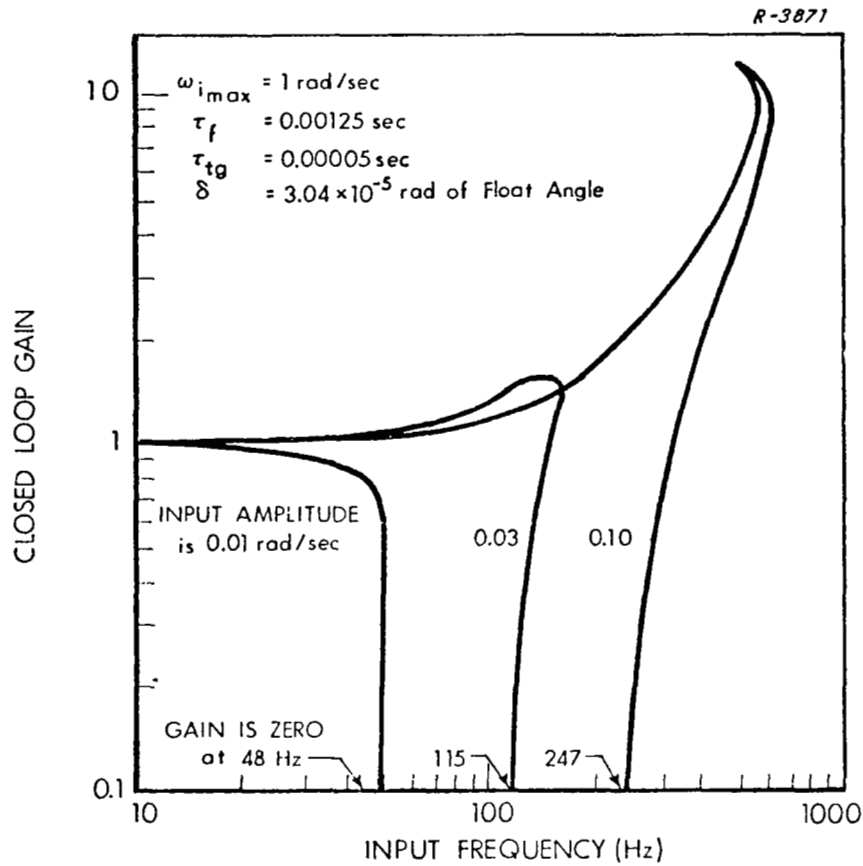


Figure 7.1-6 Effect of Input Amplitude on Closed Loop Gain of a Representative Ternary Gyro Loop

$$\frac{4D}{\pi} \sqrt{1 - \left(\frac{\delta}{A}\right)^2} = -\frac{A \cos \varphi}{L_1 L_2} \pm \frac{1}{L_1 L_2} \sqrt{L_1^2 W^2 - A^2 \sin^2 \varphi} \quad (7.1-7)$$

If this equation is expanded to eliminate the radicals the result is an eighth order polynomial in the float angle magnitude, A,

$$b_1 A^8 + b_2 A^6 + b_3 A^4 + b_4 A^2 + b_5 = 0 \quad (7.1-8)$$

from which the roots can be numerically extracted using a digital computer. Since Eq. (7.1-8) has only even powers of A, half of the roots will have

negative real parts. But A must be real, positive, and greater than the nonlinearity threshold, δ . Physically these requirements can be interpreted by referring to Fig. 7.1-1. The variable A cannot be complex, since it is the magnitude of the float angle; and, in addition, if the float angle is less than the nonlinearity threshold, δ , the relay will not close and the system output will be zero. Imposing these two conditions on the roots of Eq. (7.1-8) gives a maximum of four possible values for A . These roots shall be referred to as "valid values" of A .

The valid values of A correspond to intersections of the curves in Fig. 7.1-4. The main advantage of the analytic method is that the problem can now be solved by computer and many solutions can be generated in a much shorter time than with the graphical technique. A digital computer program was written to make these calculations and generate plots of the ternary gyro frequency response curves. (Reference 3 contains a set of response curves for the Honeywell 334A gyro generated by this program). Some very interesting but unexpected behavior was uncovered through the use of this program; the appearance of so-called "frequency islands" is discussed presently. This phenomenon had not been revealed using the graphical technique.

Frequency Islands — in addition to jump resonance, another interesting characteristic of the ternary gyro's response to sinusoidal inputs has been predicted using the computer program described above. It has also been observed on an analog simulation (see Section 7.2). This phenomenon is referred to as a "frequency island" in the ensuing discussion.

A single frequency island, labeled "curve 2", is illustrated in the magnitude transfer characteristic shown in Fig. 7.1-7. In normal practice, a ternary gyro frequency response curve is obtained by keeping the input amplitude constant and increasing the input frequency, while measuring or calculating the system output magnitude and phase. When this procedure is followed the frequency island is not observed. However, it can be observed by holding the input frequency constant and varying the input amplitude. For example, let the input frequency be fixed at f_2 and increase the input amplitude until the float angle exceeds δ and an output is observed. If the input amplitude is subsequently decreased, the output does not drop to zero and the system continues to respond to the input. If the input amplitude is decreased until it is equal to 0.01 rad/sec, an output will still be observed. Now the system is operating on the frequency island illustrated by curve 2 in Fig. 7.1-7. The frequency can now be varied over a narrow range and the response will be seen to follow curve 2.

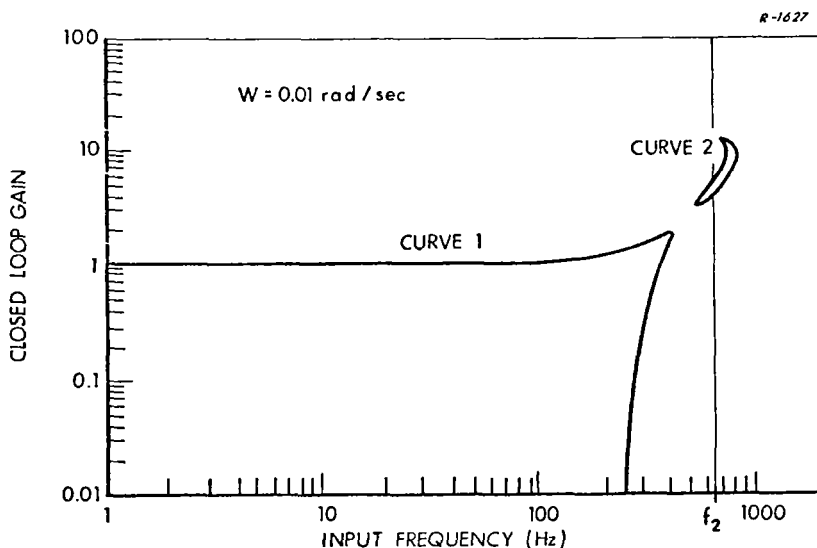


Figure 7.1-7 Ternary Gyro Response With Frequency Island

It appears that a frequency island will exist under the following circumstances: Jump resonance can occur in the loop sinusoidal response for some amplitude of input; the input magnitude under consideration is too small to produce jump resonance. Figure 7.1-8 illustrates how the frequency island develops as input amplitude is decreased. The exact input conditions at which the "main body" of the response connects with the frequency island have not been analytically predicted, but can be obtained by trial and error methods.

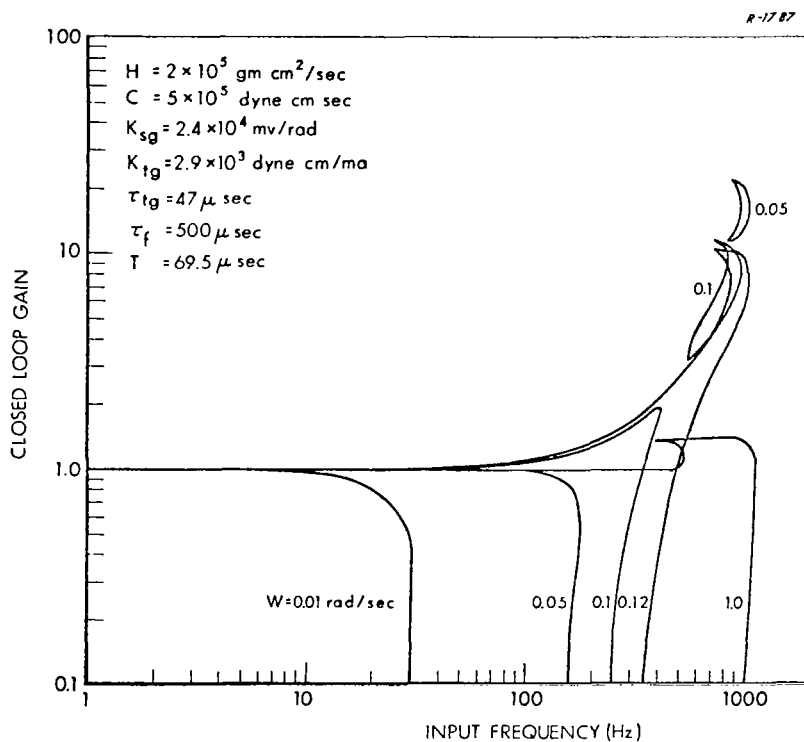


Figure 7.1-8 Ternary Gyro Transfer Characteristics Showing Development of Frequency Islands

A plot of output transfer characteristics versus input amplitude for constant frequency is shown in Fig. 7.1-9. The region in which a frequency island is observed is between input amplitudes W_A and W_B . If

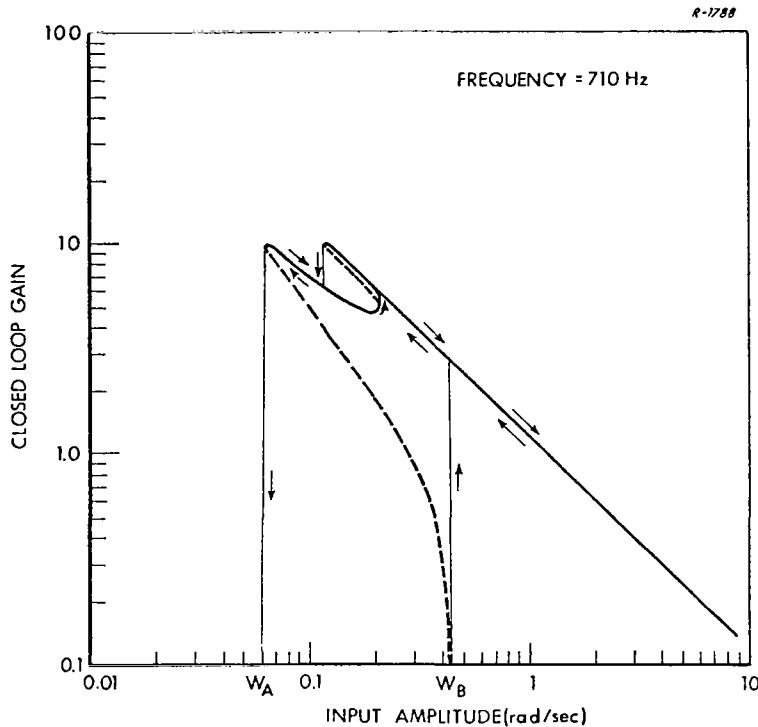


Figure 7.1-9 Gain of Ternary Gyro as a Function of Input Amplitude

input amplitude is increased from zero, no response will be seen until the magnitude of the input rate is equal to W_B . Once an output is observed we can then decrease the input magnitude until it reaches W_A . At W_A the output drops to zero. It can be seen from the figure that as the size of the input is lowered the loop gain increases. This happens because the output amplitude remains approximately constant for a wide range of inputs.

7.1.2 Response to Random Inputs

In the previous section methods were presented to obtain the sinusoidal frequency response of the ternary gyro. In practical applications the environment to which the ternary gyro is subjected is not

generally composed of pure sinusoids; it tends to be more random in nature. The response of the ternary gyro to a random input rate cannot necessarily be implied from the results of the previous section, since the derivation of the sinusoidal input describing function assumed a different form of input.* In this section the analysis is extended to handle the case where the input rate is random. A Random Input Describing Function (RIDF), as derived in Ref. 10, is used to linearize the ternary nonlinearity and the analysis is carried out in a manner similar to the sinusoidal analysis. The transfer characteristics of the nonlinearity are modeled as a constant gain (i.e., the RIDF) for a particular input. The spectral density characteristics of the output are then determined by applying standard statistical analysis techniques for linear systems.

Describing Function Analysis — A Random Input Describing Function can be used to characterize the gain of the nonlinearity to a random signal if certain assumptions are valid for the system. The basic assumption used in deriving this describing function is that the signal at the input to the nonlinearity is unbiased and has a gaussian distribution. The procedure is to calculate a linear gain such that the mean square difference between the true nonlinearity output and product of the input with the gain is minimized. The RIDF so derived depends on the standard deviation of the input as well as the form of the nonlinearity.

For the ternary gyro, if we assume that the float angle, α_0 , is a gaussian signal, the describing function for the nonlinearity is (Ref. 10)

* However, some success has been obtained in using the sinusoidal describing function to predict ternary gyro response to random inputs -- under special circumstances. This is demonstrated in Section 7.2.

$$N_R = \frac{\sqrt{2} D}{\sqrt{\pi} \sigma_{\alpha_0}} \exp \left(- \frac{\delta^2}{2\sigma_{\alpha_0}^2} \right) \quad (7.1-9)$$

where σ_{α_0} is the standard deviation of the float angle. It is reasonable to make the assumption of a gaussian input since in the ternary gyro there is sufficient low pass filtering between the output of the nonlinearity and the float angle to insure that the float angle is gaussian.

Refer to the block diagram of a ternary gyro loop shown in Fig. 7.1-2. If the input has a broad bandwidth compared to that of the gyro loop it can be viewed as white noise, i.e., the input power spectral density can be treated as a constant.

$$\Phi_{\omega_i \omega_i}(\nu) = W \text{ rad/sec} \quad (7.1-10)$$

Including the gain K_{sg} in Fig. 7.1-2 as part of the deadzone definition, the transfer function from the gyro input to the nonlinearity input, α_0 , is

$$G_{\alpha_0}(s) = \frac{\frac{H K_{sg}}{C} (\tau_{tg} s + 1) \left(\frac{T}{2} s + 1 \right)}{\tau_f \tau_{tg} \frac{T}{2} s^4 + \left(\tau_f \tau_{tg} + \tau_f \frac{T}{2} + \tau_{tg} \frac{T}{2} \right) s^3 + \left(\tau_f + \tau_{tg} + \frac{T}{2} \right) s^2 + s + \frac{K_{tg} K_{sg} N_R}{C}} \quad (7.1-11)$$

where N_R is a gain representing the response of the nonlinearity to the random signal at its input (a random input describing function). The power spectral density of the nonlinearity input is

$$\Phi_{\alpha_0 \alpha_0}(\nu) = \Phi_{\omega_i \omega_i}(\nu) \left[G_{\alpha_0}(s) \Big|_{s=j\nu} \right] \left[G_{\alpha_0}(s) \Big|_{s=-j\nu} \right] \quad (7.1-12)$$

and the mean square value of α_0 is, from linear theory

$$\sigma_{\alpha_0}^2 = \frac{1}{2\pi j} \int_{-j\infty}^{+j\infty} \Phi_{\omega_i \omega_i}(\nu) G_{\alpha_0}(j\nu) G_{\alpha_0}(-j\nu) d\nu \quad (7.1-13)$$

Substituting the assumed input spectral density into Eq. (7.1-13) gives

$$\sigma_{\alpha_0}^2 = \frac{W}{2\pi j} \int_{-j\infty}^{+j\infty} G_{\alpha_0}(j\nu) G_{\alpha_0}(-j\nu) d\nu \quad (7.1-14)$$

which can be written as

$$\sigma_{\alpha_0}^2 = \frac{W}{2\pi j} \int_{-j\infty}^{+j\infty} \frac{C(j\nu) C(-j\nu)}{D(j\nu) D(-j\nu)} d\nu \quad (7.1-15)$$

This integral has a special form which can be analytically evaluated. Using the formulas in Table 7.3-1 of Ref. 10, Eq. (7.1-15) becomes

$$\sigma_{\alpha_0}^2 = \frac{K(a_1 N_R + a_2)}{N_R(b_1 N_R + b_2)} \quad (7.1-16)$$

where

$$K = \frac{WH^2 K_{sg}}{2C K_{tg}}$$

$$a_1 = \frac{\tau_{tg}^2 T^2 K_{sg} K_{tg}}{4C} + \frac{K_{sg} K_{tg}}{C} \left[\left(\left(\tau_{tg} + \frac{T}{2} \right)^2 - \tau_{tg} T \right) \left(\frac{T}{2} (\tau_f + \tau_{tg}) + \tau_f \tau_{tg} \right) \right]$$

$$a_2 = \left(\frac{T}{2} + \tau_f + \tau_{tg} \right) \left(\frac{T}{2} (\tau_f + \tau_{tg}) + \tau_f \tau_{tg} \right) - \frac{\tau_{tg} \tau_f T}{2}$$

$$b_1 = - \frac{K_{sg} K_{tg}}{C} \left(\frac{T}{2} (\tau_f + \tau_{tg}) + \tau_f \tau_{tg} \right)^2$$

and

$$b_2 = a_2$$

Solving Eq. (7.1-16) for N_R gives

$$N_R = \frac{K a_1 - \sigma_{\alpha_0}^2 b_2}{2\sigma_{\alpha_0}^2 b_1} \pm \frac{1}{2\sigma_{\alpha_0}^2 b_1} \sqrt{\left(\sigma_{\alpha_0}^2 b_2 - K a_1 \right)^2 + 4\sigma_{\alpha_0}^2 b_1 K a_2} \quad (7.1-17)$$

Equations (7.1-9) and (7.1-17) are a pair of simultaneous relations in N_R and σ_{α_0} . One is based on analysis of the closed loop system in which the nonlinearity is modeled as a constant gain and the other is the random input describing function. Each of these equations can be plotted.

Intersections between the resultant curves will define values for N_R and σ_{α_0} which are solutions to the two equations. This technique is analogous to the graphical technique for obtaining the sinusoidal response. But here we are not required to plot a large family of curves to insure accurate results for a single representative input.

As an alternate approach we can use a digital computer program to numerically solve the two equations. Substituting Eq. (7.1-9) into Eq. (7.1-16) and rearranging gives an equation describing σ_{α_0} when a solution occurs:

$$\sigma_{\alpha_0}^2 = \frac{K \left(\frac{\sqrt{2} Da_1}{\sqrt{\pi} \sigma_{\alpha_0}} \exp \left(-\frac{\delta^2}{2\sigma_{\alpha_0}^2} \right) + a_2 \right)}{\frac{\sqrt{2} D}{\sqrt{\pi} \sigma_{\alpha_0}} \left(\frac{\sqrt{2} Db_1}{\sqrt{\pi} \sigma_{\alpha_0}} \exp \left(-\frac{\delta^2}{2\sigma_{\alpha_0}^2} \right) + b_2 \right) \exp \left(-\frac{\delta^2}{2\sigma_{\alpha_0}^2} \right)} \quad (7.1-18)$$

This nonlinear equation can be arranged to fit the general form

$$f(\sigma_{\alpha_0}) = 0 \quad (7.1-19)$$

There are several general digital computer subroutines which will solve nonlinear equations of the form of Eq. (7.1-19). Once the standard deviation of the float angle is determined by solving Eq. (7.1-18), the random input describing function gain can be calculated from Eq. (7.1-9). This can be used to determine the transfer function between the input and the float angle, Eq. (7.1-11), and the power spectral density of the float angle, Eq. (7.1-12).

If we assume, as in the sinusoidal case, that there is insignificant phase shifting between the nonlinearity input and gyro output and if all harmonic terms created by the nonlinearity are neglected, then the transfer function from input, ω_i , to output, $\hat{\omega}_i$, is

$$\frac{\hat{\omega}_i}{\omega_i}(s) = \frac{N_R K_{tg}}{H} G_{\alpha_0}(s) \quad (7.1-20)$$

for a fixed σ_{α_0} as determined from the solution of Eq. (7.1-18). The corresponding power spectral density of the output is

$$\begin{aligned} \Phi_{\omega_i \hat{\omega}_i}^{\hat{\omega}_i}(\nu) &= \Phi_{\alpha_0 \alpha_0}(\nu) \left(\frac{N_R K_{tg}}{H} \right)^2 \\ &= \left(\frac{N_R K_{tg}}{H} \right)^2 \Phi_{\omega_i \omega_i}(\nu) G_{\alpha_0}(j\nu) G_{\alpha_0}(-j\nu) \end{aligned} \quad (7.1-21)$$

A digital computer program was written to make the calculations described in this section and plot the results. Figure 7.1-10 illustrates the output magnitude transfer characteristics predicted by the above form of analysis. The in-phase and quadrature components of the transfer characteristics are defined by Fig. 7.1-10 and the resultant phase angle, φ , plotted in Fig. 7.1-11. The phase angle also defines the resultant co- and quad-spectral density between the input and output. The output power spectral density is shown in Fig. 7.1-12. Notice that, as with the sinusoidal response, the random response of the ternary gyro depends on the size of the input.

To date two major problems have prevented verification of the above analysis: lack of sufficient instrumentation for use in conjunction

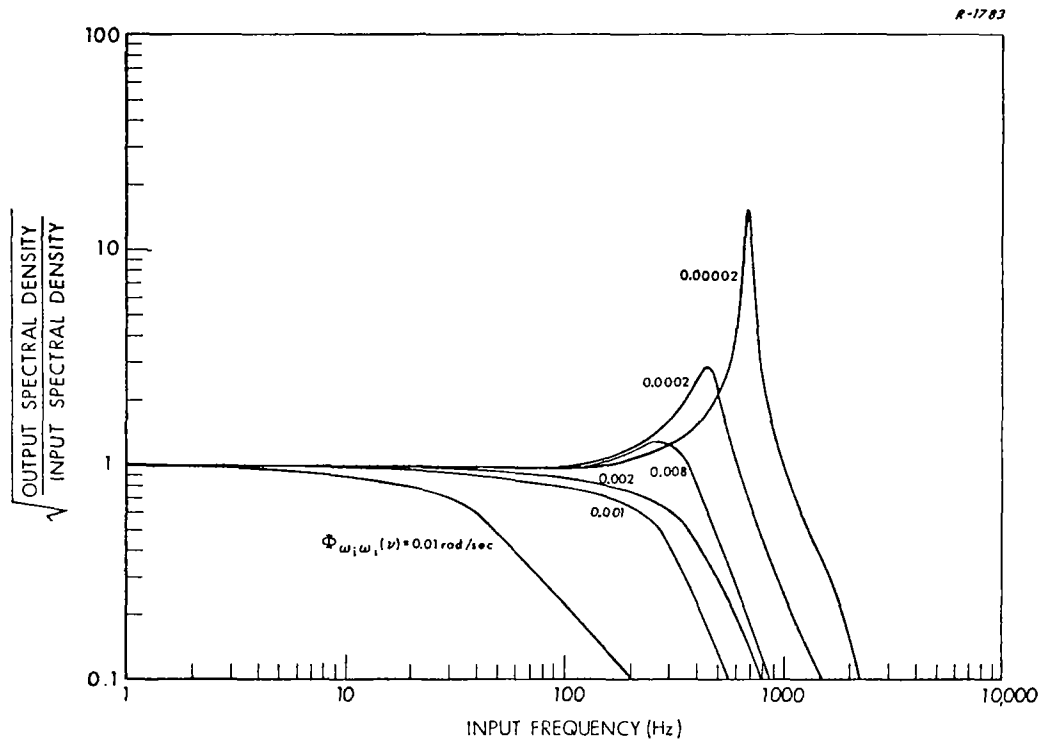


Figure 7.1-10 Output Gain Characteristic of the Ternary Gyro for a Random Input

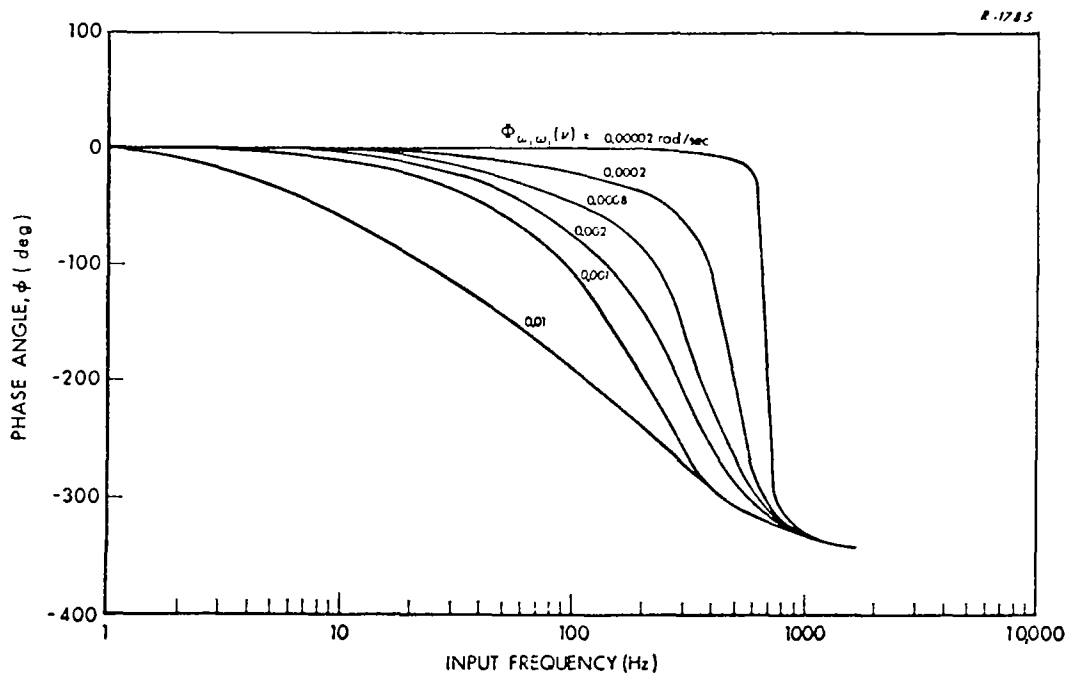


Figure 7.1-11 Output Phase Lag of Ternary Gyro for a Random Input

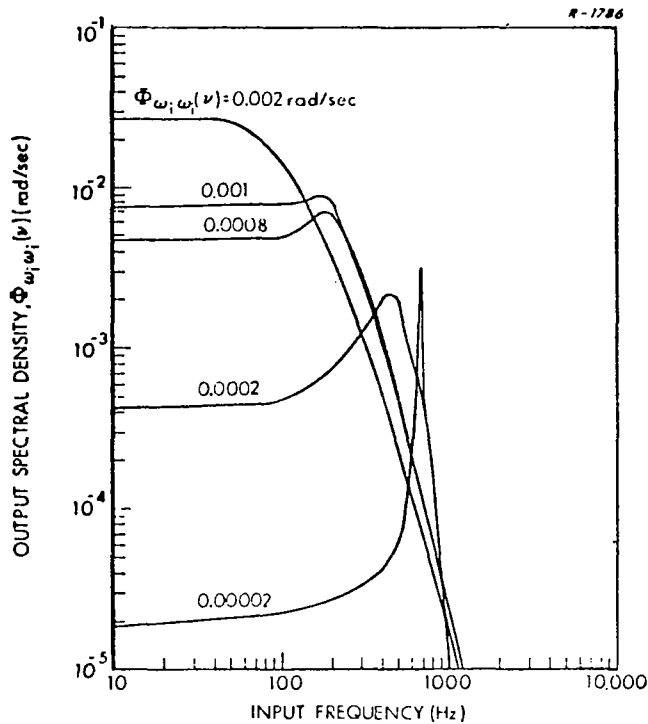


Figure 7.1-12 Power Spectral Density at the Output of the Ternary Gyro: White Noise Input

with the gyro simulation, and multimoding (see below). The instrumentation problem can be surmounted by obtaining a sufficiently "white" noise source and an accurate low frequency spectrum analyzer. The multimoding problem is more difficult to overcome.

Multimoding — Multimoding in the random response of a ternary gyro has an analogy in jump resonance in the sinusoidal response. The result of jump resonance is that the output of the ternary loop can have more than one output magnitude for the same size input. The result of multimoding is that the output power spectrum can have more than one shape for the same random input spectrum. The difference between these two effects is that in the random response, the output power spectrum spontaneously shifts between the various modes. The objective of this section is to show analytically why multimoding occurs.

In determining the random response of the ternary gyro, it was necessary to numerically solve a nonlinear equation in σ_{α_0} . If the function defined as $f(\sigma_{\alpha_0})$ in Eq. (7.1-19) is plotted as a function of the standard deviation σ_{α_0} , a curve such as that shown in Fig. 7.1-13 can result. Each intersection of this curve with the horizontal axis is a solution to Eq.(7.1-18) corresponding to a different response mode. There is simulation evidence to suggest that these modes are not necessarily stable (i.e., if the standard deviation of the float angle will stay at a magnitude corresponding to a particular mode for a finite amount of time, then it is a stable mode).

R-1782

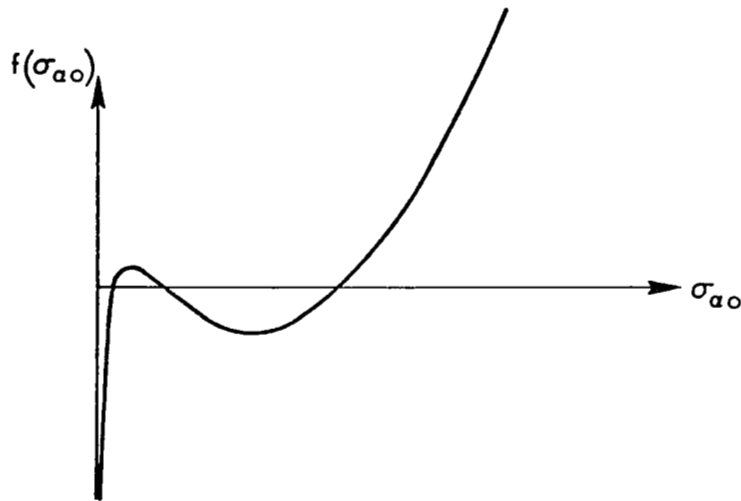


Figure 7.1-13 Nonlinear Function of the Standard Deviation of the Float Angle

In the random response of a linear system there is no analogy to multimoding. The fundamental reason for multimoding is that the effective gain of the nonlinearity is not a constant but rather varies with input conditions.

The result of the multimoding is that for a given input spectral density the gain of the gyro changes randomly, causing the spectral density

at the output to shift between the various stable modes. Multimoding is observed in the simulation as abrupt changes in the magnitude of the output signal at random time intervals. Figure 7.1-14 illustrates the time history of a ternary gyro with a broad bandwidth input, obtained from the simulation. Examining the float angle signal, there appear to be two distinct modes. (There is a possibility that the gyro response between t_1 and t_2 is a limit cycle. However, the nonlinearity threshold, δ , was selected to be well above the minimum value that should prevent a limit cycle. Since the response between t_1 and t_2 in Fig. 7.1-14 is clearly different from the response between t_3 and t_4 , we conclude that the gyro loop is operating in two distinct modes.

The gyro loop simulated appears to have at least two stable modes. These time histories are very similar to curves published by Booton (Ref. 11). In that reference, the author was not successful in isolating the different modes, however the existence of the modes was the only way he could justify his simulation results. There does not appear to be a simple way to determine the mode in which the system is operating at a given point in time. Therefore the system response is ambiguous. Figure 7.1-15 illustrates two output spectral densities predicted analytically from the same random input.

The principal problem caused by multimoding is that one value of the input can result in one of several values of output. This is analogous to the ambiguities encountered in jump resonance in the sinusoidal response, and the same objections apply.

Summary — A method for obtaining the random response of a ternary gyro has been presented in this section, although it has not been verified by analog simulation. This approach involves the use of a random input describing function to characterize the gain of the ternary nonlinearity.

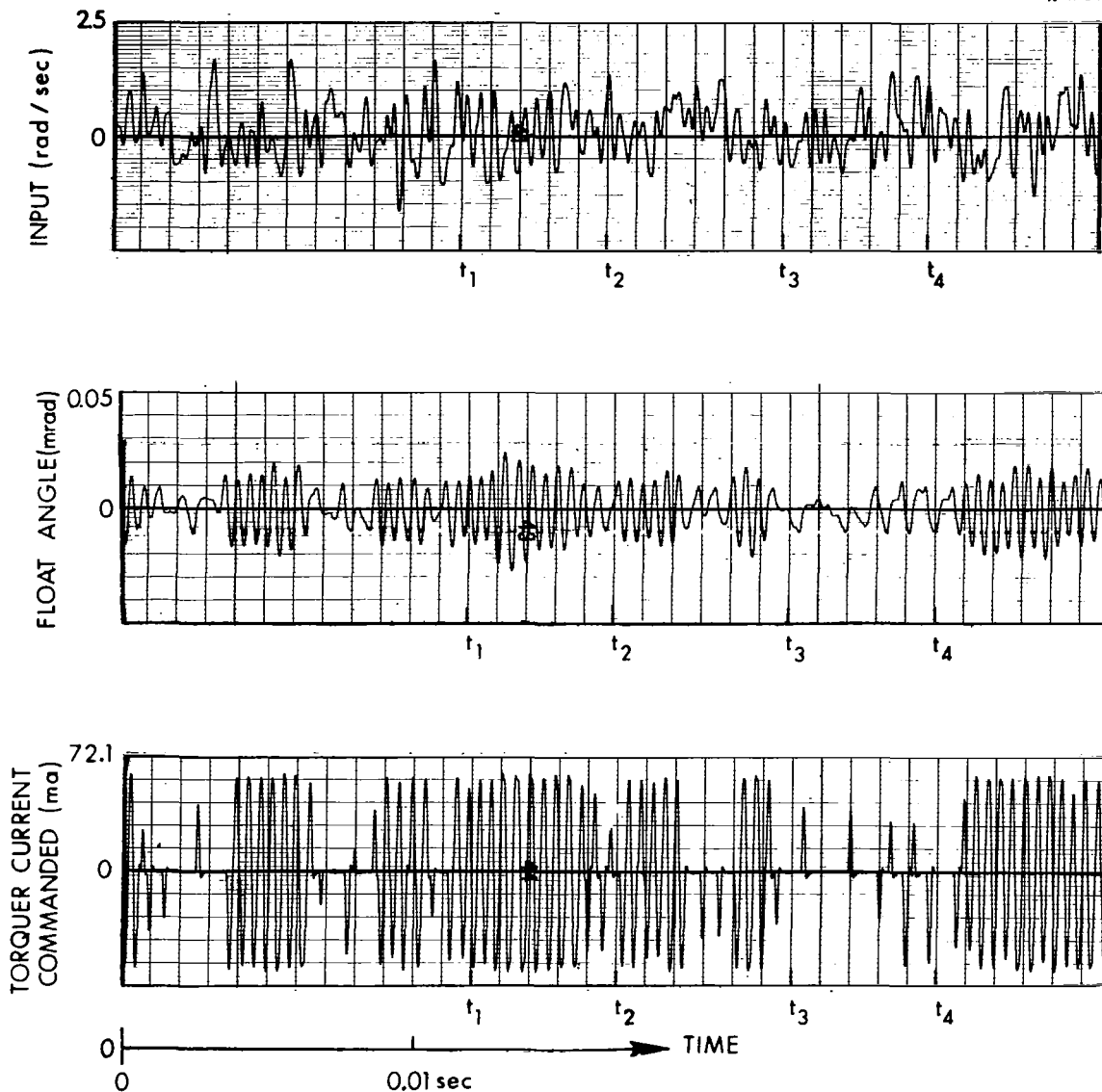


Figure 7.1-14 Time History of Ternary Gyro With a Random Input, Illustrating Multimoding

The technique displayed here was chosen because of its simplicity compared to other methods. It was also shown that multimoding causes ambiguities in the response of the ternary gyro, just as jump resonance does in the sinusoidal response.

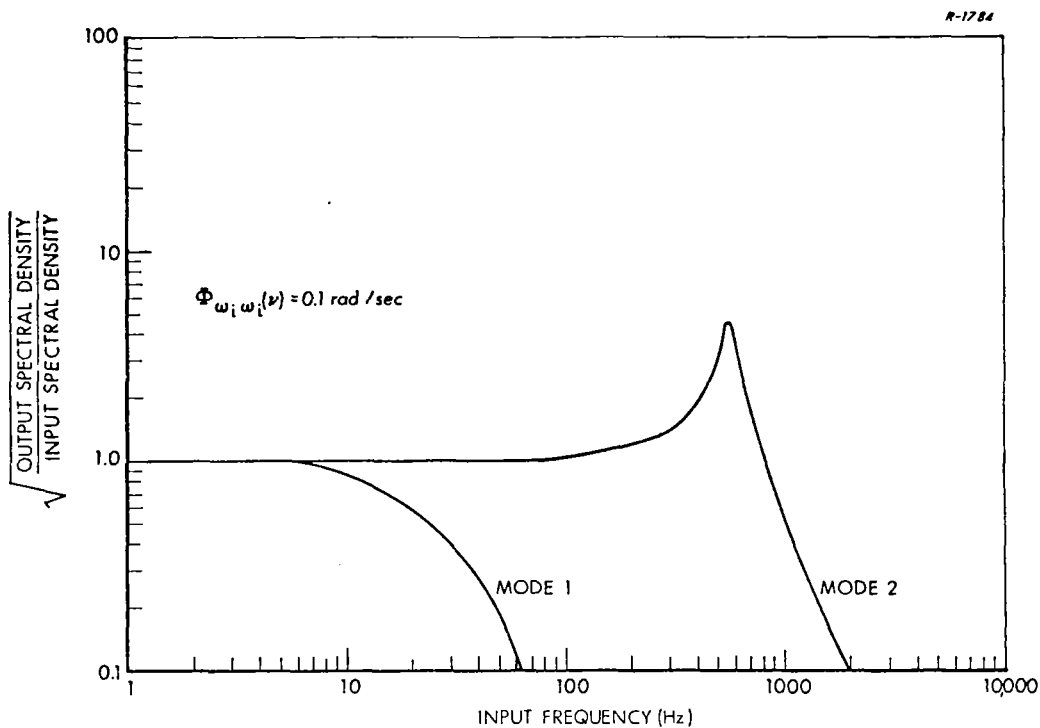


Figure 7.1-15 Gain Response for Ternary Gyro With Two Modes

7.2 SIMULATION OF THE TERNARY GYRO

The analytic techniques demonstrated in Section 7.1 provide interesting insights into the closed loop behavior of the ternary-torqued gyro loop. However, the accuracy of these predictions depends on how faithfully the describing function approximation characterizes true non-linearity performance. As a check on the validity of this approach, characteristics of certain ternary loops were computed and the results verified using computer simulation.

Sinusoidal Inputs — A set of parameters is chosen to represent a typical ternary gyro loop with second order gimbal dynamics (see Fig. 7.1-1):

$$\begin{aligned} \omega_{i_{\max}} &= 1 \text{ rad/sec} & \tau_{tg} &= 0.00005 \text{ sec} \\ \tau_f &= 0.00125 \text{ sec} & \delta &= 4.17 \times 10^{-5} \text{ rad of float angle} \end{aligned}$$

$$H/C = 1$$

With the exception of the nonlinearity deadzone δ , these are the same values as those shown in Fig. 7.1-6. A different value of deadzone was used for this comparison to ensure that no limit cycle took place in the simulated gyro loop. Oscillatory angular rate inputs with a peak amplitude of 0.1 rad/sec were applied to the simulated gyro. Figures 7.2-1 and 7.2-2 show records of the input, float angle and torquer output when two different input oscillation frequencies were simulated. The sampling rate in both cases illustrated is 1 mHz, providing essentially continuous ternary loops. The closed loop gain of this gyro is distinguished by jump resonance and a peak at 400 Hz (see Fig. 7.2-3). Discrete points obtained via simulation are indicated while the curve predicted by describing function analysis appears as a solid or dashed line. Note that the analytic response contains unstable segments in the jump resonance region which cannot be observed for any length of time by simulation. They represent unstable modes which do not occur in the actual instrument either. Agreement between the analytic and simulation results is quite good on the stable portions. The response is similar in shape to the curve seen in Fig. 7.1-6.

Figure 7.2-4 presents simulation records illustrating the behavior of the ternary gyro float angle at a jump resonance point. The input frequency is being raised so slowly that the change cannot be detected on the record, but the gyro float angle behavior shows a clear discontinuity. The gain of the gyro loop was observed to increase suddenly at the point where α_0 becomes larger. The point shown is the amplitude jump in Fig. 7.2-3 that takes place at 500 Hz as the input frequency is increased.

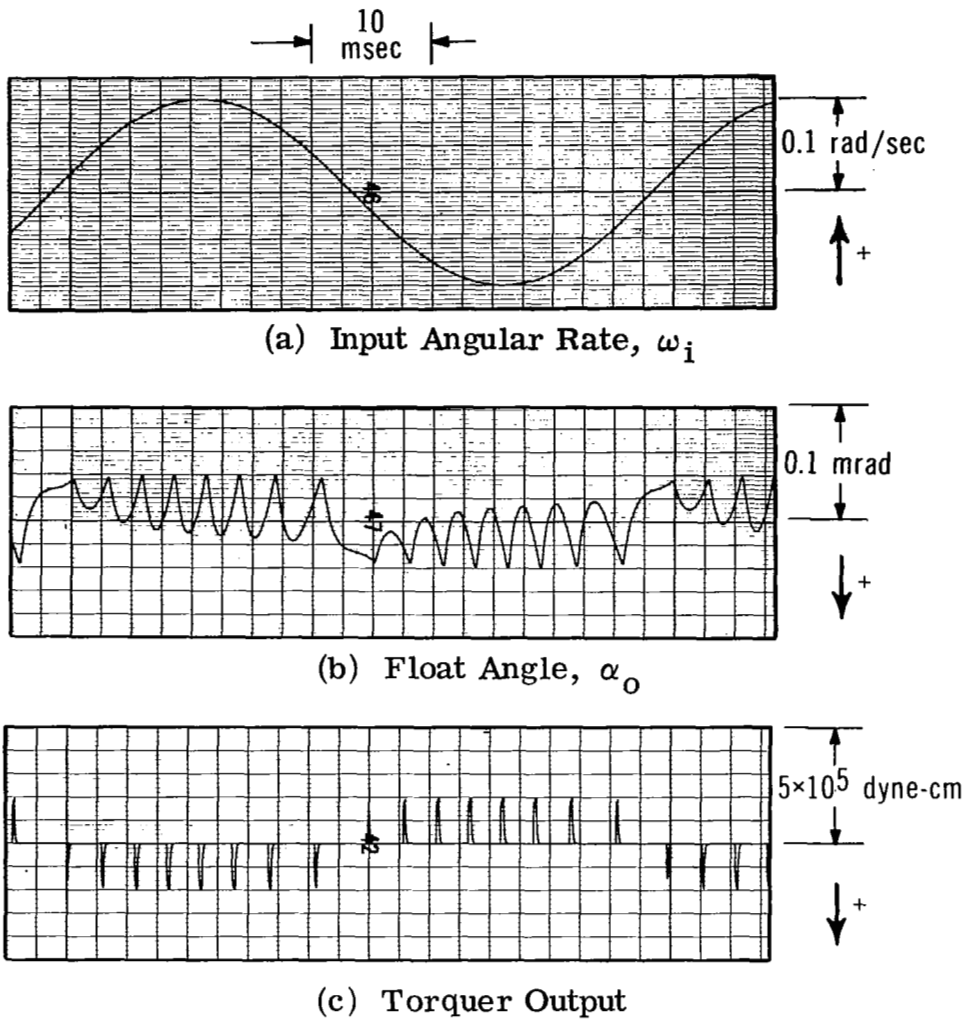


Figure 7.2-1 Ternary Gyro Simulation Records: 20 Hz Input

Frequency Islands — The existence of frequency islands was also verified using a ternary gyro simulation. Figure 7.2-5 displays some portions of the simulation record to illustrate gyro behavior as the input amplitude was slowly reduced. The lower trace shown in each box is that of the output of the zero order hold device in the gyro loop. This represents the torque level called for by the rebalance logic and is directly related to the gyro output. It can be seen that the desired rebalance torque (and consequently gyro output) remains essentially unchanged in spite of a large

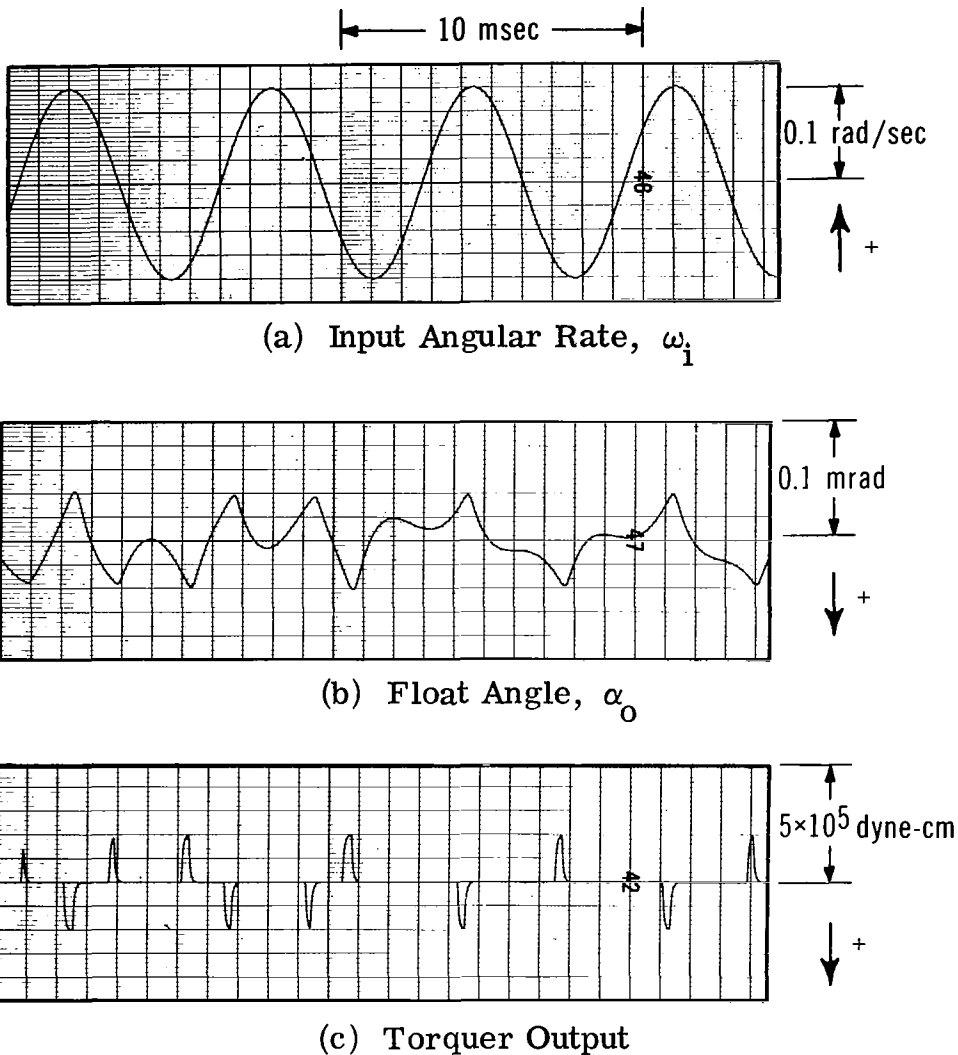


Figure 7.2-2 Ternary Gyro Simulation Records: 150 Hz Input

reduction in the gyro input magnitude. For the input shown in the last box the gyro would not exhibit an output if it had been excited by holding the input amplitude constant while raising the frequency to the value shown.

Random Inputs — In spite of the difficulties concerning multimoding that are outlined in Section 7.1.2 some success was realized by predicting the response of a ternary gyro to random inputs using the gain

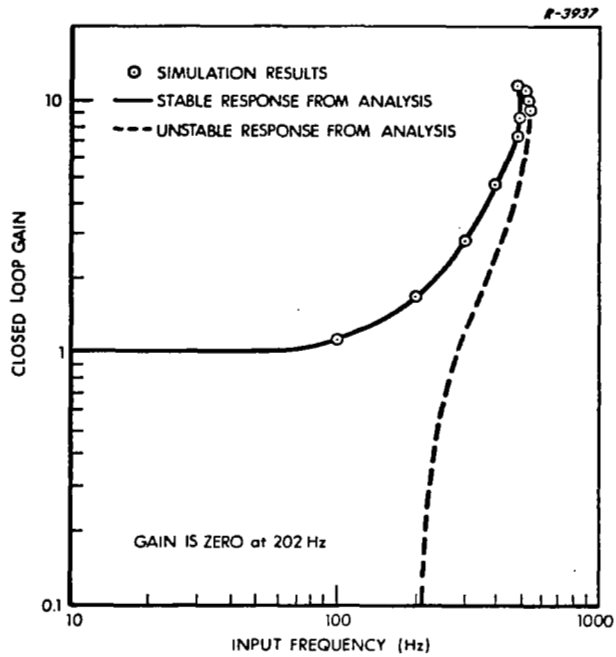


Figure 7.2-3 Gain Response of a Ternary Gyro: Comparison of Analytic and Simulation Results

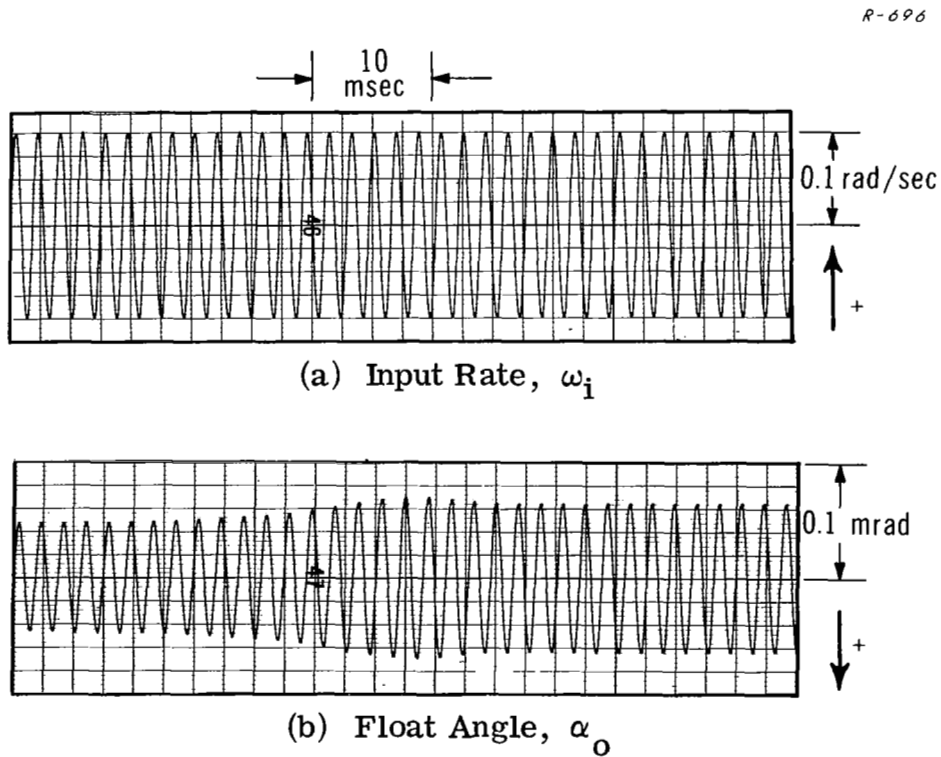


Figure 7.2-4 Ternary Gyro Simulation Record Illustrating Jump Resonance

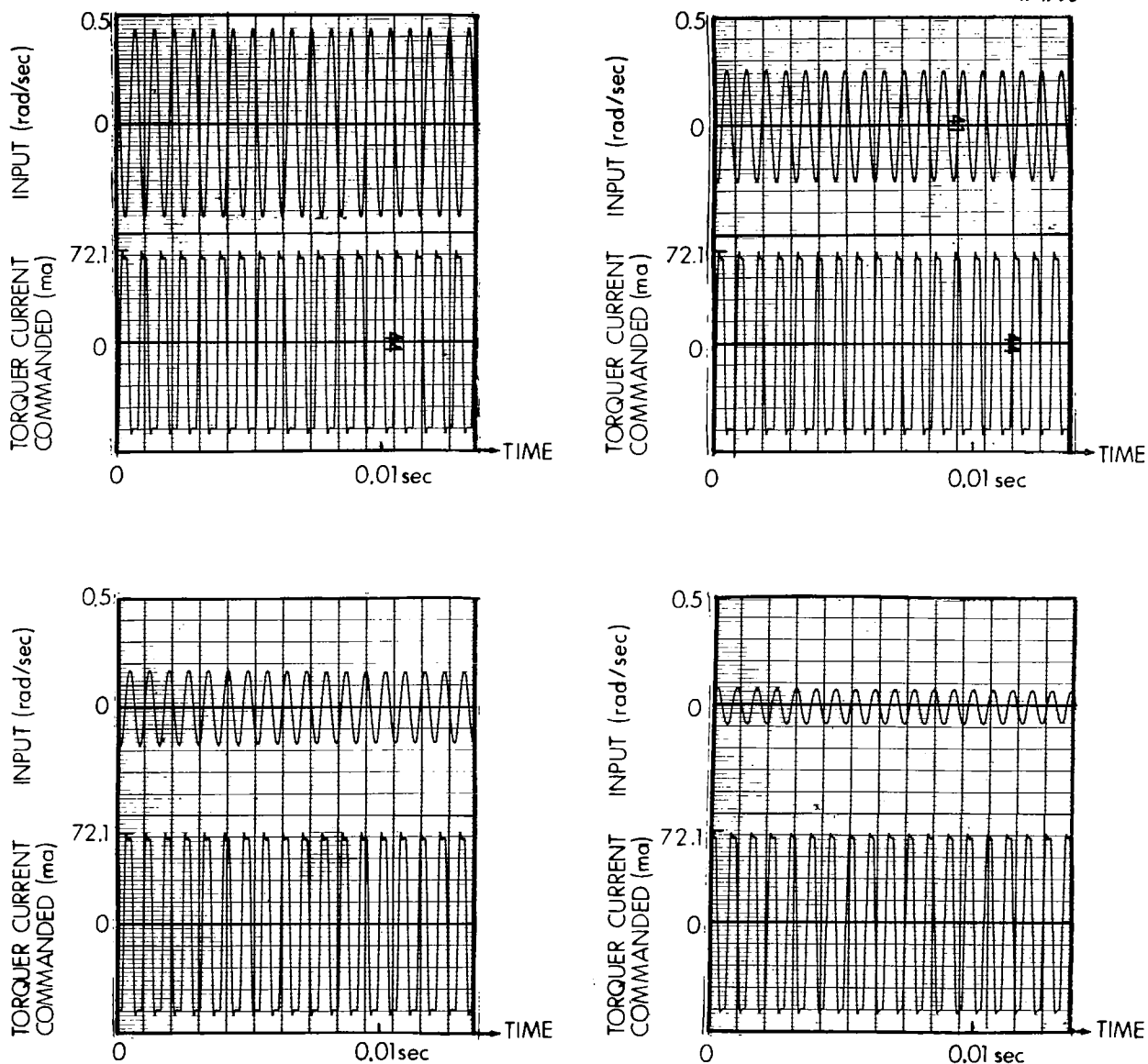


Figure 7.2-5 Ternary Gyro Simulation Record Illustrating Origin of Frequency Islands

characteristics computed from sinusoidal describing functions. However, it is believed that a wide range of situations cannot be treated with this approach.

Sinusoidal response gain characteristics were computed for a ternary pulse rebalanced gyro with the following parameters:

$$\begin{aligned}\tau_f &= 0.00125 \text{ sec} & \tau_{tg} &= 0.00005 \text{ sec} \\ \delta &= 3.04 \times 10^{-4} \text{ rad} & C &= 2 \times 10^5 \text{ dyne cm sec} \\ H &= 2 \times 10^5 \text{ gm-cm}^2/\text{sec} & \omega_{i\max} &= 1 \text{ rad/sec} \\ W &= 0.1 \text{ rad/sec}\end{aligned}$$

It was assumed that if a random input of rms magnitude, $\sigma_{\omega_i} = 0.1 \text{ rad/sec}$, was experienced by the gyro, the sensor loop would amplify or attenuate the random signals in each narrow frequency band by the same amount as it would modify a sinusoidal input at that frequency. That is, the gain curve computed using sinusoidal describing functions would represent the square root of the ratio of gyro output and input power spectral densities. Using the ternary gyro simulation the ratios of spectral densities were determined for a broad bandwidth random input with 0.1 rad/sec rms magnitude. Figure 7.2-6 illustrates the comparison between the analytically predicted ratio of spectra and those observed by simulation. Good agreement was noted up to the frequency of the peak gain predicted by analysis. Beyond that point describing function analysis predicted a complete loss of output signal (zero gain) while the simulation exhibited a rapidly diminishing gain.

Two factors prevent the general use of sinusoidal describing functions for predicting the response of ternary gyros to random inputs: At high input frequencies the ternary gyro fails to respond to a sinusoidal input but does give some response to a random input. This is illustrated by the gradual reduction in observed closed loop gain shown in Fig. 7.2-6. When the input amplitude is large enough, jump resonance regions appear in the sinusoidal response and interpretation of the curve in terms of the

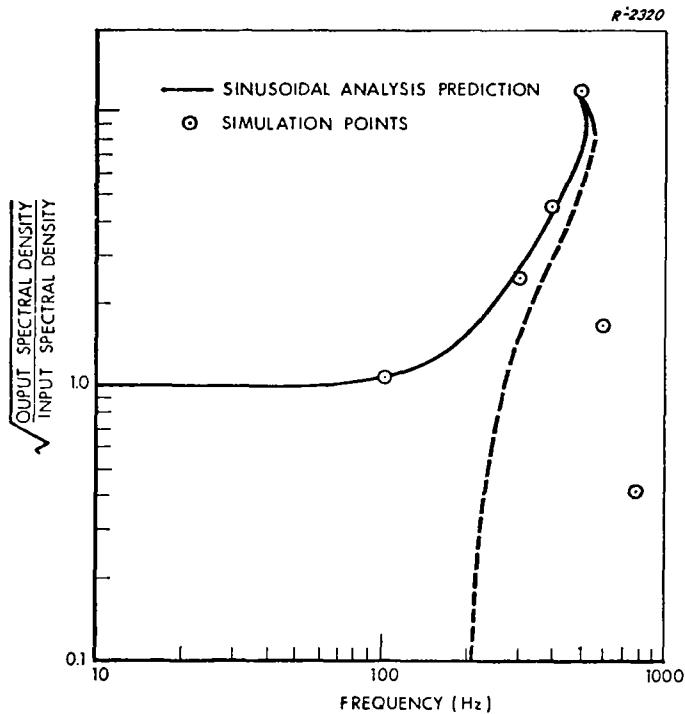


Figure 7.2-6 Random Input Response of a Ternary Gyro: Comparison of Analytical and Simulation Results

random input response is difficult. The analog to jump resonance is dual moding in the random response, predicted in Section 7.1.2 using a different and more sophisticated analytic approach. (It should be noted that there is no significant jump resonance region in Fig. 7.2-6 and analysis of this case using the approach of Section 7.1.2 does not predict dual moding.)

On the basis of these results it is possible to suggest that if the rms amplitude of a random input is a small fraction (1/10 in the case treated here) of the maximum torquer capability, the simpler sinusoidal describing function technique may be used to make a rough estimate of the gyro transmission gain to the low frequency portion of the input spectrum.

7.3 SUMMARY

It has been shown that ternary torqued instruments can be analyzed using describing functions. The analysis is somewhat more complicated than that required to treat binary torqued sensors so a digital computer program was written to reduce the labor involved. The ternary gyro is seen to exhibit an essentially input-dependent (nonlinear) response to both sinusoidal and random inputs. This is a consequence of the unmitigated nonlinear behavior of the ternary torquing logic used. Also, ambiguous operation (jump resonance and dual moding) can occur over a wide range of input magnitudes and frequencies. While considerable success was achieved in predicting the sinusoidal response, the behavior in the presence of random inputs was found particularly difficult to analyze under certain circumstances. Further work is needed in this area.

8. TIME-MODULATED REBALANCE LOOPS

In the preceding two chapters the behavior of binary and ternary pulse rebalanced sensors was analyzed with the aid of describing functions. In this chapter the response of the time-modulated loop is studied. A describing function analysis is used to analytically predict the closed loop characteristics, with analog computer simulations providing an independent check of the analysis.

8.1 ANALYSIS OF THE TIME-MODULATED GYRO

8.1.1 Response to Sinusoidal Inputs

The time-modulated loop is illustrated in Fig. 8.1-1. Note that the float and torquer dynamics are characterized in the same manner as in the binary and ternary loops treated earlier. The torquing logic for the time-modulated torquing scheme is discussed in Section 5.1. Referring to

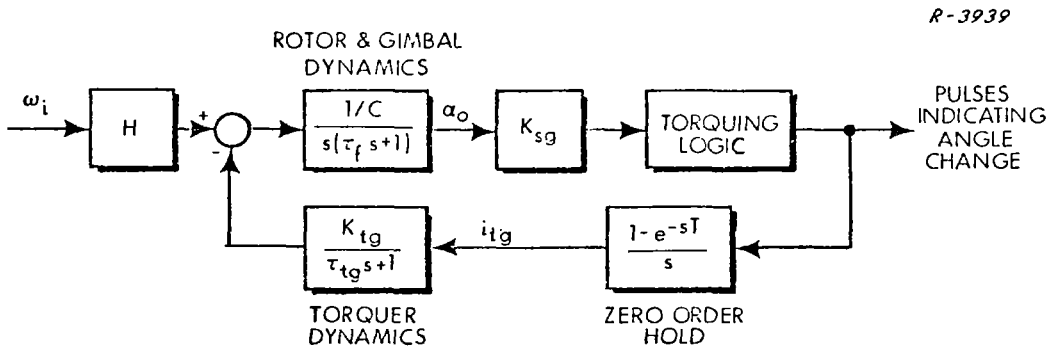


Figure 8.1-1 Gyro Rebalance Loop with Time-Modulated Pulse Torquing

Figure 5.1-4, if D is the nonlinearity drive level, the equivalent gain of the time-modulated torquing scheme to a slowly varying* signal, A , is given by the describing function (Ref. 10):

$$N_A = \frac{\text{Average output over one sawtooth period}}{A}$$

$$= \frac{D}{A_d} \quad ; \quad \text{for } A < A_d \quad (8.1-1)$$

where A_d is the peak value of the sawtooth waveform. Here it is assumed that no harmonics of the square wave torque pattern are present in the float angle. The sawtooth magnitude, A_d , is chosen to be larger in magnitude than any float angle signal encountered to ensure that the inequality required in Eq. (8.1-1) always holds.

Figure 8.1-2 shows a linearized model of the system, with the gain N_A representing the time-modulated torquing scheme. This model describes the input-output relationship of the loop with respect to slowly varying input sinusoids, neglecting output components at other than the input frequency. A linear transfer function for this loop can be written, using the figure:

$$\frac{\hat{\omega}_i(s)}{\omega_i(s)} = \frac{\frac{K_{sg} K_{tg} N_B}{C (\tau_f + \tau_{tg})}}{s^2 + \frac{1}{\tau_f + \tau_{tg}} s + \frac{K_{sg} K_{tg} N_B}{C (\tau_f + \tau_{tg})}} \quad (8.1-2)$$

* The term slowly varying means that the major frequencies present are well below the sawtooth frequency.

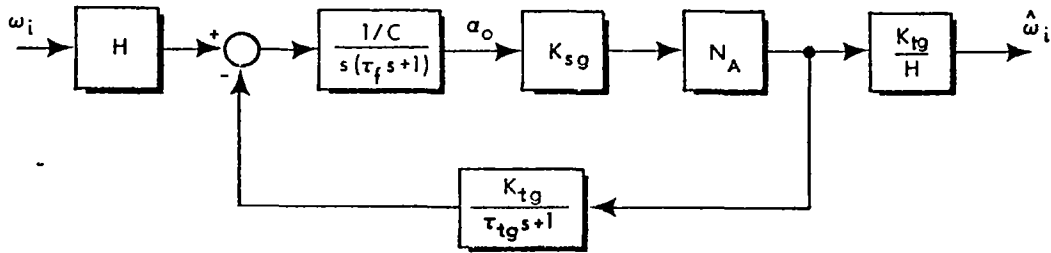


Figure 8.1-2 Linearized Representation of the Time-Modulated Loop

where a small denominator term in s^3 and a small numerator term in s (both caused by the torquer lag) have been neglected. The denominator of Eq. (8.1-2) is second order. Therefore an equivalent damping ratio, ζ , and natural resonant frequency ω_n , can be defined for this loop:

$$\zeta = \frac{1}{2} \sqrt{\frac{CA_d}{K_{sg} K_{tg} D (\tau_f + \tau_{tg})}}$$

$$\omega_n = \sqrt{\frac{K_{sg} K_{tg} D}{CA_d (\tau_f + \tau_{tg})}} \quad (8.1-3)$$

Equations (8.1-3) provide a two-parameter (ζ and ω_n) description of the linear representation of the time-modulated sensor loop. If in-loop compensation is added the description of closed loop dynamics is developed in the same manner -- the torquing logic is represented by the describing function gain N_A and the closed loop linear transfer function is prescribed.

8.1.2 Response to Random Inputs

The describing function of the time-modulated torquing logic (Eq. (8.1-1)) is independent of input signal magnitude and frequency, with the assumption that all components of a random input at frequencies greater than that of the sawtooth are filtered by the linear float dynamics. Under these circumstances the transfer characteristics of the time-modulated loop in the presence of a random input are the same as for a sinusoidal input. Thus Eq. (8.1-2) can be used to predict the response of this gyro loop to random inputs.

8.2 SIMULATION OF THE TIME-MODULATED GYRO

Section 8.1 presents a technique for analyzing the time-modulated loop. A typical gyro loop was analyzed by this method and then simulated on a hybrid computer to verify the analytically-obtained gyro transfer characteristics. In the simulation the assumptions on which the describing function technique is based were tested by including all of the details that were ignored in the analysis. A sawtooth waveform was added to the float angle signal at the input to a binary nonlinearity. The sampler was implemented and the torquer was simulated as a first order lag.

The parameters of the gyro loop simulated, most of which are identical to those used in the binary loop analysis and simulation in Chapter 6, are given below.

$$\begin{array}{ll} K_{tg} D = 2 \times 10^5 \text{ dyne-cm} & \text{Sawtooth Period} = 1 \text{ msec} \\ \tau_{tg} = 0.0001 \text{ sec} & \tau_f = 0.0025 \text{ sec} \\ \omega_{i_{max}} = 1 \text{ rad/sec} & A_d = 0.83 \text{ mrad of} \\ & \text{float angle} \end{array}$$

The sinusoidal responses obtained by analysis and simulation are shown in Fig. 8.2-1. The solid lines are analytical predictions of gain and phase shift with simulation data denoted by circles and crosses. There is generally good agreement between the two approaches. This indicates that the describing function technique can provide accurate predictions of the response of this gyro loop to sinusoidal excitations. (Note that the response shown is for frequencies well below that of the sawtooth, as required by the describing function theory employed).

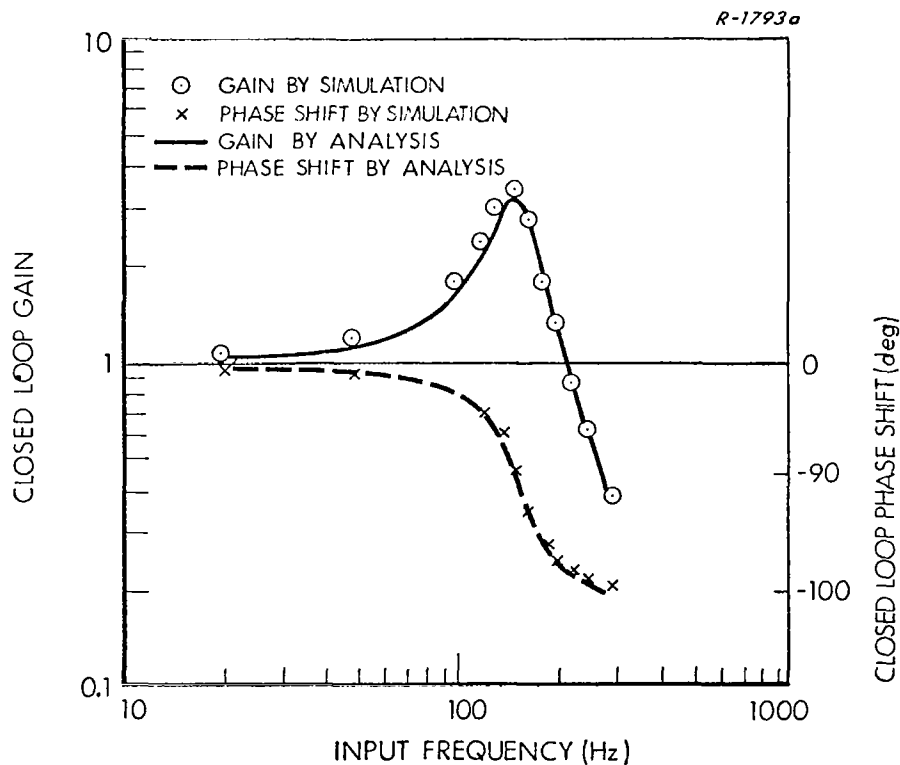


Figure 8.2-1 Sinusoidal Input Response for the Time-Modulated Gyro

The random response obtained by analysis and simulation is shown in Fig. 8.2-2. The solid lines are analytical predictions of gain with simulation data indicated by circles. The loop parameters used in this

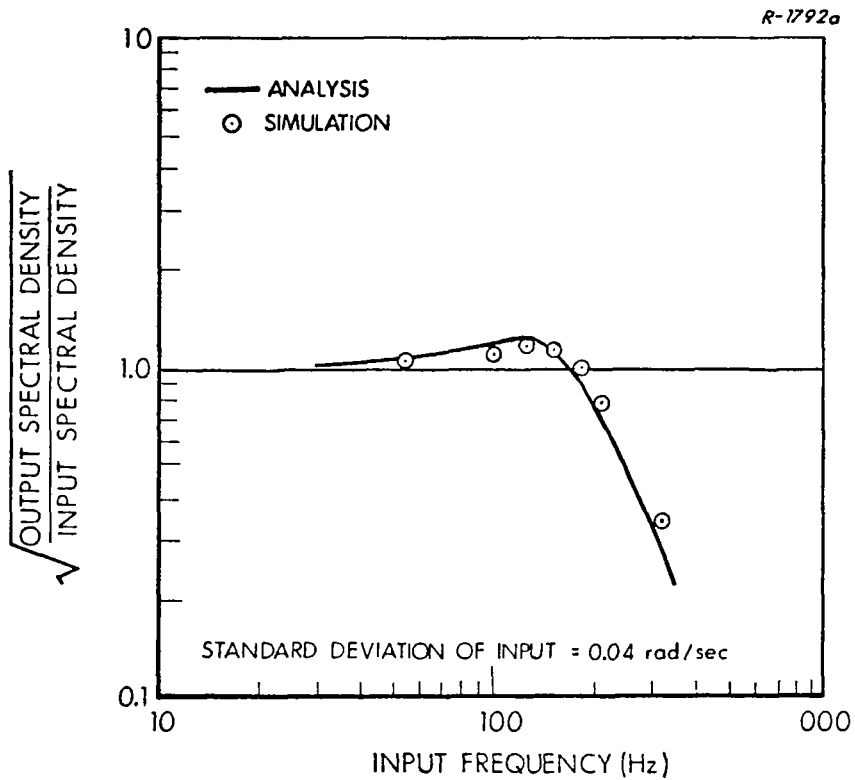


Figure 8.2-2 Random Input Response for the Time-Modulated Gyro

simulation run were the same as stated above except that the float time constant was 0.001 sec. There is close agreement between the analytic and simulation results. This indicates that the describing function outlined is a valuable analysis technique for determining the random response characteristics of sensors with time-modulation torquing.

8.3 SUMMARY

The investigation outlined in this chapter illustrates that a simple analytic technique can accurately predict the response of an inertial sensor with time-modulated torquing to sinusoidal and random excitations. As with binary and ternary loops, simulation results support the validity of the describing function approach for analyzing the time-modulated loop. The presence of the sawtooth wave (dither) at the nonlinearity input plays the same role as the limit cycle in binary torqued sensors -- it linearizes the response of the loop by fixing the effective gain of the nonlinear torquing logic. The time-modulation technique offers two significant advantages over the binary scheme in this regard: By introducing the dither artificially it can be precisely removed from the sensor output and will not be quenched by any input to the instrument. Also, finer output quantization is achieved.

The importance of the analytic techniques developed in Chapters 6, 7, and 8 is that the performance of a particular sensor design can be evaluated prior to constructing the instrument. The effects of varying instrument parameters can be predicted and a set of best parameters can be determined before prototype assembly begins.

PART III: ERROR REDUCTION

SELECTION OF SENSOR PARAMETERS
TO REDUCE SYSTEM ERRORS

In the first two parts of this report system-level errors generated by vehicle motion were explored and approximate analytic techniques for describing the response of pulse rebalanced instruments were developed. It was established that motion-induced errors in strapdown systems can degrade navigation accuracy to a level well below that needed for many applications. The calculations concerning sensor loop response were developed to permit quick and accurate assessment of strapdown system errors under a wide range of gyro and accelerometer parameters.

At this point we are equipped to explore ways of reducing the effect of the motion environment on strapdown inertial systems. Again the principal emphasis is placed on gyro design, since the calculations discussed in Section 4.2 indicate that motion-induced errors have their greatest impact on system attitude accuracy, relative to what can be achieved using a gimballed (platform) mechanization. This chapter discusses error-reduction by choosing basic parameters within the gyro, including its re-balance electronics. The subsequent chapter treats the possibility of neutralizing motion-induced errors by measuring the environment, calculating the resulting errors, and compensating them.

9.1 DESIGNABLE PARAMETERS

The availability of computer programs (such as that described in Section 4.2 and Appendix B) for establishing the magnitude of motion-induced errors in strapdown systems permits a trial-and-error approach to choosing the optimum set of inertial sensor parameters. However this

method is quite tedious because of the large number of parameters that may be varied, and a different tack is taken here. The insight gained from the analytic optimizations performed in this chapter leads to one of the major conclusions of this study -- that sensor parameter selection is of limited value in reducing strapdown system errors.

When attempting to specify a gyro that minimizes the motion-induced errors described in Chapter 2, the sources of inaccuracy can be divided into two broad categories: errors whose generation involves parameters basic to the sensor operation, and errors arising from imperfect construction and other considerations which the designer always tries to minimize. Examples of the latter category include anisotropy and torquer scale factor errors. A list of the first group, referred to hereafter as "designable parameters," is provided in Table 9.1-1. Subsequent discussion will concentrate on the designable parameters because when dealing with other error sources, the design goal is obviously to minimize them all. In many cases the designable parameters can be lumped together and the optimum design problem involves specifying the best values for groups of parameters. Figure 9.1-1 illustrates parameter groupings possible for a simple model of a ternary pulse rebalanced gyro.

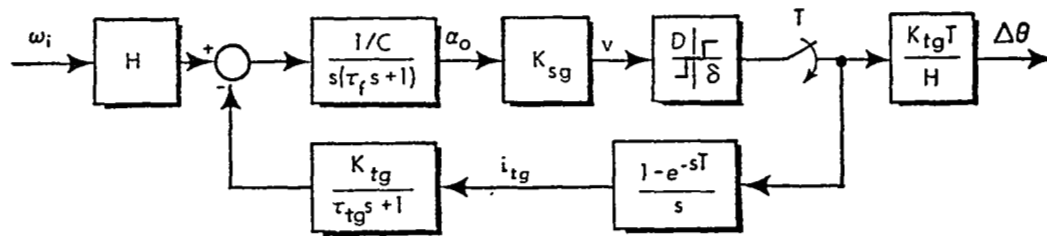
Limiting Constraints — Several gyro parameters or groups of parameters are confined within limits imposed by physical or practical considerations. For example, the parameter group $K_{tg} D/H$ (D' in Fig. 9.1-1(b)) must exceed the maximum anticipated input angular rate. If this condition is violated, the gimbal angle cannot be held near null and, in practical gyros, the gimbal will rotate until it is restrained by mechanical stops, causing the history of input angular motion stored in the float to be rendered incorrect.

TABLE 9.1-1

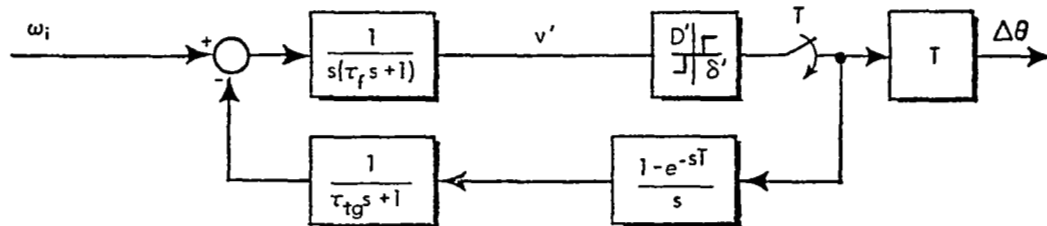
DESIGNABLE PARAMETERS: SINGLE DEGREE OF
FREEDOM FLOATED RATE INTEGRATING GYRO

Rotor Spin Angular Momentum, H	
Gimbal-Plus-Rotor Output Axis Moment of Inertia, I_{oo}	
Fluid Damping Coefficient, C	
Rotor Spin Axis Moment of Inertia, I_{ssr}	
Gimbal-Plus-Rotor Anisoinertia, $I_{ss} - I_{ii}$	
Torque Generator Time Constant, τ_{tg}	
Signal Generator Sensitivity, K_{sg}	
Torque Generator Sensitivity, K_{tg}	
Wheel Speed Regulation Loop Frequency Response	
Sample Period, T	} pulse torqued gyros
Torque Level, D	
Gimbal Angle Threshold, δ	

When a maximum gyro output increment, $\Delta\theta_{max}$, is specified in order to keep quantization and commutativity errors in the direction cosine calculations within certain bounds, the gyro sample period T must satisfy the relation: $K_{tg} DT/H \leq \Delta\theta_{max}$. (If the gimbal is not torqued for the entire period, the pulse length τ_p must be substituted for T in this relation. In other words, once the torque generator output has been scaled to imply an input angular rate, the value of an output pulse is directly



(a) Simple representation of ternary pulse rebalanced gyro loop



$$D' = \frac{DK_{tg}}{H} \quad \text{sec}^{-1}$$

$$\delta' = \frac{C}{HK_{sg}} \delta \quad \text{sec}^{-2}$$

$$v' = \frac{C}{HK_{sg}} v \quad \text{sec}^{-2}$$

(b) Illustration of parameter grouping possible

Figure 9.1-1 Parameter Grouping in a Ternary Torqued Pulse Rebalanced Gyro

related to the torque pulse period. Also, the inequality discussed earlier becomes $(\tau_p/T) K_{tg} D/H \geq \omega_{i_{\max}}$ if torquing does not occur over the entire period. These expressions may be further modified if the torquer lag precludes application of essentially rectangular torque pulses.)

A physical restriction is imposed on the rotor moments of inertia I_{ii_r} and I_{SS_r} if, as is common in single-degree-of-freedom gyros, the rotor shape is a wheel. This restriction is that $I_{ii_r} \geq I_{SS_r} / 2$.

Furthermore, since $I_{oo_r} = I_{ii_r}$ the important parameter group I_{oo}/H is bounded according to

$$\frac{I_{oo}}{H} > \frac{1}{2\Omega} \quad (9.1-1)$$

In the optimization examples which follow, the above constraints provide limits on the range over which parameters can be varied, reducing the size of the parameter space which can be searched to find the optimum.

9.2 COST FUNCTION AND REPRESENTATION OF RANDOM MOTION

The computer program discussed in Appendix B treats motion-induced errors at a much finer level of detail than is tolerable for an analytic (though approximate) approach to optimizing gyro parameters. For example, the errors are classified according to cause by the computer program. Since the goal of the analytic optimization will be minimization (in some sense) of the system attitude errors, a way must be found for combining both deterministic errors (those caused by deterministic effects such as anisoinertia) and random errors (resulting from manufacturing imperfections such as torquer assymetry). Ideally a single, generally valid measure of attitude errors is desired. Also, cumbersome descriptions of the motion environment such as spectral density functions do not lend themselves to the kind of formulation sought in this chapter. Both of these aspects of the optimization problem are treated below.

In Ref. 1 calculations of constant gyro-level errors caused by the angular motion environment were performed, based on the error sources detailed in Chapter 2. It was found that in-phase angular

oscillations about two gyro axes provide much larger total system drift rates than quadrature motions of the same size. Consequently, random angular motion will be represented in terms of a single angular rate vector, $\underline{\omega}$, having some orientation with respect to the system (and sensor) axes, as shown in Fig. 9.2-1. This permits specification of cross spectral density functions between pairs of axes in terms of a single spectral density function and proportionality constants.

R-4003

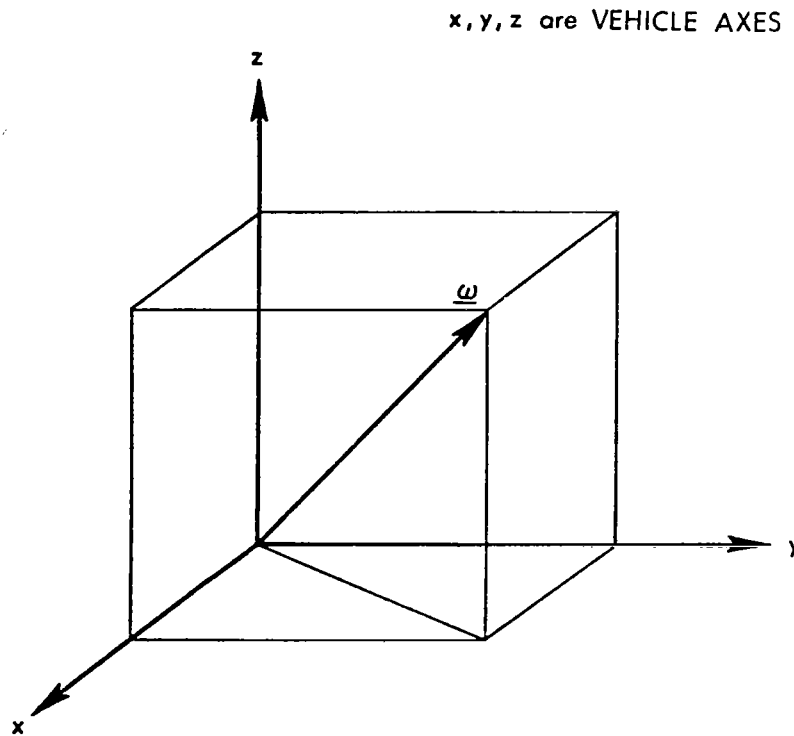


Figure 9.2-1 In-Phase Angular Oscillations

It is not realistic to expect $\underline{\omega}$ to maintain a fixed attitude within the vehicle. Instead, a simplified description of varying orientation is used; the random angular vibration vector is presumed to maintain a fixed

direction in vehicle coordinates for intervals of equal length T' and to assume a new attitude at the end of each interval. The orientations are independent from one period to any other but may obey some probability distribution to account for different amplitudes in the vibration spectra about the vehicle axes. This is a good description of important random angular motions such as structural vibration and lightly damped vehicle dynamics.

Constant Gyro Drift Rates — Over each interval for which the angular rate vector, $\underline{\omega}$, in Fig. 9.2-1 maintains a fixed orientation, the major constant (rectified) gyro errors can be expressed in terms of the spectral density function $\Phi_{\omega\omega}(\nu)$, direction cosines describing the projections of ω on the three principal axes, and the gyro transfer function, viz:

$$\begin{aligned} \text{constant gyro} \\ \text{drift rate} \end{aligned} = K_1 K_2 \int_0^{\infty} L(\nu) \Phi_{\omega\omega}(\nu) d\nu \quad (9.2-1)$$

where K_1 and K_2 are constants which represent the orientation of $\underline{\omega}$ and appropriate gyro physical parameters. The function $L(\nu)$ is included to represent gyro transmission characteristics when they appear. For example, if spin-input crosscoupling errors are considered K_2 is the steady state gyro float angle sensitivity (rad/(rad/sec)) and $L(\nu)$ is given by

$$L(\nu) = \text{Real} \left\{ G(s) \Big|_{s=j\nu} \right\} \quad (9.2-2)$$

where $G(s)$ is the Laplace Transform gyro transfer function. K_1 is the product of direction cosines between $\underline{\omega}$ and the spin and input axes of the

gyro under consideration and a minus sign precedes the expression. The effect of changing the orientation of $\underline{\omega}$ is reflected in changing values of K_1 .

Using Eq. (9.2-1), the system attitude error due to a constant gyro error grows by the amount

$$\delta(i) = K_1(i) K_2 T' \int_0^{\infty} L(\nu) \Phi_{\omega\omega}(\nu) d\nu \quad (9.2-3)$$

during the i^{th} interval of length T' . Since the orientation of $\underline{\omega}$ is independent from one interval to another the coefficient $K_1(i)$ is also independent. Assuming symmetric distributions for the orientation of $\underline{\omega}$, the following expectations hold:

$$\begin{aligned} \overline{\delta(i)} &= 0 \text{ for all } i \\ \overline{\delta(i) \delta(j)} &= 0 \text{ for } i \neq j \end{aligned} \quad (9.2-4)$$

The mean square total system attitude error at the end of N intervals is given by*

$$\overline{[\varphi(N)]^2} = \sum_{i=1}^N \overline{[\delta(i)]^2} \quad (9.2-5)$$

If T' is constant and if $\Phi_{\omega\omega}(\nu)$ and the probability distribution for the orientation of $\underline{\omega}$ are stationary,

* Equation (9.2-5) assumes that the total attitude error is small enough to allow its components to be treated additively. In other words, system accuracy must approach that of a useful navigator.

$$\overline{[\varphi(t)]^2} = N\delta^2 \quad ; \quad t = NT'$$

$$= tT'K_1^2 K_2^2 \left[\int_0^\infty L(\nu) \Phi_{\omega\omega}(\nu) d\nu \right]^2 \quad (9.2-6)$$

Note that for a given system operation time the attitude error expressed in Eq. (9.2-6) is proportional to the correlation interval T' . Equation (9.2-6) uses an integral expression to provide the average drift rate over an interval T' . However, the integral is only correct when considering averages over an infinite time. Appendix G of Ref. 1 illustrates conditions for which the integral is approximately correct for finite-time averages. We will assume those conditions are satisfied in the examples which follow.

Constant System-Level Drift Rates – Errors that rectify at the system level can be illustrated by considering the constant system drift rate resulting from output axis angular acceleration errors. These can also be viewed in terms of an integral over the random motion spectrum according to

$$\text{constant system drift rate, per gyro} = K_3^2 \frac{I_{00}}{H} \int_0^\infty L(\nu) \Phi_{\omega\omega}(\nu) d\nu \quad (9.2-7)$$

where K_3 is the direction cosine between $\underline{\omega}$ and the output axis of the gyro whose error is being considered and L is defined as

$$L(\nu) = \left[G(s) \Big|_{s=j\nu} \right]^2$$

The appearance of the second power of both K_3 and $G(j\nu)$ in Eq. (9.2-7) follows from the fact that the system-level error results from the outputs of two separate gyros. Since

$$\overline{K_3^2} \neq 0$$

the mean square system attitude error resulting in this case is not dependent on the interval T' :

$$\overline{[\varphi(t)]^2} = t^2 \overline{K_3^2} \left(\frac{I_{00}}{H} \right)^2 \left[\int_0^\infty L(\nu) \Phi_{\omega\omega}(\nu) d\nu \right]^2 \quad (9.2-8)$$

Other attitude rate errors that rectify at the system level (such as products of errors from pairs of gyros, etc.) can be treated by similar relations involving gyro transfer characteristics and direction cosines.

An attitude figure-of-merit is defined by

$$\begin{aligned} J(t) &= \overline{[\varphi(t)]^2} \\ &= AT't + Bt^2 \end{aligned} \quad (9.2-9)$$

where the first term comes from gyro errors of the type represented in Eq. (9.2-6) and the second from errors of the kind expressed in Eq. (9.2-8).

9.3 EXAMPLE I: BINARY GYROS

In this example we seek to optimize the parameters of a triad of binary pulse torqued gyros. The gyro transmission characteristics are those of a linearized second order system, and depend on τ_f and τ_{tg} according to the equations provided in Section 6.1.1. One of the basic results of that section is that the transmission characteristics of the linearized gyro loop are independent of loop gains K_{sg} , K_{tg} and D . Also, it is assumed in this example that gyro errors due to limit cycles are not allowed to reach the direction cosine calculations. Consequently, the above-mentioned three parameters do not enter the optimization problem directly. The gyro sample period, T , is not considered significant in determining the limit cycle (and therefore the transmission characteristics.). Since no maximum size for the gyro output increment, $\Delta\theta$, is stated, the sample period does not enter the examples as a parameter to be optimized. Of course a threshold, δ , does not enter the problem either. The remainder of the designable parameters listed in Table 9.1-1, a total of six, remain available for manipulation. Of these, the terms $I_{ss} - I_{ii}$ and I_{ssr} are grouped to describe the "effective anisoinertia." The time constants τ_{tg} and $\tau_f = I_{oo}/C$ describe linearized gyro dynamics, particularly the gyro bandwidth, which is equated to ω_n , the natural frequency of the closed gyro loop. The independent groups of designable parameters are reduced to three: gyro bandwidth ω_n (depending on τ_{tg} , C and I_{oo}), the ratio I_{oo}/H and the ratio of the effective anisoinertia to I_{oo} . Then the major contribution of anisoinertia errors is assumed to take place in a frequency range where the effective anisoinertia is constant, and this term is assumed to be nulled by appropriate design. The optimization takes place in the two-parameter space of the gyro bandwidth and the output axis sensitivity, I_{oo}/H .

The analytic optimization procedure to be used can be summarized as follows:

1. A starting set of gyro parameters is specified. To the extent that the effect of the individual parameters is understood, a set of values which may be close to the optimum is chosen.
2. The major system error contributors are determined for the initial gyro parameters. In the given environment some gyro error terms may not be significant and their elimination simplifies the optimization problem.
3. The system attitude error is expressed as an analytic function of the major error sources and in terms of the designable gyro parameters. The motion environment is reduced to the form of numerical coefficients at this point but gyro parameters appear explicitly in the expression.
4. The figure-of-merit is minimized with respect to all the gyro parameters appearing in the equation developed in Step 3. Since all error sources do not contribute to system error growth in the same manner (see Eq. (9.2-9)) this usually requires specification of an "evaluation time," t , and minimization of the system error at that time.
5. At the conclusion of minimization a check is made to see if the same error terms dominate when the gyro has the optimum set of parameters. If not, steps two through five are repeated as often as necessary.

The vehicle angular motion experienced by the sensor package in this problem is assumed to consist of a constant angular rate of 0.1 rad/sec about one vehicle axis and a random angular rate motion about each axis described by a constant spectral density $\Phi(\nu) = \Phi = 10^{-3}(\text{rad/sec})^2/\text{Hz}$ from zero to 1000 Hz. The random motion correlation period, T' , is

0.5 sec. This environment may be representative of that experienced in a lunar module during powered descent. The principal axes of the sensors are parallel to those of the vehicle, with the orientations illustrated in Fig. 9.3-1.

R-4002

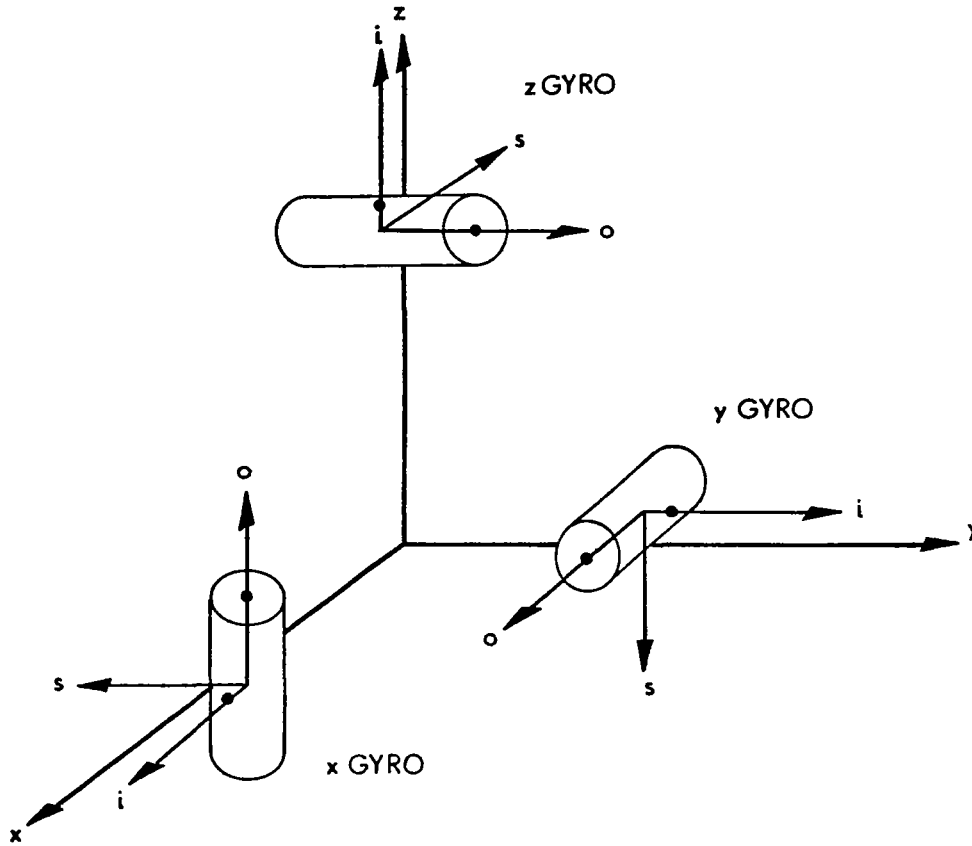


Figure 9.3-1 Orientation of Gyros for Examples I and II

Step 1 — The initial set of gyro parameters is that provided in the example of Section 4.1. In addition, the float damping coefficient and torquer time constant are 8×10^5 dyne-cm-sec and $50 \mu\text{sec}$ respectively. Linearization of a binary pulse torqued gyro with these characteristics yields a second-order gyro transfer function with natural frequency, ω_n ,

of 972 Hz and a damping ratio of 0.26. However, in order to simplify the problem the gyro is assumed to have a unity transfer function up to the natural frequency and zero elsewhere.

Step 2 — The dominant system error sources generated in the gyro whose characteristics are given above all result from random motion. They are the constant drift rates due to anisoinertia errors at high motion frequencies, spin-input crosscoupling and pseudo-coning from output axis angular acceleration errors. (Note that the same three sources of errors caused by designable parameters dominate the errors in the examples of Sections 4.1 and 4.2.) System errors arising from the constant angular rate postulated are negligible, as are system pseudo-coning errors generated by oscillatory errors in pairs of gyros. Also, since the gyro loop has unity gain over almost all of the random motion bandwidth, errors due to undetected coning motion are not significant. Of course they must be given consideration again if the gyro bandwidth is reduced as a consequence of the parameter optimization.

Step 3 — The expression for the system attitude error growth, as reflected in the figure-of-merit defined in Section 9.2, is:

$$J(t) = 3 \left[\frac{I_{oo} \Phi \omega_n}{2\pi H} \right]^2 t^2 + 3T \left\{ \left[\frac{H\Phi}{2\pi I_{oo} \omega_n} + \frac{(I_{ii} - I_{ssg}) \left(\frac{1 \text{ rad}}{\text{sec}} \right)^2}{H} \right]^2 \right\} t \quad (9.3-1)$$

The first term in Eq. (9.3-1) describes the contribution of output axis angular acceleration gyro errors through pseudo-coning. It is obtained from Eq. (9.2-8) using the following definitions

$$L(\nu) = \begin{cases} 1 & \nu \leq \omega_n \\ 0 & \nu > \omega_n \end{cases}$$

and expressing the spectral density in $(\text{rad/sec})^2/\text{rad/sec}$ and ω_n in rad/sec . The second group of terms results from constant gyro errors due to spin-input crosscoupling and high frequency (oscillations above the rotor speed regulation loop bandwidth) anisoinertia terms respectively. The crosscoupling error term derives its form from the fact that for the linear representation of the limit cycling binary gyro (see Fig. 6.1-2) the average float angle, α_o , resulting from an input angular rate, ω_i , is given by

$$\frac{\alpha_o}{\omega_i} = \frac{H}{I_{oo} \omega_n^2} \quad (9.3-2)$$

Equation (9.3-2) is obtained by algebraic manipulations involving Eqs. (6.1-8) and (6.1-9). This relation was presumed to hold for all gyro inputs up to ω_n and no crosscoupling errors were assumed to result from inputs above that frequency. The anisoinertia error term in Eq. (9.3-1) represents the effect of errors produced by oscillations above the rotor drive natural frequency. Since that frequency is typically less than 10 Hz the effect is assumed to occur over the entire bandwidth of the random motion:

$$\int_{10}^{1000} \Phi(\nu) d\nu \cong \int_0^{1000} \Phi(\nu) d\nu = (1 \text{ rad/sec})^2$$

The figure-of-merit, $J(t)$, is in $(\text{rad})^2$ and T' and t are to be specified in seconds.

It is desired to minimize $J(t)$ at some specific time, t' . By making the following definitions

$$a = \frac{t'}{T'} \qquad b = \frac{I_{ii} - I_{ssg}}{I_{oo}}$$

$$c = \frac{I_{oo}}{H} \qquad R = \frac{3\Phi^2(T')^2}{4\pi^2}$$

equation (9.3-1) can be written in a form more suitable for analytic optimization:

$$\frac{J(t')}{aR} = ac^2 \omega_n^2 + \left[\frac{1}{c\omega_n} + \frac{2\pi bc(1 \text{ rad/sec})^2}{\Phi} \right]^2 \quad (9.3-3)$$

Step 4 — It can be seen from Eq. (9.3-3) that the optimum value of the parameter group b is zero; designing the effective anisoinertia for high frequency oscillations to be zero minimizes system errors from this cause independently. Setting the partial derivatives of $J(t')/aR$ with respect to c and ω_n equal to zero provides two identical equations for the optimum groups of gyro parameters:

$$ac^4 \omega_n^4 = 1 \quad ; \quad b = 0 \quad (9.3-4)$$

indicating that a unique set of optimum gyro parameters does not exist. Evaluation of second partial derivatives reveals that Eq. (9.3-4) specifies a minimum. If ω_n is selected to permit accurate measurement of all anticipated angular rates by the gyros ($\omega_n = 1000$ Hz), Eq. (9.3-4) provides the optimum value of the parameter group c for each choice of evaluation time t' and correlation period T' . Using Eq. (6.1-14) and assuming that

$\tau_f \gg \tau_{tg}$, Eq. (9.3-4) provides a relation for I_{oo} , C and H in terms of τ_{tg} and t'/T' :

$$\frac{I_{oo} C}{H^2} \cong \frac{2\tau_{tg}}{\sqrt{a}} \quad (9.3-5)$$

The minimum value of $J(t')/aR$ is given by

$$\left[\frac{J(t')}{aR} \right]_{\min.} = 2 \sqrt{a} \quad (9.3-6)$$

Choosing $t' = 1$ min and $\omega_n = 1000$ Hz, $a = 120$ and the optimum value of the parameter group c is 4.82×10^{-5} sec (the starting value of c was 1.25×10^{-3} sec). (From the limiting constraints discussed in Section 9.1 the new value of c requires a wheel speed in excess of 100,000 rpm!) The minimum system-level error is:

$$[J(t')]_{\min.} \cong (0.41 \text{ deg})^2$$

This figure compares with a value for $J(t')$ of $(7.45 \text{ deg})^2$ when the original gyro parameters are substituted into Eq. (9.3-3). Most of the difference in the system error is the result of reducing the output axis sensitivity parameter c , causing a sharp reduction in pseudo-coning errors.

Step 5 — Computation of all the gyro-induced system errors reveals that the dominant error sources have not changed as a consequence of gyro parameter optimization. Consequently the minimization of $J(t')$ as expressed in Eq. (9.3-1) is valid.

Effect of Compensating Output Axis Acceleration Errors — In addition to selecting an optimum set of designable sensor parameters it is also possible to reduce certain motion-induced errors by measuring the environment and compensating the sensor outputs. Output axis sensitivity, which is the dominant source of error in the present example, is a well-known parameter of any gyro and its effect can be to a large extent neutralized. It is instructive to explore the impact of compensation in this example.

If we assume that output axis sensitivity errors are reduced to 10% of their former value by compensation, Eq. (9.3-3) becomes

$$\frac{J(t')}{aR} = 0.01 ac^2 \omega_n^2 + \left[\frac{1}{c\omega_n} + \frac{2\pi bc}{\Phi} (\text{rad/sec})^2 \right]^2 \quad (9.3-7)$$

The optimum set of parameters obey

$$\begin{aligned} b &= 0 \\ ac^4 \omega_n^4 &= 100 \end{aligned} \quad (9.3-8)$$

and

$$\left[\frac{J(t')}{aR} \right]_{\min.} = \frac{2\sqrt{a}}{10} \quad (9.3-9)$$

If $\omega_n = 1000$ Hz, the optimum value of c is 1.52×10^{-4} sec (requiring a wheel speed in excess of 31,400 rpm) and

$$[J(t')]_{\min.} = (0.13 \text{ deg})^2$$

Clearly, compensation can play a role in reducing motion-induced errors of this type.

9.4 EXAMPLE II: A TIME-MODULATED GYRO

This example presumes an angular motion environment representative of that which may be experienced by a strapdown inertial navigator in a large transport airplane. Random angular motion about each axis is described by a flat spectral density of $10^{-4}(\text{rad/sec})^2/(\text{rad/sec})$ (notice the units are different from those in the previous example) out to $\nu_r = 2\pi$ rad/sec and zero elsewhere. In addition, sinusoidal angular motions exist about two vehicle axes (x and z). They both have an amplitude of 0.1 rad/sec and frequency of $2\pi/10$ rad/sec (0.1 Hz). The motions are π radians out of phase ($\omega_x = B \cos \omega t$, $\omega_z = -B \cos \omega t$) and represent the dutch roll oscillation mode of the aircraft.* A gyro employing the time-modulation rebalance scheme is optimized.

Step 1 — The starting gyro parameters and sensor orientations are identical with those chosen for the first example, with the following additional parameters, which are peculiar to the time-modulation torquing technique:

$$K_{tg} D = H \omega_{i_{\max}} = 2 \times 10^5 \text{ dyne-cm}; \quad A_d = 0.25 \text{ mrad of float angle}$$

The dither amplitude is chosen to equal the magnitude of float angle growth which will occur at maximum input angular rate, in the absence of torquing:

$$A_d = \omega_{i_{\max}} T H/C$$

* The phase difference between x- and z-axis oscillations due to the dutch roll mode may range from 125 degrees up to 180 degrees for different aircraft. The 180 degree value is chosen here for simplicity.

where $T = 10^{-3}$ sec. A_d must be specified to permit calculation of cross-coupling errors from the linearized representation of the time-modulated loop discussed in Section 8.1-1. The damping ratio and natural frequency of the linearized gyro are, from the parameters stated, 0.83 and 265 Hz. In the calculations which follow the loop response will be characterized by unity gain and no phase shift up to the natural frequency and by zero gain above 265 Hz.

Step 2(a) — The significant system attitude error contributions from the sinusoidal motion result from pseudo-coning due to output axis acceleration errors in the x and y gyros and the constant errors generated in the z gyro by spin-input crosscoupling and anisoinertia effects.

Step 3(a) — Because the dutch roll oscillation axis is fixed in the vehicle, it generates gyro errors which cause system attitude errors to grow as the square of elapsed time. The appropriate anisoinertia term in this case is $I_{ii} - I_{ss}$ since the oscillation is well within any anticipated wheel speed regulation loop bandwidth. In terms of the oscillation amplitude, $B = 0.1$ rad/sec, and $\Delta I = I_{ii} - I_{ss}$, the contribution of the dutch roll (dr) motions to $J(t)$ is given by:

$$J_{dr}(t) = \left(\frac{B^2 ct}{2} \right)^2 + \left(\frac{B^2 t}{2} \left[c - d + \frac{\Delta I}{H} \right] \right)^2 \quad (9.4-1)$$

where

$$\begin{aligned} d &\triangleq \frac{HA_d}{K_{tg} D} \\ &= \frac{A_d}{\omega_{i \max}} \end{aligned}$$

If the dither amplitude is chosen as described earlier

$$d = \left(\frac{H}{C}\right) T \quad (9.4-2)$$

The first term in Eq. (9.4-1) describes the pseudo-coning error drift rate about the nominal y body axis resulting from output axis sensitivity in the x gyro. The second term is a collection of attitude errors, all represented in terms of rotation about the nominal z body axis: The first entry results from output axis sensitivity in the y gyro -- leading to a pseudo-coning error. The second and third entries are provided by rectified spin-input crosscoupling and anisoinertia effects in the z gyro.* Performing the squaring operations indicated in Eq. (9.4-1) yields:

$$J_{dr}(t) = \frac{B^4 t^2}{2} \left[c^2 + \frac{d^2}{2} + \frac{1}{2} \left(\frac{\Delta I}{H}\right)^2 - cd - \frac{c\Delta I}{H} + d\frac{\Delta I}{H} \right] \quad (9.4-3)$$

In Eq. (9.4-3) J is in (rad)² and t is in sec.

Step 2(b) -- The significant contributors to system error as a result of the random angular motion are pseudo-coning due to output axis acceleration errors, and constant gyro errors caused by spin-input cross-coupling and anisoinertia.

Step 3(b) -- In terms of the spectral density Φ and bandwidth ν_r the contribution of the random motion to J(t) is given by

$$J_r(t) = 3\Phi^2 \nu_r^2 c^2 t^2 + 3T'\Phi^2 \nu_r^2 \left(d^2 + 2\frac{\Delta I}{I_{oo}} dc + \left(\frac{\Delta I}{I_{oo}}\right)^2 c^2 \right) t \quad (9.4-4)$$

* Note that if the z gyro is rotated from the orientation in Fig. 9.3-1 by 180 deg. about its input axis the minus sign in Eq. (9.4-1) would be changed to a plus. This illustrates another point about error reduction in strapdown systems -- the orientation of the instruments can sometimes be chosen to reduce dynamic errors.

Defining

$$f = \frac{\Delta I}{I_{00}}$$

and noting that for this problem

$$\frac{B^4}{2} \gg 3\Phi^2 \nu_r^2$$

The expression for $J(t')$ is

$$\frac{J[t']}{a(T')^2} \cong \frac{aB^4}{2} \left[c^2 + \frac{d^2}{2} + \frac{f^2 c^2}{2} - cd - fc^2 + fcd \right] + 3\Phi^2 \nu_r^2 \left[d^2 + 2fcd + f^2 c^2 \right] \quad (9.4-5)$$

Step 4 — In Eq. (9.4-5) the quantities c and d cannot be negative, but f can take on any value. When the definitions of c , d , and f are substituted into Eq. (9.4-5) it becomes evident that the right side of the equation is a function of the designable parameters H , C , I_{00} , and ΔI . Also because of the definition of J , the right side is never negative. A steepest descent computer technique was used to determine the optimum values of the designable parameters. Table 9.4-1 lists the original parameters and the optimum set found by the computer program when the value $a = 120$ ($T' =$ one minute, $t' = 2$ hr) is specified. It is obvious from Eq. (9.1-1) that the optimal value of I_{00} called for in Table 9.4-1 is not realizable; an excessive wheel speed is called for.

The parameter optimization was performed a second time with constraint that $I_{00} \geq 40 \text{ gm-cm}^2$ (a wheel speed in excess of 24,000 rpm if H remains unchanged). The results are listed in Table 9.4-2. As a

TABLE 9.4-1

ORIGINAL AND OPTIMAL SET OF DESIGNABLE
PARAMETERS: NO PRACTICALITY CONSTRAINTS

Parameter	Original Value	Optimal Value
Angular Momentum, H, (gm-cm ² /sec)	2.00×10^5	2.00×10^5
Damping Coefficient, C, (dyne-cm-sec)	8.00×10^5	8.00×10^5
Output Axis Inertia, I_{oo} , (gm-cm ²)	250	3.53×10^{-2}
Low Frequency Anisoinertia, $I_{ii} - I_{ss}$, (gm-cm ²)	-4.00	-49.9

TABLE 9.4-2

ORIGINAL AND OPTIMAL SET OF DESIGNABLE
PARAMETERS: PRACTICALITY CONSTRAINT ON I_{oo}

Parameter	Original Value	Optimal Value
Angular Momentum, H, (gm-cm ² /sec)	2.00×10^5	2.00×10^5
Damping Coefficient, C, (dyne-cm-sec)	8.00×10^5	8.00×10^5
Output Axis Inertia, I_{oo} , (gm-cm ²)	250	40.0
Low Frequency Anisoinertia, $I_{ii} - I_{ss}$, (gm-cm ²)	-4.00	-10.0

consequence of the optimization, the cost function (evaluated at $t' = 2$ hr) is reduced from $(3.34 \text{ deg})^2$ to $(0.41 \text{ deg})^2$.

Step 5 — The dominant error sources do not change as a result of the above optimization.

Effect of Compensating Output Axis Acceleration Errors — Let us assume that output axis angular acceleration errors are reduced to 10% of their gross value by compensation, and continue to impose the constraint that $I_{00} \geq 40 \text{ gm-cm}^2$. The optimal set of gyro parameters, determined by the steepest descent procedure, is shown in Table 9.4-3. As a result of the compensation the cost function (at $t' = 2$ hr) was reduced from $(3.34 \text{ deg})^2$ to $(0.36 \text{ deg})^2$ before optimization. Choosing the best set of parameters further reduces the cost to $(0.04 \text{ deg})^2$, at the expense of producing float (gimbal and rotor) inertia characteristics that are untypical of current gyros. Clearly a major reduction in system errors caused by vibration effects may be achieved by compensation alone. The manipulation of gyro parameters, with potential impact on other important factors (such as weight, size, power, random drift, etc.) can achieve similar results when taken alone or can complement the compensation when both techniques are used.

Summary — The question of lowering vibration-induced system-level attitude errors through proper selection of gyro parameters has been analyzed. It was shown that the major errors result from certain parameters which are largely unavoidable (at least in the single-degree-of-freedom gyro); consequently, reducing system errors requires sweeping changes in certain gyro inertia characteristics. Even when physical constraints on these parameters are not violated, it is possible that by redesigning the sensor to reduce one set of dynamic errors

TABLE 9.4-3

ORIGINAL AND OPTIMAL SET OF DESIGNABLE
PARAMETERS: OUTPUT AXIS ERRORS COMPENSATED

Parameter	Original Value	Optimal Value
Angular Momentum, H, (gm-cm ² /sec)	2.00×10^5	2.00×10^5
Damping Coefficient, C, (dyne-cm-sec)	8.00×10^5	8.00×10^5
Output Axis Inertia, I_{oo} , (gm-cm ²)	250	40.0
Low Frequency Anisoinertia, $I_{ii} - I_{ss}$, (gm-cm ²)	-4.00	-460

other causes of error will be increased. Using approximate analyses, it was shown that proper compensation of a major source of motion-induced gyro errors yields an order-of-magnitude reduction in the system drift rate, without necessitating redesign of the sensors. The use of compensation to reduce dynamic errors is discussed in detail in the next chapter.

10.1 INTRODUCTION

It has been shown in Chapter 2 that strapdown gyros and accelerometers are subject to errors which are a consequence of rotation about their output and spin axes as well as their input axes. Because these errors result for parameters which are essential to the operation of strapdown components, it is desirable to develop methods to reduce or eliminate their effects. Recognizing the presence of specific dynamic error sources one may devise several approaches to compensate component outputs, in order to obtain a better estimate of input angular and linear motion. In this chapter several compensation methods for single-degree-of-freedom (SDF) strapdown gyros are illustrated, recognizing that similar approaches are valid for SDF accelerometers.

Before certain dynamic errors may be compensated, knowledge of the angular motion about axes other than the input (sensitive) axis of a strapdown gyro must be available. To achieve this the three gyros (assumed here to be oriented with their input axes orthogonal) which are already present to provide three-dimensional system attitude information may be employed. In practice one may utilize the measurements made by all three gyros to generate signals for compensating any one gyro.

Fundamentally, there are two distinct classes to which various compensation techniques belong. To illustrate one category, consider the signal flow diagram depicted in Fig. 10.1-1, where the dotted lines indicate that additional blocks are understood to be present to form the compensation for each channel. The approach illustrated employs filters, labeled compensation calculation, which process gyro outputs. The addition of the filter does not close any new feedback loops. That is, each compensated gyro output

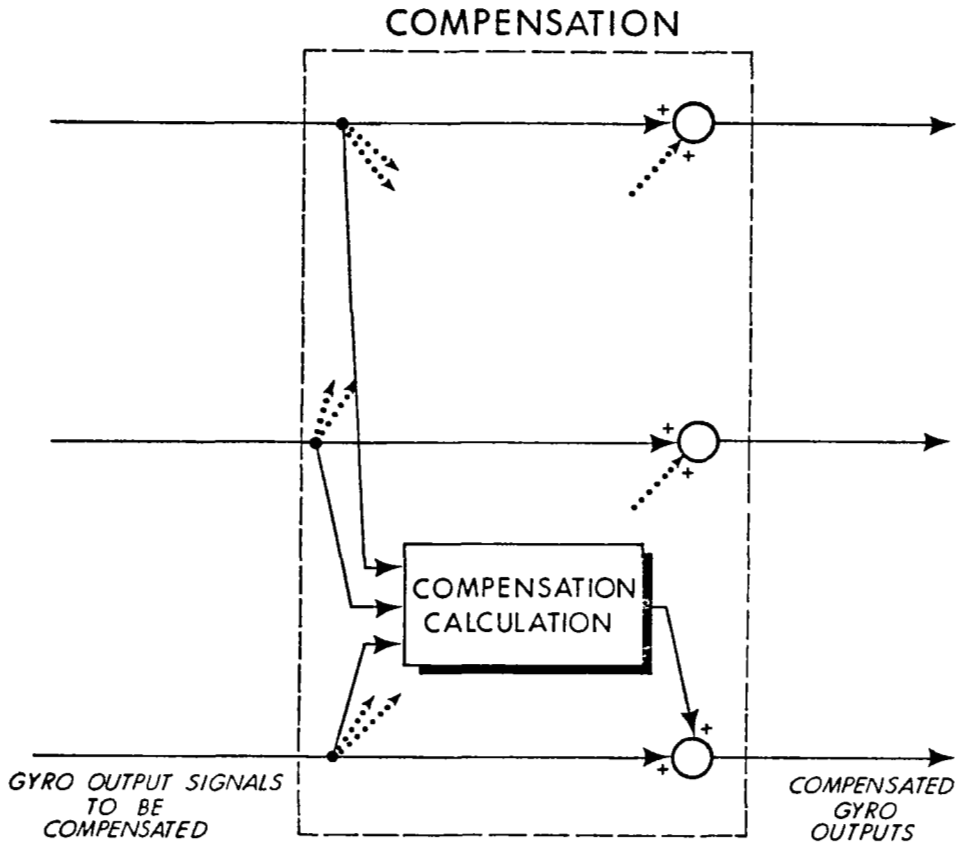


Figure 10.1-1 Open Loop Compensation

does not depend directly on any other compensated output. Consequently, the approach can be referred to as open loop compensation. The open loop compensation of Fig. 10.1-1 is accomplished through the use of the filters, whether they be implemented in a digital or analog manner.

In contrast to the above technique, it is possible to introduce compensating signals in such a way that new feedback loops are closed. To demonstrate, consider Fig. 10.1-2 where a closed information loop is illustrated in the compensation of one gyro; the dotted lines indicate that similar operations are performed for the remaining gyros. The closed circuit can be seen by tracing the path of signals from the compensated

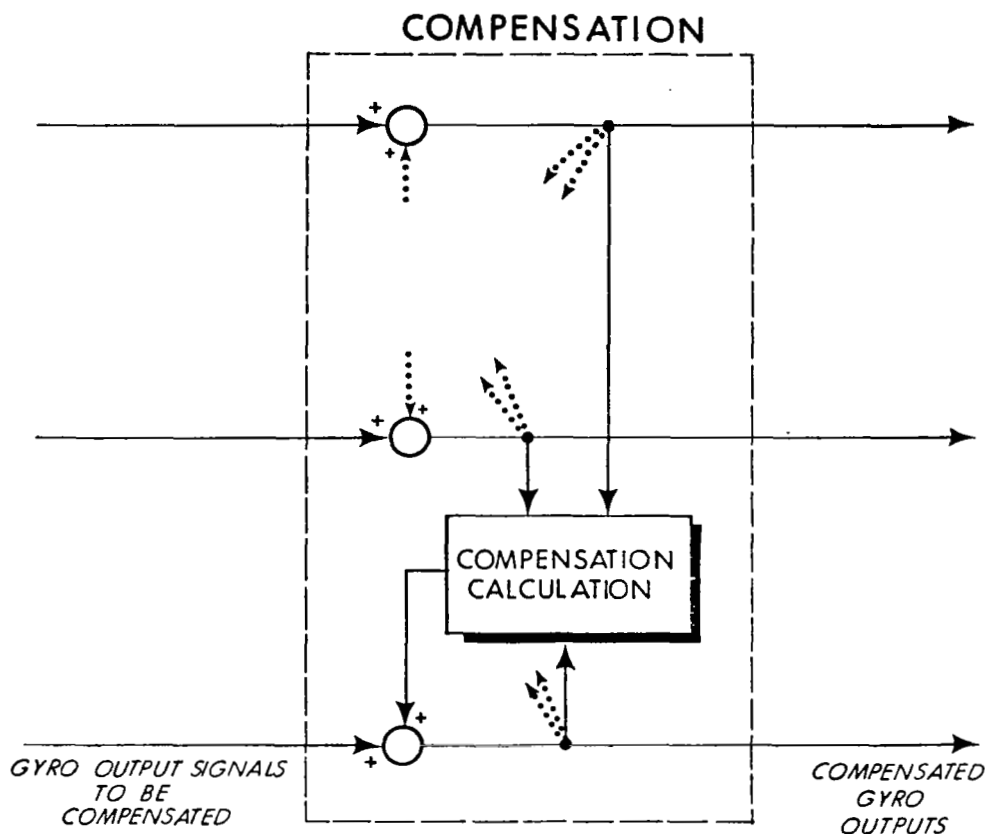


Figure 10.1-2 Closed Loop Compensation

output and proceeding through the filters until the starting point is reached again. This can be referred to as closed loop compensation.

Note that "closed-loop" refers to the fact that new feedback loops are closed, and by so doing, each compensated gyro output depends directly on another. This type of operation may be entirely performed in a digital computer. Alternately, the outputs of the compensation calculations in Fig. 10.1-2 can be used to drive gyro torquers. In any case however, one must pay careful attention to stability when this technique is employed.

10.2 COMPENSATING CROSSCOUPLING ERRORS

Crosscoupling errors are introduced into a gyro's output when its float (gimbal) angle is off null and angular motion is present about the nominal spin axis at the same time. This is illustrated in Fig. 10.2-1. The crosscoupling torque results from the fact that a portion of case motion about the spin reference axis (SRA) is projected along the actual gimbal input axis. The torque is given by $-H\omega_s\alpha_0$ (when α_0 is small), where H is the spin angular momentum, ω_s is the rate applied about the SRA and α_0 is the float angle. When the gyro float angle is off null, motion about the case spin axis is sensed, generating a torque which is indistinguishable from that caused by motion about the case input axis. A signal flow diagram depicting this behavior is shown in Fig. 10.2-2. It should be noted that this kind of error is basic to the single-degree-of-freedom (SDF) gyro, which relies on a non-zero float angle to infer motion about the input axis.

It has been shown in Chapter 2 that crosscoupling can result in both oscillatory errors and constant errors. For example, constant errors occur when the gyro float angle and motion about the spin axis are in-phase sinusoids. A constant error torque due to crosscoupling may introduce severe system attitude errors while oscillatory error torques may not be as objectionable because their long-term average value is zero.

10.2.1 An Approach to Compensation

It was proposed in Ref. 14 that the angular motion measured by a gyro triad (a set of three gyros whose input axes are orthogonal) be used to generate compensation torques for nulling errors in the individual gyros. We consider here the closed loop compensation afforded by measuring the

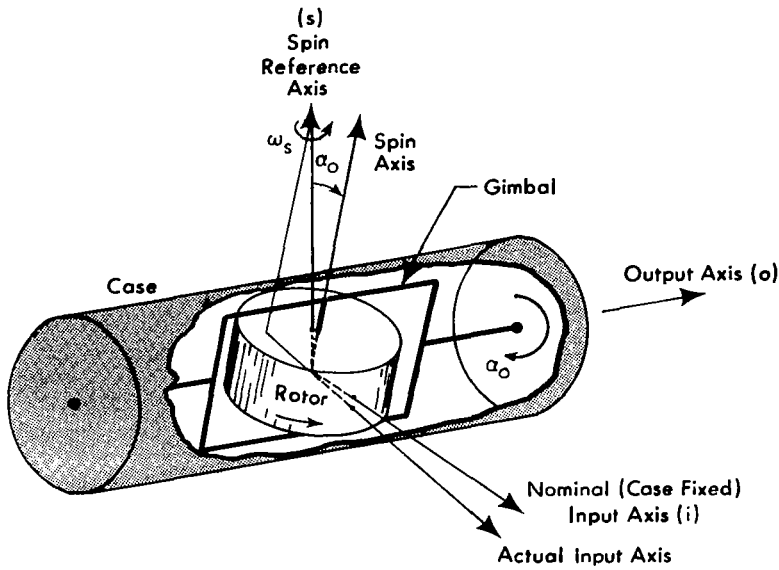


Figure 10.2-1 Source of Crosscoupling Error

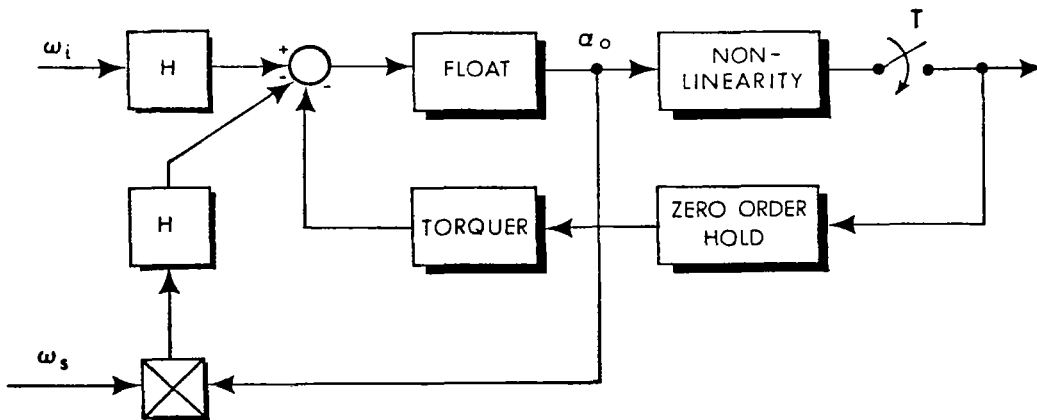


Figure 10.2-2 Signal Flow Diagram Illustrating Crosscoupling Errors

angular rate about the spin axis of a gyro to compute a corrective torque, which when applied to the gyro float tends to cancel the error due to cross-coupling. This idea extends easily enough to the three gyros in an orthogonal set. The basic approach is illustrated in Fig. 10.2-3 where, for simplicity, only the compensation of a single gyro is shown. Gyro A experiences angular motion about its spin and input axes which generates a crosscoupling error. The second gyro (B) measures the angular rate about the spin axis of the first in order to provide information for compensation. (For simplicity, identical parameters are assumed for gyros A and B). The crosscoupling error torque appears as the product of the spin axis rate and the float angle of A. (Its formation is traced by the heavy lines in the figure.) The compensation technique takes the output pulse train of B, multiplies it by the float angle of A and applies a correction torque to A. A similar procedure would be followed to compensate gyro B and the third gyro in the triad (not shown).

Ignoring the dynamics of the torque generators, the compensation torque, M_c , is given by

$$M_c(t) = K_{tg} \alpha_o(t) x(t) \quad (10.2-1)$$

and the crosscoupling error torque, M_e , is

$$M_e(t) = -H \alpha_o(t) \omega_s(t) \quad (10.2-2)$$

These two torques oppose each other in the compensated gyro giving a net torque

$$M_c(t) - M_e(t) = \alpha_o(t) \left(K_{tg} x(t) - H \omega_s(t) \right) \quad (10.2-3)$$

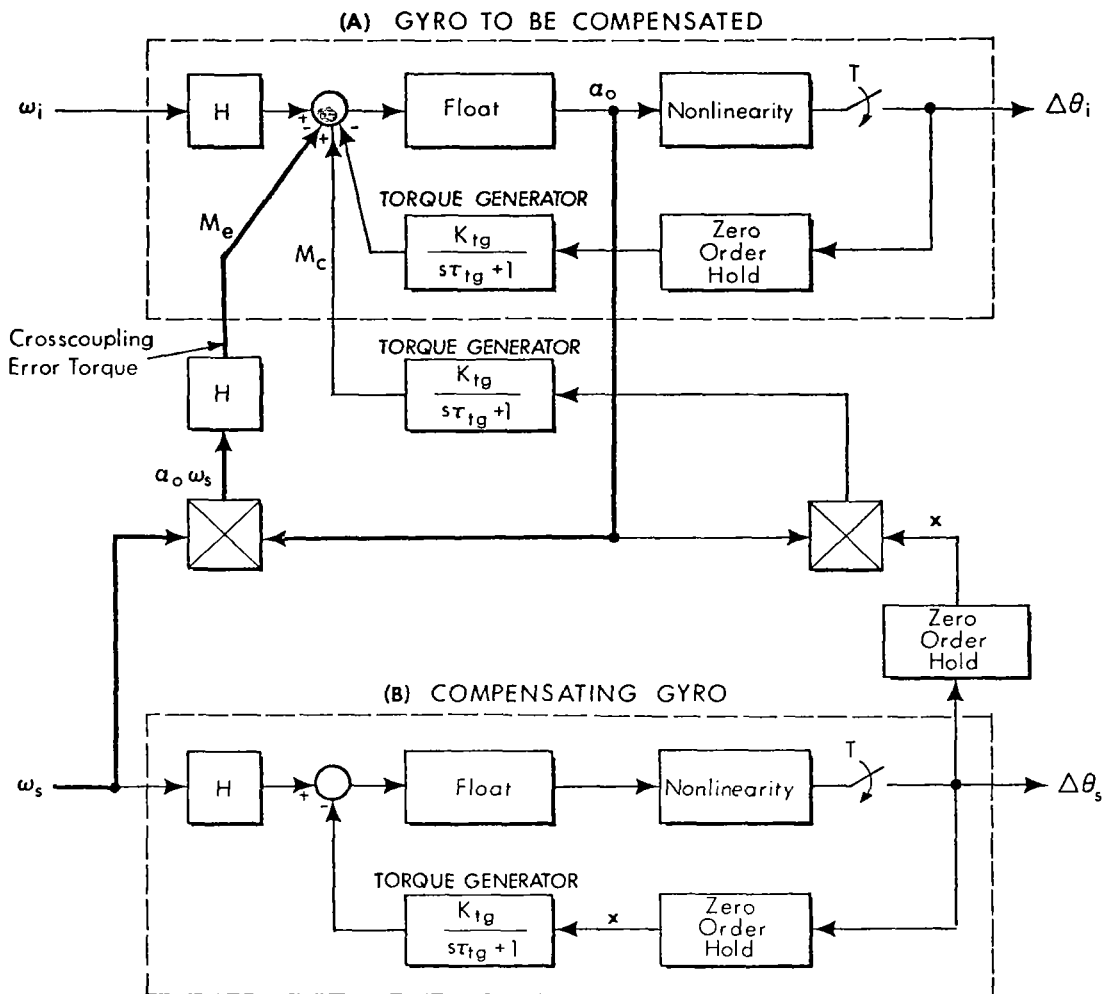


Figure 10.2-3 Block Diagram of Crosscoupling Error Compensation of One Gyro

Earlier it was demonstrated that, at least when the input ω_s is in a certain range of frequencies, one component of the torquer current, $x_f(t)$, is related to the input to gyro B by

$$x_f(t) = \frac{H}{K_{tg}} \omega_s(t) \quad (10.2-4)$$

As a consequence of Eq. (10.2-4)

$$M_c(t) - M_e(t) = \alpha_o(t) K_{tg} x_h(t) \quad (10.2-5)$$

where $x_h(t)$ represents harmonic components of $x(t)$. There exist three common cases for which the average value of the expression given by Eq. (10.2-5) is zero. These occur

- When $x_h(t)$ and $\alpha_o(t)$ are random uncorrelated variables and at least one of them is unbiased.
- When ω_s is constant (in which case the $x_h(t)$ can only consist of a sum of coherent sinusoids) and α_o is not a coherent sinusoid.
- When ω_s and ω_i are in-phase sinusoids, as would be generated by an oscillation occurring in the plane of the spin and input axes.

The accuracy and stability of this compensation approach is difficult to assess analytically because the float angle measurements act as random time-varying (and not completely independent) gains. While the interconnected information loops do not introduce any practical problem other than additional complexity, no theoretical treatment of stability was found for this situation. Therefore a simulation study was undertaken to investigate the properties of the compensation.

10.2.2 Simulation Results

At first, two gyros of the ternary rebalance type for which a representative set of parameters was chosen were simulated, with compensation as illustrated in Fig. 10.2-3. Ternary nonlinearities were simulated. The input axes were assumed to be at right angles to each other. This simulation was exercised for the case in which the input and

spin axis angular rates were in-phase sinusoids. The compensation proved successful in removing constant crosscoupling errors from the compensated gyro. With sinusoidal inputs of amplitude 0.1 rad/sec on both axes, the compensation was effective at frequencies up to about 100 Hz.

This success prompted evaluation of a gyro triad in which each gyro was compensated by one of the others--closed loop compensation. Not only was the simulation observed to be stable, but when in-phase sinusoids were applied about the two appropriate axes of each gyro, the compensation reduced constant crosscoupling errors by about 80%. This percentage was obtained by comparing the crosscoupling error indicated by one gyro with no compensation to the error obtained when full closed loop compensation was employed. As with the single compensated gyro, crosscoupling error reduction was effective over the range of frequencies up to about 100 Hz.

10.3 COMPENSATING OUTPUT AXIS ERRORS

It was shown in Chapter 2 that a single-degree-of-freedom strap-down gyro will indicate a false input angular motion when experiencing angular acceleration about its output axis. This effect is referred to as output axis (OA) angular acceleration error. Specifically, it results from gyro case motion about the output axis and float inertia. In the absence of a rebalance mechanism, the angular position of the float relative to the case changes when angular acceleration is experienced by the gyro case. Because this float angle cannot be distinguished from that caused by motion about the input axis, one can interpret the effect of output axis angular acceleration in terms of a torque applied about the gyro output axis. The apparent error torque due to this effect is given by

$$\text{effective OA error torque} = I_{oo} \dot{\omega}_o \quad (10.3-1)$$

where I_{oo} is the effective rotational inertia of the float about its output axis and $\dot{\omega}_o$ is the angular acceleration about the case output axis.

The output axis angular acceleration error would not have a deleterious effect on the performance of a single strapdown gyro if only sinusoidal motion were experienced about its output axis. This is true because the average error would tend to zero. However, OA error in an orthogonal set of gyros can lead to another error known as pseudo-coning. Pseudo-coning can introduce constant system attitude drift rates; basically it results from a combination of an oscillatory error in angular motion measured about one axis and a true oscillatory motion about an orthogonal axis, of the same frequency and with the appropriate relative phase. Output axis errors tend to be most damaging in this manner. Furthermore, most pseudo-coning errors due to OA sensitivity are not dependent on particular correlations between motions about different system axes, but appear when any vibratory angular motion is present. For this reason, techniques are desired for compensating OA angular acceleration error.

10.3.1 Open Loop Compensation

It is desired to employ a simple mathematical model of a single-degree-of-freedom strapdown gyro in the analysis of techniques to compensate OA errors; using a more complex one would render the problem intractable. Consequently, the strapdown gyro is modeled as a second order linear system with the structure shown in Fig. 10.3-1, where a and b may be related to gyro parameters and H is the angular momentum of the

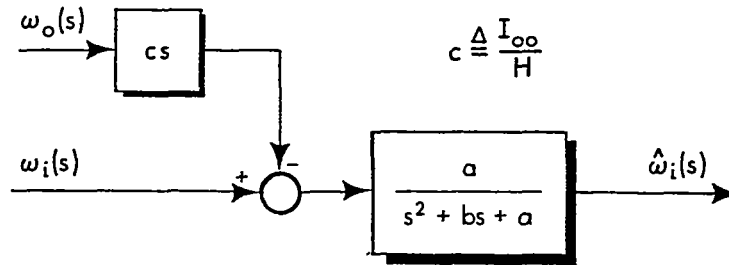


Figure 10.3-1 Linear Mathematical Model of Strapdown Gyro

gyro rotor at normal operating speed. Note that the parameter c is the ratio between the effective rotational inertia of the gimbal about the output axis, I_{oo} , and H . Because it is a measure of sensitivity to output axis angular acceleration, it is desired that c be as small as possible.

Considering only input axis motion, examination of Fig. 10.3-1 shows that in a well designed strapdown gyro the ratio $|\hat{\omega}_i|/|\omega_i|$ is approximately one for frequencies less than \sqrt{a} . That is, the bandwidth of the gyro is approximately \sqrt{a} . It can also be seen that the greater the value of H , the less effect output axis motion will have on the gyro's indicated rate, $\hat{\omega}_i$. It is clear that in order to compensate errors introduced by output axis motion, information about that motion must be gained. For a strapdown system this may be done by employing a set of three gyros, which might be arranged as shown in Fig. 10.3-2.

One approach for employing the information obtained by the three sensors to reduce or eliminate errors due to motion about the output axes is illustrated in Fig. 10.3-3. This is classified as open loop compensation. It is valid for frequencies within the bandwidth of each gyro. Note that the portion of the figure enclosed by a dotted line represents the compensation and the remainder reflects the behavior of the three identical gyros. The

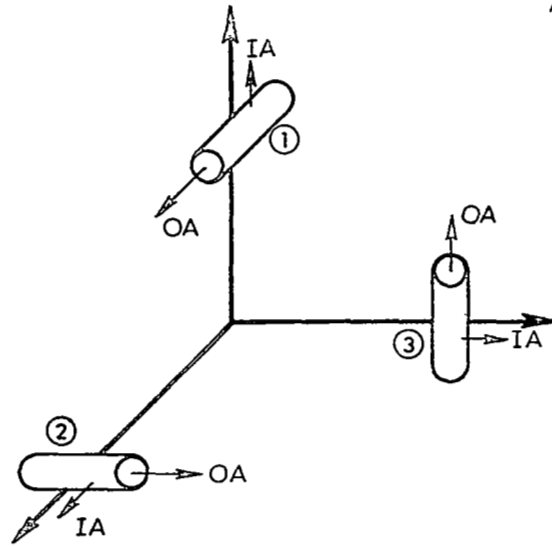
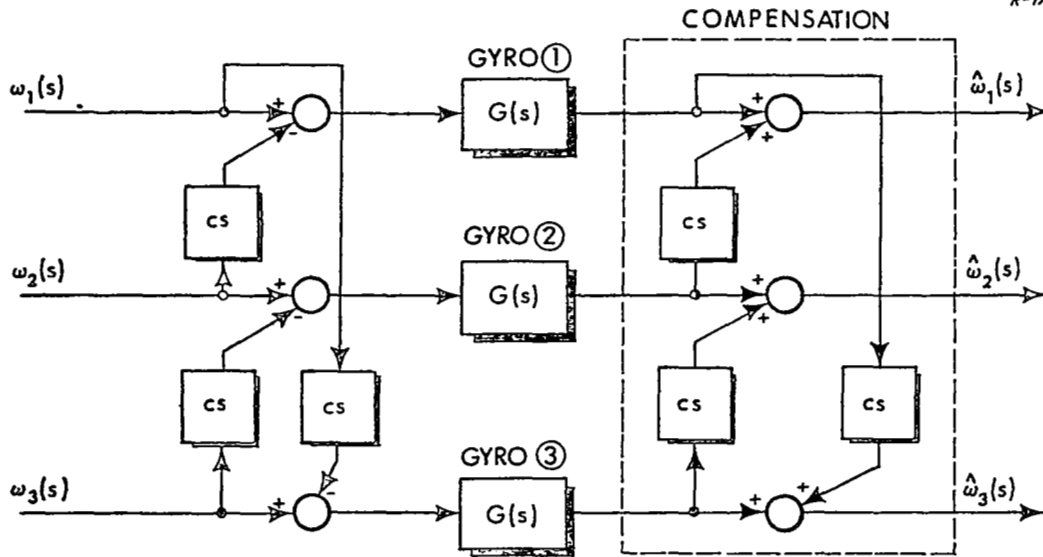


Figure 10.3-2 A Specific Orientation of Three Gyros with Input Axes Orthogonal



$$G(s) = \frac{a}{s^2 + bs + a}$$

Figure 10.3-3 Open Loop Compensation for Three Orthogonal Gyros

rationale of the open loop compensation of Fig. 10.3-3 is as follows: Because gyro (2) measures the angular motion about the output axis of gyro (1) it is reasonable to add c times the derivative of (2)'s output to the output of (1) in an effort to cancel the output axis angular acceleration error. Similar corrections may be applied to the outputs of gyros (2) and (3).

Owing to the symmetry of Fig. 10.3-3, it is only necessary to analyze three transfer characteristics to assess the value of this open loop compensation technique. Specifically, the following transfer functions need to be determined: $\hat{\omega}_1(s)/\omega_2(s)$; $\hat{\omega}_2(s)/\omega_2(s)$; $\hat{\omega}_3(s)/\omega_2(s)$. They are found to be

$$\frac{\hat{\omega}_1(s)}{\omega_2(s)} = 0 \quad (10.3-2)$$

$$\frac{\hat{\omega}_2(s)}{\omega_2(s)} = G(s) \quad (10.3-3)$$

$$\frac{\hat{\omega}_3(s)}{\omega_2(s)} = - (cs)^2 G(s) \quad (10.3-4)$$

Equation (10.3-2) shows that the OA angular acceleration error has been removed from gyro (1).

Equation (10.3-4) indicates that an error is present in the output of gyro (3) even though no motion was assumed to exist about its input or output axes. The nature of this error is as follows: Referring back to Fig. 10.3-1, one observes that the response to output axis motion is given by

$$\frac{\hat{\omega}_i(s)}{\omega_o(s)} = \frac{-acs}{s^2 + bs + a} \quad (10.3-5)$$

Equations (10.3-2) through (10.3-4) illustrate that the price paid for removing the effect of output axis error from gyro (1) is to introduce cs times the error that would be present in that gyro without compensation, into the output of gyro (3). For angular motion at frequencies such that $|cs| < 1$, this type of compensation is beneficial, because it reduces the net effect due to output axis angular acceleration error in the three gyros in the triad. Using a typical value of $c = 10^{-3}$ sec, this compensation is beneficial for frequencies less than about 160 Hz. The smaller the value of c , the greater the range of frequencies over which this compensation may be used effectively.

Some mention should be made about the implementation of the compensation technique illustrated in Fig. 10.3-3. Because a perfect differentiator does not exist, circuits which approximate a differentiation over a finite frequency range must be employed to mechanize the operation. Difficulties are further compounded if it is desired to recover angular acceleration from gyro outputs which represent incremental angular motion. This requires "differentiating" twice. In any case, the differentiation operation can introduce errors beyond those which have already been discussed, because of the necessarily imperfect implementation.

If it is known that angular vibrations about a particular axis are dominant, one might want to orient the gyros as depicted in Fig. 10.3-4. It can be seen that for angular vibration about axis ① only, no output axis errors result. Also, if open loop compensation is employed in a manner analogous to that which was just discussed, the residual output

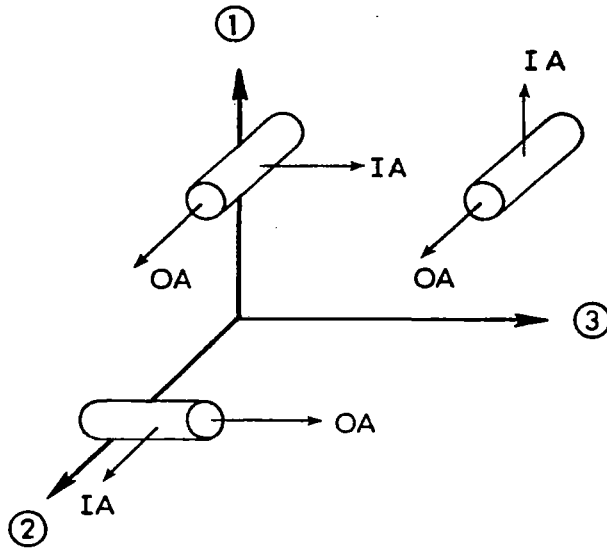


Figure 10.3-4 Orientation of Three Single-Degree-of-Freedom Strapdown Gyros

axis errors for motion about axes ② or ③ are similar to those in the previous case.

10.3.2 Closed Loop Compensation Using Corrective Torquing

In Section 10.3.1 no new feedback loops were closed about the individual gyros themselves. Only manipulation of their outputs was performed. The compensation approach discussed here, one incorporating corrective torquing, does involve the closing of new feedback loops about the gyros.

Employing the linear model of the gyro displayed in Fig. 10.3-1, consider the compensation approach in Fig. 10.3-5, indicating that a corrective (error compensation) torque is applied to each gyro. Since

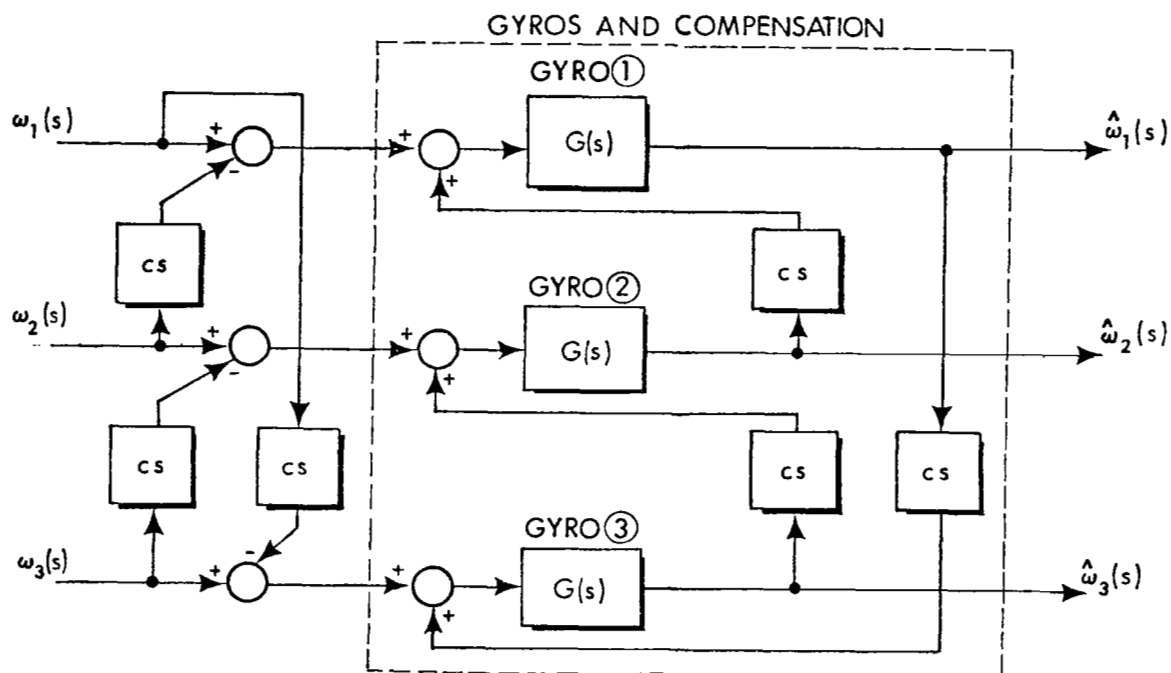


Figure 10.3-5 Closed Loop Compensation Involving Corrective Torquing

gyro (2) yields a direct measure of the rate applied about the output axis of gyro (1), that signal is used to generate a corrective torque which is applied to gyro (1) in an effort to cancel the output axis error. Since each compensating signal depends directly upon the compensated output of another gyro, new feedback loops are closed; corrective torquing of this type is a form of closed loop compensation. Note that the output of gyro (2) is not a perfect measure of its input; consequently, one would not expect this compensation technique to precisely eliminate the OA error in (1).

Output Axis Error Reduction – To determine the effect of the closed loop corrective torquing, the following transfer functions are calculated.

$$\frac{\hat{\omega}_2(s)}{\omega_2(s)} = \frac{a \left[(s^2 + bs + a)^2 - (cs)^3 a^2 \right]}{(s^2 + bs + a)^3 - (cs)^3 a^3} \quad (10.3-6)$$

$$\frac{\hat{\omega}_1(s)}{\omega_2(s)} = \frac{-acs (s^2 + bs) (s^2 + bs + a)}{(s^2 + bs + a)^3 - (cs)^3 a^3} \quad (10.3-7)$$

$$\frac{\hat{\omega}_3(s)}{\omega_2(s)} = \frac{-a^2 (cs)^2 (s^2 + bs)}{(s^2 + bs + a)^3 - (cs)^3 a^3} \quad (10.3-8)$$

Note that the magnitude of the transfer function expressed by Eq. (10.3-6) tends to unity as the signal frequency approaches zero, while those expressed by Eqs. (10.3-7) and (10.3-8) tend to zero. The transfer characteristics expressed by Eqs. (10.3-6), (10.3-7), and (10.3-8) are plotted in Figs. 10.3-6, 10.3-7 and 10.3-8 as functions of frequency for the following set of representative gyro parameters.

$$\begin{aligned} a &= \nu_n^2 = 10^6 \text{ sec}^{-2} & b &= 2\zeta\nu_n = \sqrt{2} \times 10^3 \text{ sec}^{-1} \\ c &= 1.25 \times 10^{-3} \text{ sec} & \zeta &= 0.707 \end{aligned} \quad (10.3-9)$$

The quantity ν_n is the natural frequency of the linear second order system representing the gyro and ζ is the corresponding damping ratio. Assurance

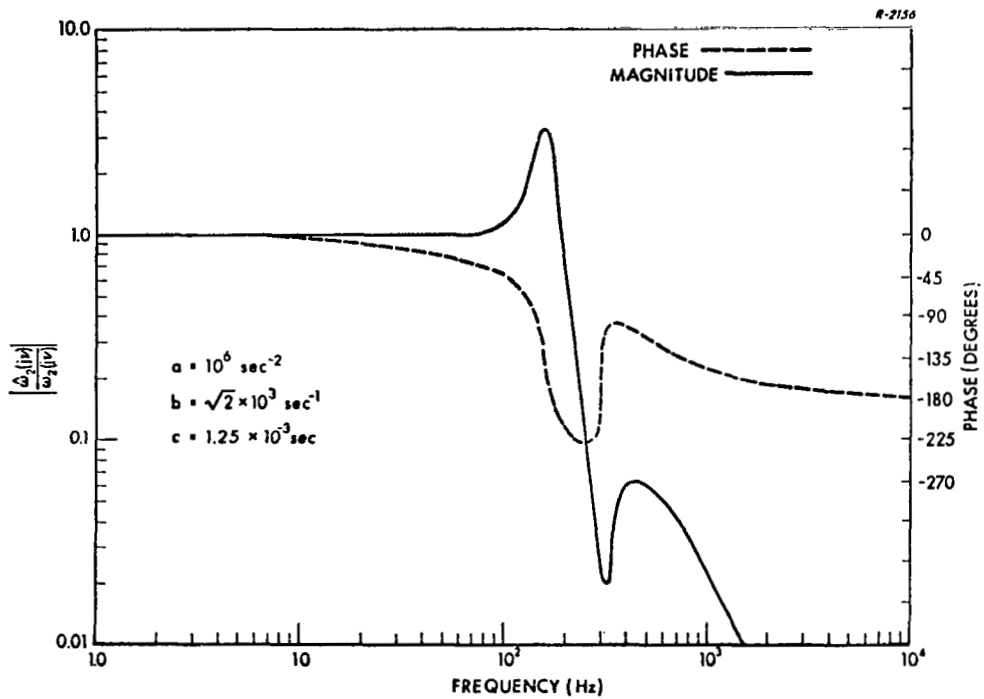


Figure 10.3-6 Magnitude and Phase of Transfer Function Expressed in Eq.(10.3-6)

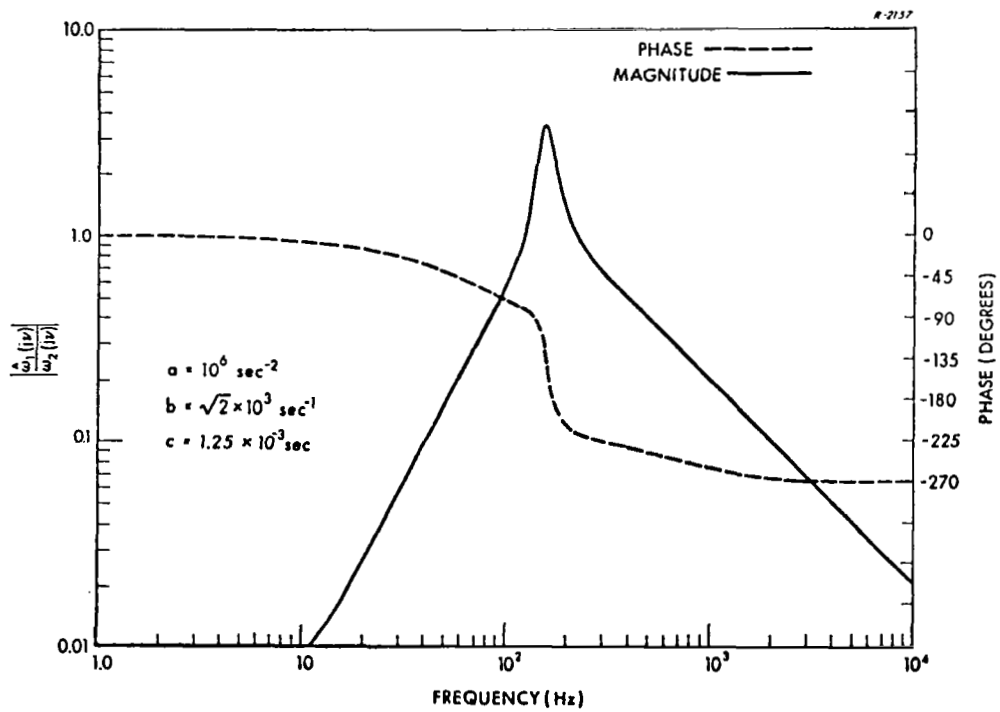


Figure 10.3-7 Magnitude and Phase of Transfer Function Expressed in Eq.(10.3-7)

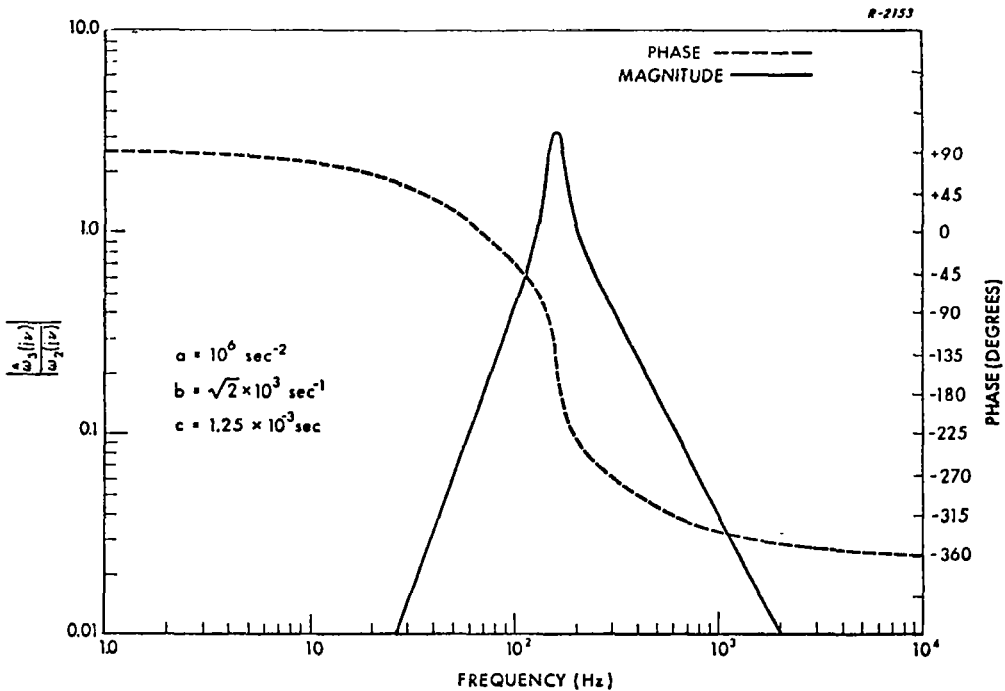


Figure 10.3-8 Magnitude and Phase of Transfer Function Expressed in Eq.(10.3-8)

that this particular closed loop system is stable was obtained by establishing that the eigenvalues of the system all lie in the left half of the complex plane for the values of a , b and c given in Eq. (10.3-9).

In order to assess the value of employing this compensation technique, refer back to Fig. 10.3-1. The uncompensated gyro transfer functions relating angular motion about input and output axes to indicated output are:

$$\frac{\hat{\omega}_1(s)}{\omega_1(s)} = \frac{a}{s^2 + bs + a} \quad (10.3-10)$$

$$\frac{\hat{\omega}_i(s)}{\omega_o(s)} = \frac{-acs}{s^2 + bs + a} \quad (10.3-11)$$

The transfer functions expressed by Eqs. (10.3-10) and (10.3-11) are plotted in Figs. 10.3-9 and 10.3-10 for the same representative gyro parameters used in Figs. 10.3-6 through 10.3-8.

Now the compensated and uncompensated transfer characteristics may be compared. The transfer function relating indicated input rate to a rate about the output axis of gyro (1) (compensated) is expressed by Eq. (10.3-7). The corresponding uncompensated transfer function is given by Eq. (10.3-11). Examination of Figs. 10.3-7 and 10.3-9 show that the corrective torquing has the greatest effect in reducing output axis error at frequencies less than about 110 Hz, the range in which most vehicle motion usually occurs. Note there is essentially no improvement at higher frequencies, and that the compensation does introduce some peaking at the frequency range 110 - 270 Hz. The price paid for this benefit is seen by examining Figs. 10.3-6 and 10.3-10 where the response of compensated and uncompensated gyros to angular motion about the input axis are plotted. Note that while the compensation significantly reduced errors due to OA angular acceleration (except for some peaking between 110 - 270 Hz), the compensated input axis transfer function has been modified; specifically, a resonance peak occurs in the range 100 - 190 Hz. Nevertheless, for the range of frequencies up to about 100 Hz, the input response is unchanged.

Examination of Fig. 10.3-8 shows that an error due to motion about the input axis of gyro (2) is introduced into the output of gyro (3) when the closed loop compensation is employed. This can be a source of system drift rate; examination of Figs. 10.3-6 and 10.3-8 reveals that in the frequency range 0 - 100 Hz, where the majority of the power associated with vehicular motion is likely to be concentrated, the relative phase between errors introduced in gyro (3) and motion sensed by gyro (2) will produce pseudo coning errors. However, comparison of Figs. 10.3-6, 10.3-8, 10.3-9

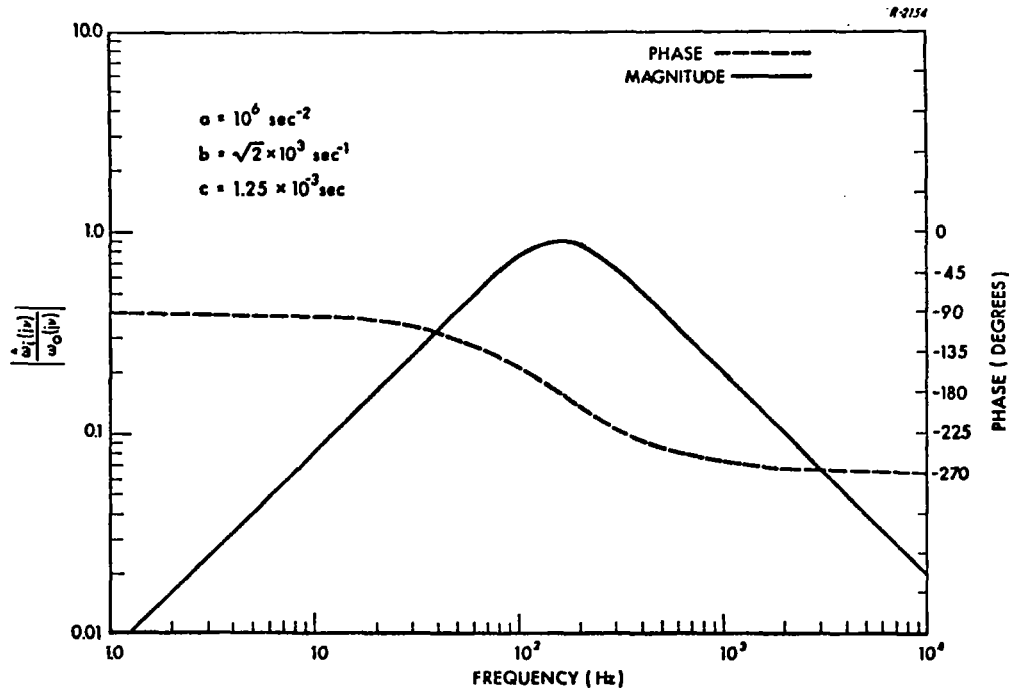


Figure 10.3-9 Magnitude and Phase of the Transfer Function Expressed in Eq. (10.3-11)

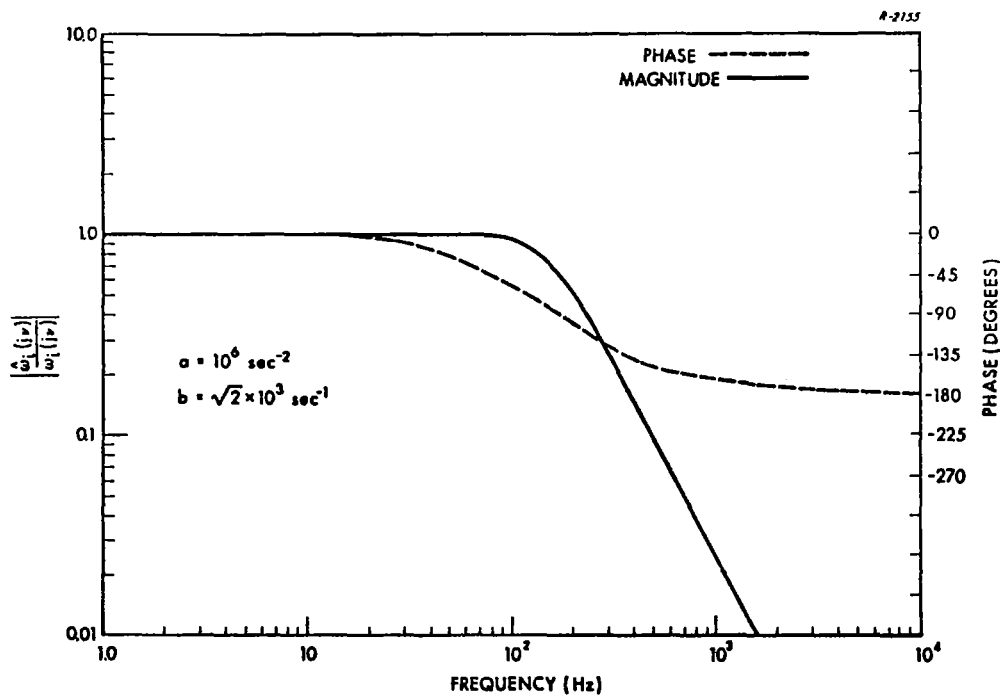


Figure 10.3-10 Magnitude and Phase of the Transfer Function Expressed in Eq. (10.3-10)

and 10.3-10 indicates that, for motion occurring at frequencies below 100 Hz, the error introduced by compensation is significantly less than that which would result if no compensation were used. Therefore, for the situation treated here compensation affords a decided benefit to system performance.

Study of these transfer functions shows that for gyros with a large uncompensated bandwidth, closed loop compensation of output axis dynamic error tends to destabilize the system. This may be seen by dividing the characteristic equation associated with Eq. 10.3-6 by a^3 and letting a approach infinity. The result is, in the limit, the third order equation

$$1 - (cs)^3 = 0 \quad (10.3-12)$$

Equation (10.3-12) has one root in the right half of the complex plane, indicating an unstable system for large values of a . This observation leads to the conclusion that not all gyros may be compensated in exactly this manner.

Additionally, the damping ratio, ζ , associated with each gyro must be near critical in order that compensation be effective. This is demonstrated by expanding the characteristic equation of the closed loop system as follows:

$$s^6 + 3bs^5 + 3(a+b^2)s^4 + (b^3 - a^3c^3 + 6ab)s^3 + 3a(a+b^2)s^2 + 3a^2bs + a^3 = 0 \quad (10.3-13)$$

As b vanishes the coefficients of several of the powers of s in Eq. (10.3-13) tend to zero. A necessary condition for all the roots of Eq. (10.3-13) to lie in the left half of the complex plane is that all the coefficients must be of the same sign and non-zero (Ref. 15). Therefore for fixed bandwidth and a given value of c , reducing b alone (equivalent to reducing ζ , the damping

ratio) tends to destabilize the compensation. It is not easy to determine the necessary and sufficient conditions on a and b such that for a given c the system is stable, because to do so involves finding the region in a-b space which satisfies six inequality constraints (most of which are nonlinear). Rather, it is simpler to test system stability when a, b, and c are specified.

10.3.3 Closed Loop Compensation in a Computer

It was noted that new feedback loops were closed in the corrective torquing compensation technique of Section 10.3.2. However, if other considerations restrict the electrical interconnection of gyros, or if it is desired to employ only external data processing, then the digital computer which is employed for system attitude computation may be used to implement closed loop compensation. By this it is meant that new information loops are closed via the computations executed within the computer itself.

Decoupling Filter - One may postulate the existence of a filter (implemented digitally) which decouples the errors produced by angular motion about the output axis of an SDF strapdown gyro. To illustrate, assume that the three gyros of Fig. 10.3-2 are identical in all respects and that the total package is subjected to angular oscillations about the input axis of each gyro. Treating output axis errors only and employing the simplified mathematical model of gyro transmission characteristics illustrated in Fig.10.3-1, one may write

$$\underbrace{\begin{bmatrix} \hat{\omega}_1 \\ \hat{\omega}_2 \\ \hat{\omega}_3 \end{bmatrix}}_{\underline{\hat{\omega}}} = \frac{a}{s^2 + bs + a} \begin{bmatrix} 1 & -cs & 0 \\ 0 & 1 & -cs \\ -cs & 0 & 1 \end{bmatrix} \underbrace{\begin{bmatrix} \omega_1 \\ \omega_2 \\ \omega_3 \end{bmatrix}}_{\underline{\omega}} \quad (10.3-14)$$

where $\underline{\hat{\omega}}$ is the vector of measured input rates, and $\underline{\omega}$ is the vector of true input angular rates. The presence of the off-diagonal terms in Eq. (10.3-14) reflects the errors in measured rates caused by output axis angular acceleration. Because it is desired to extract $\underline{\omega}$ from $\underline{\hat{\omega}}$ (i. e. reconstruct the true input signals exactly), one can postulate a set of calculations which solve Eq. (10.3-14) for $\underline{\omega}$ in terms of $\underline{\hat{\omega}}$. The result is

$$\begin{bmatrix} \omega_1 \\ \omega_2 \\ \omega_3 \end{bmatrix} = \frac{s^2 + bs + a}{aD(s)} \begin{bmatrix} 1 & cs & (cs)^2 \\ (cs)^2 & 1 & cs \\ cs & (cs)^2 & 1 \end{bmatrix} \begin{bmatrix} \hat{\omega}_1 \\ \hat{\omega}_2 \\ \hat{\omega}_3 \end{bmatrix} \quad (10.3-15)$$

where

$$D(s) \triangleq 1 - (cs)^3$$

Several important conclusions can be drawn by examining Eq. (10.3-15). Inspection of $D(s)$ shows that the characteristic polynomial of the filter is not Hurwitz, i. e., the dynamics of the filter are unstable. In addition, the instability is independent of the dynamics of the gyro, so long as the gyro is modeled as a stable linear system. This result, using similar analysis, was reported in Ref. 16. The fact that the decoupling

filter described turned out to be unstable indicates that it is not possible to eliminate OA error by employing just the three identical gyros of Fig. 10.3-2. Rather one must be satisfied with trying to reduce the effects of OA error, with no hope of completely eliminating it.

Output Error Reduction – The open loop compensation of Fig. 10.3-3 illustrates that uncompensated signals are employed to correct other such signals. It would appear worthwhile to utilize the corrected signals in Fig. 10.3-3 to modify the other corrected signals, recognizing that this will cause new feedback loops to be closed. The change to Fig. 10.3-3 is depicted in Fig. 10.3-11, where only the modification is illustrated.

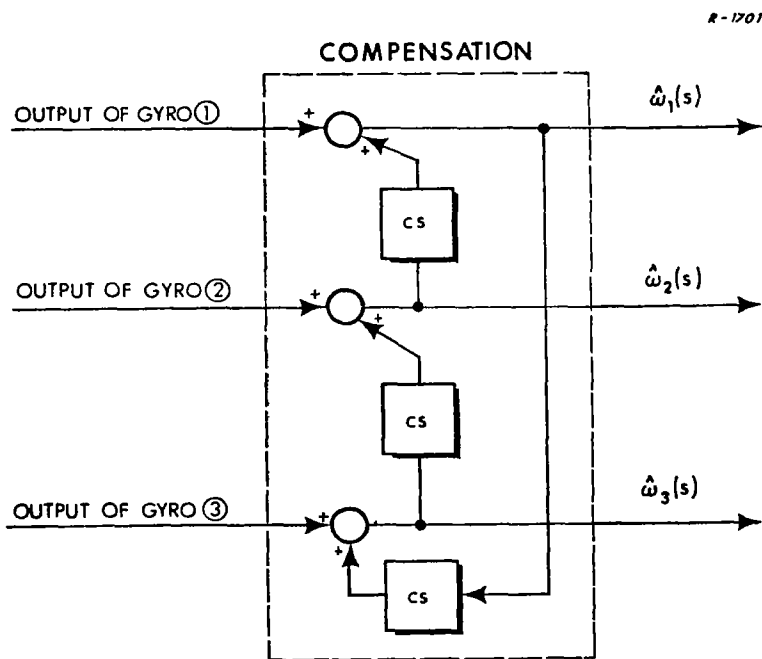


Figure 10.3-11 Unstable Closed Loop Compensation in a Computer

While at first this might appear to be a reasonable approach to closed loop compensation, closer examination of the correction loop shown indicates it is unstable. That is, the characteristic equation of the correction loop is given by

$$1 - (cs)^3 = 0 \quad (10.3-16)$$

which has one root in the right half of the complex plane. This approach, if it were realizable, would provide perfect compensation. The instability of this formulation is equivalent to that which was established for the decoupling calculations described by Eq. (10.3-15). Note that the present formulation is simpler than the decoupling filter in that the gyros are not within the compensation loop.

Should the compensation approach of Fig. 10.3-11 be employed with just two gyros whose input axes are orthogonal, one would also draw the conclusion that the correction loop is unstable.

The structure of the closed loop compensation of Fig. 10.3-5 suggests that it is possible to stabilize the correction loop of Fig. 10.3-11. Consider Fig. 10.3-12 where the signal flow is the same as in Fig. 10.3-11 except that a dynamic element with transfer function $G(s)$ is added into each of the correction signal paths. (Fig. 10.3-12 is compatible with the left half of Fig. 10.3-3). It can be noted that Fig. 10.3-12 is actually a rearrangement of Fig. 10.3-5; one sees that corresponding transfer functions will be identical. Consequently, all the observations regarding the reduction of output axis error in the discussion of Fig. 10.3-5 apply here as well. We can conclude that this form of closed loop compensation, while not perfect, affords useful reduction in the propagation of errors due to output axis angular acceleration.

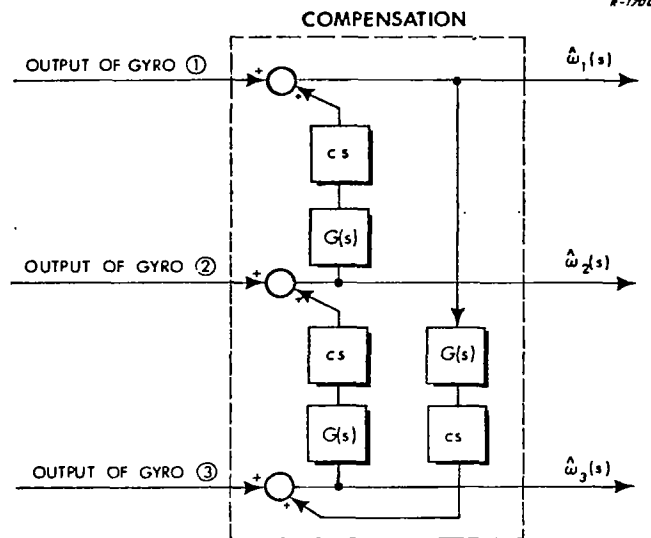


Figure 10.3-12 Stable Closed Loop Compensation in a Computer

10.4 COMPENSATING ANISOINERTIA ERROR

As discussed in Section 2.1, the effective aniso inertia error torque applied about the gyro input axis has two components. One is caused by the inequality in moments of inertia of the gyro-gimbal combination about the spin and input axes; the other is produced by the failure of the rotor speed control to maintain a constant rotor spin rate relative to the gyro gimbal. Repeating Eq. (2.1-9) we have

$$\text{aniso inertia error torque} = (I_{ss} - I_{ii})\omega_s \omega_i + I_{ss_r} \delta\Omega \omega_i \quad (10.4-1)$$

where

I_{ii} = rotational inertia of the rotor and gimbal combination about the input axis.

I_{ss_r} = rotational inertia of the rotor alone about the spin axis.

I_{ss} = rotational inertia of the rotor and gimbal combination about the spin axis.

ω_s = angular rate of the case about the spin axis.

ω_i = angular rate of the case about the input axis.

$\delta\Omega$ = change in rotor spin rate relative to the gimbal.

The quantity $\delta\Omega$ is related to ω_s by Eq. (2.1-8):

$$\delta\Omega(s) = - \frac{s^2}{s^2 + K_h/I_{ss_r}} \omega_s(s)$$

Note that this model predicts an oscillatory speed regulator. In practice the regulator is observed to be very lightly damped. Hence a more exact model is given by the expression,

$$\delta\Omega(s) = - \frac{s^2}{s^2 + 2\zeta \sqrt{\frac{K_h}{I_{ss_r}}} s + \frac{K_h}{I_{ss_r}}} \omega_s(s) \quad (10.4-2)$$

where ζ is the damping ratio.

The effective aniso inertia torque cannot be distinguished from the ideal gyroscopic torque and therefore it produces an error in the angular velocity indicated by the gyro, as illustrated in Fig. 10.4-1. The transfer function $M(s) \triangleq G(s)/H$ represents the assumed linear dynamics of the gyro normalized by the value of H , and $\hat{\omega}_i$ is an estimate of the input angular rate ω_i . The error in $\hat{\omega}_i$ caused by aniso inertia effects can be viewed as resulting from the "error" signal e in Fig. 10.4-1, related to ω_s by

$$\frac{e(s)}{\omega_s(s)} = (I_{ss_g} - I_{ii}) \left[\frac{s^2 + 2\zeta \sqrt{\frac{K_h}{I_{ss_r}}} \left(\frac{I_{ss} - I_{ii}}{I_{ss_g} - I_{ii}} \right) s + \frac{K_h (I_{ss} - I_{ii})}{I_{ss_r} (I_{ss_g} - I_{ii})}}{s^2 + 2\zeta \sqrt{\frac{K_h}{I_{ss_r}}} s + \frac{K_h}{I_{ss_r}}} \right]$$

$\triangleq T_a(s)$ (10.4-3)

where

$$I_{ss_g} \triangleq I_{ss} - I_{ss_r}$$

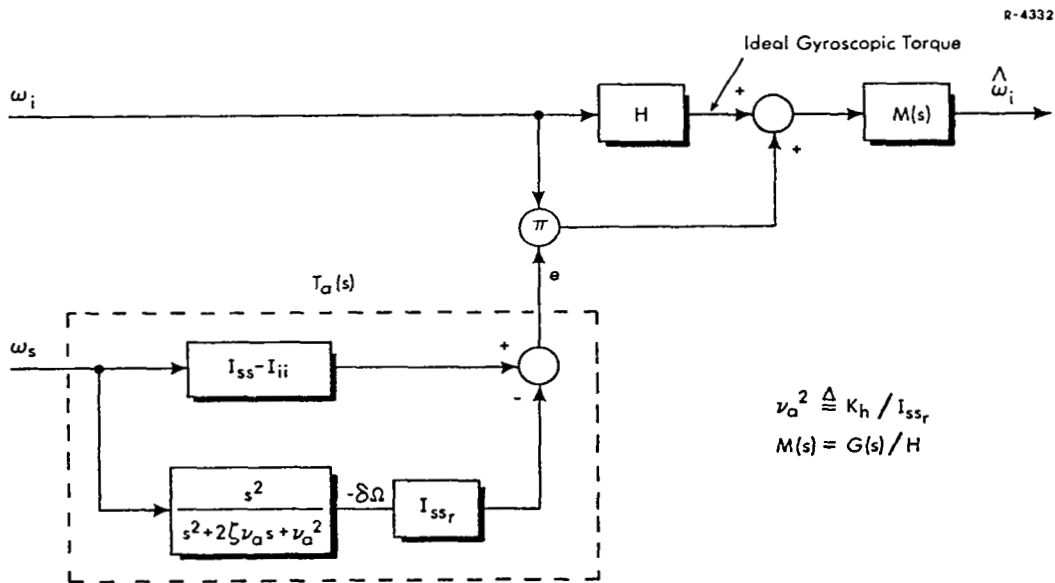


Figure 10.4-1 Block Diagram Illustrating Effect of Anisoinertia Torque on Gyro Output

As we observed in Chapter 2, in some circumstances it is possible to design the gyro so that e is small. In particular, if ω_s varies slowly, then

$$T_a(s) \cong T_a(0) = I_{ss} - I_{ii}$$

Hence the error signal will be small if $I_{ss} \cong I_{ii}$. On the other hand if ω_s varies rapidly,

$$T_a(s) \cong T_a(\infty) = I_{ssg} - I_{ii}$$

and the error will be small if $I_{ssg} \cong I_{ii}$. However, it is clear that the design parameters cannot be selected to make $T_a(s)$ identically zero when ω_s can take on a range of frequencies.* Therefore techniques for compensating anisoinertia errors are needed. In this section, methods which make use of the known relationships between the error torque, ω_s , and ω_i are investigated.

10.4.1 Closed Loop Compensation

It is evident from Fig. 10.4-1 that the effective anisoinertia torque can be estimated if estimates of ω_i and ω_s are available and if $T_a(s)$ is known. In particular,

$$\begin{array}{l} \text{estimated anisoinertia} \\ \text{error torque} \end{array} = \hat{\omega}_i \hat{e}$$

$$\hat{e}(s) = \tilde{T}_a(s) \hat{\omega}_s(s) \quad (10.4-4)$$

where $\tilde{T}_a(s)$ is a compensation network which has dynamic characteristics that closely approximate $T_a(s)$. If the estimated error torque can be

* For contemporary gyros, this statement is true if ω_s has a bandwidth of more than 2 or 3 Hz.

calculated in this fashion, it can be subtracted from the input to the gyro torquer in Fig. 10.4-1, thereby approximately cancelling the actual error torque. A condition that must hold in order that the gyro outputs be good approximations to the actual angular velocities is that the compensated system must be stable -- i. e., the closed loop poles should be in the left-half complex plane. In general the global stability properties of the system are difficult to determine because of the nonlinear structure of the feedback compensation, shown in Fig. 10.4-2. However some insight can be gained into system behavior if the nonlinearities are linearized about an operating condition that permits local stability properties to be investigated.

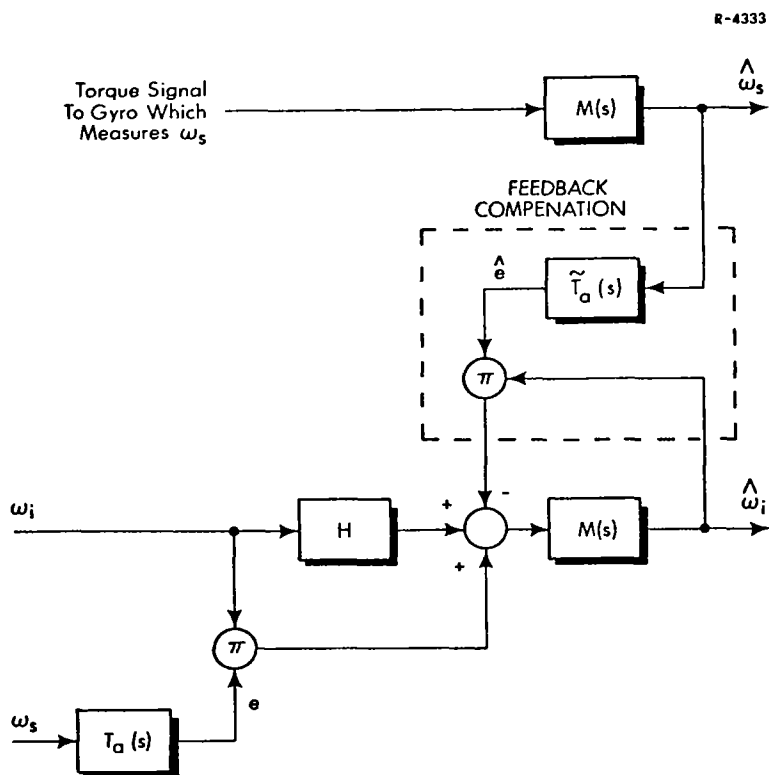


Figure 10.4-2 Mechanization of Closed Loop Anisoinertia Error Compensation Technique for a Single Gyro

A linear analysis of the compensated system is facilitated if the following assumptions are made for each of the three gyros:

- The angular velocities ω_i and ω_s are constant.
- $\hat{\omega}_i = \tilde{\omega}_i + \delta\omega_i$ where $\tilde{\omega}_i$ is the portion of $\hat{\omega}_i$ produced by ω_i and the error torque alone in Fig. 10.4-2.
- $I_{ss} = I_{ii}$
- The three gyros are oriented so that each gyro input axis points in the same direction as the spin axis of one other gyro.

With these conditions imposed, the linearized closed loop dynamics for the propagation of small, time-varying errors in indicated angular rates are given in Fig. 10.4-3. The subscripts x, y, and z denote $\tilde{\omega}_i$ and $\delta\omega_i$ for each of the three gyros. The local stability properties of the system can be inferred by considering the locus of closed loop poles as a function of the net loop gain.

If we neglect the gyro dynamics (that is, $G(s) \cong 1$) then Fig. 10.4-3 reduces to Fig. 10.4-4. If $\tilde{T}_a(s)$ is made identical to $T_a(s)$, the open loop poles in Fig. 10.4-4 are near the imaginary axis with an undamped natural frequency of $\sqrt{K_h/I_{SS_r}}$ and damping ratio ζ . From Eq. (10.4-3) it follows that the total loop gain in Fig. 10.4-4 is

$$\frac{\left(I_{SS_g} - I_{ii}\right)^3 \tilde{\omega}_x \tilde{\omega}_y \tilde{\omega}_z}{H^3}$$

which can have either a positive or negative algebraic sign. Ordinarily the possibility of negative gain together with lightly damped open loop poles would be a troublesome situation from the standpoint of closed loop

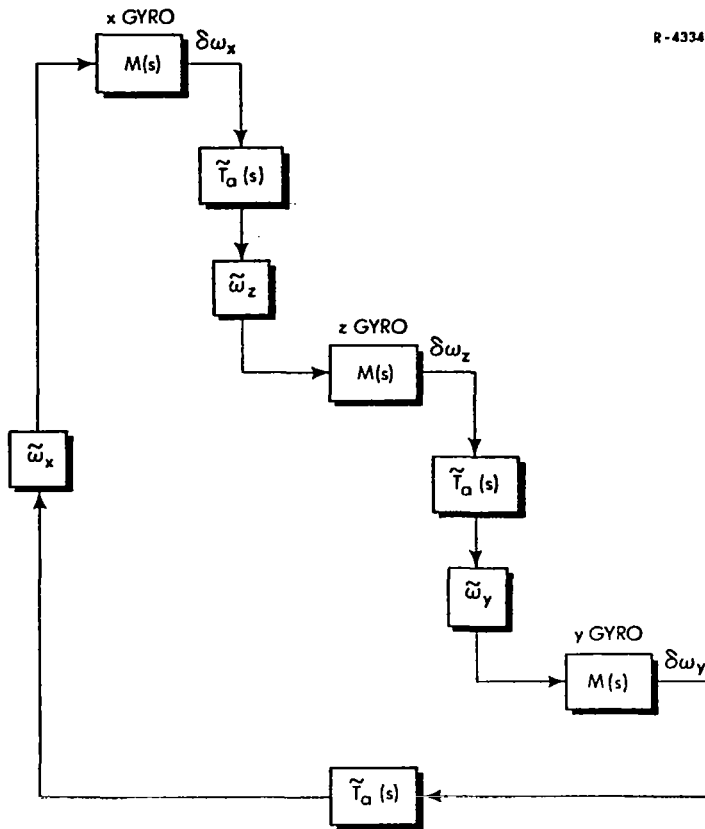


Figure 10.4-3 Linearized Error Flow Diagram When Anisoinertia-Rotor Speed Errors are Reduced by Closed Loop Compensation

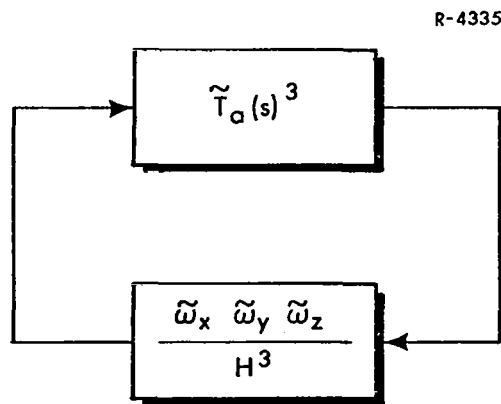


Figure 10.4-4 Simplified Linearized Closed Loop System Associated With Fig. 10.4-3

stability. However, the magnitude of this gain is very small for typical values of input angular velocity, moments of inertia, and gyro angular momentum. Hence, the closed loop poles are generally quite close to the open loop poles. Using representative parameter values -- $\zeta = 0.0025$, $I_{ii} = 600 \text{ gm-cm}^2$, $I_{SS} = 600 \text{ gm-cm}^2$, $H = 4.0 \times 10^5 \text{ gm-cm}^2/\text{sec}$, $K_h = 1.6 \times 10^5 \text{ gm-cm}^2/\text{sec}^2$, $I_{SSr} = 400 \text{ gm-cm}^2$ -- we find that the system remains stable so long as

$$|\tilde{\omega}_x \tilde{\omega}_y \tilde{\omega}_z| < 1000 \text{ (rad/sec)}^3$$

Input angular velocities are not likely to exceed one radian per second in most applications so that the closed loop compensation technique provides adequate stability margin in the linearized system. This conclusion remains unchanged if the gyro design assumptions are altered -- i. e., if $I_{SS} \neq I_{ii}$. It is emphasized that this analysis treats only local stability properties. To verify system stability under actual operating conditions, computer simulation of the closed loop compensation technique should be performed.

If the three gyros are oriented as in Fig. 10.3-4, where two spin axes are parallel, the linearized closed loop stability properties are determined by the closed loop system shown in Fig. 10.4-5. If $\tilde{T}_a(s) = T_a(s)$ in this case, we find by the same argument used for Fig. 10.4-4 that the linearized closed loop system is stable for all realistic input angular velocities.

Having verified that the closed loop compensation technique is at least locally stable, it is desirable to evaluate its ability to reduce the anisoinertia error. To do this consider the set of three compensated gyros illustrated in Fig. 10.4-6, corresponding to the orientation given

in Fig. 10.3-4. To carry out the analysis we shall assume that $T_a(s)$ has the form

$$\tilde{T}_a(s) = \left(I_{ss_g} - I_{ii} \right) \left[\frac{s^2 + 2\tilde{\zeta} \sqrt{\frac{K_h}{I_{ss_r}} \left(\frac{I_{ss} - I_{ii}}{I_{ss_g} - I_{ii}} \right)} s + \frac{K_h (I_{ss} - I_{ii})}{I_{ss_r} (I_{ss_g} - I_{ii})}}{s^2 + 2\tilde{\zeta} \sqrt{\frac{K_h}{I_{ss_r}}} s + \frac{K_h}{I_{ss_r}}} \right] \quad (10.4-5)$$

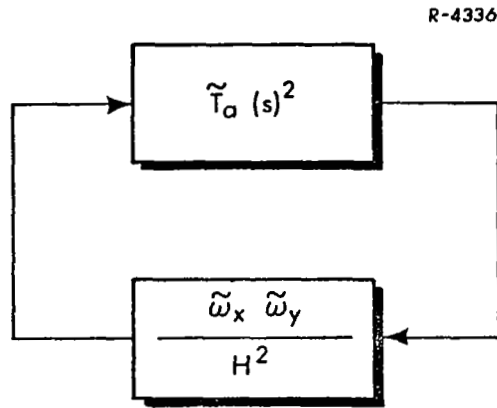


Figure 10.4-5 Simplified Linearized Closed Loop System Associated With Fig. 10.3-4

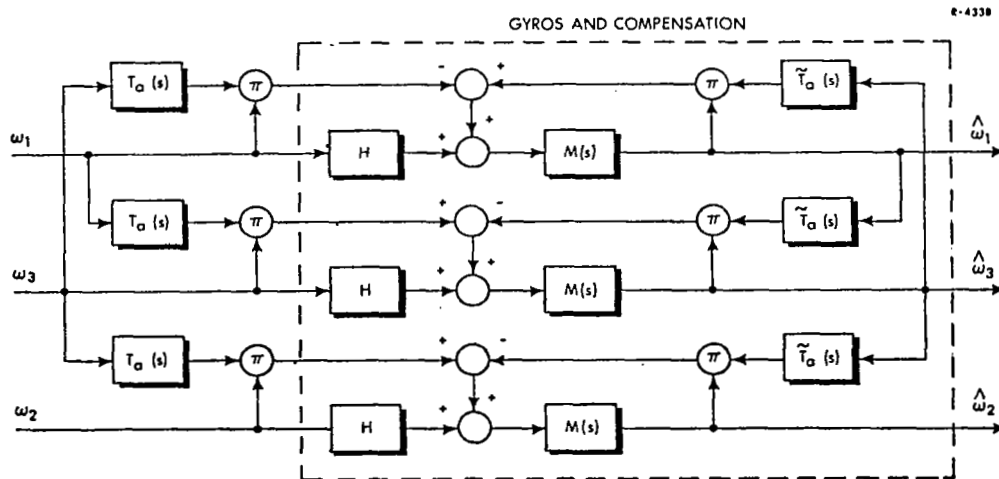


Figure 10.4-6 Closed Loop Compensation for the System Represented by Fig. 10.3-4

This permits the compensation network to have a damping ratio, $\tilde{\zeta}$, which is different from that of the rotor wheel speed control loop in the event that it is necessary to damp induced transient signals or to suppress the effects of noise. In addition, we shall assume that the gyros all have identical dynamic characteristics and the input angular velocities are identical sinusoids,

$$\omega_i = \omega = A \sin \nu t; \quad i = 1, 2, 3 \quad (10.4-6)$$

where ν is a constant frequency. The most harmful errors in the estimates of angular velocity are those which are constant, thereby contributing a monotonically increasing error in knowledge of angular position. Consequently we are interested in determining the average errors in $\hat{\omega}_i$ ($i = 1, 2, 3$) and comparing them with the error, $\Delta\omega_i$, which would exist if no compensation were applied. A measure of this performance is expressed by the ratios

$$\eta_i = \left| \frac{\overline{\hat{\omega}_i - \omega_i}}{\overline{\Delta\omega_i}} \right|; \quad i = 1, 2, 3 \quad (10.4-7)$$

where the overbars denote time averages.

It is clear from Fig. 10.4-6 that the time average gyro errors without compensation are*

$$|\overline{\Delta\omega_i}| \triangleq |\overline{\Delta\omega}| = \frac{A^2}{2H} \left| T_a(j\nu) \cos(\angle T_a(j\nu)) \right|; \quad i = 1, 2, 3 \quad (10.4-8)$$

* The symbol, $\angle T_a(j\nu)$, denotes the phase angle of $T_a(j\nu)$.

Thus the bias errors at the outputs of the uncompensated gyros are identical. With compensation, the largest contributions to the error in angular velocity will be provided by the gyro dynamics (which creates a difference between $\omega_i(s)$ and $\hat{\omega}_i(s)$, for example) and any mismatch between $\tilde{T}_a(s)$ and $T_a(s)$. Therefore, it follows from Fig. 10.4-6 that to first order

$$\left| \overline{\hat{\omega}_i - \omega_i} \right| \cong \frac{A^2}{2H} \left| \left| T_a(j\nu) \right| \cos(\Delta T_a(j\nu)) - \left| G(j\nu) \right|^2 \left| \tilde{T}_a(j\nu) \right| \cos(\Delta \tilde{T}_a(j\nu)) \right|$$

$$i = 1, 2, 3 \quad (10.4-9)$$

Combining Eqs. (10.4-7), (10.4-8), and (10.4-9), we have

$$\eta_i = \eta = \left| 1 - \frac{\left| G(j\nu) \right|^2 \left| \tilde{T}_a(j\nu) \right| \cos(\Delta \tilde{T}_a(j\nu))}{\left| T_a(j\nu) \right| \cos(\Delta T_a(j\nu))} \right| \quad i = 1, 2, 3$$

$$(10.4-10)$$

To examine a representative case, we assume the parameter values

$$I_{ss_g} = I_{ii} = 300 \text{ gm-cm}^2 \quad I_{ss_r} = 300 \text{ gm-cm}^2$$

$$H = 4.63 \times 10^5 \text{ gm-cm}^2/\text{sec} \quad K_h = 1.45 \times 10^5 \text{ gm-cm}^2/\text{sec}^2$$

$$\zeta = 0.0025 \quad A = 0.28 \text{ rad/sec}$$

$$G(s) = \frac{a_1 s + 1}{b_4 s^4 + b_3 s^3 + b_2 s^2 + b_1 s + 1}$$

$$a_1 = 0.143 \quad b_3 = 1.20 \times 10^{-6}$$

$$b_1 = 0.143 \quad b_4 = 1.65 \times 10^{-11}$$

$$b_2 = 6.87 \times 10^{-4} \quad (10.4-11)$$

Substituting the above quantities into Eqs. (10.4-3), (10.4-5), (10.4-8), and (10.4-10), we obtain the curves in Fig. 10.4-7 giving η and $|\overline{\Delta\omega}|$ as functions of the input frequency ν and the compensation network damping ratio, $\tilde{\zeta}$ (note that $|\overline{\Delta\omega}|$ is independent of $\tilde{\zeta}$, and η is independent of the input amplitude).

The parameter values given above are chosen so that

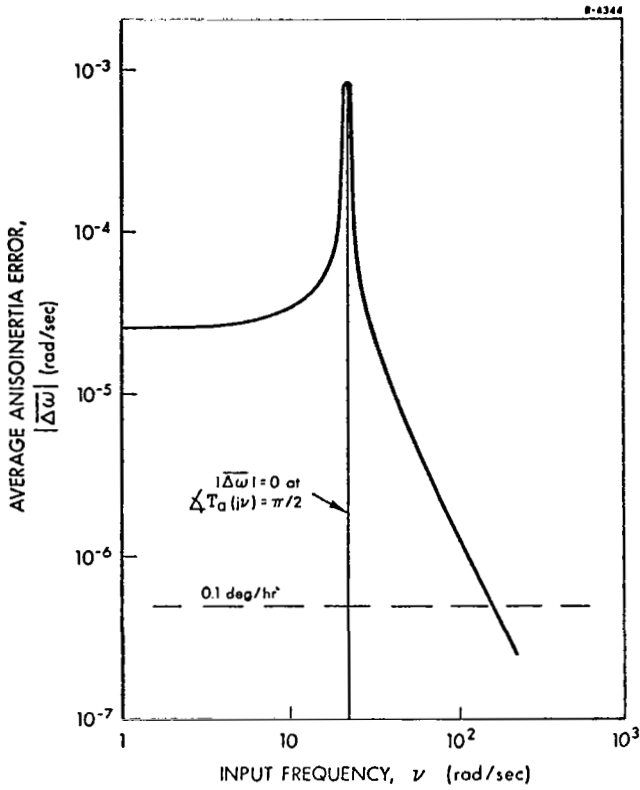
$$I_{ss_g} - I_{ii} = 0$$

Under this condition we see from Eq. (10.4-3) that

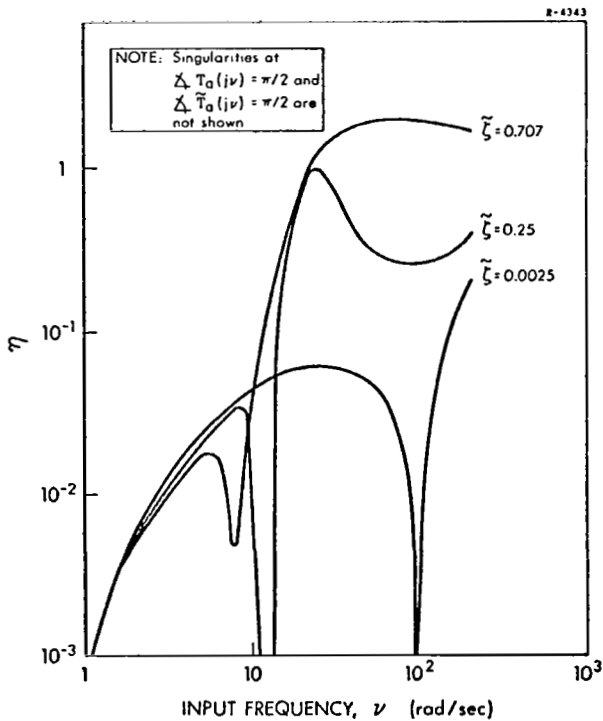
$$\lim_{s \rightarrow \infty} T_a(s) = 0$$

Thus the effectiveness of the compensation network, as reflected by the parameter η , can be permitted to degrade with increasing frequency; this is a convenient condition from the standpoint of mechanization. Observe from Fig. 10.4-7(a) that the compensation technique should reduce the anisoinertia error by one to three orders of magnitude at frequencies below 100 rad/sec in order to achieve an acceptable error level (say 0.1 deg/hr), for the input amplitude given in Eq. (10.4-11). The curves in Fig. 10.4-7(b) indicate that for large compensation damping ratios, insufficient error reduction is achieved at frequencies within the range, $10 \leq \nu \leq 100$ rad/sec. Consequently it is desirable to have the compensation network damping ratio as close as possible to that of the rotor speed regulator.

To obtain further improvement over that achieved with $\tilde{\zeta} = 0.0025$ in Fig. 10.4-7(b), it will be necessary to add compensation to suppress the effect of the gyro dynamics, $G(j\nu)$, in Eq. (10.4-10). This possibility is investigated in more detail in the next section for the case of open loop compensation.



(a) Average anisoinertia error without compensation:
 $A = 0.28 \text{ rad/sec}$



(b) Ratio of average anisoinertia error with compensation to that without compensation

Figure 10.4-7 Performance of Closed Loop Anisoinertia Error Compensation Technique

The above discussion indicates the amount of anisoinertia error reduction likely to be achieved with closed loop compensation. From the standpoint of mechanization, this technique requires that a compensating torque signal be applied at the input of each gyro. In some applications it may be more convenient to apply all compensation at the gyro output, in an open loop configuration. This is investigated in the next section.

10.4.2 Open Loop Compensation

Open loop anisoinertia error compensation of a single gyro is illustrated in Fig. 10.4-8. The concept is similar to that given in Fig. 10.4-2 except that the estimated anisoinertia error torque is converted to an estimated error in angular velocity, $\Delta \hat{\omega}$, which is subtracted from the gyro output. Note that in order to generate the estimated error torque, a transfer function $\tilde{T}_a(s)$ is again employed. Just as in the case of closed loop compensation, we desire $\tilde{T}_a(s)$ to be a good approximation to $T_a(s)$. However, exact equality between the two transfer functions may not be desirable because $T_a(s)$ is very lightly damped. If there is any noise introduced into the system -- e. g., gyro quantization noise -- then the compensation network should be designed to prevent an unacceptable level of noise amplification. In this discussion we shall assume that $T_a(s)$ and $\tilde{T}_a(s)$ are given by Eqs. (10.4-3) and (10.4-5). To gain some insight into the performance of this compensation technique, we consider its application to a navigation system containing three identical gyros oriented as shown in Fig. 10.3-4. This case will also provide a comparison with the closed loop compensation method discussed in the preceding section.

Another property of Fig. 10.4-8 is the use of a transfer function, $\tilde{M}(s)$, in the compensating network that is not necessarily identical to $M(s)$.

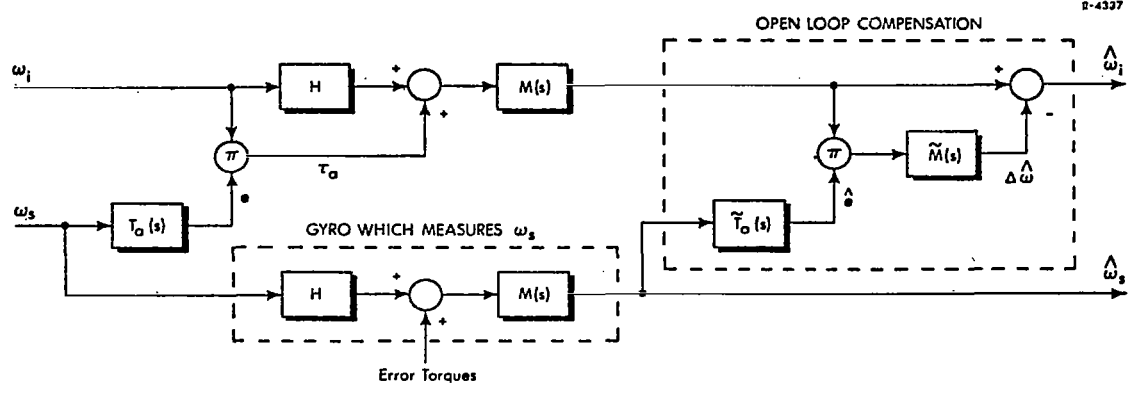


Figure 10.4-8 Mechanization of Open Loop Anisoinertia Error Compensation Technique for a Single Gyro

In particular, it is expedient to choose $\tilde{M}(s) = 1/H$ to keep the compensation dynamics as simple as possible. This provides adequate reduction of constant and low frequency anisoinertia errors and avoids the additional computation associated with the gyro dynamics.

Applying the open loop compensation technique to the system of gyros shown in Fig. 10.3-4, we obtain the configuration shown in Fig. 10.4-9. To evaluate this system we shall assume the same conditions on system operation as in the preceding section -- namely, the gyros have identical transfer functions and input angular velocities, as given by Eq. (10.4-6). The system performance will be measured in terms of the ratio between average angular velocity errors, with and without open loop compensation, given by Eq. (10.4-7).

With the above conventions established, it follows from Fig. 10.4-9 that the calculation for $|\overline{\Delta\omega_i}|$, required in Eq. (10.4-7), is the same as in Eq. (10.4-8). The error in $\hat{\omega}_i$ when compensation is used is obtained in a manner similar to that used in the preceding section. Neglecting terms involving the ratio A^4/H^3 ,

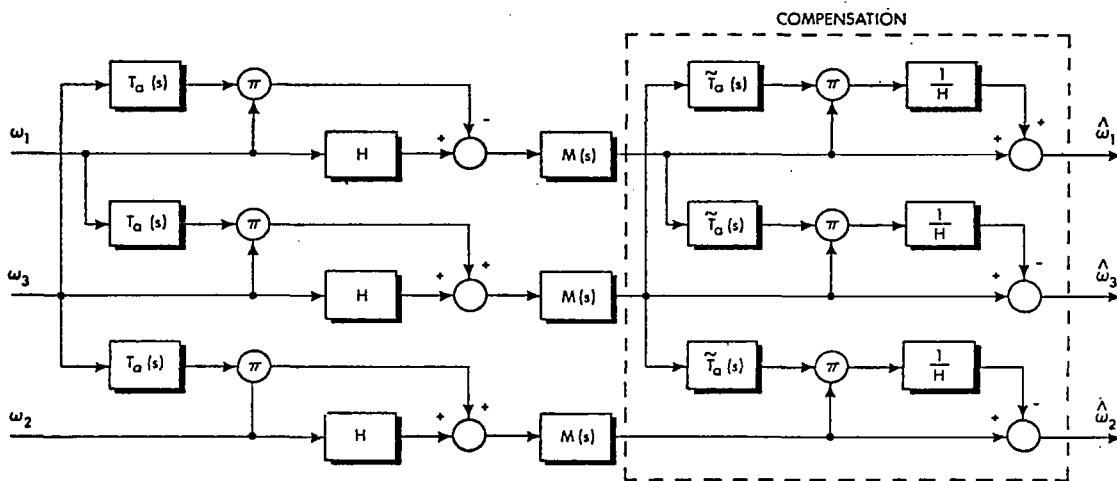


Figure 10.4-9 Open Loop Compensation for System Represented by Fig. 10.3-4

$$|\hat{\omega}_i - \omega_i| \cong \frac{A^2}{2H} \left| |T_a(j\nu)| \cos(\angle T_a(j\nu)) - |G(j\nu)|^2 |\tilde{T}_a(j\nu)| \cos(\angle \tilde{T}_a(j\nu)) \right|;$$

$$i = 1, 2, 3 \quad (10.4-12)$$

Thus Eq. (10.4-12) is the same as Eq. (10.4-9); the ratio η_i ($i = 1, 2, 3$) defined in Eq. (10.4-7) and evaluated for the case of open loop compensation is the same as in Eq. (10.4-10). From the above discussion it is clear that the curves for η in Fig. 10.4-7 also apply for open loop compensation; within the accuracy of the approximations used here, open loop and closed loop compensation provide identical relief from anisoinertia errors. Therefore it is recommended that open loop compensation be employed in order to avoid the question of whether the system using closed loop compensation in Fig. 10.4-6 is globally stable.

We observe from Fig. 10.4-7(b) that when $\tilde{\zeta} = \zeta = 0.0025$, there is a remaining anisoinertia error caused by the fact that gyros are not perfect, i.e., $G(j\nu) \neq 1$, just as there was for closed loop compensation. The magnitude of the gyro transfer function specified in Eq. (10.4-11) is

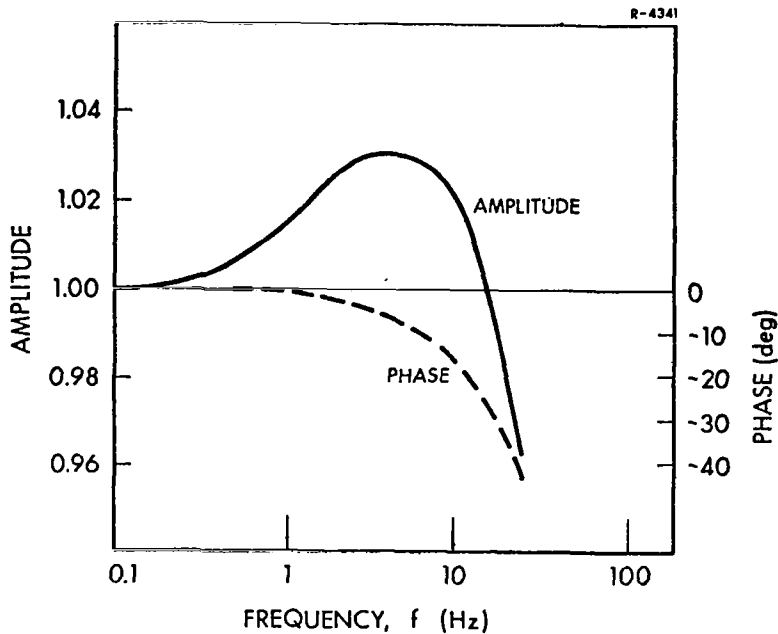


Figure 10.4-10 Amplitude-Phase Characteristics for $G(j2\pi f)$ in Eq. (10.4-11)

plotted in Fig. 10.4-10. Over the frequency range shown the amplitude curve has approximately second-order characteristics; that is

$$G(s) \cong \frac{\nu_g^2}{s^2 + 2\zeta_g \nu_g s + \nu_g^2}$$

where ζ_g and ν_g are chosen to provide a good approximation to the curve in Fig. 10.4-10. If it is necessary to achieve additional reduction in the aniso inertia error, some means of compensating for the gyro distortion must be provided. One method of accomplishing this is to insert compensating networks $G_c(s)$ at the inputs to the compensation network in Fig. 10.4-9, having magnitude characteristics which are approximately the inverse of that shown in Fig. 10.4-10. For example,

$$G_c(s) = \frac{K(s^2 + 2\zeta_g \nu_g s + \nu_g^2)}{(s + \alpha)(s + \beta)}$$

where α and β are chosen outside the frequency range of interest and K provides a d-c gain of unity,

$$\frac{K\nu^2}{\alpha\beta} = 1$$

This choice of gain yields undistorted low frequencies at the expense of amplifying high frequencies in the compensation network. Implementation of such compensation imposes an additional computational burden on the system; it should only be used if the error reduction indicated in Fig. 10.4-7(b) is not adequate. Note that the same modification can be applied to the closed loop compensation technique in Fig. 10.4-6.

Effect of Noise — A conclusion of the earlier analysis is that the open loop anisoinertia compensation can be made to perform better by choosing $\tilde{T}_a(s)$ closer to $T_a(s)$. This observation confirms our expectations in the case where the gyros introduce no extraneous signals into the angular velocity measurement. However, we pointed out earlier that in a practical gyro additional error signals are generally present that may adversely effect compensation accuracy, particularly if $\tilde{T}_a(s)$ is too lightly damped. To model this situation, we shall assume that the gyro-induced errors can be represented as an additive term, $n_i(t)$, at the output of each gyro, as illustrated in Fig. 10.4-11. If we assume that each gyro error is a zero-mean gaussian random process, a convenient measure of its effect on the system output is the mean square value of the corresponding random component added to ω_i by the compensation network. This quantity, denoted by σ_i^2 , represents the strength of the noise added to the angular velocity estimates by the open loop compensation technique. To analyze the effect of gyro noise we shall treat the most pessimistic case; all the signals $n_i(t)$ are identical -- i. e., $n_i(t) = n(t)$ for all i . Consequently $\sigma_i^2 = \sigma^2$ is the same for each gyro output.

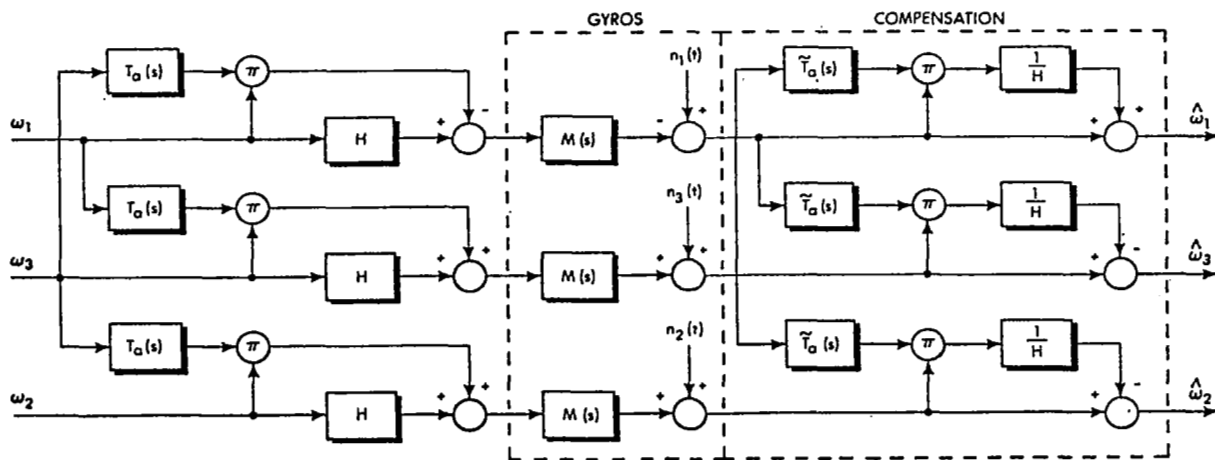


Figure 10.4-11 Open Loop Compensation for System Represented by Fig. 10.3-4, Including Gyro-Induced Errors

If we assume that the spectrum of the noise input is flat having bandwidth B (in units of rad/sec), which is large compared with the bandwidth of $\tilde{T}_a(s)$, and if

$$E\{n(t)^2\} = q \quad (10.4-13)$$

then it can be shown from standard power spectral density analysis techniques that

$$\sigma^2 = \frac{\pi q^2}{H^2 B} \tilde{\zeta} \nu_a (I_{ss} - I_{ii})^2 \left(1 + \frac{1}{4\tilde{\zeta}^2} + \frac{8\pi\tilde{\zeta}\nu_a}{B} \right) \quad (10.4-14)$$

where we have set $I_{ii} = I_{ssg}$ and ν_a is the undamped natural frequency of $T_a(s)$,

$$\nu_a = \sqrt{\frac{K_h}{I_{ssr}}} \quad (10.4-15)$$

A figure of merit for the operation of the compensation network with respect to the noise input is defined by

$$\mu \triangleq \frac{\sigma}{q} = \frac{(I_{ss} - I_{ii})}{H} \sqrt{\left(\frac{\pi \tilde{\zeta} \nu_a}{B}\right) \left(1 + \frac{1}{4\tilde{\zeta}^2} + \frac{8\pi \tilde{\zeta} \nu_a}{B}\right)} \quad (10.4-16)$$

which represents the fractional increase in the rms measurement noise in $\hat{\omega}_i$ ($i = 1, 2, 3$) due to the compensation network. For any application of interest, one can plot μ as a function of $\tilde{\zeta}$. Note that as the latter approaches zero, μ approaches infinity as expected. However, for the representative parameter values we have been using in this investigation, (Eq. (10.4-11)), if we set $\tilde{\zeta} = \zeta = 0.0025$ and assume a conservatively narrow noise bandwidth of 10 Hz, it follows from Eq. (10.4-16) that $\mu \cong 0.01$. Since there is no motivation to choose $\tilde{\zeta} < \zeta$, we conclude that the anisoinertia compensation does not introduce appreciable noise amplification in most situations of interest. Consequently for the application considered here, we can safely set $\tilde{T}_a(s) = T_a(s)$, thereby achieving the reduction in average anisoinertia error predicted by the curve in Fig. 10.4-7(b) corresponding to $\tilde{\zeta} = \zeta = 0.0025$.

Simulation Results — To obtain verification of the performance characteristics given in Fig. 10.4-7(b), a computer simulation of the system in Fig. 10.4-11 was performed including a detailed model of the single-degree-of-freedom gyro dynamics and nonlinear torquing loop. The gyros use a time-modulation pulse-rebalance torquing method; most of the model parameters were taken from the specifications for the Hamilton Standard RI 1170 gyro. Moments of inertia and input frequency and amplitude were specified as in Eq. (10.4-11). Because the gyro output is digital, the compensation network $\tilde{T}_a(s)$ was implemented as a digital filter. The latter was constructed assuming $\tilde{\zeta} = \zeta$ and neglecting the zero in the numerator of Eq. (10.4-5). Three different input frequencies in the low, resonant, and high frequency regions of the compensation network

were applied; $\nu = 6.13, 21.2,$ and 49.0 rad/sec. The system output, $\hat{\omega}_1$, was averaged over 4, 10, and 20 periods of the input frequency respectively and the resulting values of η are given in Fig. 10.4-12; the theoretical curve for $\tilde{\zeta} = 0.0025$ from Fig. 10.4-7(b) is shown for comparison.

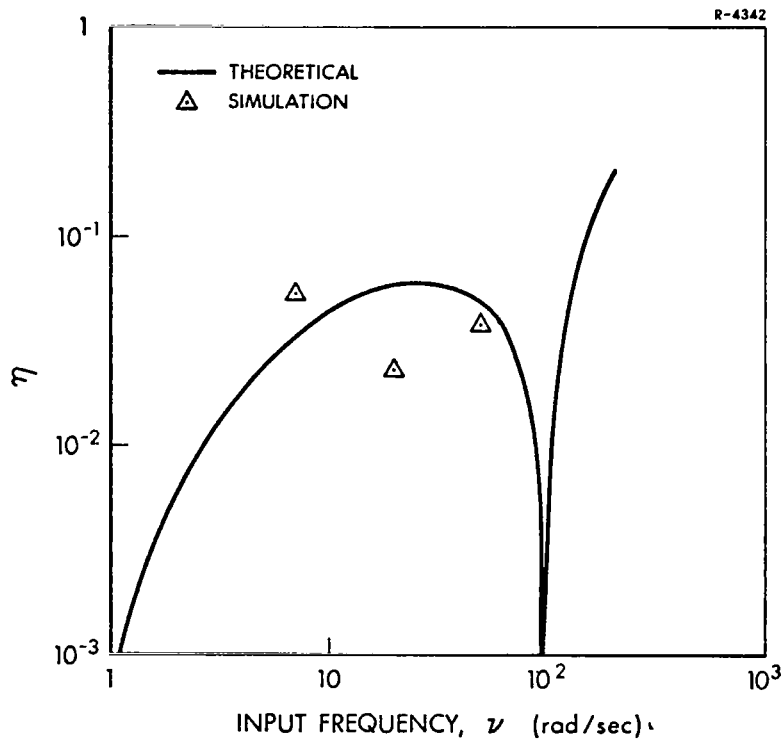


Figure 10.4-12 Evaluation of Open Loop Anisoinertia Compensation by Computer Simulation

The differences between the simulation results and the theoretical curve arise from a combination of causes. First, the gyro dynamics acting on the input angular velocity cause a transient signal in the output of the lightly damped compensation network $\tilde{T}_a(s)$ which is not identical to the transient signal from the rotor wheel speed regulator. Consequently, $\hat{\omega}_1$ contains a transient error signal. Secondly, the time interval over which $\hat{\omega}_1$ is averaged is not equal to a multiple of the transient signal period, and the interval is too short to "average out"

the transient signal. However, the simulation results verify that reduction of anisoinertia errors is possible using open loop compensation and that the amount of reduction can be predicted analytically. Also, as we have pointed out, additional improvement can be obtained by accounting for the effects of gyro dynamics.

10.5 SUMMARY

Several concepts of open loop and closed loop compensation of dynamic errors in single-degree-of-freedom strapdown gyros have been presented. It was shown through simulation that crosscoupling errors can be substantially reduced in a set of three orthogonal gyros employing closed loop compensation. Analyses were also performed which indicate that output axis angular acceleration errors can be reduced in a set of three orthogonally mounted gyros, using either open loop or closed loop compensation. In the latter work, a simplified mathematical model of a strapdown gyro was employed to make the analysis tractable and errors introduced by differentiation were ignored. Both compensation techniques were found to be effective over a useful frequency range, up to about 110 Hz, when representative gyro parameters were used. Finally, it was demonstrated that both closed and open loop compensation can be employed to reduce anisoinertia errors. The question of system stability cannot be answered with full satisfaction for the closed loop anisoinertia compensation; because of nonlinearities only conditions for local stability have been obtained. Since the error reductions achieved with closed and open loop techniques are the same to first order, it is recommended that the latter be used to avoid the possibility of unstable operation. The performance prediction for open loop compensation was verified by computer simulation.

PART IV: SUMMARY

11.1 SUMMARY

The research reported in this document has as its goal investigation of motion-induced errors in strapdown inertial navigation systems and the development of techniques for reducing those errors to an acceptable level. Initially, detailed error models for single-degree-of-freedom gyros and accelerometers were developed. The motion-induced errors in these two sensors were discussed in some detail, particularly with regard to their source within the instrument and the motions that produce them. The progression of sensor-level errors into system-level drift rates and acceleration errors was discussed and the means by which seemingly innocuous gyro and accelerometer errors are translated into serious system errors were illustrated.

The potential harm caused by interactions between strapdown sensors and the rigorous motion environment to which they are subjected was demonstrated at two levels of complexity. Simple calculations involving a set of representative strapdown single-degree-of-freedom gyros and a control system limit cycle indicated several sources of motion-induced drift rates in excess of 1 deg/hr. Also, using a complex computer program developed during the series of investigations this document summarizes, motion-induced strapdown system errors were calculated for a measured helicopter environment. In the latter case the vibration environment was described by a set of 36 spectral density functions measured during flight. It was shown that the particular strapdown inertial system analyzed will generate system-level drift rates of magnitude in excess of 0.1 deg/hr -- considerably worse than current platform systems. Using

the helicopter vibration data and the same set of inertial sensors, the computer program was employed to compare strapdown system accuracy with the gyros in the torque balanced and single-axis-platform (SAP) modes. The results showed that two major sources of system drift rate are eliminated when the gyro is used in the SAP mode. However, the net drift rate still exceeds 0.1 deg/hr about two system axes.

One of the goals of the research reported here was the development of techniques for analytically predicting strapdown system errors, so that the impact of changing various sensor parameters can be evaluated without having to build and test actual instruments. One significant obstacle to such analyses existed at the start of this work. Most strapdown gyros and accelerometers employ nonlinear pulse torquing techniques, and their closed loop behavior cannot be treated with the wide range of analytic tools developed for linear systems. Describing function techniques were employed to provide approximate methods for analyzing the behavior of strapdown inertial sensors and systems. Furthermore, the results predicted by analysis were compared with detailed simulations of the sensors and close agreement was observed in almost all cases. As indicated by the describing function treatment, ternary-rebalanced instruments exhibit a nonlinear behavior while the binary and time-modulation torqued instruments can, with appropriate calculations, be viewed as linear loops over a wide range of inputs. Responses to both sinusoidal and random inputs were investigated.

When the way was clear to analyze the effects of instrument parameters on system-level errors, several simple examples of parameter optimization were worked. The results indicate that if a rather free choice of gyro parameters is available sizeable reductions in system-level errors can be achieved by proper parameter selection.

Unfortunately several of the changes suggested to optimize the gyros studied would prove impractical if carried out to the extent indicated by analysis. When broad practical limitations were placed on the range of parameters available it was found that the error reduction achieved may be unsatisfactory; the major motion-induced errors in strapdown systems using single-degree-of-freedom gyros and accelerometers result from characteristics of these instruments which are basic to their operation.

Since parameter optimization, per se, was found to be a doubtful way to achieve good strapdown system accuracy another technique, active compensation, was explored. Using measurements of the motion environment and having accurate knowledge regarding the major causes of sensor and system errors, the error torques on the instruments can be computed and the errors can be removed from the system at one of several places. Active compensation of three major sources of motion-induced system drift rate -- anisoinertia, gyro crosscoupling and pseudo-coning -- were examined. Both feedback and feedforward compensation were discussed and it was determined that outputs from the basic gyro triad can be used to reduce motion-induced errors by at least an order of magnitude. This technique, together with careful selection of gyro parameters can be of major value in bringing strapdown system accuracy to the level of gim-balled systems.

The work summarized in this report has established and verified a number of analytic and computer techniques for strapdown sensor and system design. Their use will enable the guidance engineer to side-step all but the final steps in fabricating and testing a high accuracy strapdown inertial navigation system.

11.2 CONCLUSIONS

This report traces the development of analytic techniques for computing the effect of the strapdown system motion environment and the investigation of several means for reducing the impact of motion-induced errors on system accuracy. The major conclusions of the research are as follows:

- Motion-induced error torques in single-degree-of-freedom (SDF) strapdown gyros and accelerometers can cause errors in strapdown inertial navigation systems which are considerably larger than those in contemporary gimballed navigators.
- Strapdown gyros operating in the Single-Axis-Platform (SAP) mode are less prone to motion-induced error torques. Two factors related to the SAP mode help reduce errors; the gyro is essentially isolated from angular motion about its input axis and it is operated as a null-seeking device, eliminating torquer scale factor errors. However, failure to isolate the gyro from angular motion about its output axis allows a major source of system-level error, pseudo-coning, to remain and the magnitude of system errors when the gyros are in the SAP mode may still be unacceptable.
- Proper selection of single-degree-of-freedom sensor parameters can improve strapdown system accuracy in most cases, but the degree of error reduction may not be satisfactory. This stems from the observation that the major causes of motion-induced error torques in SDF gyros and accelerometers are related to essential parameters of the instruments (e.g., pendulosity, gimbal and rotor inertias, etc.) rather than imperfect construction. Consequently, large reductions in sensor error torques cannot be achieved without changing the underlying mode of operation of the device. Even

moderate parameter changes (i. e., reducing gimbal output axis moment of inertia) may be counterproductive and raise other error sources to serious levels.

- Active compensation, using the outputs of the basic strapdown sensor triads, can be used to reduce the effects of the three major causes of motion-induced gyro errors -- crosscoupling, anisoinertia, and output axis inertia. The errors generated by angular motions up to 100 Hz can in each case be reduced by at least an order of magnitude. Active compensation can take two basic forms -- closed loop or feedback compensation and open loop or feedforward compensation. The former appears to have no distinct advantage over the latter and the stability of the closed loop compensation approach is often difficult to assess.
- Describing functions provide a good technique for performing approximate analyses of the closed loop behavior of pulse-torqued inertial instruments. Response to both sinusoidal and random inputs was investigated and the results of analyses were well borne out by detailed simulations.
- While describing functions proved very useful in analyzing the response of ternary torqued gyros, the process of analysis is somewhat more complex and less rewarding in this case. The ternary gyro response is nonlinear and highly dependent on the magnitude of the input signal. The gyro loop tends to exhibit ambiguous behavior over certain ranges of input frequencies and/or amplitudes.
- It has been demonstrated in the course of this work that the size of motion-induced errors at the system level can be calculated without undue difficulty and that these errors can be related to certain gyro, accelerometer and computer parameters for a given

motion environment. The analytic developments treated in this report enable the designer to select sensors or sensor parameters and compensation to meet the system accuracy requirements without going through an iterative process of fabrication and testing.

Finally, several problems related to the work described herein remain largely untreated. Further work is needed to explore the value of in-loop compensation to improve the response characteristics of strap-down inertial sensors. This is particularly true for ternary gyros, whose high frequency behavior in the absence of compensation is unsatisfactory. When the value of in-loop compensation is established for all three pulse torquing techniques, a clear-cut choice between the different approaches may emerge. Also, the role of different attitude update and navigation algorithms should be investigated further. They have a definite impact on the transmission of gyro errors into the system calculations and the conversion of oscillatory sensor errors into serious system-level errors.

APPENDIX A

MOTION INDUCED ERROR TORQUES FOR THE SINGLE-DEGREE-OF-FREEDOM GYRO AND PENDULOUS ACCELEROMETER

A.1 GYROS

A.1.1 Angular Motion

The single-degree-of-freedom gyro float torques caused by case angular motion are derived herein. We begin by noting that the inertia torques on the float assembly (i.e., gimbal plus rotor) can be found from the expression

$$\underline{M}_f = \left(\frac{d\underline{H}_f}{dt} \right)_I \quad (\text{A.1-1})$$

where \underline{M}_f represents external (non-inertial) torques and the right side of Eq. (A.1-1) is the rate of change in angular momentum of the float, relative to inertial space. Rewriting this equation relative to the gimbal coordinate frame using the law of Coriolis yields

$$\underline{M}_f = \left(\frac{d\underline{H}_f}{dt} \right)_G + \underline{\omega}_{IG} \times \underline{H}_f \quad (\text{A.1-2})$$

where $\underline{\omega}_{IG}$ is the angular velocity of the gimbal with respect to inertial space. At this point we adopt the notation of subscripted square brackets to denote the frame in which vectors are expressed. Thus, writing components of all vectors of Eq. (A.1-2) in the gimbal (G) frame* yields

* Note that the float and gimbal coordinate frames are identical in this discussion. The expression "float" is used to represent the physical system composed of both gimbal and rotor.

$$\left[\underline{M}_f \right]_G = \left[\left(\frac{d\underline{H}_f}{dt} \right)_G \right]_G + \left[\underline{\omega}_{IG} \right]_G \times \left[\underline{H}_f \right]_G \quad (\text{A.1-3})$$

Continuing, note that the angular velocity of the gimbal with respect to inertial space can be written as the vector sum of the angular velocity of the case with respect to inertial space and the angular velocity of the gimbal with respect to the case, viz:

$$\left[\underline{\omega}_{IG} \right]_G = \left[\underline{\omega}_{IC} \right]_G + \left[\underline{\omega}_{CG} \right]_G \quad (\text{A.1-4})$$

Figure A.1-1 illustrates the geometry of rotor, gimbal, and case, including possible misalignment of the rotor relative to the gimbal ($\underline{\beta}$) and the gimbal relative to the case ($\underline{\alpha}$). With the exception of α_o , all other components of $\underline{\alpha}$ and $\underline{\beta}$ are assumed constant. Let the quantities \hat{o} , \hat{s} , and \hat{i} denote unit vectors along the o, s, and i axes, respectively, with the obvious extensions to the primed coordinate systems. The required terms in Eq. (A.1-4) can now be written as:

$$\left[\underline{\omega}_{CG} \right]_G = \dot{\alpha}_o \hat{o}' \quad (\text{A.1-5})$$

and

$$\left[\underline{\omega}_{IC} \right]_G = \left[\underline{\omega}_{IC} \right]_C - \underline{\alpha} \times \left[\underline{\omega}_{IC} \right]_C \quad (\text{A.1-6})$$

where the right hand side of Eq. (A.1-6) is ultimately expressed in the G frame. If we define

$$\left[\underline{\omega}_{IC} \right]_C = \omega_o \hat{o} + \omega_s \hat{s} + \omega_i \hat{i} \quad (\text{A.1-7})$$

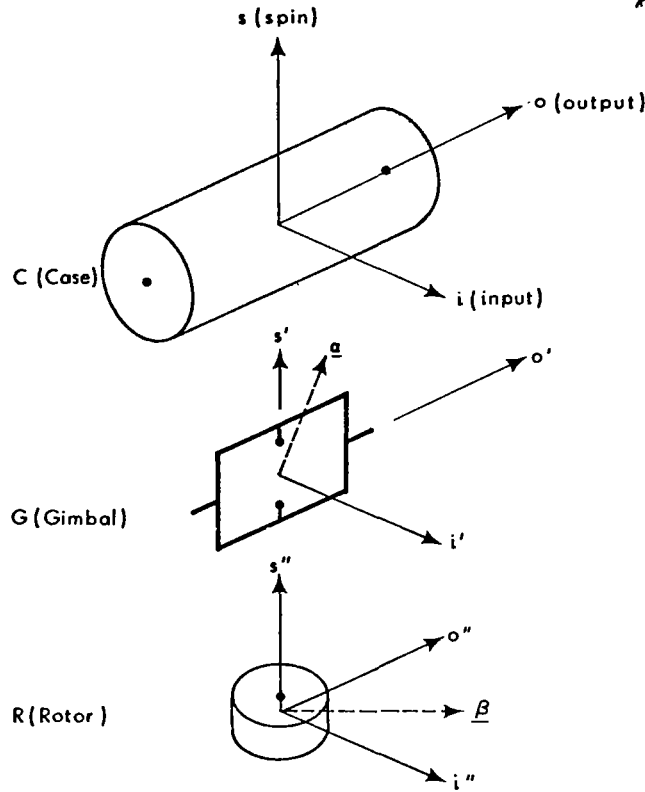


Figure A. 1-1 Exploded View of Single-Degree-of-Freedom Gyro Showing Small Misalignment Angles, $\underline{\alpha}$ and $\underline{\beta}$

then it follows that

$$\begin{aligned}
 \left[\underline{\omega}_{IC} \right]_G &= \omega_o \hat{o}' + \omega_s \hat{s}' + \omega_i \hat{i}' - \begin{vmatrix} \hat{o}' & \hat{s}' & \hat{i}' \\ \alpha_o & \alpha_s & \alpha_i \\ \omega_o & \omega_s & \omega_i \end{vmatrix} \\
 &= (\omega_o - \alpha_s \omega_i + \alpha_i \omega_s) \hat{o}' + (\omega_s + \alpha_o \omega_i - \alpha_i \omega_o) \hat{s}' + (\omega_i - \alpha_o \omega_s + \alpha_s \omega_o) \hat{i}'
 \end{aligned}
 \tag{A.1-8}$$

The angular momentum of the float assembly can be written as the vector dot product of the float moment of inertia tensor (second-order

tensor or dyad) and the angular velocity of the gimbal with respect to inertial space. The float angular momentum (\underline{H}_f) can be written as the vector sum of the gimbal angular momentum (\underline{H}_g) and the rotor angular momentum (\underline{H}_r), viz:

$$\left[\frac{\underline{H}_f}{-f} \right]_G = \left[\frac{\underline{H}_g}{-g} \right]_G + \left[\frac{\underline{H}_r}{-r} \right]_G \quad (\text{A.1-9})$$

Operations with the moment of inertia tensor yield

$$\left[\frac{\underline{H}_g}{-g} \right]_G = \left(\underline{I}_{-o_g} \cdot \left[\frac{\underline{\omega}_{IG}}{-IG} \right]_G \right) \hat{o}' + \left(\underline{I}_{-s_g} \cdot \left[\frac{\underline{\omega}_{IG}}{-IG} \right]_G \right) \hat{s}' + \left(\underline{I}_{-i_g} \cdot \left[\frac{\underline{\omega}_{IG}}{-IG} \right]_G \right) \hat{i}' \quad (\text{A.1-10})$$

where

$$\begin{aligned} \underline{I}_{-o_g} &\triangleq I_{oo_g} \hat{o}' + I_{os_g} \hat{s}' + I_{oi_g} \hat{i}' \\ \underline{I}_{-s_g} &\triangleq I_{os_g} \hat{o}' + I_{ss_g} \hat{s}' + I_{si_g} \hat{i}' \\ \underline{I}_{-i_g} &\triangleq I_{oi_g} \hat{o}' + I_{si_g} \hat{s}' + I_{ii_g} \hat{i}' \end{aligned} \quad (\text{A.1-11})$$

I_{oo_g} , etc., are the gimbal moments of inertia and I_{os_g} , etc., are the gimbal products of inertia. For the rotor we write (where R is the rotor frame)

$$\left[\frac{\underline{H}_r}{-r} \right]_G = \left[\frac{\underline{H}_r}{-r} \right]_R + \underline{\beta} \times \left[\frac{\underline{H}_r}{-r} \right]_R \quad (\text{A.1-12})$$

where, as before, the right hand side of this equation is ultimately resolved in the G frame. Also,

$$\left[\frac{\underline{H}_r}{-r} \right]_R = \left(\underline{I}_{-o_r} \cdot \left[\frac{\underline{\omega}_{IR}}{-IR} \right]_R \right) \hat{o}'' + \left(\underline{I}_{-s_r} \cdot \left[\frac{\underline{\omega}_{IR}}{-IR} \right]_R \right) \hat{s}'' + \left(\underline{I}_{-i_r} \cdot \left[\frac{\underline{\omega}_{IR}}{-IR} \right]_R \right) \hat{i}'' \quad (\text{A.1-13})$$

where, in principal axes, we get:

$$\underline{I}_{O_r} = I_{OO_r} o'' \quad \underline{I}_{S_r} = I_{SS_r} s'' \quad \underline{I}_{i_r} = I_{ii_r} i'' \quad (\text{A.1-14})$$

and

$$\begin{aligned} \left[\underline{\omega}_{IR} \right]_R &= \left[\underline{\omega}_{GR} \right]_R + \left[\underline{\omega}_{IG} \right]_R \\ &= \Omega_s \hat{s}'' + \left[\underline{\omega}_{IG} \right]_G - \underline{\beta} \times \left[\underline{\omega}_{IG} \right]_G \end{aligned} \quad (\text{A.1-15})$$

Ω_s is the rotor speed relative to the gimbal.

At this point it is possible to compute all of the basic expressions of interest. The results are given below, with all calculations valid to first-order in small angles. Terms comprised of products of inertia multiplied by small angles have also been dropped.

$$\left[\underline{\omega}_{IG} \right]_G = (\dot{\alpha}_O + \omega_O - \alpha_S \omega_i + \alpha_i \omega_S) \hat{o}' + (\omega_S + \alpha_O \omega_i - \alpha_i \omega_O) \hat{s}' + (\omega_i - \alpha_O \omega_S + \alpha_S \omega_O) \hat{i}' \quad (\text{A.1-16})$$

$$\begin{aligned} \left[\underline{H}_f \right]_G &= \left[I_{OO} (\dot{\alpha}_O + \omega_O - \alpha_S \omega_i + \alpha_i \omega_S) + I_{OS_g} (\omega_S + \alpha_O \omega_i) + I_{Oig} \omega_i \right. \\ &\quad \left. + I_{OO_r} \beta_i (\omega_S + \alpha_O \omega_i) - I_{SS_r} \beta_i (\Omega_S + \omega_S + \alpha_O \omega_i) \right] \hat{o}' \\ &\quad + \left[I_{SS} (\omega_S + \alpha_O \omega_i - \alpha_i \omega_O) + I_{OS_g} (\dot{\alpha}_O + \omega_O) + I_{Sig} \omega_i \right. \\ &\quad \left. + I_{SS_r} (\Omega_S + \beta_O \omega_i - \beta_i (\omega_O + \dot{\alpha}_O)) + I_{OO_r} \beta_i (\dot{\alpha}_O + \omega_O) - I_{ii_r} \beta_O \omega_i \right] \hat{s}' \\ &\quad + \left[I_{ii} (\omega_i - \alpha_O \omega_S + \alpha_S \omega_O) + I_{Oig} (\dot{\alpha}_O + \omega_O) + I_{Sig} \omega_S \right. \\ &\quad \left. - I_{ii_r} \beta_O \omega_S + I_{SS_r} \beta_O (\Omega_S + \omega_S) \right] \hat{i}' \end{aligned} \quad (\text{A.1-17})$$

where

$$I_{oo} = I_{oo_g} + I_{oo_r} \quad I_{ss} = I_{ss_g} + I_{ss_r} \quad I_{ii} = I_{ii_g} + I_{ii_r} \quad (\text{A.1-18})$$

Recalling Eq. (A.1-3) we get the following expression relating non-inertial torques about the float output axis to the angular motions experienced by (and within) the gyro:

$$\begin{aligned} \left[M_f \right]_{o'} &= I_{oo} (\ddot{\alpha}_o + \dot{\omega}_o) + (I_{ii} - I_{ss}) \omega_s \omega_i - H \omega_i + I_{os_g} \left[\dot{\omega}_s - \omega_o \omega_i \right] \\ &+ I_{oi_g} \left[\dot{\omega}_i + \omega_o \omega_s \right] + I_{si_g} \left[\omega_s^2 - \omega_i^2 \right] + \alpha_o \left[(I_{ss} - I_{ii}) (\omega_s^2 - \omega_i^2) + H \omega_s \right] \\ &+ \alpha_s \left[- (I_{ss} - I_{ii}) \omega_o \omega_s - H \omega_o - I_{oo} \dot{\omega}_i \right] + \alpha_i \left[(I_{ss} - I_{ii}) \omega_o \omega_i + I_{oo} \dot{\omega}_s \right] \\ &+ \beta_o \left[(I_{ss_r} - I_{ii_r}) (\omega_s^2 - \omega_i^2) + H \omega_s \right] + \beta_i \left[(I_{ss_r} - I_{oo_r}) (-\dot{\omega}_s + \omega_o \omega_i) - I_{ss_r} \dot{\Omega}_s \right] \end{aligned} \quad (\text{A.1-19})$$

where we have used the definition

$$H = I_{ss_r} \Omega_s$$

The interpretation of Eq. (A.1-19) can be illustrated by focusing on the term $-H\omega_i$, frequently the only effect considered when the angular motion environment is benign. The equation indicates that in the presence of an input angular rate ω_i a negative torque with magnitude $H\omega_i$ must be applied to the gimbal output axis if the other terms, particularly those describing gimbal-to-case relative motion ($\dot{\alpha}_o$, $\ddot{\alpha}_o$), are zero. If the gyro float is viewed as a torque summation device the inertia reaction error torques constructively applied about its output axis, τ_e , are, from Eq. (A.1-19),

$$\begin{aligned}
\tau_e = & -I_{oo}(\ddot{\alpha}_o + \dot{\omega}_o) + (I_{ss} - I_{ii})\omega_s \omega_i + I_{os_g} (\omega_o \omega_i - \dot{\omega}_s) - I_{oi_g} (\dot{\omega}_i + \omega_o \omega_s) \\
& + I_{si_g} (\omega_i^2 - \omega_s^2) + \alpha_o \left[(I_{ii} - I_{ss}) (\omega_s^2 - \omega_i^2) - H\omega_s \right] \\
& + \alpha_s \left[(I_{ss} - I_{ii}) \omega_o \omega_s + H\omega_o + I_{oo} \dot{\omega}_i \right] + \alpha_i \left[(I_{ii} - I_{ss}) \omega_o \omega_i - I_{oo} \dot{\omega}_s \right] \\
& + \beta_o \left[(I_{ii_r} - I_{ss_r}) (\omega_s^2 - \omega_i^2) - H\omega_s \right] + \beta_i \left[(I_{ss_r} - I_{oo_r}) (\dot{\omega}_s - \omega_o \omega_i) + I_{ss_r} \dot{\omega}_s \right]
\end{aligned} \tag{A.1-20}$$

A.1.2 Linear Motion

Gyro torques produced by linear case accelerations occur in gimbaled as well as strapdown systems. For purposes of discussion, these terms are grouped under the headings of Mass Unbalance and Linear Compliance. To be strictly correct the error torques are described in terms of specific force rather than acceleration.

Mass Unbalance — Mass unbalance torque is caused by a displacement between the output axis and the float center of mass. The component about the output axis can be expressed as

$$\tau_e = m \left([\underline{f}]_G \times \underline{\delta} \right) \cdot \hat{o}' \tag{A.1-21}$$

where m is the mass of the gimbal and rotor combination, $\underline{\delta}$ is the vector of constant displacement between the gimbal-rotor center of mass and the output axis expressed in gimbal coordinates, and $[\underline{f}]_G$ is the specific force

vector, similarly resolved.* Since δ in the gyro is very small the additional terms added by misalignment between the gimbal and case axes are ignored; viz:

$$[\underline{f}]_G \cong [\underline{f}]_C$$

and Eq. (A.1-21) yields

$$\tau_e = m (\delta_i f_s - \delta_s f_i) \quad (\text{A.1-22})$$

There exists another torque which, although not a mass unbalance term, is proportional to the first power of specific force along the output axis. Hence, it is included here. It is attributed to damping fluid thermal convection currents resulting from a temperature gradient and an acceleration field along the output axis. For uniformity with Eq. (A.1-21) this term can be written in the form

$$\begin{array}{l} \text{thermal convection} \\ \text{error torque} \end{array} = m \delta_o f_o \quad (\text{A.1-23})$$

Linear Compliance – Consider the linear compliance matrix

$$[K] = \begin{bmatrix} K_{oo} & K_{os} & K_{oi} \\ K_{so} & K_{ss} & K_{si} \\ K_{io} & K_{is} & K_{ii} \end{bmatrix} \quad (\text{A.1-24})$$

where the first and second subscripts denote the directions of deflection and applied specific force, respectively. The linear compliance

* Specific force is taken here to be the difference between the linear acceleration with respect to inertial space and that acceleration called for by the net gravitational force; symbolically, $\underline{f} = \underline{a} - \underline{G}$.

coefficients account for the net effect of both rotor and gimbal deflection. Terms with the same subscripts are called direct-compliances, while terms with different subscripts are called cross-compliances. It follows from the definition of the compliance matrix that, for slowly varying inputs an additional, acceleration-dependent mass displacement,

$$\underline{\delta} = m [K] \underline{f} \quad (\text{A.1-25})$$

occurs. As in the case of the constant mass unbalance, we compute the linear compliance torque about the float output axis in the form

$$\begin{aligned} \text{linear compliance error torque} &= m \left([\underline{f}]_G \times \underline{\delta} \right) \cdot \hat{o}' \\ &\cong m \left([\underline{f}]_C \times \underline{\delta} \right) \cdot \hat{o}' \\ &= m^2 \left[K_{io} f_o f_s + K_{is} f_s^2 + (K_{ii} - K_{ss}) f_i f_s - K_{so} f_o f_i - K_{si} f_i^2 \right] \end{aligned}$$

(A.1-26)

Observe that each of the terms in Eq. (A.1-26) can produce a non-zero average torque in the presence of linear vibrations of the same frequency.

It is to be noted that, for high frequency vibration inputs, the dynamic counterpart to Eq. (A.1-25) must be employed. In this spring-mass linear compliance system, resonance phenomena are, of course, encountered. Discussion of these phenomena can be found in Ref. 5.

A.2 PENDULOUS ACCELEROMETERS

Errors introduced in the single-degree-of-freedom (SDF) pendulous accelerometer are discussed below. Whenever possible the error torque mechanisms are related to those given for the single-degree-of-freedom gyroscope in Section A.1.

A.2.1 Angular Motion

The SDF pendulous accelerometer is illustrated in Fig. A.2-1. Two major differences between this representation of the instrument and that presented for the SDF gyro are obvious. The direction perpendicular to the output and input directions is called the pendulum (p) axis rather than

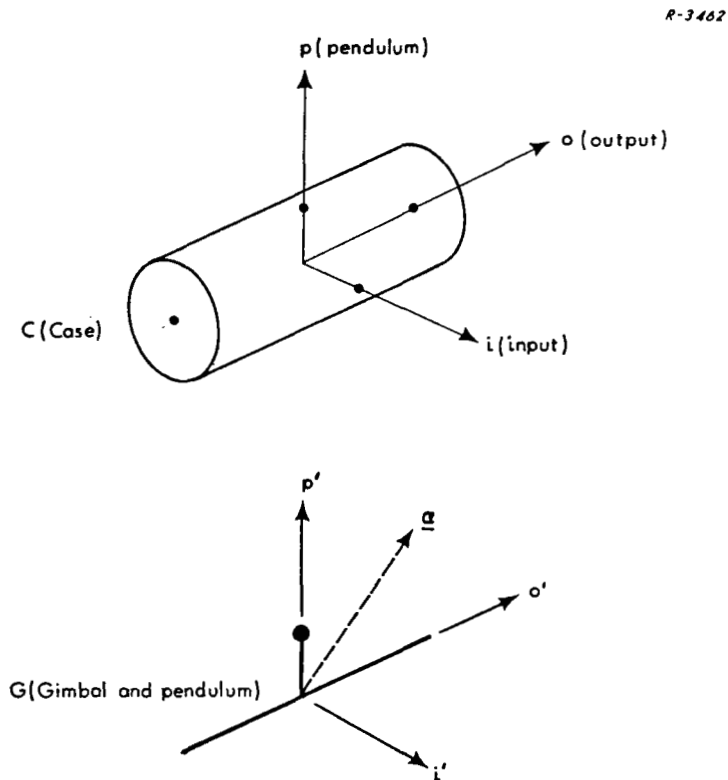


Figure A.2-1 Exploded View of Single-Degree-of-Freedom Pendulous Accelerometer Showing Small Misalignment Angle, α

the spin (s) axis. Also, the instrument is assumed to consist of only two basic parts: a case and a combination gimbal and pendulum. The error torques induced in the SDF pendulous accelerometer by angular motion can be expressed by modifying the equations developed in Section A.1. As a result of the instrument model shown in Fig. A.2-1, all terms in Equation (A.1-20) which involve β_o and β_i are dropped, and the subscript g is deleted because the gimbal and pendulum are considered as a single rigid body. The subscript p is substituted for s in the remaining terms. Also, since there is no spinning wheel involved, all terms involving angular momentum, H, and the spin rate of the rotor relative to the gimbal, Ω_s , are deleted. The resulting expression for output axis torque produced by angular motion is;

$$\begin{aligned}
 \tau_e = & -I_{oo}(\ddot{\alpha}_o + \dot{\omega}_o) + (I_{pp} - I_{ii})\omega_p\omega_i + I_{op}(\omega_o\omega_i - \dot{\omega}_p) \\
 & -I_{oi}(\dot{\omega}_i + \omega_o\omega_p) + I_{pi}(\omega_i^2 - \omega_p^2) + \alpha_o(I_{ii} - I_{pp})(\omega_p^2 - \omega_i^2) \\
 & + \alpha_p \left[(I_{pp} - I_{ii})\omega_o\omega_p + I_{oo}\dot{\omega}_i \right] + \alpha_i \left[(I_{ii} - I_{pp})\omega_o\omega_i - I_{oo}\dot{\omega}_p \right] \quad (A.2-1)
 \end{aligned}$$

Since the ideal accelerometer is insensitive to angular motion, all of the terms in Eq. (A.2-1) must be considered as error torques in the SDF pendulous accelerometer. However, as in the case of the SDF gyro, the first term, $-I_{oo}\ddot{\alpha}_o$, together with any damping torque about the instrument output axis, is usually considered as part of the unavoidable sensor dynamics and included in any "ideal" SDF pendulous accelerometer model.

A.2.2 Linear Motion

Error torques generated by linear motion (acceleration) of the SDF pendulous accelerometer can be established using the error torque expression, Eq. (A.1-21). For the accelerometer a significant mass unbalance is vital to the instrument's operation and misalignments between the gimbal and case cannot be ignored when describing the specific force in gimbal axes:

$$[\underline{f}]_G = [\underline{f}]_C - \underline{\alpha} \times [\underline{f}]_C \quad (\text{A.2-2})$$

Substituting Eq. (A.2-2) into Eq. (A.1-21), the output axis torque in a pendulous accelerometer is given by

$$\text{output axis torque} = -m\delta_p (f_i + \alpha_o f_p - \alpha_p f_o) + m\delta_i (f_p + \alpha_i f_o - \alpha_o f_i) \quad (\text{A.2-3})$$

The effect of linear compliance on accelerometer errors can be illustrated by describing the center of mass displacement as a function of specific force:

$$\begin{aligned} \delta_p &= m (K_{pi} f_i + K_{po} f_o + K_{pp} f_p) + \delta'_p \\ \delta_i &= m (K_{ii} f_i + K_{io} f_o + K_{ip} f_p) + \delta'_i \end{aligned} \quad (\text{A.2-4})$$

Substituting Eq. (A.2-4) into Eq. (A.2-3) and recognizing that the term $m\delta'_p f_i$ is the measurement sought, an error torque equation results:

$$\begin{aligned} \tau_e \cong & m\delta'_p (\alpha_p f_o - \alpha_o f_p) + m\delta'_i (f_p + \alpha_i f_o - \alpha_o f_i) \\ & + m^2 \left[K_{ip} f_p^2 + K_{io} f_o f_p + (K_{ii} - K_{pp}) f_i f_p - K_{po} f_i f_o - K_{pi} f_i^2 \right] \end{aligned}$$

APPENDIX B

DETAILED CALCULATIONS OF
VIBRATION-INDUCED STRAPDOWN SYSTEM ERRORS

A first step in devising means for correcting vibration-sensitive errors in strapdown systems is identification of the error sources that will predominate in a particular environment. A convenient approach is to derive error expressions that are functions of the linear and angular vibrations experienced by the navigator and determine average error values from the spectral characteristics of this motion. The development of this type of error analysis is presented in this appendix, along with a description of a computer program which calculates error values from the spectral data.

B.1 ERROR PROPAGATION EQUATIONS

General equations for the propagation of errors in a strapdown navigation system are

$$\delta \ddot{\underline{r}}_i = \delta \left[\underline{C}_i^s \underline{a}_s \right] - \delta \underline{G} \quad (\text{B.1-1})$$

$$\delta \dot{\underline{C}}_i^s = \delta \left[\underline{C}_i^s \underline{\Omega}_s \right] \quad (\text{B.1-2})$$

where

i = inertial reference coordinate frame

s = system coordinate frame

C_i^s = transformation matrix: s frame to i frame

\underline{r}_i = inertial position of the navigator

\underline{G} = specific force due to gravity

\underline{a}_s = total navigator acceleration resolved in system coordinates

$\underline{\omega}_s$ = total navigator angular rate resolved in system coordinates

Ω_s = skew-symmetric matrix composed from navigator total angular rate components about system axes.

$\delta\underline{G}$, etc. = error in \underline{G} , etc.

If the vibrational and nominal motions of the navigator are considered separately, it is possible to isolate the vibration-induced error contributions in these expressions.

$$\underline{a}_s = \underline{a}_{\text{nominal}} + C_s^b \underline{a}_b \quad (\text{B.1-3})$$

$$\Omega_s \cong \Omega_{\text{nominal}} + C_s^b \Omega_b C_b^s \quad (\text{B.1-4})$$

where

b = body coordinate frame, defining actual orientation of the navigator

s = system coordinate frame, defining nominal orientation of the navigator

\underline{a}_b = linear vibration vector, resolved in body coordinates

$\underline{\omega}_b$ = angular rate vibration vector resolved in body coordinates

Ω_b = skew-symmetric matrix composed from navigator angular rate vibration components about body axes

C_s^b = transformation matrix from actual body frame to nominal body frame -- a function of the rotational vibrations

Assuming the nominal motions are perfectly sensed and substituting these definitions into Eqs. (B.1-1) and (B.1-2) yields

$$\delta \ddot{\underline{r}}_i = \delta C_i^s \underline{a}_s - \delta \underline{G} + C_i^s \left[\delta \left(C_s^b \underline{a}_b \right) \right] \quad (\text{B.1-5})$$

$$\delta \dot{C}_i^s = \delta C_i^s \Omega_s + C_i^s \left[\delta \left(C_s^b \Omega_b C_b^s \right) \right] \quad (\text{B.1-6})$$

The bracketed expressions in these equations contain those errors induced by the vibration environment. In perturbing these expressions, it is necessary to distinguish between the true vibrations experienced by the system, and those indicated by the navigation computer. Accordingly, the convention has been adopted that error quantities are defined as the difference between true and indicated ($\hat{\quad}$) quantities.

$$\delta \left[C_s^b \underline{a}_b \right] \triangleq \hat{C}_s^b \hat{\underline{a}}_b - C_s^b \underline{a}_b \quad (\text{B.1-7})$$

$$\delta \left[C_s^b \Omega_b C_b^s \right] \triangleq \hat{C}_s^b \hat{\Omega}_b \hat{C}_b^s - C_s^b \Omega_b C_b^s \quad (\text{B.1-8})$$

$$\delta C_s^b \triangleq \hat{C}_s^b - C_s^b \quad (\text{B.1-9})$$

$$\delta \underline{a}_b \triangleq \hat{\underline{a}}_b - \underline{a}_b \quad (\text{B.1-10})$$

$$\delta \Omega_b \triangleq \hat{\Omega}_b - \Omega_b \quad (\text{B.1-11})$$

Substituting Eqs. (B.1-9) through (B.1-11) into Eqs. (B.1-7) and (B.1-8) and eliminating the true quantities can yield the following expressions:

$$\delta \left[C_{s-b}^b \right] = \delta C_{s-b}^{b\hat{a}} + \hat{C}_s^b \delta a_{-b} - \delta C_s^b \delta a_{-b} \quad (\text{B.1-12})$$

$$\delta \left[C_s^b \Omega_b C_b^s \right] = \left[\hat{C}_s^b \delta \Omega_b + \delta C_s^b \hat{\Omega}_b - \delta C_s^b \delta \Omega_b \right] \hat{C}_b^s + C_s^b \Omega_b \delta C_b^s \quad (\text{B.1-13})$$

Since the oscillations experienced by the navigator are of low amplitude, the indicated transformation matrix can be approximated as

$$\hat{C}_s^b \cong \begin{bmatrix} 1 & -\hat{\phi}_z & \hat{\phi}_y \\ \hat{\phi}_z & 1 & -\hat{\phi}_x \\ -\hat{\phi}_y & \hat{\phi}_x & 1 \end{bmatrix}$$

$$\cong I + \hat{C}' \quad (\text{B.1-14})$$

where

$$\hat{C}'(t) = \int_0^t \hat{\Omega}_b dt, \text{ a skew-symmetric matrix composed from body angular vibrations}$$

Since a similar set of relations applies for C_s^b , the true value of the transformation matrix,

$$\delta C_s^b = \hat{C}' - C'$$

$$\cong \delta C' \quad (\text{B.1-15})$$

Also, because of the skew-symmetric nature of C_s^b and C_b^s :

$$\begin{aligned}\hat{C}_b^s &= -\hat{C}_s^b \\ \delta C_b^s &= -\delta C_s^b\end{aligned}\tag{B.1-16}$$

When Eqs. (B.1-14), (B.1-15) and (B.1-16) are substituted into Eqs. (B.1-12) and (B.1-13), and terms which cannot rectify (products of three matrices) are eliminated, the following expressions result:

$$\delta \left[C_{s-b}^b a_b \right] = \delta \underline{a}_b + \hat{C}' \delta \underline{a}_b + \delta C' \hat{a}_b - \delta C' \delta \underline{a}_b\tag{B.1-17}$$

$$\delta \left[C_s^b \Omega_b C_b^s \right] = \delta \Omega_b + \delta C' \Omega_b - \hat{\Omega}_b \delta C' - \hat{C}' \delta \Omega_b - \delta \Omega_b \hat{C}' - \delta C' \Omega_b + \delta \Omega_b \delta C'\tag{B.1-18}$$

When only those oscillatory errors which rectify at the system level are considered Eq. (B.1-18) simplifies to

$$\delta \left[C_s^b \Omega_b C_b^s \right] = \delta \Omega_b + 2 \left[\hat{C}' \delta \Omega_b + \delta C' \hat{\Omega}_b + \delta \Omega_b \delta C' \right]\tag{B.1-19}$$

The complete set of navigation error equations are then obtained by substituting Eqs. (B.1-17) and (B.1-19) into Eqs. (B.1-5) and (B.1-6):

$$\delta \ddot{\underline{r}}_i = \delta C_i^s \underline{a}_s - \delta \underline{G} + C_i^s \left[\delta \underline{a}_b + \hat{C}' \delta \underline{a}_b + \delta C' \hat{a}_b - \delta C' \delta \underline{a}_b \right]\tag{B.1-20}$$

$$\delta \dot{C}_i^s = \delta C_i^s \Omega_s + C_i^s \left[\delta \Omega_b + 2(\hat{C}' \delta \Omega_b + \delta C' \Omega_b - \delta C' \delta \Omega_b) \right]\tag{B.1-21}$$

The computer program is designed to calculate average values for a variety of instrument-level and system-level error sources over an ensemble of vibration time histories. All of these error sources can be described in terms of the bracketed expressions in Eqs. (B.1-20) and (B.1-21). The ensemble average error values can then be treated as constants in a separate error analysis to determine the effect of vibrations on navigation accuracy.

A vibration which is rectified in the gyros or accelerometers -- because of a mismatch of moments of inertia, for example -- is represented by the first term within the brackets of Eqs. (B.1-20) and (B.1-21) respectively. Vibrations may also excite purely oscillatory errors in the instruments which are combined in the system attitude or navigation calculations with correctly measured vibrations to produce a rectified error. These system level errors are described by the remaining bracketed terms. The matrices \hat{C}' and $\delta C'$ represent the actual and erroneously indicated oscillations appearing in the transformation matrix. The terms involving these parameters in Eq. (B.1-20) are known as sculling errors and the corresponding terms in Eq. (B.1-21) are identified as coning errors.

B.2 VIBRATION SPECTRAL DATA

Many serious vibration-induced errors in strapdown systems, whether they rectify within the instruments or in the system attitude and navigation calculations, are functions of products of accelerations and angular velocities. A typical error can be represented as the function $\rho(t)$ given by

$$\rho(t) = K \omega_{d_x}(t) \omega_{d_y}(t) \quad (\text{B.2-1})$$

where

d = orthogonal data coordinate frame in
which the vibrations are defined

$\omega_{d_x}(t)$ = angular rate vibration about the x data
frame axis

$\omega_{d_y}(t)$ = angular rate vibration about the y data
frame axis

K = a representative error coefficient

The time-average value of the error $\rho(t)$ is proportional to the time-average of the signal product $\omega_{d_x}(t) \omega_{d_y}(t)$. It can be shown (Refs. 18, and 19) that the time-average value of a signal product is equal to the integral of the real component of the appropriate cross spectral density. In this example, the relationship is given by:

$$\lim_{T \rightarrow \infty} \frac{1}{2T} \int_{-T}^T \rho(t) dt = K \left\{ \lim_{T \rightarrow \infty} \frac{1}{2T} \int_{-T}^T \omega_{d_x}(t) \omega_{d_y}(t) dt \right\}$$
$$\triangleq K \int_0^{\infty} d\nu \Phi_R(\nu, \omega_{d_x}, \omega_{d_y}) \quad (\text{B.2-2})$$

The R subscript in Eq. (B.2-2) denotes the real component of the complex number:

$$\Phi(\nu, \omega_{d_x}, \omega_{d_y}) \triangleq \Phi_R(\nu, \omega_{d_x}, \omega_{d_y}) + j \Phi_I(\nu, \omega_{d_x}, \omega_{d_y}) \quad (\text{B.2-3})$$

where

$$\Phi\left(\nu, \omega_{d_x}, \omega_{d_y}\right) = \text{the cross spectral density of } \omega_{d_x}(t) \text{ and } \omega_{d_y}(t)$$

and the real and imaginary components are defined as:

$$\Phi_R\left(\nu, \omega_{d_x}, \omega_{d_y}\right) = \text{the co-spectral density of } \omega_{d_x}(t) \text{ and } \omega_{d_y}(t)$$

$$\Phi_I\left(\nu, \omega_{d_x}, \omega_{d_y}\right) = \text{the quadrature spectral density of } \omega_{d_x}(t) \text{ and } \omega_{d_y}(t)$$

The co-spectral density defines the frequency content of the in-phase components of $\omega_{d_x}(t)$ and $\omega_{d_y}(t)$ which appear in the signal product. The frequency content of the product of the out-of-phase components, for which $\omega_{d_y}(t)$ is assumed to lead $\omega_{d_x}(t)$ by $\pi/2$ radians, is defined by the quadrature spectral density. The time-average values of many of the errors considered in this analysis are functions of quadrature spectral densities. In this example, $\Phi_I(\nu, \omega_{d_x}, \omega_{d_y})$ would appear in Eq. (B.2-2) if K were frequency dependent (if K had real and imaginary components).

The shorthand notation shown in Eq. (B.2-4) is adopted:

$$\Phi_{xy}(\nu) \triangleq \Phi\left(\nu, \omega_{d_x}, \omega_{d_y}\right) \quad (\text{B.2-4})$$

Also, a superscript bar, such as in $\bar{\rho}(t)$ for example, will be used to denote the average value of a function.

Many of the errors defined in the computer program are similar to $\rho(t)$ in that they involve products of angular velocity components. Other

errors are defined in terms of products of acceleration components or products of acceleration and angular velocity. Expressions similar to Eq. (B.2-2) are derived to determine the average values of these errors in terms of frequency spectra. The following relationships are useful in determining the spectral data necessary for generating error values in the computer program. The cross spectral density of $\omega_{d_x}(t)$ and $\omega_{d_y}(t)$ is given by:

$$\Phi_{xy}(\nu) \triangleq \Phi_{xy_R}(\nu) + j\Phi_{xy_I}(\nu) \quad (\text{B.2-5})$$

The complex conjugate of $\Phi_{xy}(\nu)$ is the cross spectral density of $\omega_{d_y}(t)$ and $\omega_{d_x}(t)$.

$$\Phi_{yx}(\nu) = \Phi_{xy}^*(\nu) = \Phi_{xy_R}(\nu) - j\Phi_{xy_I}(\nu) \quad (\text{B.2-6})$$

The order of the arguments is important in defining the spectral densities.

If all the possible cross-products of acceleration components, angular velocity components and products of acceleration and angular velocity are considered, 36 frequency spectra, including all the co-spectral and quadrature spectral densities, are necessary to completely describe the vibration environment in three dimensions. These spectra are defined in Eqs. (B.2-7), (B.2-8) and (B.2-9) in terms of representative error sources, which are proportional to products of angular velocity components, products of acceleration components and products of angular velocity and acceleration components respectively. The symbols Φ , Ψ and Γ represent the spectral or cross-spectral densities which describe the vibration environment associated with these three classes of error sources and K_1 , K_2 and K_3 represent frequency-dependent error coefficients common to each class.

$$\overline{K_1 \omega_d \omega_d^T} = \int_0^\infty d\nu \left\{ K_{1R}(\nu) \begin{bmatrix} \Phi_{xx}(\nu) & \Phi_{xy_R}(\nu) & \Phi_{xz_R}(\nu) \\ \Phi_{xy_R}(\nu) & \Phi_{yy}(\nu) & \Phi_{yz}(\nu) \\ \Phi_{xz_R}(\nu) & \Phi_{yz_R}(\nu) & \Phi_{zz}(\nu) \end{bmatrix} - K_{1I}(\nu) \begin{bmatrix} 0 & \Phi_{xy_I}(\nu) & \Phi_{xz_I}(\nu) \\ -\Phi_{xy_I}(\nu) & 0 & \Phi_{yz_I}(\nu) \\ -\Phi_{xz_I}(\nu) & -\Phi_{yz_I}(\nu) & 0 \end{bmatrix} \right\} \quad (\text{B.2-7})$$

$$\overline{K_2 a_d a_d^T} = \int_0^\infty d\nu \left\{ K_{2R}(\nu) \begin{bmatrix} \Psi_{xx}(\nu) & \Psi_{xy_R}(\nu) & \Psi_{xz_R}(\nu) \\ \Psi_{xy_R}(\nu) & \Psi_{yy}(\nu) & \Psi_{yz}(\nu) \\ \Psi_{xz_R}(\nu) & \Psi_{yz_R}(\nu) & \Psi_{zz}(\nu) \end{bmatrix} - K_{2I}(\nu) \begin{bmatrix} 0 & \Psi_{xy_I}(\nu) & \Psi_{xz_I}(\nu) \\ -\Psi_{xy_I}(\nu) & 0 & \Psi_{yz_I}(\nu) \\ -\Psi_{xz_I}(\nu) & -\Psi_{yz_I}(\nu) & 0 \end{bmatrix} \right\} \quad (\text{B.2-8})$$

$$\overline{K_3 a_d \omega_d^T} = \int_0^\infty d\nu \left\{ K_{3R}(\nu) \begin{bmatrix} \Gamma_{xx_R}(\nu) & \Gamma_{xy_R}(\nu) & \Gamma_{xz_R}(\nu) \\ \Gamma_{yx_R}(\nu) & \Gamma_{yy_R}(\nu) & \Gamma_{yz_R}(\nu) \\ \Gamma_{zx_R}(\nu) & \Gamma_{zy_R}(\nu) & \Gamma_{zz_R}(\nu) \end{bmatrix} - K_{3I}(\nu) \begin{bmatrix} \Gamma_{xx_I}(\nu) & \Gamma_{xy_I}(\nu) & \Gamma_{xz_I}(\nu) \\ \Gamma_{yx_I}(\nu) & \Gamma_{yy_I}(\nu) & \Gamma_{yz_I}(\nu) \\ \Gamma_{zx_I}(\nu) & \Gamma_{zy_I}(\nu) & \Gamma_{zz_I}(\nu) \end{bmatrix} \right\} \quad (\text{B.2-9})$$

For convenience, Eqs. (B.2-7), (B.2-8) and (B.2-9) are cast in terms of $\underline{\omega}_d$ and \underline{a}_d , the angular rate vibration vector and the linear vibration vector expressed in the data coordinate frame. In calculating error values in the computer program, however, it is necessary to transform the spectral densities into each instrument coordinate frame. For example, if the rotational vibrations measured in the data frame are related to the principal axes of the i^{th} gyro through an orthogonal transformation matrix B_{g_i} :

$$\underline{\omega}_i = B_{g_i} \underline{\omega}_d \quad (\text{B.2-10})$$

Errors which depend on angular motion expressed in the axis system of the i^{th} gyro can be computed using the transformation

$$\overline{K_1 \underline{\omega}_i \underline{\omega}_i^T} = B_{g_i} \left\{ \overline{K_1 \underline{\omega}_d \underline{\omega}_d^T} \right\} B_{g_i}^T \quad (\text{B.2-11})$$

Similar transformations can also be applied to express the acceleration data in sensor-fixed coordinate frames.

An example of error sources which are proportional to both real and imaginary components of the vibration spectral densities is the gyro drift which can result from coupling between angular motion about the nominal rotor spin axis and a float angle generated by angular motion about the gyro input axis. For a simple linear rebalance loop, the Laplace transform of the float angle is given by:

$$\alpha_o(s) = \frac{H}{K_{sg} K_{tg}} G(s) \omega_i(s) \quad (\text{B.2-12})$$

where

α_o = gyro output axis float angle $G(s)$ = gyro closed loop gain

H = gyro angular momentum ω_i = angular rate about the input axis

K_{sg} = signal generator gain K_{tg} = torquer gain

It can be shown that the constant vibration-induced drift rate is given by

$$\overline{-\alpha_o(t)\omega_s(t)} = -\frac{H}{K_{sg} K_{tg}} \int_0^{\infty} d\nu \left[G_R(\nu) \Phi_{is_R}(\nu) - G_I(\nu) \Phi_{is_I}(\nu) \right] \quad (\text{B.2-13})$$

The constant drift rate is a member of the class of errors described in Eq. (B.2-7) for which the frequency-dependent error coefficient is given by

$$K_1(\nu) = -\frac{H}{K_{sg} K_{tg}} G(\nu)$$

In this case, the transfer characteristics of the gyro are included in the error expression and, assuming that there is a phase shift (the imaginary

component $G_I(\nu)$ exists), the quadrature spectral density $\Phi_{IS}(\nu)$ contributes to the error value. Other errors considered in this analysis involve the transfer characteristics of the accelerometer and computer, as well as the gyro.

B.3 COMPUTER PROGRAM DESCRIPTION

The flow diagram in Fig. B.3-1 identifies the major elements of the error analysis computer program. A listing of the program, plus a brief description of the subroutines, is available from the authors. The inertial instruments listed on the diagram, the Norden 1139 single-degree-of-freedom gyro and the Kearfott 2401 pendulous accelerometer, were used in the Lunar Excursion Module Abort Sensor Assembly. The more significant sources of vibration-induced error inherent in these devices are listed in Table B.3-1. The program also contains an error model for a vibrating string accelerometer, which is described in Appendix C.

The principal program inputs, the vibration spectra, are defined at 96 points over a range of 0.75 - 2000 Hz, for each of the 36 spectral density functions. It is necessary to perform interpolations and create a few new data points within this range to facilitate the integration of the error expressions. In generating the error values, it is convenient to separate the calculation of instrument-level and system-level errors, as indicated on the flow diagram. The program is designed to calculate error values for any number of gyros, in any orientation relative to the body frame. Therefore, a number of transformations of spectral data, which will be described presently, are necessary in setting up the error expressions in the program. Integrations of the error expressions are performed by means of a 3rd-order (Simpson's Rule) algorithm.

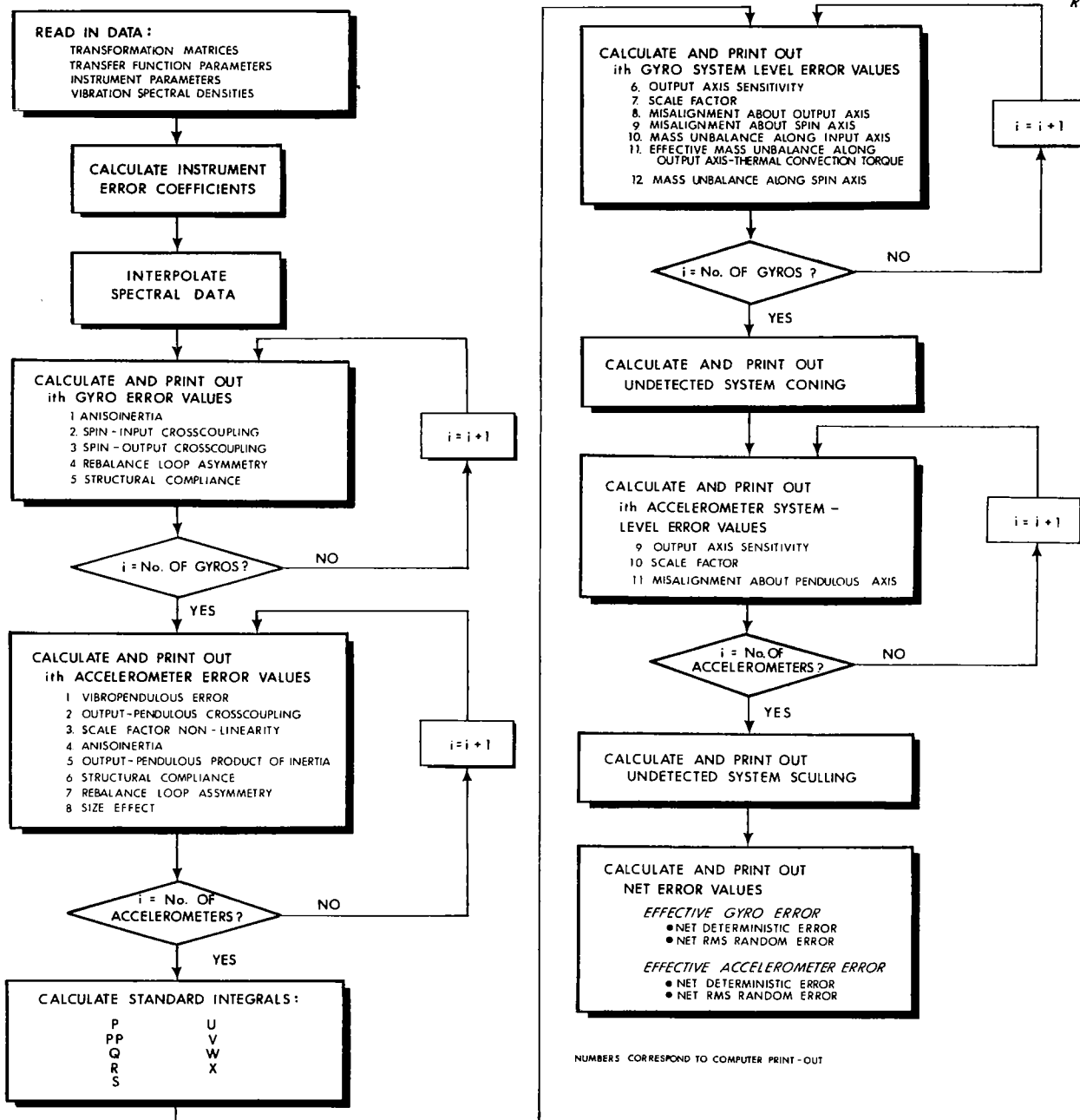


Figure B.3-1 Computer Program Flow Diagram

TABLE B.3-1

MAJOR SOURCES OF VIBRATION-INDUCED ERROR

Norden 1139 Single-Degree-of-Freedom Gyro	Kearfott 2401 Pendulous Accelerometer
<p><u>Instrument-Level Errors</u></p> <ul style="list-style-type: none"> • Anisoinertia • Spin-Input Crosscoupling • Spin-Output Crosscoupling • Rebalance Loop Asymmetry • Structural Compliance <p><u>Contributions to System-Level Errors</u></p> <ul style="list-style-type: none"> • Sensitivity to Angular Acceleration about the Output Axis (Output Axis Sensitivity) • Scale Factor • Misalignment • Mass Unbalance • Undetected System Coning 	<p><u>Instrument-Level Errors</u></p> <ul style="list-style-type: none"> • Vibropendulous Error (Input-Pendulous Axis Crosscoupling) • Output-Pendulous Axis Crosscoupling • 2nd order nonlinearity • Anisoinertia • Output-Pendulous Axis Product of Inertia • Structural Compliance • Rebalance Loop Asymmetry • Size Effect <p><u>Contributions to System-Level Errors</u></p> <ul style="list-style-type: none"> • Sensitivity to Angular Acceleration about the Output Axis (Output Axis Sensitivity) • Scale Factor • Misalignment • Undetected System Sculling

The contribution of each error source considered in the analysis is printed out as a vector of angular velocity error, or acceleration error where appropriate. These error vectors are also defined in later paragraphs. The coefficient associated with each error expression may be either a deterministic quantity or a random variable. Examples of each type are presented in the discussion of instrument error sources in Section B.3-1. Individual deterministic angular velocity error vectors, defined for instrument- and system-level error sources, are summed to calculate a net deterministic angular velocity error vector. The separate angular velocity errors having random (but constant) coefficients are root-sum-squared, resulting in a vector whose components are the rms angular velocity errors about each system coordinate axis. Similar calculations are carried out for deterministic and random accelerometer error vectors. The four output vectors can be regarded as the deterministic and rms random values of effective gyro and accelerometer vibration-induced error. These can be applied as constant inputs to a separate error analysis, defined according to Eqs. (B.1-20) and (B.1-21), to determine the effect of major vibration-induced errors on navigator performance.

B.3.1 Instrument-Level Errors

The sources of output axis disturbance torques which are inherent in single-degree-of-freedom gyros and pendulous accelerometers are discussed at length in Chapter 2. In the presence of vibrations, many of these disturbances lead to constant error torques within the instruments. The major sources of such errors for the inertial instruments considered in this analysis are listed in Table B.3-1, and the error integrals, as they are defined in the program, are presented in Tables B.3-2 and B.3-3. A list of the symbols employed in these and later expressions is given in

TABLE B.3-2

MAJOR GYRO ERROR EXPRESSIONS

Anisoinertia	$\left(\frac{I_{ss} - I_{ii}}{H} \right) \int_0^{\infty} d\nu \phi_{is_R}(\nu) + \frac{I_{ss}}{H} \int_0^{\infty} d\nu \left(Q_R(\nu) \phi_{is_R}(\nu) - Q_I(\nu) \phi_{is_I}(\nu) \right)$
Spin-Input Crosscoupling	$-\left(\frac{1}{K_{sf} K_{po} K_{ac} K_{dc}} \right) \int_0^{\infty} d\nu \left(G'_R(\nu) \phi_{is_R}(\nu) - G'_I(\nu) \phi_{is_I}(\nu) \right)$
Spin-Output Crosscoupling	$\frac{I_{oo}}{(H K_{sf} K_{po} K_{ac} K_{dc})} \int_0^{\infty} \nu d\nu \left(G'_R(\nu) \phi_{os_I}(\nu) + G'_I(\nu) \phi_{os_R}(\nu) \right)$
Rebalance Loop Asymmetry (rms error)	$\frac{\epsilon}{\pi} \left[\int_0^{\infty} d\nu G(\nu) ^2 \phi_{ii}(\nu) \right]^{1/2}$
Structural Compliance (rms error)	$\int_0^{\infty} d\nu \left[K'_{so} \psi_{oi_R}(\nu) + K'_{si} \psi_{ii}(\nu) + (K'_{ss} - K'_{ii}) \psi_{is_R}(\nu) - K'_{io} \psi_{os_R}(\nu) - K'_{is} \psi_{ss}(\nu) \right]$

Table B.3-4. The sensor transfer functions appear in several error expressions and are calculated in the program in terms of their real and imaginary components.

$$\hat{\omega}_i = G(\nu) \omega_i \tag{B.3-1}$$

$$\hat{a}_i = A(\nu) a_i \tag{B.3-2}$$

TABLE B. 3-3

MAJOR ACCELEROMETER ERROR EXPRESSIONS

<p>Vibropendulous Error</p>	$-\frac{1}{(K_{sf} K_{po} K_{ac} K_{dc})} \int_0^{\infty} d\nu \left(A'_R(\nu) \Psi_{ipR}(\nu) - A'_I(\nu) \Psi_{ipI}(\nu) \right)$
<p>Output-Pendulous Error</p>	$\frac{I_{oo}}{(PK_{sf} K_{po} K_{ac} K_{dc})} \int_0^{\infty} \nu d\nu \left(A'_R(\nu) \Gamma_{piI}(\nu) - A'_I(\nu) \Gamma_{piR}(\nu) \right)$
<p>Scale Factor Nonlinearity (rms error)</p>	$K_2 \int_0^{\infty} d\nu \Psi_{ii}(\nu)$
<p>Anisoinertia</p>	$\left(\frac{I_{pp} - I_{ii}}{P} \right) \int_0^{\infty} d\nu \Phi_{ipR}(\nu)$
<p>Output-Pendulous Product of Inertia</p>	$\frac{I_{op}}{P} \int_0^{\infty} d\nu \Phi_{ioR}(\nu)$
<p>Structural Compliance (rms error)</p>	$\int_0^{\infty} d\nu \left[K'_{pi} \Psi_{ii}(\nu) + K'_{po} \Psi_{ioR}(\nu) + (K'_{pp} - K'_{ii}) \Psi_{ipR}(\nu) - K'_{io} \Psi_{opR}(\nu) - K'_{ip} \Psi_{pp}(\nu) \right]$
<p>Rebalance Loop Asymmetry (rms error)</p>	$\frac{\epsilon}{\pi} \left[\int_0^{\infty} d\nu A(\nu) ^2 \Psi_{ii}(\nu) \right]^{1/2}$
<p>Size Effect for Accelerometer # 1</p>	$\int_0^{\infty} d\nu \left\{ -p_{x1} (\Phi_{pp}(\nu) + \Phi_{oo}(\nu)) + p_{y1} \Phi_{ioR}(\nu) + p_{z1} \Phi_{ipR}(\nu) + p_{x3} G(\nu)A(\nu) C(\nu) ^2 \Phi_{oo}(\nu) + p_{x2} G(\nu)A(\nu) C(\nu) ^2 \Phi_{pp}(\nu) - p_{y3} [G_R(\nu)A_R(\nu) - G_I(\nu)A_I(\nu)] C(\nu) ^2 \Phi_{ioR} - p_{y3} [G_I(\nu)A_R(\nu) + G_R(\nu)A_I(\nu)] C(\nu) ^2 \Phi_{ioI} - p_{z2} [G_R(\nu)A_R(\nu) - G_I(\nu)A_I(\nu)] C(\nu) ^2 \Phi_{ipR} - p_{z2} [G_I(\nu)A_R(\nu) + G_R(\nu)A_I(\nu)] C(\nu) ^2 \Phi_{ipI} \right\}$

TABLE B. 3-4

LIST OF SYMBOLS

(For Tables B. 3-2 and B. 3-3)

$\Phi(\nu)$	angular velocity spectral densities	$C(\nu)$	transfer function representing navigation system computer operation
$\Psi(\nu)$	linear acceleration spectral densities	$Q(\nu)$	gyro wheel speed control loop transfer function
$\Gamma(\nu)$	spectral densities of products of angular velocity and linear acceleration	<u>Transfer Function Parameters</u> <u>Applicable to Both Instruments</u>	
$V(\nu)$	Fourier transform	J, F, B	sensor transfer function parameters
ν	radian frequency	T_1, T_2, T_4	compensation network parameters
R	subscript; real component	T_a, T_b, T_c	bandpass filter parameters
I	subscript; imaginary component	K_{po}	sensor pickoff gain
i, o, s	subscripts; gyro coordinate frame, input axis, output axis, spin axis	K_{ac}	demodulator ac gain
i, o, p	subscripts; accelerometer coordinate frame, input axis, output axis, minus pendulous axis	K_{dc}	compensation network dc gain
α_o	angular displacement about sensor output axis; the gyro float angle or the pendulous accelerometer gimbal angle	K_{sg}	signal generator gain
$G(\nu)$	gyro transfer function relating input motion to indicated output	K_{tg}	torque generator gain
$G'(\nu)$	gyro transfer function relating input motion to α_o	K_{sf}	instrument scale factor
$A(\nu)$	accelerometer transfer function relating input motion to indicated output	<u>Gyro Parameters</u>	
$A'(\nu)$	accelerometer transfer function relating input motion to α_o	H	gyro angular momentum
		I_{ii}	moment of inertia of the gimbal-rotor combination about the gyro input axis
		I_{oo}	moment of inertia of the gimbal-rotor combination about the gyro output axis

TABLE B. 3-4 (Continued)

LIST OF SYMBOLS

(For Tables B. 3-2 and B. 3-3)

I_{ssg}	moment of inertia of the gimbal about the gyro spin axis	I_{pp}	moment of inertia of the pendulum-gimbal combination about the accelerometer pendulous axis
I_{ssr}	moment of inertia of the about the gyro spin axis	I_{op}	product of inertia of the pendulum-gimbal combination about the accelerometer output and pendulous axes
$K'_{is} \triangleq \frac{m}{H} K_{is}$	where m is the rotor mass and K_{is} is the structural compliance coefficient relating rotor center of mass displacement along the gyro input axis to acceleration along the gyro spin axis; similar expressions apply for the other coefficients	$K'_{ip} \triangleq \frac{m}{P} K_{ip}$	where m is the mass gimbal-pendulum structure and K_{ip} is the structural compliance coefficient relating the gimbal-pendulum center of mass displacement along the accelerometer input axis to acceleration along the accelerometer pendulous axis; similar expressions apply for the other coefficients
$\delta'_i \triangleq \frac{m}{H} \delta_i$	where m is the rotor mass and δ_i is the displacement of the float center of mass along the input axis; similar expressions apply for the other coefficients	e	
SF _g	gyro output scale factor error	SF _a	accelerometer output scale factor error
D _{g_o} , D _{g_s}	misalignment of the gyro coordinate frame about the output and spin axes respectively.	K ₂	accelerometer output scale factor non-linearity
ε	torque generator scale factor asymmetry	D _{ap}	misalignment of the accelerometer coordinate frame about the pendulous axis
<u>Accelerometer Parameters</u>		ε	torque generator scale factor asymmetry
P	pendulosity of pendulum-gimbal combination	p	vector of displacement components of accelerometer axis system from the body coordinate frame
I _{ii}	moment of inertia of the pendulum-gimbal combination about the accelerometer input axis		
I _{oo}	moment of inertia of the pendulum-gimbal combination about the accelerometer output axis		

where

$\hat{\omega}_i$ = gyro indication of angular velocity
 ω_i about its sensitive axis

\hat{a}_i = accelerometer indication of acceleration
 a_i along its sensitive axis

and $G(\nu)$ and $A(\nu)$ are the closed loop gyro and accelerometer transfer functions respectively, defined as

$$G(\nu) \triangleq G_R(\nu) + j G_I(\nu)$$

$$A(\nu) \triangleq A_R(\nu) + j A_I(\nu)$$

The parameters of these closed loop transfer functions are input variables to the computer program. A linearized error model, applicable to both sensors, which is employed in defining these parameters, is shown in Fig. B. 3-2. In the program, it is presently assumed that the transfer characteristics for all gyros and for all accelerometers are identical.

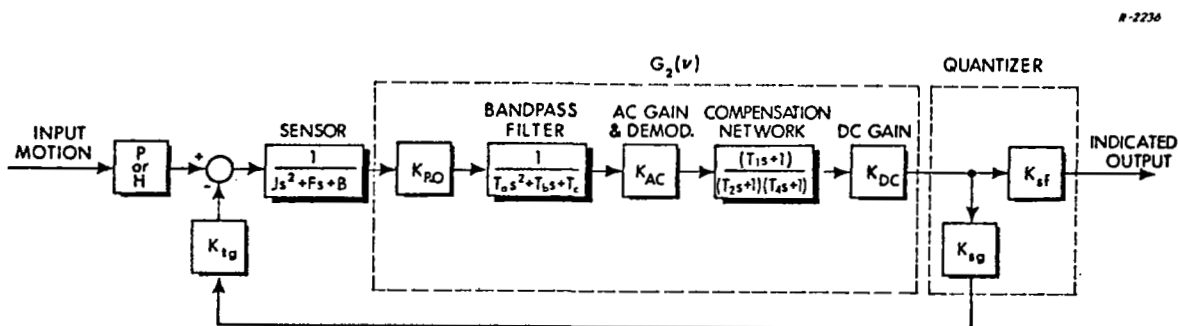


Figure 4. 3-2 Linearized Model for Gyros and Accelerometers

Gyro Error Sources – Anisoinertia error torques are a common source of vibration-induced error in a single-degree-of-freedom gyro. If the moments of inertia about the input and spin axes of the device are not matched, an error proportional to the product of the angular motion about these axes is created. The spin axis angular motion of the gyro case and gimbal is transferred to the rotor through the wheel speed control loop, which is modeled in the program as a 2nd-order transfer function.

$$Q(s) = \frac{\omega_r^2}{s^2 + 2\zeta\omega_r s + \omega_r^2}$$

where

ω_r = natural frequency of wheel speed control loop

ζ = damping ratio

s = Laplace variable

The spin axis inertia of the rotor can be considered coupled to the float only at vibration frequencies below the bandwidth of the control loop. Consequently, it is impossible to eliminate anisoinertia effects at both high and low angular vibration frequencies by choosing inertia properties.

The float angle generated by angular motion about the gyro input axis can couple with angular motion about the nominal rotor spin axis to produce a gyro drift rate having a non-zero average value. This effect is known as spin-input crosscoupling. The transfer function which relates the output angle to the input motion is defined as

$$G'(\nu) = \frac{G(\nu)}{K_{sf} G_2(\nu)} \quad (\text{B. 3-3})$$

The symbols appearing in the denominator of Eq. (B. 3-3) are defined in Fig. B. 3-2.

Spin-output crosscoupling is a similar source of vibration-induced error in which the float angle is generated by angular acceleration about the gyro output axis.

Asymmetry in the scale factor relating gyro output to the rebalance torque applied can result in a constant drift rate if the vibration frequency is within the loop bandwidth. In this analysis, linear rebalance electronics are assumed, for which the torquer gain for applying positive rebalance moments is $(1 + \epsilon)$ times that for negative moments. It can be shown that the error expression given in Table B.3-2 also applies for pulse rebalanced gyros, with an appropriate definition of ϵ .

Linear vibrations can also cause disturbance torques about the gyro output axis due to compliance in the gimbal and rotor structure. Although the structural compliance coefficients can be frequency-dependent, constant coefficients were assumed in deriving the error expression given in Table B.3-2.

Accelerometer Error Sources – Many of the vibration-induced errors which are significant for a pendulous accelerometer are similar to those defined for the single-degree-of-freedom gyro. The mechanisms for describing linear compliance errors, and also rebalance loop errors, are identical for these two devices. Anisoinertia affects propagate in the same way in both instruments, except there is no rotor in the pendulous accelerometer; the decoupling effects present in the gyro, a function

of the wheel speed control loop, are not present in the accelerometer. Vibropendulous error in the accelerometer, a function of linear vibrations, is analogous to spin-input crosscoupling in the gyro. A transfer function similar to that defined in Eq. (B.3-3) is calculated in the program to generate the crosscoupling error values. Sensitivity to angular acceleration about the output axis, an important source of gyro error, also results in crosscoupling errors in the pendulous accelerometer. This error source involves the coupling of angular and linear vibrations acting on the instrument and is identified in the program as output-pendulous axis crosscoupling. Constant errors involving the products of output axis and pendulous axis moments of inertia, which may be significant in a pendulous accelerometer, are included in the program as well. Scale factor nonlinearity in the accelerometer results in constant errors which are proportional to the square of acceleration along the sensitive axis of the device. The data available for the Kearfott 2401 (see Table 4.2-1) indicates that this effect may be important and it is also included in the program. An additional consideration is the physical separation of the accelerometer from the center of the strapdown navigator, which can result in erroneous indications of acceleration in a rotational vibration environment. The latter is referred to as "size effect." Size effect error includes components that rectify at the system level so that the transfer characteristics of the system computer, represented by

$$C(\nu) = C_R(\nu) + jC_I(\nu)$$

appear in the error expressions. An approximate computer model is presented in a later section.

The detailed error expressions are summarized in Table B.3-3. In the program, an input, output, pendulous axis coordinate system (i, o, p)

is defined for each accelerometer and this frame is employed in computing the error values.

Transformation of Error Values — Frequency-domain integration of the error expressions for each instrument yields the average values of the vibration-induced errors, in terms of false indications of motion parallel to each instrument sensitive axis. In order to express these errors in a form compatible with Eqs. (B.1-20) and (B.1-21), it is necessary to transform them into the body frame, a coordinate frame fixed in the navigator. The direction cosines describing the orientation of the sensitive axis of each instrument relative to this body frame are provided as input data to the computer program. The errors are then transformed into the body frame as they are calculated. For example, the j^{th} error source for the i^{th} gyro is expressed in body coordinates as

$$\left[\frac{\delta\omega_{b_j}}{g_i} \right]_i = \frac{d}{g_i} \delta\omega_j \quad (\text{B. 3-4})$$

where

$\frac{d}{g_i}$ = vector of direction cosines relating the i^{th} gyro sensitive axis to body axes

Accelerometer errors are transformed into the body frame in a similar fashion.

Some of the error coefficients defined in the program and listed in Tables B.3-2 and B.3-3 may be random variables. For example, compliance coefficients are often given as the rms value of a zero-mean random variable, defined for an ensemble of instruments. Other parameters, such as moments of inertia, can be more easily measured and are generally treated as deterministic quantities for a particular instrument. In

establishing the net effect of vibration-induced instrument errors, the deterministic errors can be added directly, but it is necessary to treat the the random errors statistically. The relation employed in calculating deterministic gyro error is given in Eq. (B.3-5):

$$\underline{\delta\omega}_b = \sum_{i=1}^{n_g} \sum_{j=1}^{n_{dg}} \left[\underline{\delta\omega}_{bj} \right]_i \quad (\text{B.3-5})$$

where

$$\begin{aligned} n_g &= \text{number of gyros} \\ n_{dg} &= \text{number of deterministic} \\ &\quad \text{gyro error sources} \end{aligned}$$

The components of the vector $\underline{\delta\omega}_b$ appear as elements of $\delta\Omega_b$ in Eq.(B.1-21). A similar equation is employed to calculate net deterministic accelerometer error.

It is assumed that the random error sources are uncorrelated with one another and a root-sum-square of these contributions is performed to calculate a net rms value. For example, the rms gyro error along the x body axis can be expressed as

$$\sigma_{\delta\omega_{bx}} = \left\{ \sum_{i=1}^{n_g} \sum_{j=1}^{n_{rg}} \left(\left[\underline{\delta\omega}_{bj_x} \right]_i \right)^2 \right\}^{1/2} \quad (\text{B.3-6})$$

where

$$n_{rg} = \text{number of random gyro error sources}$$

Similar expressions define the rms gyro errors along the x and y body axes and the three components of rms accelerometer error.

B.3.2 System-Level Errors

The potential sources of constant and growing errors at the system level fall into two classes: those created by vibration-induced errors in the inertial instruments and those due to vibrations occurring at frequencies beyond the instrument bandwidths. (See Chapter 3 for further discussion.) Expressions defining the average values of system-level errors can be derived by an expansion of the product terms within the brackets in Eqs. (B.1-20) and (B.1-21). This expansion yields terms of the form $\delta\varphi_y \hat{a}_z$ where $\delta\varphi_y$ is the angular error about the y body axis and \hat{a}_z is the indicated acceleration along the z body axis. Average error values are determined as the sum of the average values of a number of such product terms. It is therefore more convenient to use an alternate (Ref.20) form of Eq. (B.2-2) in defining the error integrals.

$$\begin{aligned} \lim_{T \rightarrow \infty} \frac{1}{2T} \int_{-T}^T \delta\varphi_y(t) \hat{a}_z(t) dt &= \int_0^{\infty} d\nu \Gamma_R(\nu, \delta\varphi_y, \hat{a}_z) \\ &= \lim_{T \rightarrow \infty} \frac{1}{T} \int_0^{\infty} d\nu \left\{ V_{\delta\varphi_y}(\nu) V_{\hat{a}_z}^*(\nu) \right\}_R \end{aligned} \quad (4.3-7)$$

where

$$\begin{aligned} V_{\delta\varphi_y}, V_{\hat{a}_z} &= \text{Fourier transforms of } \delta\varphi_y, \hat{a}_z \\ \Gamma_R(\nu, \delta\varphi_y, \hat{a}_z) &= \text{the real component of the} \\ &\quad \text{cross-spectral density of} \\ &\quad \delta\varphi_y \text{ and } \hat{a}_z \end{aligned}$$

In order to derive the error expressions, it is first necessary to define Fourier transforms for all the terms resulting from an expansion of Eqs. (B.1-20) and (B.1-21). A representative sample of the required set of transforms is contained in Table B.3-5. Note that all of these expressions involve the transfer functions of an inertial instrument and also the navigation system computer. System-level errors must be treated in this fashion, since the magnitude and phase of the sensed vibrations are altered as they are processed through the instrument and the computer to the point where rectification constructively occurs. Only the transfer characteristics

TABLE B.3-5

DEFINITIONS OF FOURIER TRANSFORMS

Indicated Acceleration	$V_{\hat{a}_z}(\nu) \triangleq A(\nu) C(\nu) V_{a_z}(\nu)$
Indicated Angular Velocity	$V_{\hat{\omega}_z}(\nu) \triangleq G(\nu) C(\nu) V_{\omega_z}(\nu)$
Indicated Rotation	$V_{\hat{\phi}_z}(\nu) \triangleq -j \frac{G(\nu)C(\nu)}{\nu} V_{\omega_z}(\nu)$
Undetected Acceleration	$V_{\delta a_z}(\nu) \triangleq [1 - A(\nu) C(\nu)] V_{a_z}(\nu)$
Undetected Rotation	$V_{\delta \phi_z}(\nu) \triangleq -j \frac{[1 - G(\nu) C(\nu)]}{\nu} V_{\omega_z}(\nu)$
Gyro Output Axis Sensitivity	$V_{\delta \omega_x}(\nu) \triangleq j\nu \frac{I_{oo}}{H} G(\nu) C(\nu) V_{\omega_y}(\nu)$
Accelerometer Scale Factor	$V_{\delta a_x}(\nu) \triangleq (SF_a) A(\nu) C(\nu) V_{a_x}(\nu)$

of the computer are considered in this analysis. Other mechanization problems such as word length, algorithm errors, etc., which are also present in a strapdown system, are ignored. An approximate sample-and-hold model is used to represent the computer:

$$C(\nu) = \frac{1 - e^{-j\nu\tau}}{j\nu\tau} \quad (\text{B. 3-8})$$

where τ is the computer algorithm cycle time, assumed to be the same for both attitude and navigation calculations.

Given the necessary Fourier transforms, Eq. (B. 3-7) can be applied to determine the error integrals in terms of vibration environment cross-spectral densities. A number of simplifications can be made in defining these integrals. For example, it can be shown that the coning error terms in Eq. (B. 1-21) reduce to a skew-symmetric matrix whose elements are components of the vector

$$\overline{\delta\omega'} = 2 \begin{bmatrix} \overline{\delta\varphi_y \hat{\omega}_z} + \overline{\hat{\varphi}_y \delta\omega_z} - \overline{\delta\varphi_y \delta\omega_z} \\ - \overline{\delta\varphi_x \hat{\omega}_z} - \overline{\hat{\varphi}_x \delta\omega_z} + \overline{\delta\varphi_x \delta\omega_z} \\ \overline{\delta\varphi_x \hat{\omega}_y} + \overline{\hat{\varphi}_x \delta\omega_y} - \overline{\delta\varphi_x \delta\omega_y} \end{bmatrix} \quad (\text{B. 3-9})$$

where the bar denotes the average value of the error vector. In determining pseudo-coning error values the second-order terms in $\delta\omega'$, involving products of error coefficients, are neglected. These terms are also neglected in calculating pseudo-sculling errors, and the contributions of gyro and accelerometer errors to pseudo-sculling can be considered separately by defining the vectors

$$\underline{\delta a'} = \begin{bmatrix} \overline{\delta\varphi_y \hat{a}_z} - \overline{\delta\varphi_z \hat{a}_y} \\ \overline{\delta\varphi_z \hat{a}_x} - \overline{\delta\varphi_x \hat{a}_z} \\ \overline{\delta\varphi_x \hat{a}_y} - \overline{\delta\varphi_y \hat{a}_x} \end{bmatrix} \quad \left(\begin{array}{l} \text{contribution of} \\ \text{gyro errors} \end{array} \right) \quad (\text{B. 3-10})$$

$$\underline{\delta a''} = \begin{bmatrix} \overline{\hat{\varphi}_y \delta a_z} - \overline{\hat{\varphi}_z \delta a_y} \\ \overline{\hat{\varphi}_z \delta a_x} - \overline{\hat{\varphi}_x \delta a_z} \\ \overline{\hat{\varphi}_x \delta a_y} - \overline{\hat{\varphi}_y \delta a_x} \end{bmatrix} \quad \left(\begin{array}{l} \text{contribution of} \\ \text{accelerometer} \\ \text{errors} \end{array} \right) \quad (\text{B. 3-11})$$

Table B. 3-6 contains a sample of the error expressions as they appear in the computer program.

The calculation of system-level error values, is made more efficient by the use of matrices of standard integrals, which are defined in Table B.3-7. These matrices are defined in the data coordinate frame and the system-level errors, as expressed in Table B.3-6, are referenced to body coordinates. Therefore, a transformation of the spectral data is required in the program to properly set up the error expressions in terms of the standard integrals. For example, the vector of pseudo-coning error values resulting from scale factor error in the i^{th} gyro is given by

$$(\underline{\delta\omega'})_i = 2SF_g \begin{bmatrix} s'_{23} & - & s'_{32} \\ s'_{31} & - & s'_{13} \\ s'_{12} & - & s'_{21} \end{bmatrix} \quad (\text{B. 3-12})$$

TABLE B.3-6

TYPICAL SYSTEM-LEVEL ERROR EXPRESSIONS

Undetected System Coning	$2 \int_0^{\infty} \frac{d\nu}{\nu} \left[1 - G(\nu) C(\nu) ^2 \right] \Phi_{yz_I}(\nu)$
Undetected System Sculling	$\int_0^{\infty} \frac{d\nu}{\nu} \left\{ \Gamma_{zy_I}(\nu) + C(\nu) ^2 \left[\left(G_I(\nu) A_R(\nu) - G_R(\nu) A_I(\nu) \right) \Gamma_{zy_R}(\nu) - \left(G_R(\nu) A_R(\nu) + G_I(\nu) A_I(\nu) \right) \Gamma_{zy_I}(\nu) \right] \right\}$
Gyro Output Axis Sensitivity	$.2 \frac{I_{00}}{H} \int_0^{\infty} d\nu \Phi_{00}(\nu) G(\nu) C(\nu) ^2$
Accelerometer Scale Factor	$SF_a \int_0^{\infty} \frac{d\nu}{\nu} C(\nu) ^2 \left[\left(G_I(\nu) A_R(\nu) - G_R(\nu) A_I(\nu) \right) \Gamma_{xz_R}(\nu) - \left(G_R(\nu) A_R(\nu) + G_I(\nu) A_I(\nu) \right) \Gamma_{xz_I}(\nu) \right]$

where the scalars s' are elements of the matrix

$$S' = M S b_{-g_i} \frac{d}{-g_i}^T \tag{B.3-13}$$

The vector d_{g_i} is defined in Eq. (B.3-4) and M , also a program input, represents the transformation from the data to the body coordinate frame.

TABLE B.3-7

DEFINITIONS OF STANDARD INTEGRALS

$$P \triangleq - \int_0^{\infty} d\nu |G(\nu) C(\nu)|^2 \begin{bmatrix} \phi_{xx}^*(\nu) & \phi_{xy}^*(\nu) & \phi_{xz}^*(\nu) \\ \phi_{xy}^*(\nu) & \phi_{yy}^*(\nu) & \phi_{yz}^*(\nu) \\ \phi_{xz}^*(\nu) & \phi_{yz}^*(\nu) & \phi_{zz}^*(\nu) \end{bmatrix}$$

$$S \triangleq \int_0^{\infty} \frac{d\nu}{\nu} |G(\nu) C(\nu)|^2 \begin{bmatrix} 0 & \phi_{xy_1}(\nu) & \phi_{xz_1}(\nu) \\ -\phi_{xy_1}(\nu) & 0 & \phi_{yz_1}(\nu) \\ -\phi_{xz_1}(\nu) & -\phi_{yz_1}(\nu) & 0 \end{bmatrix}$$

$$PP \triangleq - \int_0^{\infty} d\nu G(\nu) A^*(\nu) |C(\nu)|^2 \begin{bmatrix} \phi_{xx}(\nu) & \phi_{xy}(\nu) & \phi_{xz}(\nu) \\ \phi_{xy}^*(\nu) & \phi_{yy}(\nu) & \phi_{yz}(\nu) \\ \phi_{xz}^*(\nu) & \phi_{yz}^*(\nu) & \phi_{zz}(\nu) \end{bmatrix}$$

$$U \triangleq - \int_0^{\infty} \frac{d\nu}{\nu} |G(\nu) C(\nu)|^2 \begin{bmatrix} \Gamma_{xx_1}(\nu) & \Gamma_{yx_1}(\nu) & \Gamma_{zx_1}(\nu) \\ \Gamma_{xy_1}(\nu) & \Gamma_{yy_1}(\nu) & \Gamma_{zy_1}(\nu) \\ \Gamma_{xz_1}(\nu) & \Gamma_{yz_1}(\nu) & \Gamma_{zz_1}(\nu) \end{bmatrix}$$

$$Q \triangleq \int_0^{\infty} d\nu G(\nu) A^*(\nu) |C(\nu)|^2 \begin{bmatrix} \Gamma_{xx}^*(\nu) & \Gamma_{yx}^*(\nu) & \Gamma_{zx}^*(\nu) \\ \Gamma_{xy}^*(\nu) & \Gamma_{yy}^*(\nu) & \Gamma_{zy}^*(\nu) \\ \Gamma_{xz}^*(\nu) & \Gamma_{yz}^*(\nu) & \Gamma_{zz}^*(\nu) \end{bmatrix}$$

$$V \triangleq -j \int_0^{\infty} \frac{d\nu}{\nu} G(\nu) A^*(\nu) |C(\nu)|^2 \begin{bmatrix} \psi_{xx}(\nu) & \psi_{xy}(\nu) & \psi_{xz}(\nu) \\ \psi_{xy}^*(\nu) & \psi_{yy}(\nu) & \psi_{yz}(\nu) \\ \psi_{xz}^*(\nu) & \psi_{yz}^*(\nu) & \psi_{zz}(\nu) \end{bmatrix}$$

$$R \triangleq -j \int_0^{\infty} \frac{d\nu}{\nu} G(\nu) A^*(\nu) |C(\nu)|^2 \begin{bmatrix} \Gamma_{xx}^*(\nu) & \Gamma_{yx}^*(\nu) & \Gamma_{zx}^*(\nu) \\ \Gamma_{xy}^*(\nu) & \Gamma_{yy}^*(\nu) & \Gamma_{zy}^*(\nu) \\ \Gamma_{xz}^*(\nu) & \Gamma_{yz}^*(\nu) & \Gamma_{zz}^*(\nu) \end{bmatrix}$$

$$W \triangleq - \int_0^{\infty} \frac{d\nu}{\nu} \begin{bmatrix} \phi_{xy_1}(\nu) \\ \phi_{yz_1}(\nu) \\ \phi_{xz_1}(\nu) \end{bmatrix}$$

$$X \triangleq \int_0^{\infty} \frac{d\nu}{\nu} \begin{bmatrix} 0 & \Gamma_{xy_1}(\nu) & \Gamma_{xz_1}(\nu) \\ \Gamma_{yx_1}(\nu) & 0 & \Gamma_{yz_1}(\nu) \\ \Gamma_{zx_1}(\nu) & \Gamma_{zy_1}(\nu) & 0 \end{bmatrix}$$

The vector $\underline{b}_{g_{i1}}$ is the first row of the B_{g_i} matrix defined in Eq. (B.2-6), which can be expressed as

$$B_{g_i} = \begin{bmatrix} \text{---} & \underline{b}_{g_{i1}}^T & \text{---} \rightarrow \\ \text{---} & \underline{b}_{g_{i2}}^T & \text{---} \rightarrow \\ \text{---} & \underline{b}_{g_{i3}}^T & \text{---} \rightarrow \end{bmatrix} \quad (\text{B.3-14})$$

Similar transformations of the standard integrals can be defined for all of the system-level error sources.

APPENDIX C

MOTION-INDUCED ERRORS IN VIBRATING STRING ACCELEROMETERS

This appendix describes motion-induced errors in vibrating string accelerometers, in terms compatible with the strapdown system error computer program described in Appendix B.

An illustration of the vibrating string accelerometer (VSA) is provided in Fig. C-1. The vibrating strings, string 1 and string 2 in the figure, are identical and are excited at their natural frequency of vibration. In the presence of accelerations along the sensitive axis the two masses deflect, increasing the tension (and hence the vibrational frequency) in one string, and decreasing it in the other. The frequency difference is proportional to the acceleration along the sensitive axis according to

$$\Delta\mu = \mu_1 - \mu_2 = Kf_x \quad (C-1)$$

where the x-axis is defined as the sensitive axis of the device and the scale factor K is given by

$$K = \frac{m}{2\ell_0} \sqrt{\frac{T_0}{h}} \left[\frac{1}{T_0} - \frac{2}{k\ell_0} \right] \quad (C-2)$$

m = mass of proof mass

ℓ_0 = nominal length of vibrating string

h = mass/length of string

T_0 = nominal tension in vibrating string

k = string stiffness coefficient

f_x = specific force along the sensitive axis

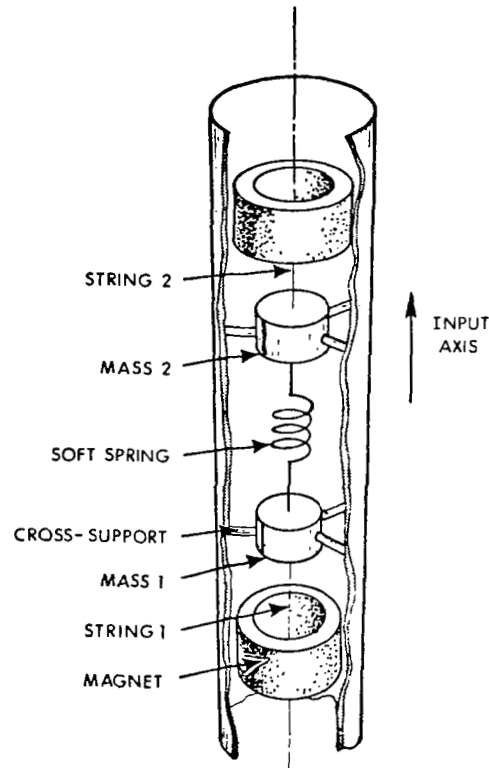


Figure C-1 Vibrating String Accelerometer
(AMBAC Industries D4e Model)

The use of two identical vibrating strings eliminates the even powers of f_x in the frequency difference expression, so that there is no rectification of linear vibrations. The two proof masses, separated by a soft spring, are necessary to avoid coupling of the string vibrations. The center spring also eliminates frequency differences created by expansion of the case structure. It transmits tension, however, and does not introduce any significant non-linearity into the VSA output. The symmetric supporting wires are very stiff in compression to reduce cross-axis sensitivity but they allow the proof masses to deflect along the sensitive axis in response to applied acceleration.

The following sources of VSA error are considered to be the most significant contributors to rectified acceleration error in the presence

of vibrations. Where appropriate, a physical description of the error is included.

Proof Mass Differences — The elimination of even-ordered non-linear terms in the frequency difference expression, Eq. (C-1), is achieved only if both halves of the VSA are identical. A difference in the two proof masses, expressed as

$$m_1 = m_2(1 + \epsilon)$$

will cause the frequency difference (accelerometer output) to depend on f_x^2 ; a non-zero average error is generated in a linear vibration environment. This can be expressed in terms of the sensitive axis acceleration power spectral density, Ψ_{xx} ;

$$\begin{aligned} \text{average acceleration error} \\ \text{due to proof mass differences} \end{aligned} = \frac{K_1}{K} \int_0^{\infty} \Psi_{xx}(\nu) d\nu \quad (C-3)$$

where K_1 is given by

$$K_1 = - \frac{m_2^2 \epsilon}{2k_0^2 \sqrt{hT_0}}$$

and K is the instrument scale factor defined in Eq. (C-2).

Differences in Spring Stiffness — A similar non-linear error term is introduced by differences in the stiffness coefficients of strings 1 and 2. If this difference is defined by

$$k_1 = k_2(1 + \epsilon)$$

the average value of the vibration-induced error is given by

$$\text{average acceleration error due to differences in string stiffness} \cong \left[\left(\frac{m^2 \epsilon}{4k_2^2 \ell_0^2 \sqrt{h T_0}} \right) / K \right] \int_0^\infty \Psi_{xx}(\nu) d\nu \quad (\text{C-4})$$

Mass Unbalance — If the center-of-mass of the proof mass is not coincident with its center of suspension, defined by the intersection of the supporting wire and vibrating string axes, an effective mass unbalance is created. The component of this mass unbalance along the sensitive axis, η_x , causes a torque, L, in the presence of cross-axis accelerations.

$$L_z = m \eta_x a_y$$

$$L_y = -m \eta_x a_z$$

Since the cross-axis supports have a relatively low rotational stiffness to allow for deflection of the proof mass, this disturbing torque must be balanced by increased tension in the vibrating string. The string tension will increase regardless of the sign of the disturbing torque, so that, considering only one proof mass, the apparent specific force along the VSA sensitive axis, given by Eq. (C-5), has a non-zero mean.

$$\delta f_x \cong - \frac{km \eta_x^2}{2bT_0^2} f_y^2 \quad (\text{C-5})$$

A similar expression exists for acceleration along the VSA z-axis. In general, cross-axis vibrations will induce a periodic increase in the tension of both vibrating strings due to proof mass unbalance, and hence an increase in their frequencies of vibration. Since the difference in string frequencies

is interpreted as a change in acceleration, these effects tend to cancel out. The error that is rectified is a function of the difference in the absolute values of the mass unbalance coefficients of the two proof masses. If we describe that difference as

$$|\eta_1| = (1 + \epsilon)|\eta_2|$$

the average acceleration error is given by

$$\text{average acceleration error due to mass unbalance} \cong - \frac{\epsilon k m}{b T_0^2} \eta_2^2 \int_0^\infty \Psi_{yy}(\nu) d\nu \quad (\text{C-6})$$

Cross-axis vibrations along the z-axis result in a constant drift rate in the same fashion.

Supporting Wire Compression — The cross-supports of the VSA proof masses are very stiff in compression to reduce the cross-axis sensitivity of the device. Any deflection of one of the proof masses induces an apparent sensitive axis acceleration that is a function of the square of the cross-axis acceleration.

$$\delta f_x = - \frac{km}{2l_0 k_\perp} f_y^2 \quad (\text{C-7})$$

where k_\perp is the stiffness coefficient of the supporting wires. Since both proof masses are deflected, a net acceleration error is present only if the stiffness coefficients of the two sets of supporting wires are different;

$$k_{\perp 1} = (1 + \epsilon) k_{\perp 2}$$

In that case, the average vibration-induced error is given by

$$\text{average acceleration error due to supporting wire compression} = - \frac{\epsilon km}{l_0 k_{\perp 2}^2} \int_0^{\infty} \Psi_{yy}(\nu) d\nu \quad (C-8)$$

The error due to z-axis linear vibrations is similarly defined.

Rotational Compliance — Because the design must permit the proof masses to deflect in the presence of sensitive-axis accelerations, the supporting wires provide little resistance to rotation of the proof mass. Therefore, the disturbing torque resulting from the angular rotation of the VSA case must be balanced by an increase in vibrating string tension. The effect is similar to that described for mass unbalance coefficients; ideally, the frequency changes cancel. If we allow for a difference in the cross-axis moments of inertia of the two proof masses

$$I_{yy1} = (1 + \epsilon) I_{yy2}$$

the average angular-vibration-induced error is given by

$$\text{average acceleration error due to rotational compliance} \cong \frac{\epsilon k}{bmT_0^2} I_{yy2}^2 \int_0^{\infty} \Phi_{yy}(\nu) \frac{d\nu}{\nu^2} \quad (C-9)$$

The effect of z-axis angular vibrations is described by an expression similar to Eq. (C-9).

Coriolis Effect — The physical separation of the two proof masses introduces a relative acceleration between them in the presence of angular

motion. If we assume that the separation distance, c , is fixed, the relative error is given by

$$\delta f_x = -(\omega_z^2 + \omega_y^2)c$$

The constant error contribution induced by random angular vibrations is given by

$$\begin{array}{l} \text{average acceleration error} \\ \text{due to Coriolis effect} \end{array} = -c \int_0^\infty d\nu \left[\Phi_{zz}(\nu) + \Phi_{yy}(\nu) \right] \quad (\text{C-10})$$

All of the previously described VSA errors depend upon manufacturing imperfections -- unmatched proof masses, unequal stiffnesses, etc. -- in the VSA. The coriolis effect, on the other hand, results from a physical characteristic of the instrument which is unavoidable. Hence, it is potentially a major source of vibration-induced accelerometer error.

Pseudo-Skulling -- Vibration-induced acceleration errors can couple with the correctly sensed angular rotations of the strapdown package to produce a pseudo-skulling effect. A major source of constant pseudo-skulling errors is VSA scale factor error introduced by proof mass differences. The oscillatory acceleration errors produced combine in the system calculation with angular oscillations which have the same frequency and phase to give a constant acceleration error in the nominal direction of one of the system axes. The average error generated by the x-accelerometer, y-gyro combination is given by

$$\begin{array}{l} \text{average pseudo-skulling error} \\ \text{due to proof mass differences} \end{array} = \frac{\epsilon}{2} \int_0^\infty \frac{d\nu}{j\nu} G(\nu)A(\nu) \Gamma_{yx}(\nu) \quad (\text{C-11})$$

where ϵ is the percent difference in the proof mass. This appears as an erroneous acceleration along the z system axis. The expression can be expanded in terms of the co-spectral and quadrature components. There are many other sources of pseudo-skulling error, all of which can be developed in a similar manner using the accelerometer error equations presented above.

APPENDIX D

ERROR DYNAMICS FOR SINGLE-AXIS-PLATFORM GYROS

In a single-axis-platform (SAP) configuration, the strapdown gyro is gimballed about its input axis to allow free rotation between the vehicle and the gyro. Ideally, the gyro itself does not rotate about its input axis when viewed from an inertial reference frame and the rate-of-change of the gimbal angle can be interpreted in terms of the angular rate of the vehicle. SAP outputs for three orthogonal body-fixed axes provide the angular motion information needed for attitude matrix calculations in the strapdown system. Any rotation of the gyro about its input axis causes a precession of the gyro float about its output axis (see Fig. D-1). The sensed precession angle is used to drive a torque motor which rotates the gyro case about its input axis in the reverse direction, to null the precession angle. The SAP output is in error by any residual rotation of the gyro about its input axis, whether caused by a combination of vehicle motion and gimbal friction or by unwanted torques on the output gimbal. In a vibration environment, the most serious rebalancing errors are those caused by disturbance torques about the gyro output axis which can result in a constant gyro drift rate. In this Appendix, the SAP transfer characteristics which describe gyro response to a general motion environment are derived in order to determine the nature of vibration-induced gyro drift rates.

Following Fig. D-1, the torque balance equation about the gyro input axis can be expressed as

$$B(\omega_i - \dot{\epsilon}_i) - T_g = (\dot{\underline{H}})_i \quad (D-1)$$

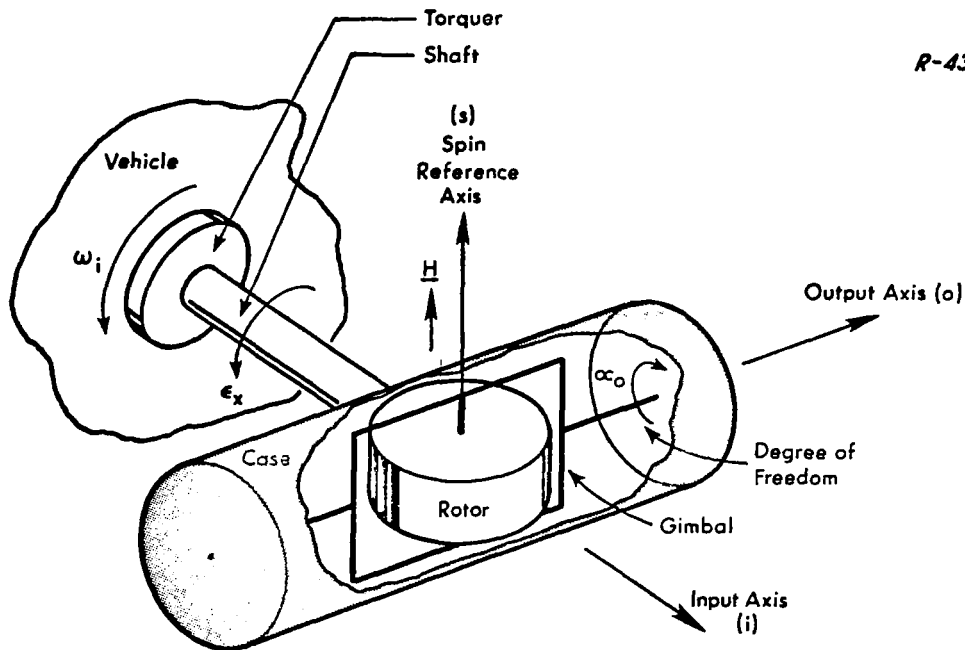


Figure D-1 Single-Axis-Platform Gyro

where

T_g = torque applied to the gimbal shaft by the torque generator

$(\dot{H}_I)_i$ = input axis component of the rate of change of gyro angular momentum with respect to inertial space

ω_i = input axis component of the inertial angular rate of the vehicle

ϵ_i = inertial rotation angle of the gyro about its input axis

B = coefficient of viscous damping between the shaft and the vehicle.

The Laplace transform transfer function for the applied torque T_g is given by (Ref. 17)

$$T_g = \frac{K/R}{\tau_m s + 1} \left[L(s) \alpha_o(s) - 60K (\omega_i(s) - s \epsilon_i(s)) \right] \quad (D-2)$$

where

K = constant flux motor coefficient

R = armature resistance

α_o = gyro float angle

$L(s)$ = float angle to input armature voltage transfer function

τ_m = torque motor time constant

The major torques acting about the gyro input axis to produce a time rate of change of angular momentum are represented in the equation

$$\left(\dot{\underline{H}}_I \right)_i = I_{iiG} \ddot{\epsilon}_i + H (\omega_o + \dot{\alpha}_o) \quad (D-3)$$

where

I_{iiG} = moment of inertia of the gyro and SAP gimbal shaft about the gyro input axis

ω_o = output axis component of the inertial angular rate of the vehicle

Substituting Eqs. (D-2) and (D-3) into (D-1) and using Laplace transform notation results in the expression

$$\begin{aligned}
& B \left[\omega_i(s) - s\epsilon_i(s) \right] - \frac{K_1 L(s)}{\tau_m s + 1} \alpha_o(s) + \frac{K_2}{\tau_m s + 1} \left[\omega_i(s) - s\epsilon_i(s) \right] \\
& = I_{ii_G} s^2 \epsilon_i(s) + H \left[\omega_o(s) + s\alpha_o(s) \right] \tag{D-4}
\end{aligned}$$

where $K_1 = K/R$ and $K_2 = 60K^2/R$.

The gyro float angle α_o reflects both gyro rotation about its input axis and the disturbance torques which act about the gyro output axis. A general expression for this behavior is given by

$$\alpha_o(s) = \frac{H/C}{s(I_{oo}/C + 1)} \left(s\epsilon_i(s) - M_d(s) \right) \tag{D-5}$$

where

$M_d(s)$ = output axis component of the disturbance torques acting on the gyro float

I_{oo} = moment of inertia of the gimbal-rotor combination about the gyro output axis

C = viscous damping coefficient of the gyro float

$I_{oo}/C \triangleq \tau_f$, gyro float time constant

Substituting Eq. (D-5) into (D-4) and combining terms results in the expression

$$\left\{ \left[I_{ii} G + \frac{H^2/C}{s(\tau_f s + 1)} \right] s + \left[B + \frac{K_2}{\tau_m s + 1} + \frac{(H/C) K_1 L(s)}{s(\tau_f s + 1)(\tau_m s + 1)} \right] \right\} s \epsilon_i(s)$$

$$= \left[B + \frac{K_2}{\tau_m s + 1} \right] \omega_i(s) - H \omega_o(s) + \left[\frac{(H/C) K_1 L(s)}{s(\tau_f s + 1)(\tau_m s + 1)} + \frac{H^2/C}{(\tau_f s + 1)} \right] M_d(s)$$

(D-6)

It is convenient to express the effects of vehicle vibrations in terms of the gyro input axis drift, $s \epsilon_i(s)$. Equation (D-6) can be rearranged as

$$s \epsilon_i(s) = G_1(s) \omega_i(s) + G_2(s) \omega_o(s) + G_3(s) M_d(s) \quad (D-7)$$

where $G_1(s)$, $G_2(s)$ and $G_3(s)$ represent the appropriate transfer characteristics derived from Eq. (D-6). This general expression is used to define the system-level vibration-induced errors in the SAP system in the manner outlined in Ref. 3.

APPENDIX E

DESCRIBING FUNCTION CALCULATIONS

Describing Function – The describing function for a nonlinearity may be defined as follows (Ref. 10):

$$\begin{aligned} N_A(A) &= \frac{\text{phasor representation of output component at frequency } \omega}{\text{phasor representation of input component at frequency } \omega} \\ &= \frac{A_1(A)}{A} \exp(j\varphi_1(A)) \end{aligned} \quad (\text{E-1})$$

where $A_1(A)$ and $\varphi_1(A)$ represent the amplitude and phase of the first-harmonic in the output of the nonlinearity when its input is

$$\begin{aligned} x &= A \sin \omega t \\ &= A \sin \psi \end{aligned} \quad (\text{E-2})$$

Denoting the output of the nonlinearity by $y(s)$, Fourier series manipulations result in the following form for $N_A(A)$

$$N_A(A) = \frac{j}{\pi A} \int_0^{2\pi} y(A \sin \psi) e^{-j\psi} d\psi \quad (\text{E-3})$$

If the nonlinearity is odd and memoryless, this can be simplified to

$$N_A(A) = \frac{4}{\pi A} \int_0^{\pi/2} y(A \sin \psi) \sin \psi d\psi \quad (\text{E-4})$$

Example 1 — Figure E-1(a) illustrates a sinusoidal input and the corresponding output for a binary (two-level) nonlinearity. From Eq. (E-4), the describing function is computed as

$$\begin{aligned} N_A(A) &= \frac{4}{\pi A} \int_0^{\pi/2} D \sin \psi \, d\psi \\ &= \frac{4D}{\pi A} \end{aligned} \quad (\text{E-5})$$

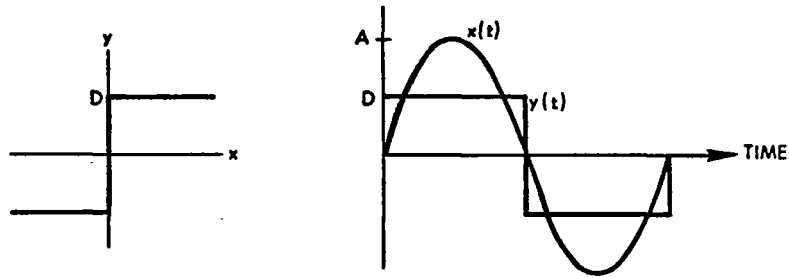
Example 2 — Figure E-1(b) illustrates a sinusoidal input and the corresponding output for a ternary (three-level) nonlinearity. From Eq. (E-4), the describing function is computed as

$$\begin{aligned} N_A(A) &= \frac{4}{\pi A} \int_{\psi_1}^{\pi/2} D \sin \psi \, d\psi \\ &= \frac{4D}{\pi A} \cos \psi_1 \\ &= \frac{4D}{\pi A} \sqrt{1 - \left(\frac{\delta}{A}\right)^2} \end{aligned} \quad (\text{E-6})$$

Dual Input Describing Function — For our present purposes we define the dc gain of a nonlinearity to be the ratio of dc output to dc input, over one limit cycle period. Thus, for $x = B + A \sin \psi$, we get

$$N_B(A, B) = \frac{1}{2\pi B} \int_0^{2\pi} y(B + A \sin \psi) \, d\psi \quad (\text{E-7})$$

Example 3 — The model input and corresponding output waveforms for a binary nonlinearity are shown in Fig. E-2a. Equation (E-7) yields



(a) Binary (Two-level) Nonlinearity

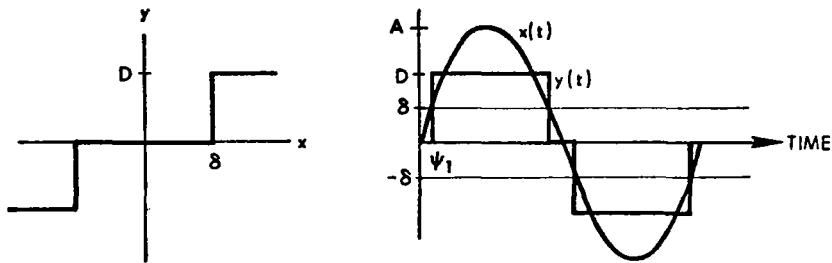
(b) Ternary (Three-level) Nonlinearity, $\psi_1 = \sin^{-1}(\delta/A)$

Figure E-1 Nonlinearity Input and Output Waveforms

$$\begin{aligned}
 N_B(A, B) &= \frac{1}{2\pi B} \left[\int_0^{\pi + \psi_2} D \, d\psi + \int_{\pi + \psi_2}^{2\pi - \psi_2} (-D) \, d\psi + \int_{2\pi - \psi_2}^{2\pi} D \, d\psi \right] \\
 &= \frac{2D}{\pi B} \psi_2 \\
 &= \frac{2D}{\pi B} \sin^{-1} \left(\frac{B}{A} \right) \qquad (E-8)
 \end{aligned}$$

Example 4 — A two-segment piecewise-linear asymmetric nonlinearity is illustrated in Fig. E-2b. Equation (E-7) yields, for the equivalent dc gain,

$$\begin{aligned}
 N_B(A, B) &= \frac{1}{2\pi B} \left[\int_0^{\pi + \psi_2} m_1 (B + A \sin \psi) d\psi + \int_{\pi + \psi_2}^{2\pi - \psi_2} m_2 (B + A \sin \psi) d\psi \right. \\
 &\quad \left. + \int_{2\pi - \psi_2}^{2\pi} m_1 (B + A \sin \psi) d\psi \right] \\
 &= \frac{m_1 + m_2}{2} + \frac{m_1 - m_2}{\pi} \left[\psi_2 + \frac{A}{B} \cos \psi_2 \right] \\
 &= \frac{m_1 + m_2}{2} + \frac{m_1 - m_2}{\pi} \left[\sin^{-1} \frac{B}{A} + \frac{A}{B} \sqrt{1 - \left(\frac{B}{A}\right)^2} \right] \quad (E-9)
 \end{aligned}$$

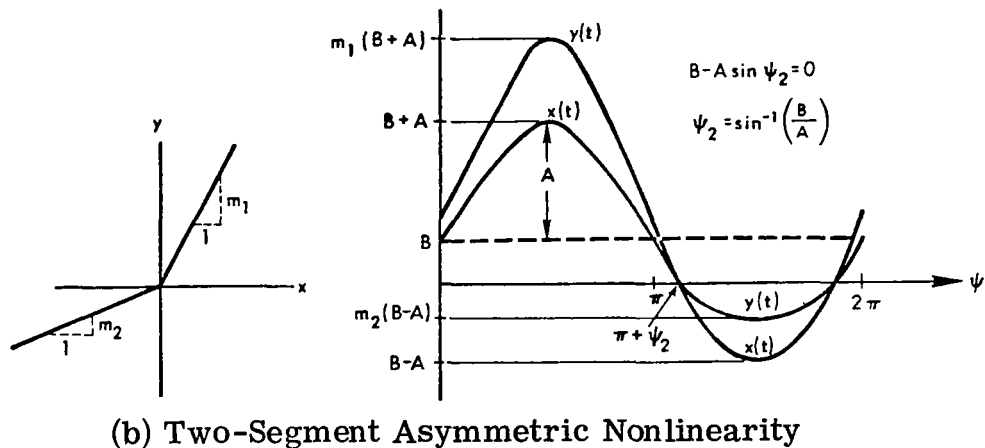
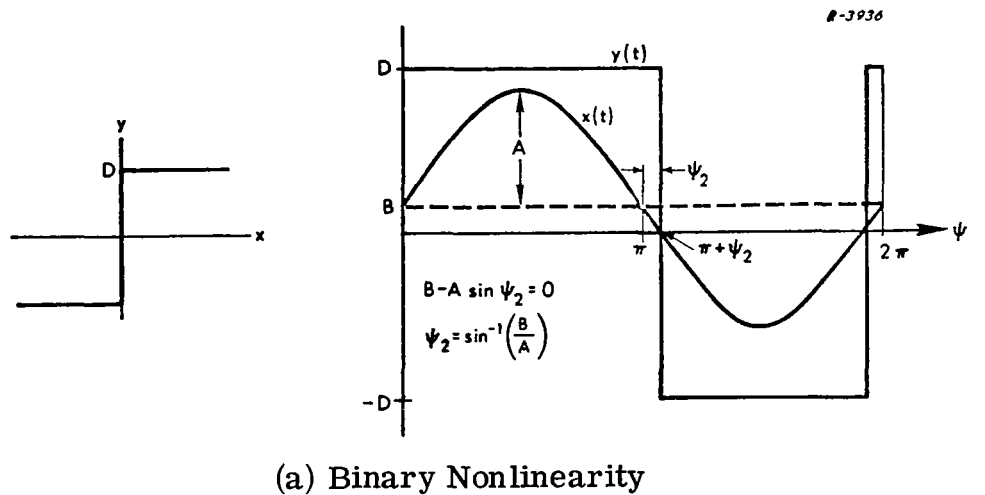


Figure E-2 Input and Output Waveforms for Two Nonlinearities with Bias Plus Sinusoid Input

REFERENCES

1. Gelb, A. and Sutherland, A.A., Jr., "Design of Strapdown Gyroscopes for a Dynamic Environment," Interim Scientific Report, The Analytic Sciences Corp., TR-101-2, January, 1968.
2. Sutherland, A.A., Jr., and Beebee, W.S., "Design of Strapdown Gyroscopes for a Dynamic Environment," Interim Scientific Report II, The Analytic Sciences Corp., TR-101-4, January, 1969, (NASA CR-1396).
3. Koenigsberg, W.D., Dunn, J.C., and Fagan, J.H., "Design of Strapdown Gyroscopes for a Dynamic Environment," Phase III Final Report, The Analytic Sciences Corp., TR-101-6, March, 1970.
4. Weinstock, H., "Effect of Angular Vibration on Gyroscope Performance," M.I.T. Department of Aeronautics and Astronautics, Notes from Summer 1963 Program 16.39S.
5. Weinstock, H., "Effects of Linear Vibration on Gyroscope Instruments," M.I.T. Department of Aeronautics and Astronautics, Notes from Summer 1963 Program 16.39S.
6. Goodman, L.E., and Robinson, A.R., "Effect of Finite Rotations on Gyroscopic Sensing Devices," ASME Journal of Applied Mechanics, June, 1958, pp. 210-213.
7. Sher, L., and Fagan, J.H., "Strapdown Navigator Errors in a Vibration Environment," Proc. of the Fifth Inertial Guidance Test Symposium, Holloman Air Force Base, New Mexico, October, 1970.
8. Isakson, D., "Linear and Angular Vibration Measurement of V/STOL Aircraft," Final Report, Contract NAS12-2028, Hamilton Standard Division, United Aircraft Corp., Windsor Locks, Conn., April, 1970.
9. Farrell, J. L., "Performance of Strapdown Inertial Attitude Reference Systems," AIAA Journal of Spacecraft, Vol. 3, No. 9, September 1966, pp. 1340-1347.

10. Gelb, A., and VanderVelde, W.E., Multiple-Input Describing Functions and Nonlinear System Design, McGraw-Hill Book Co., Inc., August 1968.
11. Booton, R.C., Jr., Mathews, M.V., and Siefert, W.W., "Nonlinear Servomechanisms with Random Inputs," M.I.T. DACL Report 70, August, 1953.
12. Hatanaka, H., "The Frequency Response and Jump-Resonance Phenomena of Nonlinear Feedback Control Systems," Trans. ASME, J. Basic Eng., Vol. D-85, June, 1963, pp. 236-242.
13. Fukuma, A., and Matsubara, M., "Jump Resonance Criteria of Nonlinear Systems," IEEE Trans. Automatic Control, Vol. AC-11, No. 4, October 1966, pp. 699-706.
14. Gelb, A. and Sutherland, A.A., Jr., "Design of Strapdown Gyroscopes for a Dynamic Environment," Semi-Annual Report, The Analytic Sciences Corp., TR-101-1, 7 July, 1969.
15. D'Azzo, J.J., and Houpis, C.H., Feedback Control System Analysis and Synthesis, 2nd Edition, McGraw-Hill Book Co., 1966.
16. Bar-Itzhack, I.Y., "Strapdown Inertial Navigation," Doctoral Dissertation, University of Pennsylvania, Dept. of E.E., 1968.
17. Bar-Itzhack, I.Y., "Strapdown SAP Gyro in a Back-to-Back Configuration," IEEE Trans. on Automatic Control, Vol. AC-14, No. 6, December 1969.
18. Laning, J.H. and Battin, R.H., Random Processes in Automatic Control, McGraw-Hill Book Co., Inc., 1956.
19. Mason, S.J. and Zimmerman, H.J., Electronic Circuits, Signals and Systems, John Wiley and Sons, Inc., 1960.